UNIVERSITÀ DEGLI STUDI DI CAMERINO

School of Advanced Studies

Doctorate course in

"Computer Science"

Science and Technology

Seismic reliability of buildings isolated with rubber bearings

PhD Student

Dott. Fabio Micozzi

Supervisor

Prof. Andrea Dall'Asta

Curriculum coordinator

Prof Emanuela Merelli

Seismic reliability of buildings isolated with rubber bearings

by

Fabio Micozzi

Doctor of Philosophy in Computer Science – Science and Technology
University of Camerino, Italy

Contents

List of Figures

List of Tables

List of Acronyms

CLS	*Collapse Limit State (NTC)*
CS	*Conditional Spectrum*
CSSB	*Concave Surface Slider Bearing*
D/C	*Demand Capacity ratio*
DLS	*Damage Limit State (NTC)*
EDP	*Engineering Demand Parameter*
eG	*existing gravity load designed building*
eS	*existing seismic load designed building*
FSB	*Flat Slider Bearing*
GC	*global collapse*
GMPE	*Ground Motion Prediction Equation*
HDRB	*High Damping Rubber Bearing*
HPP	*Homogeneous Poisson Process*
IM	*intensity measure*
IML	*intensity measure level*
LSLS	*Life Safety Limit State (NTC)*
NTC	*Norme Tecniche per le Costruzioni (CS.LL.PP., 2008, 2018)*
NTHA	*Nonlinear Time History Analysis*
PBEE	*performance-based earthquake engineering*
POA	*PushOver Analysis*
PSHA	*Probabilistic Seismic Hazard Assessment*
Tr	*Return Period*
UHS	*Uniform Hazard Spectrum*
UPD	*usability-preventing damage*

CHAPTER 1

1 Introduction

1.1 Premise

"The art of Civil Engineering is to foresee the unforeseeable". These are the first few words of Calgaro and Gulvanessian (2001) and in these few words are condensed all the challenges that engineers face in their activities. Engineering design is an "art" because it is a non-straightforward process producing unique objects within a context involving tangible and intangible inputs and not only the rational solution of a technical problem. Structural design combines subjective decision-making (e.g., heuristics), concerning judgment, aesthetic and conceptualization of complex problems, and objective knowledge (e.g., engineering science) providing predictive models and evolving according to scientific method.

There is so a fundamental difference between "*structural design*" (the practice of structural engineers, related to *knowing-how*) and the underlying "*engineering science*" (the work of engineering scientist, related to *knowing-that* or in general engineering knowledge) (Bulleit et al., 2015, Popper, Karl 1959). *Engineering science* is core or kernel of engineering design knowledge (Dias 2019). It studies and develops theoretical models to describe the behaviour of complex systems involving man-made objects and their interaction with surrounding environment.

The term Civil Engineering was born in the past to distinguish from the Military Engineering (in France, the military engineer was given formal status by the creation of a *Corps des Ingénieurs du Génie Militaire* by Maréchal Vauban) and its meaning has evolved over time (Muir Wood, 2012, Blockley, 2014). Nowadays the term relates to that branch of engineering which is concerned with the creation of structures and infrastructures for the society, as highlighted by the definition (WIKIPEDIA)

> *"Civil engineering is a professional engineering discipline that deals with the design, construction and maintenance of the physical and naturally built environment, including public works such as roads, bridges, canals, dams, airports, sewerage systems, pipelines, structural components of buildings, and railways"*

where "Civil" implying the link with the citizen and with civilization (Muir Wood, 2012). Civil Engineering differs from other branches of engineering because it usually deals with non-prototypical engineered systems, for which prototype testing is not possible and thus uncertainties are significantly increased (Blockley, 1980).

In the field of structural design, the aim of engineers is to create structures with adequate safety and serviceability under the influence of the relevant loads and actions during their lifetime. Moreover, structural design must deal with other aspects such as efficiency, environmental impact, aesthetic and economic boundary, searching an optimum balance between all of them (Blockley, 1980). Engineering also involves reconceptualizing a complex situation to facilitate analysis; it includes problem definition, not just problem solution (Bulleit et al., 2015).

Research in Civil Engineering field studies many aspects listed before, especially the most quantifiable such as models and methods used in the structural response analysis or for the safety assessment. Research in this fields is usually pure "engineering science" and, according to Popper "hard science".

Safety is one of the most important requirements for a structure and a main topic of past and current research; it is something related to the probability that undesirable event occur. For example, research into structural reliability, based upon probability theory, has been useful in determining values of partial factors for structural design but it has been mainly focused in considering random overload and understrength failure in the past. The *partial factor method* has been a big step forward for structural design, but it represents only a small part of the total global problem of structural safety (human error is the predominating cause of failure occurred in the past) (Blockley, 1980).

To limit the probability of undesirable events and ensure it is below a pre-defined threshold that can be accepted by the public opinion is a task recognized by all the codes acting nowadays worldwide. The hazards to be considered in evaluating the structural safety are many, such as over-vertical load, understrength, earthquakes, fire, floods and also explosions and vehicle impacts. Indeed, even if many theoretical tools are available to define the probabilistic response of structures and assess the consequences and costs related to the repairing damages, downtime and rebuilding (e.g., *Performance Based Earthquake Engineering* framework for earthquake hazard)(Cornell and Krawinkler, 2000, Porter, 2003), the concept of "acceptable" risk of losses and human death, resulting from structural failure, raises very sensitive questions that concern public perception. The acceptable risk is a reflection of personal and societal value judgements, as well as disaster-based experience: for example, additional requirements in regulation and codes generally follows tragedies (Calgaro and Gulvanessian, 2001, Fajfar, 2018).

According to (Calgaro, 2011) and (Fajfar 2018), the public aversion to failure and the societal desire of protection are increasing. Moreover, the vulnerability and the loss registered in our modern cities in the last decades are increasing compared to the past (Daniell et al. 2011, Munich RE 2018). In fact, despite the awareness of seismic risk is increasing, the urban environment is getting more and more complicated, interconnected and expensive (Gkoumas et al., 2015, Franchin, 2018). Research in the last decades focused on how the risk and the losses related to undesirable events can be assessed and reduced.

1.2 Motivations and objectives

Focusing on the field of earthquake engineering, the conventional seismic resistant design is intended to resist major earthquake avoiding collapse and loss of life but allowing structural and non-structural damage.

Although life safety is still an essential performance for any structure, strategic buildings such as hospitals, public office buildings and major infrastructures must achieve higher performance because of their role in the post-earthquake activities. Many private building owners, in the wake of the public aversion to failures and cost related to damages after an earthquake mentioned before, are also increasingly interested in higher performance levels of the structure (Christopoulos and Filiatrault 2006).

In the last decades, a lot of research has been conducted in developing innovative earthquake-resistant systems capable to increase the seismic performance in a more cost-effective way (Soong and Constantinou 1994, Christopoulos and Filiatrault 2006), moving from a simple life-safety design to a higher performance level. Most of the innovative anti-seismic technologies are based on the passive control of the dynamic behaviour of the structure (i.e. devices that work during an earthquake without any external energy supply, opposed to the active control where the motion of a structure is controlled or modified by means of the action of a control system through some external energy supply). Passive technologies can be divided into two groups: (*i*) systems based on energy dissipation introducing supplemental damping devices and (*ii*) systems to limit the transmission of seismic energy to the main structure by seismic isolation devices.

Structures equipped with these systems undergo low deformations and accelerations, recovering from the effects induced by the ground shaking without showing widespread damages on the structural components and regaining the initial status in a timely and efficient manner (Scozzese 2019). The advantages of these systems compared to standard structures are:

- Reduction of downtime or even continued functionality immediately after the earthquake (only post-event inspection is required)
- Reduction of direct and indirect post-earthquake costs (costs are only related to maintenance and, if necessary, to the replacement of the devices)
- Safety of the occupants is ensured since the damage of structural and non-structural components is avoided (safety may be endangered by non-structural elements such as partition walls, ceilings and furniture)
- Occupant perception of the earthquake is low because accelerations are reduced.

Because of the crucial role played by passive devices for the performance of structures during and after a seismic event, such devices must be designed in order to provide proper safety margins against anticipated failures and therefore to guarantee a proper level of reliability. Their premature failure may lead to an abrupt collapse of the entire structure as a very fragile system. The past research has been focused on how seismic isolation and energy dissipation devices work in reducing the damage to structural and non-structural components (Soong and Constantinou, 1994), while only recently the research started to study the reliability of these systems (Ragni et. al. 2018, Scozzese et. al. 2019, Kitayama and Constantinou 2019, Shao et al. 2019, Rezaei Rad and Banazadeh, 2018).

The work carried out in this Thesis aims to provide a contribution in the field of reliability of isolated structure equipped with High Damping Rubber Bearings (*HDRBs*), one of the most common passive technology currently used to protect strategic buildings such as hospitals. More in detail, this PhD dissertation is focused on the risk assessment of seismically isolated buildings and covers various topics ranging from the isolators modelling to the evaluation of the probability of failure, including deeper insights and original contributions on isolators modelling, evaluation of failure probability, reliability of conventional design procedures, and description of seismic hazard for isolated structures.

A set of case studies has been defined representing new isolated buildings and existing buildings designed according the current Italian code, (referred to as Norme Tecniche per le Costruzioni, or NTC, CS.LL.PP., 2008, 2018). Two sites located in Italy (i.e., L'Aquila and in Naples, both soil type C) has been considered. All the buildings have been then modelled employing state-of-art methodologies accounting for the nonlinear behaviour of both isolation system and superstructure. The structural reliability, expressed in terms of annual failure rates, has been assessed for each case according to the paradigm of P*erformance-Based Earthquake Engineering* (Cornell and Krawinkler, 2000, Porter, 2003). A performance level has been defined for both collapse (for both superstructure and isolation system) and damage of non-structural components of the superstructure and, based on global parameters, the relative failure criteria have been defined to calculate failure rates. The resulting probabilities of failure have been compared to the target reliability to check if the design code provides adequate levels of safety and which are the main parameters influencing the actual reliability of code-conforming buildings.

Part of the work on the reliability of seismically isolated buildings presented hereafter was carried out within the research program *RINTC – Rischio Implicito delle strutture progettate secondo le NTC* project (Iervolino and Dolce, 2018), which addressed the seismic structural reliability implicit by design according to the Italian code for different structural typologies.

Although this thesis is focused on *HDRBs* rubber bearings, some results regarding a hybrid isolation system composed by *HDRBs* and *Flat Sliding Bearings* (*HDRBs+FSBs*) and *concave surface sliding bearings* (*CSSBs*) are also reported for comparison purpose (Iervolino and Dolce 2018, Iervolino et. al. 2018, Iervolino et al. 2019, Ragni et. al, 2018, ReLUIS-RINTC 2018, Cardone et al. 2017, Cardone et al. 2019).

1.3 Outline of the thesis

After a brief introduction regarding principles and dynamic behaviour of seismic isolation, all the methods and the characteristics of the framework used within this Thesis are exposed in Chpt. 2 . Chpt. 3 contains all the models for isolation bearings, superstructure and hazard assessment, with particular attention on the specific feature necessary to assess reliability of isolated buildings. Chpt. 4 reports the design procedure and the description of the outcoming case studies. Then, for each of them, a risk assessment in terms of performance levels for collapse and damage of isolated systems has been carried out. More in detail, these results are grouped based on the specific isolator's model used in the time history analyses. Both new seismically isolated structures and existing structure retrofitted with rubber bearings located in two sites (L'Aquila and Naples) have been assessed. At the end of chapter are resumed all annual rates of collapse and the annual rates of damage, highlighting similarities and differences of case studies results. The comparison is extended also to some results of equivalent fixed-base structure, showing a significant difference between isolated structure and fixed-base one up to an order of magnitude. The source of this difference is therefore identified in the hazard assessment procedure made for isolated buildings and the other structures like RC fixed-base structures. For this reason, further hazard assessment is carried out in Chpt. 5 using the most recent Italian tools and methods available; a comparison between the reliability results based on the new hazard and the previous ones shows a reduction of the differences between isolated structures and fixed-base structures. Moreover, an innovative procedure to calculate the hazard curves directly from the record selection sets has been used. In this way a clear quantitative comparison of the hazard intensity has been carried out, showing that different choices during the hazard assessment may significantly affect the hazard level and consequently the reliability results.

1.4 Chapter's references

Blockley, D. I., 1980. The nature of structural design and safety. Chichester, UK: Ellis Horwood Limited.

Blockley, D., 2014. Structural engineering: a very short introduction, 1st ed. ed, Very short introductions. Oxford University Press, Oxford.

Bulleit, W., Schmidt, J., Alvi, I., Nelson, E., Rodriguez-Nikl, T., 2015. Philosophy of Engineering: What It Is and Why It Matters. J. Prof. Issues Eng. Educ. Pract. 141, 02514003. https://doi.org/10.1061/(ASCE)EI.1943-5541.0000205

C.E.N. 2002. European standard EN 1990:2002. Eurocode: basis of structural design. European Committee for Standardization, Brussels, Belgium.

C.E.N. 2004. Eurocode 8: Design of Structures for Earthquake Resistance: Part 1: General Rules, Seismic Actions and Rules for Buildings, European Committee for Standardization, Brussels, Belgium.

Calgaro, J.-A., (2011) Safety philosophy of Eurocodes. ISGSR 2011 - Vogt, Schuppener, Straub & Bräu (eds) - © 2011 Bundesanstalt für Wasserbau ISBN 978-3-939230-01-4

Calgaro, J.-A., Gulvanessian. 2001. "Management of reliability and risk in the Eurocode system". IABSE International Conference "Safety, Risk and Reliability – Trends in Engineering", Malta 21-23 mars 2001

Cardone, D., Conte, N., Dall'Asta, A., Di Cesare, A., Flora, A., Leccese, G., Mossucca, A., Micozzi, F., Ponzo, F.C., Ragni, L., 2017. RINTC PROJECT: NONLINEAR ANALYSES OF ITALIAN CODE-CONFORMING BASE-ISOLATED BUILDINGS FOR RISK OF COLLAPSE ASSESSMENT, Proc. of 6th ECCOMAS Thematic Conference on Computational Methods in Structural Dynamics and Earthquake Engineering (COMPDYN 2017), Rhodes Island, Greece. pp. 1732–1747. https://doi.org/10.7712/120117.5525.19365

Cardone, D., Conte, N., Dall'Asta, A., Di Cesare, A., Flora, A., Lamarucciola, N., Micozzi, F., Ponzo, F., Ragni, L., 2019. RINTC-E PROJECT: THE SEISMIC RISK OF EXISTING ITALIAN RC BUILDINGS RETROFITTED WITH SEISMIC ISOLATION, in COMPDYN 2019 - 7th ECCOMAS Thematic Conference on Computational Methods in Structural Dynamics and Earthquake Engineering, Crete, Greece. https://2019.compdyn.org/proceedings/pdf/19921.pdf

Christopoulos, C., Filiatrault, A., 2006. Principles of Passive Supplemental Damping and Seismic Isolation - IUSS Press - Eucentre Press. Pavia, Italy

Cornell CA, Krawinkler H. 2000. Progress and challenges in seismic performance assessment. PEER News; 3(2).

CS.LL.PP. 2008. Norme tecniche per le costruzioni," Gazzetta Ufficiale della Repubblica Italiana 29. (In Italian.)

CS.LL.PP. 2018. Aggiornamento delle norme tecniche per le costruzioni," Gazzetta Ufficiale della Repubblica Italiana 42. (In Italian.)

Daniell, J.E., Khazai, B., Wenzel, F., Vervaeck, A., 2011. The CATDAT damaging earthquakes database. Nat. Hazards Earth Syst. Sci. 11, 2235–2251. https://doi.org/10.5194/nhess-11-2235-2011

Dias, P., 2019. Philosophy for Engineering: Practice, Context, Ethics, Models, Failure, SpringerBriefs in Applied Sciences and Technology. Springer Singapore, Singapore. https://doi.org/10.1007/978-981-15-1271-1

Fajfar, P., 2018. "Analysis in seismic provisions for buildings: past, present and future", The fifth Prof. Nicholas Ambraseys lecture. Bull Earthquake Eng 16, 2567–2608. https://doi.org/10.1007/s10518-017-0290-8

Franchin, P., 2018. Research Needs Towards a Resilient Community, in: Pitilakis, K. (Ed.), Recent Advances in Earthquake Engineering in Europe: 16th European Conference on Earthquake Engineering-Thessaloniki 2018. Springer International Publishing, Cham, pp. 661–691. https://doi.org/10.1007/978-3-319-75741-4_28

Gkoumas, K., Petrini F., Bontempi F., 2015. Design for Robustness, Resilience and anti-Fragility in the Built and Urban Environment: Considerations from a civil Engineering Point of View. Proceedings of the 4th International Workshop on Design in Civil and Environmental Engineering.

Iervolino, I., Dolce, M., 2018. Foreword to the Special Issue for the RINTC (The Implicit Seismic Risk of Code-Conforming Structures) Project. Journal of Earthquake Engineering 1–4. https://doi.org/10.1080/13632469.2018.1543697

Iervolino, I., Spillatura, A., Bazzurro, P., 2018. Seismic Reliability of Code-Conforming Italian Buildings. Journal of Earthquake Engineering 22, 5–27. https://doi.org/10.1080/13632469.2018.1540372

I. Iervolino, A. Spillatura, P. Bazzurro. 2019. RINTC-E project: towards the assessment of the seismic risk of existing buildings in Italy, in COMPDYN 2019 - 7th ECCOMAS Thematic Conference on Computational Methods in Structural Dynamics and Earthquake Engineering, Crete, Greece. https://2019.compdyn.org/proceedings/pdf/20038.pdf

Kitayama, S., Constantinou, M.C., 2019. Probabilistic seismic performance assessment of seismically isolated buildings designed by the procedures of ASCE/SEI 7 and other enhanced criteria. Engineering Structures 179, 566–582. https://doi.org/10.1016/j.engstruct.2018.11.014

Muir Wood, D., 2012. Civil engineering: a very short introduction, 1st ed. ed, Very short introductions. Oxford University Press, Oxford.

Munich Re NatCatSERVICE, 2018 Münchener Rückversicherungs-Gesellschaft, NatCatSERVICE – https://natcatservice.munichre.com/

Popper Karl R. 1959. The logic of scientific discovery. London: Hutchinson of London.

Porter, K.A. (2003). An overview of PEER's performance-based earthquake engineering methodology. Proc. Ninth International Conference on Applications of Statistics and Probability in Civil Engineering (ICASP9) July 6-9, 2003, San Francisco, CA. Civil Engineering Risk and Reliability Association (CERRA), 973-980, http://spot.colorado.edu/~porterka/Porter-2003-PEER-Overview.pdf

Ragni, L., Cardone, D., Conte, N., Dall'Asta, A., Cesare, A.D., Flora, A., Leccese, G., Micozzi, F., Ponzo, C., 2018. Modelling and Seismic Response Analysis of Italian Code-Conforming Base-Isolated Buildings. Journal of Earthquake Engineering 0, 1–33. https://doi.org/10.1080/13632469.2018.1527263

Rezaei Rad, A., Banazadeh, M., 2018. Probabilistic Risk-Based Performance Evaluation of Seismically Base-Isolated Steel Structures Subjected to Far-Field Earthquakes. Buildings 8, 128. https://doi.org/10.3390/buildings8090128

Scozzese, F., Dall'Asta, A., Tubaldi, E., 2019. Seismic risk sensitivity of structures equipped with anti-seismic devices with uncertain properties. Structural Safety 77, 30–47. https://doi.org/10.1016/j.strusafe.2018.10.003

Shao, B., Mahin, S.A., Zayas, V., 2019. Achieving targeted levels of reliability for low-rise seismically isolated structures. Soil Dynamics and Earthquake Engineering 125, 105744. https://doi.org/10.1016/j.soildyn.2019.105744

Soong, T.T., Constantinou, M.C. (Eds.), 1994. Passive and Active Structural Vibration Control in Civil Engineering, CISM International Centre for Mechanical Sciences. Springer Vienna, Vienna. https://doi.org/10.1007/978-3-7091-3012-4

Wikipedia, the free encyclopedia. Civil Engineering. https://en.wikipedia.org/wiki/Civil_engineering

CHAPTER 2

2 State of the art

2.1 Seismic isolation

Seismic isolation of buildings is based on the disconnection between foundation and superstructure (i.e., the portion of the structure above the isolation system) using isolation bearings. These devices are characterized by a low horizontal stiffness, usually much lower than the lateral stiffness of the superstructure, and by the capacity of undergoing horizontal displacement of the order of tenths of centimetres while maintaining vertical support. The superstructure horizontal motion is therefore decoupled from the ground motion and the displacements are concentrated at the isolators' level.

From a dynamic point of view, seismic isolation shifts the fundamental period of vibration of the structure beyond the predominant period of earthquakes (usually between 0.1 and 1s), thus avoiding resonance. Usually the isolation period is set higher than 2s and recently technological advancements are pushing forward to reach periods higher than 4s. In this way, seismic isolation deflects the earthquake energy by changing the dynamics of the system. If the superstructure is stiff, higher modes contribute only marginally to the seismic response. In this case, the isolated system behaves almost equivalently to a single degree of freedom (SDOF) one, with the superstructure behaving as a rigid mass.

Additional damping is usually provided to the system to suppress possible resonance at the isolation frequency and reduce the total displacement of isolation bearings (Naeim and Kelly, 1999, Christopoulos and Filiatrault 2006).

High technology internal equipment of strategic buildings such as hospitals equipment are vulnerable to interstory drift (i.e., displacement between two floors) and floor accelerations. Seismic isolation is very effective to protect these strategic buildings because it reduces simultaneously both drifts and accelerations.

The number of seismically isolated buildings is growing and nowadays they are more tens of thousands worldwide (Clemente and Martelli, 2017). Only in Japan, according to the Japan Society of Seismic Isolation (JSSI, 2018) until the end of 2017, more than 4500 big isolated buildings have been built. There are many large-scale projects worldwide regarding residential complex, airport terminals, bridges and so on protected with seismic isolation (Clemente and Martelli, 2017). Some of the largest isolated structures in the world have been recently finished (for example Apple park, California, 2017, Adana Integrated Health Campus, 2017, Tokyo Skytree East Tower, 2012, Isparta City Hospital, 2016, Logistic Park Hino, 2015) (Scott Lewis 2017), confirming that the superior performance of isolated structure is also economically affordable.

The effectiveness of seismic isolation in reducing damage has been widely investigated in the literature and it has been confirmed by the reconnaissance reports after the major earthquakes: seismically isolated buildings performed well, under seismic actions even exceeding the design ones, and continued to be used immediately after the earthquakes, with no loss of building functionality (AIJ, 2012, Morita and Takayama, 2017). The Lu Shan County hospital behaviour during the Lushan earthquake in 2013 is one of the clearest examples of superior performance of seismically isolated buildings. The hospital was composed of three buildings, but only one had been seismically isolated; the isolated building didn't suffer any damage or loss of functionality and all the injured people received first aid assistance there. On the contrary, the other two blocks, built according to traditional anti-seismic design, suffered damage to structural and non-structural components; even if they didn't collapse, they were fully out of service (Clemente and Martelli, 2017, Fu Lin Zhou, 2015).

Only few cases of isolation failures have been registered worldwide and none of them, to the author's opinion, can be directly related to the failure of isolated system when these were designed correctly following code provisions. For example, the Sendai-Tobu Viaduct during the 2011 Tohoku earthquake elastomeric bearings were strongly damaged, but it isn't clear if the failure is related to an inappropriate design of the bearings or an unexpected interaction between adjacent decks (Kawashima, 2012). There are also other failures registered worldwide (Zayas et al., 2017) related to a wrong design (underestimation of the earthquake displacement demand of Trans-European Motorway in Bolu, Turkey)(Roussis et al. 2008), or directly related to a low quality of the production procedure (delamination of rubber bearings due to only dead loads during the construction) (Zayas et al., 2017). Another case of close-to-collapse event is the Los Caras bridge in Ecuador. During the 7.8 Mw (magnitude) Muisne earthquake the devices of one pier reached a very high displacement of 60cm (while the other 37 piers bearings underwent only a displacement around 30cm) due to an unexpected more flexible foundation of this pier than the others (Morales et. al. 2019). The bearings used in this bridge (the Triple Friction Pendulum, TFP, Fenz, and Constantinou 2008) provided a good performance: the outer retainer ring avoided the over-stroke and the downfall of the inner slider out of the external plates, resulting only in damage to the devices. But even in this case the unexpected behaviour is more related to a geotechnical issue than to an inadequate isolation design.

The performance of seismically isolated buildings can be also described in terms of resilience and robustness. In general, the concept of seismic resilience is related to the ability to overcome earthquake impacts through situation assessment, rapid response, and effective recovery strategies (measured in terms of reduced failure probabilities, reduced consequences, reduced time to recovery)(Bruneau et al., 2003). Another definition, more structural aimed, is reported in (Pitiliakis, 2015):

> *"Resilience referring to a single element at risk or a system subjected to natural and/or manmade hazards usually goes towards its capability to recover its functionality after the occurrence of a disruptive event. It is affected by attributes of the system, namely robustness (for example residual functionality right after the disruptive event), rapidity (recovery rate), resourcefulness and redundancy after the occurrence of a disruptive event."*

These last four attributes are also called the "*4R's*" (Franchin 2018).

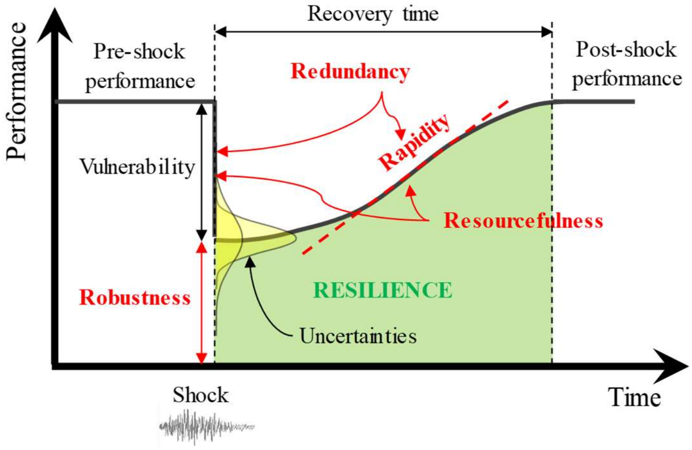

Figure 1. Resilience and the "4R's" (from Pitilakis 2015 and Franchin 2018)

Seismically isolated buildings are characterized by high resilience: losses are very low and the rapidity in recover is very high. For seismic intensities lower or equal the design one damages could be considered zero, without any loss of functionality, as confirmed also by recent real scale test of isolated structure on shaking table (Chen et al. 2016, Pantoli et al. 2016). But what about robustness? The term robustness can also indicate the ability to limit the consequences of exceptional events, not considered in the structural design. Many modern building codes refer to the need of robustness, in the sense that the *consequences of structural failure should not be disproportional to the effect causing failure* (CEN2002, Baker et al., 2008, Bontempi et al., 2007). Seismic actions are characterized by a high level of uncertainties that are only partially considered in the design process by the *partial factor design* (Calgaro and Gulvanessian, 2001, Fajfar, 2018); consequently, very different response can be observed under similar events. In this field, the robustness of structures plays a fundamental role for safety of people and constructions.

As discussed before, while seismic isolation systems can be regarded as resilient ones in the sense that they are very effective in reducing or totally avoiding damage and downtime for low-medium intensity earthquakes, they appear to be not very robust with respect to rare seismic inputs with intensity much higher than the design one. In other words, seismically isolated structures are affected by the so called "*cliff edge effect*", that is, according to the International Atomy Energy Agency (IAEA) safety glossary (IAEA 2018):

> *"An instance of severely abnormal conditions caused by an abrupt transition from one status of a facility to another following a small deviation in a parameter or a small variation in an input value".*

Indeed, finding and mitigating cliff edge effects is the main objective in the safety assessment of strategic buildings such as nuclear power plants (*NPPs*). For seismically isolated *NPPs* the cliff edge effect is related to the failure of seismic isolation devices or the collision of the superstructure with the retaining walls around the structure (Nishida et al., 2018). To better understand this concept, Nishida made a comparison between the performances of an earthquake resistant structure and a base isolated structure for *NPPs*.

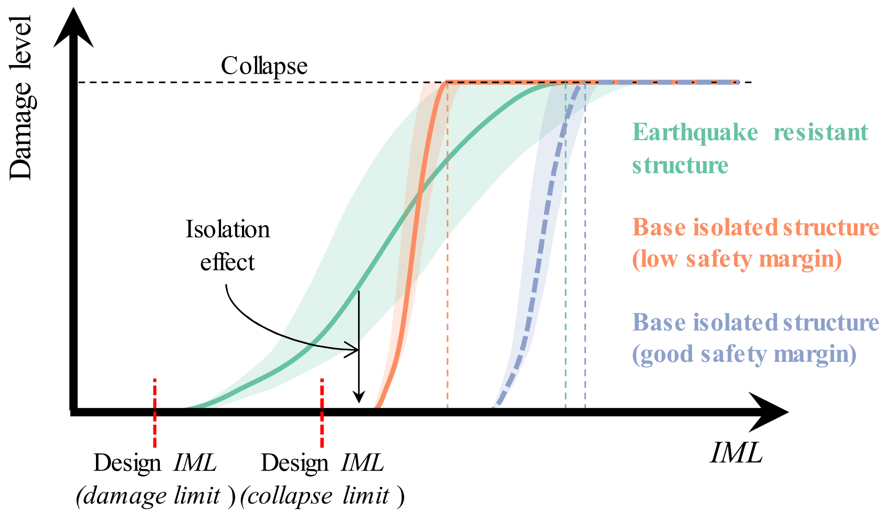

Figure 2. Seismic performance for earthquake resistance and base isolated structure beyond design earthquake (from Nishida et al. 2018)

To better understand the behaviour of seismically isolated structure respect to earthquake resistant structure with ductile behaviour (such as RC frame structures) Figure 2 shows levels of damage respect to the *Intensity Measure Level* (*IML*) of the seismic action. A standard system (green curve) is designed to avoid damage for frequent earthquake (*damage limit*) and to avoid collapse through structural damage for rare earthquakes (*collapse limit*). Uncertainties related to post-elastic behaviour are significant and so the seismic response variability is important (green area). On the contrary, seismically isolated buildings (orange curve) are designed to avoid damage even for high intensity earthquakes, and minimum requirements prescribed by the seismic codes guarantee that the collapse occur only for seismic higher than the design one (*collapse limit*). The margin between the design and the critical value of displacement is related to the safety factor used in the design. Since superstructure behaviour of isolated systems is expected to be in the linear elastic region until the bearings reach critical levels of displacements and the isolation behaviour is well known up to the design condition plus safety factors, response uncertainties are strongly reduced. But if this safety factors are too small collapses of isolated structure could be more frequent than earthquake resistant structure because the cliff edge effect occurs for quite low seismic intensities. But using a proper safety factor in the design (or an higher seismic design input) it is easily possible to achieve a proper level of reliability (blue curve) equivalent or higher than standard structures. From a different point of view, the *cliff edge effect* is therefore a possible positive feature of isolated structures. As shown Figure 2, the uncertainties of the response are lower than the equivalent earthquake resistant structure, leading to a sort of "step function" for the level of damage conditioned to the level of the earthquake intensity and consequently the safety factors can be better defined than standard structures.

In other words, the response of isolated structures is predicted more accurately than the response of fixed-base structures, because of the very low level of uncertainties in the response, as confirmed also by several blind engineering analysis contests in Japan (Zayas et al., 2017), further proving the reliability of the design. Even if this brittle behaviour is somehow undesirable (and it can be mitigated by energy absorber for the impact or plastic stoppers), the key point is to understand how much it can affect the reliability of the structure, or better whether particular failure modes triggered by seismic intensities beyond the design basis contribute significantly to the probability of failure (Booth and Baker, 2000).

Considering the "*4R's*" of Figure 1, seismic isolation shows very high performance in terms of rapidity. The recovery time is very low or equal to zero for low-medium intensity earthquake. Moreover, low uncertainties guarantee an high reliability of the system response while robustness could be low (see Figure 4).

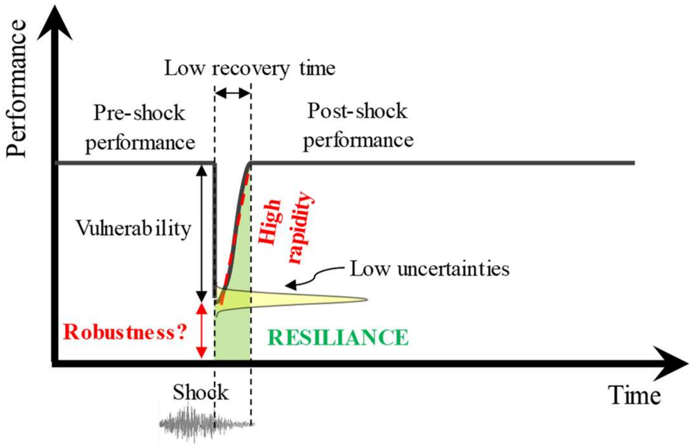

Figure 3. Performance of seismically isolated building

One of the first work on the safety of base isolated structures is the one of Kikuchi et al. (1995), who investigated the seismic response of a two degree of freedom (2DOF) nonlinear model. This study highlighted the advantages of seismic isolation with respect to traditional design, but also showed that seismically isolated structures designed with reduced lateral shear force (equivalently, with a large behaviour factor, i.e. the lateral force reduction factor used in the design) can exhibit significant inelastic actions and an unacceptable behaviour. In a later work (Kikuchi et al. 2008), the response of yielding seismically isolated structures was further studied, showing that sufficient lateral strength must be provided in the isolated superstructure, such that elastic or essentially elastic response dominates in a significant seismic event. In this way, a proper level of safety is achieved.

Nakazawa et al. (2011) performed incremental dynamic analysis (IDA) on a non-linear 2DOF model of an isolated building to determine the collapse margin ratio based on the FEMA P695 procedures (FEMA, 2009). Following the Japanese practice of seismic design, the strength of the superstructure was assumed in the range of 0.15 to 0.40 of the superstructure weight (common practice in Japan considers the value 0.3). In terms of modelling, they considered a trilinear degrading hysteretic behaviour for the superstructure and a combination of non-linear models for isolation, dampers and pounding with the retaining walls. Moreover, they considered the following ultimate states: (*i*) fracture of the bearing (after hardening behaviour of the rubber); (*ii*) collision of the superstructure with surrounding retaining walls; (*iii*) excessive damage in the superstructures. It is worth to note that the fracture shear limit of the rubber bearings in this study was fixed to 450%; beyond this limit the restoring force was replaced by the friction between the isolation layer and its foundation (assuming a post fracture behaviour, even if the fall down of the isolation layer due to isolator fracture is not considered). They also stated that robustness of the base-isolated buildings is generally considered lower than that of fixed-based structures.

Kitayama and Constantinou (2018) and Shao et al. (2019) assessed the reliability levels of seismically isolated steel frames (6 and 3-story respectively) designed according to ASCE/SEI 7-16, using triple friction pendulum bearings. The model used was a MDOF two-dimensional representation of the structure; the force-resisting frame in the principal direction was explicitly modelled with fiber non-linear elements. They showed that isolated structure designed according to ASCE/SEI 7 minimum requirements of either 2010 or 2016 may have unacceptable probability of collapse in the Risk-Targeted Maximum Considered Earthquake and the probability of collapse in the MCER becomes acceptable when they are designed with enhanced criteria of a lateral force reduction factor lower than 1.0 and providing a stiffening behaviour and an increase displacement capacity of the bearings respect to the displacement demand. The authors also highlighted the need to extend these studies to other structural systems (e.g., concrete frames), to other seismic isolation systems and to other sites, including near-fault sites. The last one is a key point, because the hazard scenario could strongly influence the results. It is also worth to note that the model used was only two-dimensional and no consideration regarding the three-dimensional behaviour of the isolation systems was made. First attempt to analyse different isolation systems in a three-dimensional model can be found in Rezaei Rad and Banazadeh (2018). Kitayama and Constantinou (2019) also investigated on their model (the one of Kitayama and Constantinou (2018)) the behaviour of isolated buildings in terms of performance levels other than the collapse one, such as those related to

damage of structural and non-structural components (monitored via peak drift, residual drift and average floor spectra acceleration).
In this context, the work carried out in this PhD thesis (and partially published in Ragni et al., 2018) is one of the first study on the reliability of seismically isolated structures on a full three-dimensional model considering various hazards and isolation systems.

2.2 Seismic risk assessment

Seismic risk assessment aims to define the probability of a structural system attaining an unsatisfactory performance (*failure*) within a reference lifetime. There are two different alternative probabilistic approach: (*i*) direct, simulation-based approach, (*ii*) conditional, *Intensity Measure* based approach (*IM* based) (Cornell 2005, Bradley et al. 2015). Despite the former generally represent the most robust way for estimating seismic risk, it is usually limited to the research field because of its complexity and because the computational effort is usually very demanding. Differently, the latter instead has been developed within the last 20 years with the main purpose of making seismic risk estimation a more practice-oriented and affordable task. The key of the *IM*-based approach is the definition of a specific parameter (the *Intensity Measure*) that represents properly the ground motion intensity of the earthquake. The use of this *IM* allows the seismic risk estimation procedure to be split into separate probabilistic steps: the first step concerns the seismic hazard characterization through a proper statistical representation of the IM; the second stage aims at evaluating the system vulnerability conditional to specific values assumed by the intensity measure (Scozzese, 2017). The *IM*-based (conditional) method has been introduced within the *Performance-Based Earthquake Engineering* (*PBEE*) probabilistic framework (Cornell and Krawinkler, 2000, Porter, 2003), developed by the Pacific Earthquake Engineering Research (PEER) Center as a reaction to the large amount of damage and economic losses (both direct and indirect due to repair) registered right after the 1994 Northridge and 1995 Kobe earthquakes. In *PBEE*, the final probabilistic output comes from the direct application of the total probability theorem, which allows for the combination of the partial results of several steps. There are different versions of the framework. The number and the types of steps depend on which result the assessment is aimed (e.g. probability of failure, loss analysis, final decision making), but they can be divided in three groups: a first part where there is the hazard assessment, a middle part where there is the system vulnerability assessment and a final part where there is the consequences assessment. Each step leads to a specific measure to determine as output quantity, and next steps use the output from the previous stage as input. The efficiency of such a conditional method is strictly related to the choice of the measure selected to link the *PBEE* framework's steps.

If the final target is the probability of failure, the risk assessment can be represented, according to the classical *PBEE* framework as in Figure 4. The reliability of the system (probability of failure), which is the target of this framework, can be quantified in terms of annual failure rate λ_f (mean frequency of occurrence of failure in a year the undesirable outcome).

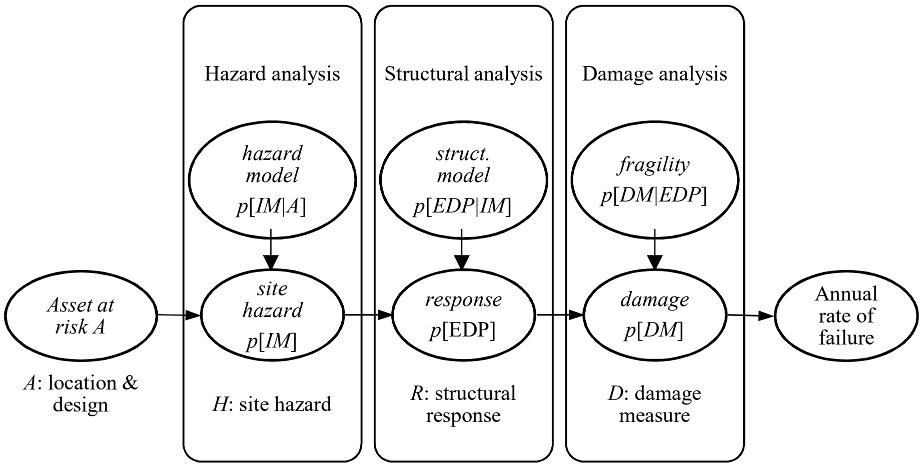

Figure 4: Adaptation of the PEER framework for the seismic risk assessment

The probabilistic steps are briefly recalled below, while a deeper discussion of the first two steps of the framework, of interest for the aims of the present thesis, is provided afterwards.

Hazard analysis: it is the analysis aimed to evaluate the mean annual frequency of exceedance of various seismic intensity levels at a particular site (Porter, 2019), called *Probabilistic Seismic Hazard Assessment* (*PSHA)*. As mentioned before, this involves selecting an adequate intensity measure (*IM*) as a synthetic descriptor of the earthquake intensity. The analysis output is expressed in terms of seismic hazard curves, providing the mean annual rate of exceedance of various *IM* levels.

Structural analysis: procedure to define the structural response, described by means of one or more Engineering Demand Parameters (*EDPs*). The output of interest is represented by the probability $p[EDP|IM]$. For these purposes, a set of nonlinear dynamic analyses is performed under a suite of ground motion records which should be ideally representative of the seismic hazard at the different *IM* levels (Jalayer, 2003, Luco and Cornell 2007, Jalayer and Cornell, 2009,). There are different methods for estimating the conditional probability $p[EDP|IM]$ (incremental dynamic analysis, multi-stripe analysis, cloud analysis) (Mackie and Stojadinovic, 2003).

Damage analysis: in this step, the structural response described through the *EDPs* is associated to quantifiable damage states. The *Fragility* is a mathematical function that expresses the probability that some undesirable event occurs (typically that an asset reaches or exceeds some clearly defined limit state) as a function of some measure of environmental excitation (typically a measure of acceleration, deformation, or force). It can be defined also as the cumulative distribution function of the capacity of an asset to resist an undesirable limit state (Porter, 2019).

It is worth to note that the decomposition that is at the base of *PBEE* relies upon the fundamental Markovian assumption that conditioned on *EDP*, *DM* is independent of *IM* (Kiureghian, 2005).

The *failure* of the system can be related to different performances of the system like a level of structural damage that is so high to make more economical to demolish than to repair the building, or a level of structural and non-structural damage that leads to the loss of serviceability. These performance levels can be associated to either global or local *EDPs*. Typical global *EDPs* are the inter-story drifts, able to furnish an indirect measure of structural damage (Kitayama et al. 2018, Kitayama et al. 2019) whereas local *EDPs* (Tubaldi et al., 2016; Dall'Asta et al., 2017; Freddi et al., 2013; Freddi et al., 2017; Mackie and Stojadinovic, 2003; Lupoi et al., 2002) are related to some specific element response (i.e., beam's plastic deformation, forces on dissipation device, etc.).

2.2.1 Seismic risk and design codes

Although current design codes for structures set target reliability levels, they fail in providing an explicit control of the seismic structural performance in the assessment and design stage (Gkimprixis et al. 2019, Iervolino et al. 2018). *Performance-Based Earthquake Engineering* and all the later evolutions (FEMA P-695, FEMA P-58, CNR 2014, CEN 2017) allow the explicit quantification of risk of collapse and of damage limit states, but these procedures are *"too complex and lengthy for routine use in the design"* (Haselton et al., 2017), and it is *"extremely unlikely that these methods will be adopted in seismic codes in the foreseeable future as a mandatory option"* (Fajfar, 2018).

Attempts to close the gap between probabilistic target and affordable methods for design are current research topic, and they can be gathered under the risk-targeting (Luco et al., 2007, Gkimprixis et al., 2019, Žižmond and Dolšek, 2019), and possibly will find their way into the next generation of codes.

Even if different approaches are implemented in modern codes (and fully explicit probabilistic approach would be included in few years or are still partially included), the current procedure mostly used by the engineers is the so-called *load-resistance-factor-design* (Ellingwood, 2000), better known as *partial factor design*. It is a compromise between probabilistic approach and a deterministic format (from here the name *semi-probabilistic* format) in which the structural safety verification is carried out by Calgaro (2011):

- selecting appropriate representative values of the various random variables (actions and resistances),
- applying a set of calibrated partial factors,
- applying safety margins, more or less apparent, in the various models (models of actions, of effects of actions and of resistances)
- verifying, in most common case, that the effect of the action (such as internal force), is lower than the resistance.

More in detail, current approaches for earthquake design of structures set a series of performance thresholds, or *Limit States,* that should not be exceeded under ground-motion intensities that have a specified exceedance probability in a given time interval at the building site.

The partial factors in the codes, for example in the Eurocodes, have been calibrated by using structural reliability methods to ensure a target failure probability of $7.2 \cdot 10^{-5}$ for common structures, during the entire working life (Calgaro, 2011, CEN 2002, HANDBOOK2). But it is well known that partial factor design, although has represented a giant leap in earthquake resistant design when introduced, does not allow to explicitly control the reliability of the designed structure for earthquake actions, that is ultimately unknown (Iervolino and Dolce, 2018).

Moreover, as stated in the introduction, the tolerable probability of failure is not only related to consequences in terms of risk to life and potential economic losses, but also a reflection of societal judgements (Fajfar, 2018). Target provided by the standard changed during time due to the developing of research. For example, in EN1990 (CEN 2002) the annual probability of failure is about $P_f \approx 10^{-6}$ (HANDBOOK2). But this is a value too low for seismic risk, unreachable by complying

with current seismic codes. For example, according to ASCE/SEI 7-16, the absolute collapse probability target is 1% in 50 years, that is a probability of failure $P_f = 2 \times 10^{-4}$. (ASCE, 2017). This is the most popular value for the annual probability of failure (Fajfar, 2018), and it is also suggested in the draft Annex to the revised Eurocode 8 (CEN 2017, Dolsek 2017). It is also comparable to the probabilities of failure estimated for buildings compliant with current seismic codes (Fajfar, 2018). Therefore, the current state of the art for reliability target is a different value of probability of failure for seismic action and the other load conditions (gravity load, wind, snow…). A reason for this bias is that the different perception of the failure related to an earthquake is somehow considered more acceptable respect to a gravity load failure. Moreover, it is also reasonable that current standards provide an economically-balanced level of security.

2.2.2 RINTC Framework

In the framework of the *RINTC* project (Iervolino et al. 2018) the *PBEE* framework presented is only partially used. After the *PSHA* and the structural analysis the damage analysis is simply based on two different performance levels: the *usability-preventing damage* (*UPD*) and *global collapse* (*GC*). They are two different failure criteria (threshold) representing two conditions related to the real loss of functionality and the real collapse of the building and the related loss of human lives respectively. The definition of these two limits is provided afterwards (Table 1 and Table 20), because they depend on the type of model used for the bearings in the analysis.

It is possible to demonstrate that if earthquake occurrence can be described as a *homogenous Poisson process* (*HPP*), so that hazard is memoryless and do not vary over time, also the counting process of earthquakes capable of causing failure is an *HPP*, characterized by the λ_f rate and the response system is time independent. Thus, the probability that failure will occur at least once in any interval time ΔT is given by:

$$P_f = 1 - \exp(-\lambda_f \cdot \Delta T) \tag{2-1}$$

The failure rates are obtained for all the case-study buildings and for both *GC* and *UPD*, according the theorem of total probability, integrating the structural fragility and the seismic hazard for the site where the structures are located (and so also designed) by:

$$\lambda_f = \int_0^{+\infty} P[failure \mid IM = x] \cdot \mid d\lambda_{IM}(x) \mid \tag{2-2}$$

In Eqn. (5-2), $\lambda_{IM}(x)$ is the annual rate of exceedance of an *IM* causing the exceedance of an *intensity measure* (*IM*) equal to a specific value, $IM = x$, at the building site (from *PSHA*) and $P[failure|IM = x]$, $\forall$x is the fragility of the structure. In the *RINTC* project, the adopted *IM* is the 5% damped (pseudo)spectral acceleration at the fundamental period of the structure, $Sa(T_1)$ or simply *Sa*. The seismic hazard is computed considering the same source model adopted by the Italian seismic code (CS.LL.PP., 2008, 2018) to define the seismic design actions. The response assessment of the structures is carried out through a *multi-stripe dynamic analysis* (Jalayer, 2003), providing a probabilistic characterization of the seismic response for a range of ground-motion intensities at the site of interest. For this purpose, the domain of the *IM* is discretized into ten values and the seismic response was assessed, for each of these *IM* values, via nonlinear dynamic analysis. At each of the 10 levels, 20 ground-motion records are selected, all featuring the same *IM* value. The sample of 20 response values collected in this way forms a so-called stripe, because, in a hypothetical plot of response versus *IM*, they are all aligned at the same *Intensity Measure Level* (*IML*).

For each designed structure, the fragility can be computed via the following approach (Iervolino et. al., 2018):

$$P[failure \mid IM = x_i] = \\ = \left\{1-\Phi\left[\frac{\log(edp_f - \mu_{\log(EDP)|IM=x_i}}{\sigma_{\log(EDP)|IM=x_i}}\right]\right\}\left(1-\frac{N_{col,IM=x_i}}{N_{tot,IM=x_i}}\right)+\frac{N_{col,IM=x_i}}{N_{tot,IM=x_i}} \quad (2\text{-}3)$$

In Eqn. (2-3), *EDP* (i.e., the engineering demand parameter) represent the structural response (e.g., maximum inter-story drift) and edp_f is the structural capacity for the performance of interest. The quantities $\mu_{\log(EDP)|IM=x_i}$ and $\sigma_{\log(EDP)|IM=x_i}$ are the mean and standard deviation of the logarithms of *EDP* when $IM = x_i$; $i = \{1,\ldots,10\}$ conditional on no-collapse, while $\Phi(\cdot)$ is the cumulative Gaussian distribution function and $N_{col,IM=x_i}$ is the number of collapse cases (i.e., those reaching numerical instability according to the terminology of (Shome and Cornell 2000). Finally, $N_{tot,IM=x_i}$ is the number of ground-motion records, here 20, with $IM = x_i$; $i = \{1,\ldots,10\}$.

Although Eqn. (2-3) is the general framework, a nonparametric approach has been used in selected cases; i.e., $P[failure|IM = x]$ has been empirically evaluated by counting the number of records for which failure has been observed, $N_{f,IM=x_i}$, as shown in Eqn.

$$P[failure \mid IM = x_i] = \frac{N_{f,IM=x_i}}{N_{tot,IM=x_i}} \quad (2\text{-}4)$$

This is the case of seismically isolated buildings, where multiple collapse mechanisms related to different *EDPs* of the superstructure and isolation system may contribute to the global collapse, thus making impossible to the use of Eqn. (2-3).

2.3 Collapse mechanism of seismically isolated buildings

The superstructure and the isolation system of base-isolated buildings can be considered as two components of an in-series system. The seismic response at the design level of input is substantially equivalent to a single degree of freedom system where the displacements are concentrated at the isolation level while the superstructure behaves substantially as a rigid body and takes minor role in the global response of the system. For higher intensity earthquakes, instead, the weaker element of the two components rules the failure of the whole system.

Regarding the superstructure, it is known that the behaviour of isolated structures after yielding is fundamentally different from that of fixed-base structures (Kikuchi, 2008) and the ductility demand after yielding is much higher, rapidly leading to the collapse of the superstructure. On the other hand, the collapse mechanism of rubber bearings is not unique. It notably depends on the geometric shape, i.e. the primary and the secondary shape factors (Mizukoshi et al. 1992). Consequently, all of them must be monitored.

2.3.1 Seismic isolation

Many past studies focused on the rubber bearings collapse. Mizukoshi et al. (1992) performed loading tests combining different vertical loads and shear deformation on laminated rubber bearings with various geometric shapes to assess the effects of the primary and secondary shape factors on the failure limit characteristics. They defined three collapse mechanism: shear type (direct shear failure), compression type (buckling dominated) and an intermediate one called bending type. They investigated not only the behaviour under compression but also under tension, reaching the tension limit, or a combined tension-shear limit. They consequently fully defined a sort of failure domain in terms of compression, tension and shear for each isolator tested. They concluded that for high shape factors or in general for low compression levels, the shear failure mode is dominant and the deformation limit is almost constant. Instead, for slender bearings the failure capacity in combined compression and shear is strongly related to the shape factors and the failure mode type is the buckling one. Moreover, tension doesn't affect the shear capacity. So, these tests highlight the three collapse modes that may occur for *HDRBs*, namely: (*i*) *shear*, (*ii*), *buckling* and (*iii*) *tension*.

The former and the latter depend only on the rubber compound capacity and the quality of production procedure used by the manufacturers, while the buckling one is related to the shape factors and the current stress deformation state of the bearing (vertical load and horizontal displacement). The quality of the manufacturing is of paramount importance for the final reliability of seismic isolators (Zayas et al., 2017) and the production technology is in continuous development. Experimental results on bearing capacity are not always are in accordance. For example, a recent work (Nishi et al. 2019) tested the shear displacement capacity of bearings with similar characteristics but made by different manufacturers. The average shear strain capacity (defined as the ratio between the shear displacement and the total rubber height) ranged from 300% (for a medium shear stiffness rubber) to more than 450% (it was not possible to break the bearings). Consequently, a pragmatic choice must be done on the available literature. Moreover, the collapse of a single bearing doesn't necessarily lead to the global collapse of the system. For example, in (Monzon et al. 2016) although the buckling condition was reached in some bearings during a shaking table test on an isolated steel bridge, the isolation system greatly survived the experiment without any major damage.

Regarding the shear failure mode, a lower bound limit for rubber failure in terms of shear deformation is 260% (Montuori et al., 2016) regardless the shape factor value and the applied pressure. This is confirmed by experimental results (Kawamata and Nagai 1992, Mizukoshi et al. 1992, Muramatsu et al. 2004, Nishi, 2019) showing values usually in the range of 350-500%. Other experimental works summarized in (Montuori et al., 2016) define a limit value of the shear deformation based on the secondary shape factor (S_2), where a value of γ_{lim}/S_2 equal to 1.0 is considered for low secondary shape factor ($S_2 = 3.5$) while $\gamma_{lim}/S_2 = 0.6$ for higher secondary shape factor ($S_2 = 5.8$). In the first case, representing a slender bearing, the failure occurs mainly for a combination of bending and shear whereas in the second one, representing a squat bearing, for simple shear. In this work a shear deformation $\gamma_{lim} = 350\%$ is used, which also corresponds to the maximum deformation reached in the experimental campaign used for the calibration of the *HDRB* model (see Chpt. 3.2.1). In the RINTC project, the attainment of the *GC* performance level was conventionally assumed to occur when 50% of elastomeric devices developed a shear strain greater than or equal to 350%. However, depending on the S_1 shape factor and on the compression load acting on the bearing, for low S_2 values the first failure may occur for buckling. Regarding the buckling failure mode, the value of P/P_{cr} ratio between the current axial load and the variable critical buckling load (according to Kumar et al., 2014) has been evaluated step-by-step. Since the vertical load can be very different during the earthquake due to the rocking component it is possible to have a single or few bearings in the buckling condition while the others work properly. So, the global collapse performance level is attained only when 50% of elastomeric devices simultaneously reach a value of the axial compressive force higher than the critical buckling load, i.e. $P/P_{cr} \geq 1$ for more than 50% of the bearings simultaneously. Finally, as regards the tension failure mode, recent experimental results (Kumar et al., 2015) showed that elastomeric bearings in some cases can sustain large tensile strains of up to 100% following cavitation without rupture but in other cases this value is reduced. For this work an axial tensile strain equal to 0.5 has been assumed as limit value. The *GC* condition is conventionally attained when 50% of elastomeric devices develops an axial tensile strain greater than or equal to the assumed threshold value.

As mentioned before, in base-isolated buildings the superstructure and the isolation system can be considered as two components of an in-series system, and the *GC* must be representing of both (the collapse of either sub-system induces the collapse of the whole system). Consequently, *GC* is a multi-criteria approach, depending on the typology and the associated failure modes of the isolation devices. The *GC* of the isolation system is attained when the first of the possible collapse mechanisms occurs. For example, for *HDRBs* the attainment of the shear collapse can be anticipated with respect to the buckling collapse depending on the shape factors but also on the scragging (reduction of the horizontal stiffness) accumulated during the earthquake. Scragging reduces the shear force and consequently the vertical force related to the rocking of the superstructure, while increases the shear deformation. This can switch the first collapse from a buckling mode to a shear mode. So, the limit values of the *EDPs* associated with each failure mode have been controlled through all the *NTHAs* (Nonlinear Time History Analysis) and post-processed to find which of them have been first attained. The limit values of the engineering demand parameters associated with each failure mode are reported in Table 1.

Sometimes isolation systems are composed by a combination of rubber bearings and *Flat Slider Bearings* (*FSBs*). Sliders support vertical load without provide significant horizontal stiffness and they are used to increase the isolation period of the system, but they can collapse due to extreme horizontal displacement losing their support capacity. Sliders failure mode is attained for a horizontal displacement equal to the displacement capacity of the device increased an over-stroke. For the *FSB* system where sliders work together with *HDRBs*, the over-stroke is taken equal to 1/2 of the sliding pad diameter ($\Phi p/2$, equal to 150mm).

ISOLATION DEVICE	*FAILURE MODE*	*EDP threshold*	*DESCRIPTION*
HDRBs	Buckling	$P/P_{cr}=1$	50% of elastomeric devices reaches a value of axial compression force equal to the critical buckling load
	Tension	$\varepsilon_t \geq 0.50$	50% of elastomeric devices reaches an axial tensile strain (ε_t) greater than or equal to 50%
	Shear	$\gamma_r \geq 3.5$	50% of elastomeric devices reaches a shear strain (γ_r) greater than or equal to 3.5
FSBs	Over-stroke	$d_u = d_{max,FSB}+\Phi_p/2$	The horizontal displacement of the centre of gravity of the isolation floor is equal to the collapse limit value

Table 1. GC for the isolation systems

2.3.2 Superstructure

The collapse criterion for the isolated superstructure is the same as for a fixed-base structure. It is usually related to a displacement demand higher than specific limit. This limit depends on the characteristics of the structure. It is noteworthy that seismically isolated structures are subjected to higher ductility demand after reaching the yielding point (i.e. the end of the almost elastic phase in the pushover curve) with respect to fixed-base structures because the frequency of the lateral base shear force is lower than the natural frequency of the superstructure. In this way the superstructure is subjected to a sort of quasi-static force during the earthquake. This has the effect of significantly reducing the energy dissipation resulting from repeated inelastic excursions, increasing the displacement demand (Kikuchi et al., 2008). So, even if the collapse is related to a displacement limit, it is important to provide sufficient lateral strength to the superstructure. In this work, a conventional collapse criterion has been adopted for the superstructure collapse. In particular, the collapse occurs when, in one of the two main directions, the maximum top displacement (with respect to the isolation system), derived from the analyses is greater than (or equal to) the top displacement corresponding to a decrease of 50% of the lateral strength from *Pushover analysis* (*POA*) carried out on the fixed-based superstructure, with a force distribution proportional to the storey masses. Details about this conventional choice can be found in (ReLUIS-RINTC Workgroup, 2018) and (Ricci et al. 2018). Figure 5 shows an example of the limit top displacements derived from *POA* of the fixed-base superstructure of a case study showed afterwards.

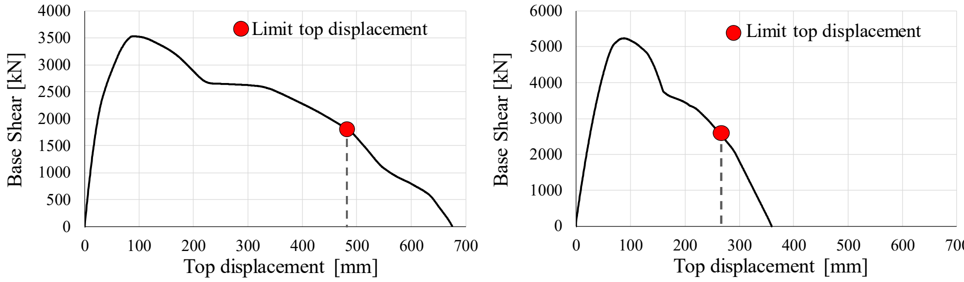

Figure 5. GC limits in X and Y dir. in terms of roof displacements of the superstructure, as derived from POA

2.4 Chapter's references

AIJ Architectural Institute of Japan Editor (2012), "Preliminary Reconnaissance Report of the 2011 Tohoku-Chiho Taiheiyo-Oki Earthquake" DOI 10.1007/978-4-431-54097-7

ASCE 2017 Minimum design loads and associated criteria for buildings and other structures, ASCE/SEI

7-16. American Society of Civil Engineers, Reston

Baker, J.W., Schubert, M., Faber, M.H., 2008. On the assessment of robustness. Structural Safety 30, 253–267. https://doi.org/10.1016/j.strusafe.2006.11.004

Bradley, B. A., Burks, L. S., & Baker, J. W. (2015). Ground motion selection for simulation-based seismic hazard and structural reliability assessment. Earthquake Engineering & Structural Dynamics, 44(13), 2321-2340.

Bontempi, F., Giuliani, L., Gkoumas, K., 2007. Handling the exceptions: robustness assessment of a complex structural system 7.

Booth, E.D., Baker, M.J., (2000). SIMPLIFIED METHODS FOR SEISMIC RELIABILITY ANALYSIS, 12WCEE

Bruneau, M., Chang, S.E., Eguchi, R.T., Lee, G.C., O'Rourke, T.D., Reinhorn, A.M., Shinozuka, M., Tierney, K., Wallace, W.A., von Winterfeldt, D., 2003. A Framework to Quantitatively Assess and Enhance the Seismic Resilience of Communities. Earthquake Spectra 19, 733–752. https://doi.org/10.1193/1.1623497

Calgaro, J.-A., (2011) Safety philosophy of Eurocodes. ISGSR 2011 - Vogt, Schuppener, Straub & Bräu (eds) - © 2011 Bundesanstalt für Wasserbau ISBN 978-3-939230-01-4

Calgaro, J.-A., Gulvanessian. 2001. "Management of reliability and risk in the Eurocode system". IABSE International Conference "Safety, Risk and Reliability – Trends in Engineering", Malta 21-23 mars 2001

C.E.N. 2002. European standard EN 1990:2002. Eurocode: basis of structural design. European Committee for Standardization, Brussels, Belgium.

CEN. 2017. Draft Annex F (Informative): simplified reliability-based verification format, Annex to European standard EN 1998–1. Eurocode 8: design of structures for earthquake resistance. Part 1: general rules, seismic action and rules for buildings. European Committee for Standardization. Brussels (Prepared by Dolsek M, Zizmond J, Kosic M, Lazar Sinkovic)

Chen, M.C., Pantoli, E., Wang, X., Astroza, R., Ebrahimian, H., Hutchinson, T.C., Conte, J.P., Restrepo, J.I., Marin, C., Walsh, K.D., Bachman, R.E., Hoehler, M.S., Englekirk, R., Faghihi, M., 2016. Full-Scale Structural and Nonstructural Building System Performance during Earthquakes: Part I – Specimen Description, Test Protocol, and Structural Response. Earthquake Spectra 32, 737–770. https://doi.org/10.1193/012414EQS016M

Christopoulos, C., Filiatrault, A., 2006. Principles of Passive Supplemental Damping and Seismic Isolation - IUSS Press - Eucentre Press. Pavia, Italy

Clemente, P., Martelli, A., (2017). ANTI-SEISMIC SYSTEMS: WORLDWIDE APPLICATION AND CONDITIONS FOR THEIR CORRECT USE, 16th WCCE, Chile.

CNR. 2014. Guide for the probabilistic assessment of the seismic safety of existing buildings, Report CNRDT 212/2013. CNR—Advisory Committee on Technical Recommendations for Construction, Rome

Cornell CA (2005) On earthquake record selection for nonlinear dynamic analysis. In: Proceedings of the Luis Esteva symposium, Mexico City, Mexico

Cornell CA, Krawinkler H. Progress and challenges in seismic performance assessment. PEER News 2000; 3(2).

Dall'Asta, A., Scozzese, F., Ragni, L., & Tubaldi, E. (2017). Effect of the damper property variability on the seismic reliability of linear systems equipped with viscous dampers. Bulletin of Earthquake Engineering, 15(11), 5025-5053.

EERI 2012. Performance of Engineered Structures in the Mw 9.0 Tohoku, Japan, Earthquake of March 11, 2011. Special Earthquake Report.

Ellingwood, B. R. 2000. LRFD: implementing structural reliability in professional practice. Engineering Structures 22, 106–115. doi:10.1016/S0141-0296(98)00099-6.

Fajfar, P., 2018. "Analysis in seismic provisions for buildings: past, present and future", The fifth Prof. Nicholas Ambraseys lecture. Bull Earthquake Eng 16, 2567–2608. https://doi.org/10.1007/s10518-017-0290-8

FEMA. 2009. Quantification of building seismic performance factors. Report FEMA P695. Washington DC, USA: Federal Emergency Management Agency.

FEMA. 2012. "Seismic Performance Assessment of Buildings." Report FEMA P-58, Federal Emergency Management Agency, Washington DC, U.S.A., 2012.

Fenz, D.M., Constantinou, M.C., 2008. Spherical sliding isolation bearings with adaptive behavior: Theory. Earthquake Engineering & Structural Dynamics 37, 163–183. https://doi.org/10.1002/eqe.751

Franchin, P., 2018. Research Needs Towards a Resilient Community, in: Pitilakis, K. (Ed.), Recent Advances in Earthquake Engineering in Europe: 16th European Conference on Earthquake Engineering-Thessaloniki 2018. Springer International Publishing, Cham, pp. 661–691. https://doi.org/10.1007/978-3-319-75741-4_28

Freddi, F., Tubaldi, E., Ragni, L., Dall’Asta, A. (2013). Probabilistic Performance Assessment of low-ductility RC frames retrofitted with dissipative braces. Earthquake Engineering & Structural Dynamics, 42(7), 993-1011.

Freddi, F., Padgett, J.E., Dall'Asta, A. (2017). Probabilistic Seismic Demand Modeling of Local Level Response Parameters of an RC Frame. Bulletin of Earthquake Engineering, 15(1), 1-23.

Fu Lin Zhou, (2015) “Earthquake tragedy and application of seismic isolation, energy dissipation and other seismic control systems to protect structures in China”, from “Avezzano 1915-2015: cento anni di ingegneria sismica”, ENEA, DOI 10.12910/EAI2015-077

Gkimprixis, A., Tubaldi, E., Douglas, J., 2019. Comparison of methods to develop risk-targeted seismic design maps. Bull Earthquake Eng 17, 3727–3752. https://doi.org/10.1007/s10518-019-00629-w

HANDBOOK 2 - IMPLEMENTATION OF EUROCODES - RELIABILITY BACKGROUNDS. 2004. Guide to the basis of structural reliability and risk engineering related to Eurocodes, supplemented by practical examples LEONARDO DA VINCI PILOT PROJECT CZ/02/B/F/PP-134007. Prague

Haselton, C.B., Baker, J.W., Stewart, J.P., Whittaker, A.S., Luco, N., Fry, A., Hamburger, R.O., Zimmerman, R.B., Hooper, J.D., Charney, F.A., Pekelnicky, R.G., 2017. Response History Analysis for the Design of New Buildings in the NEHRP Provisions and ASCE/SEI 7 Standard: Part I - Overview and Specification of Ground Motions. Earthquake Spectra 33, 373–395. https://doi.org/10.1193/032114EQS039M

IAEA. 2018. Safety Glossary, Terminology Used in Nuclear Safety and Radiation Protection, 2018 Edition

Iervolino, I., Dolce, M., 2018. Foreword to the Special Issue for the RINTC (The Implicit Seismic Risk of Code-Conforming Structures) Project. Journal of Earthquake Engineering 1–4. https://doi.org/10.1080/13632469.2018.1543697

Iervolino, I., Spillatura, A., Bazzurro, P., 2018. Seismic Reliability of Code-Conforming Italian Buildings. Journal of Earthquake Engineering 22, 5–27. https://doi.org/10.1080/13632469.2018.1540372

Jalayer F., Cornell C.A., 2009. Alternative non-linear demand estimation methods for probability-based seismic assessments, Earthquake Engineering and Structural Dynamics, 38(8), 951–972.

Jalayer, F. (2003) “Direct Probabilistic seismic analysis: implementing nonlinear dynamic assessment,”Ph.D. thesis, Department of Civil and Environmental Engineering, Stanford University, Stanford,CA, USA.

JSSI. 2018. The Japan Society of Seismic Isolation. SI_data_2018 (until the end of 2017). https://www.jssi.or.jp/english/aboutus/techinfo.html

Kasai, K., Mita, A., Kitamura, H., Matsuda, K., Morgan, T.A., Taylor, A.W., 2013. Performance of Seismic Protection Technologies during the 2011 Tohoku-Oki Earthquake. Earthquake Spectra 29, 265–293. https://doi.org/10.1193/1.4000131

Kawamata, S., and K. Nagai. 1992. "Ultimate deformation capacity of isolators." International workshop on recent developments in base-isolation techniques for buildings, Tokyo.

Kawashima K. (2012), “DAMAGE OF BRIDGES DUE TO THE 2011 GREAT EAST JAPAN EARTHQUAKE” Journal of Japan Association for Earthquake Engineering, Vol.12, No.4(Special Issue)

Kikuchi M., Tamura K., Wada A., 1995. SAFETY EVALUATION OF BASE-ISOLATED STRUCTURES. Transactions of AIJ 60, 65–73. (in Japanese) https://doi.org/10.3130/aijs.60.65_1

Kikuchi, M., Black, C.J., Aiken, I.D., 2008. On the response of yielding seismically isolated structures. Earthquake Engng Struct. Dyn. 37, 659–679. https://doi.org/10.1002/eqe.777

Kitayama, S., Constantinou, M.C., 2018. Collapse performance of seismically isolated buildings designed by the procedures of ASCE/SEI 7. Engineering Structures 164, 243–258. https://doi.org/10.1016/j.engstruct.2018.03.008

Kitayama, S., Constantinou, M.C., 2019. Probabilistic seismic performance assessment of seismically isolated buildings designed by the procedures of ASCE/SEI 7 and other enhanced criteria. Engineering Structures 179, 566–582. https://doi.org/10.1016/j.engstruct.2018.11.014

Kiureghian, A. D. (2005). Non-ergodicity and PEER's framework formula. Earthquake engineering & structural dynamics, 34(13), 1643-1652.

Kumar, M., Whittaker, A.S., Constantinou, M.C., 2014. An advanced numerical model of elastomeric seismic isolation bearings: AN ADVANCED NUMERICAL MODEL OF ELASTOMERIC SEISMIC ISOLATION BEARINGS. Earthquake Engineering & Structural Dynamics 43, 1955–1974. https://doi.org/10.1002/eqe.2431

Kumar, M., Whittaker, A.S., Constantinou, M.C., 2015. Experimental investigation of cavitation in elastomeric seismic isolation bearings. Engineering Structures 101, 290–305. https://doi.org/10.1016/j.engstruct.2015.07.014

Luco, N., & Cornell, C. A. (2007). Structure-specific scalar intensity measures for near-source and ordinary earthquake ground motions. Earthquake Spectra, 23(2), 357-392.

Lupoi G, Lupoi A, Pinto PE. Seismic risk assessment of RC structures with the “2000 SAC/FEMA” method. Journal of Earthquake Engineering 2002; 6(4):499– 512.

Mackie KR, Stojadinovic B. Comparison of incremental dynamic, cloud, and stripe methods for computing probabilistic seismic demand models. Proceedings of the 2005 ASCE Structures Congress 2005; New York, NY.

Mizukoshi, K., Yasaka, A., Iizuka, M., Takabayashi, K., (1992). Failure test of laminated rubber bearings with various shapes. Earthquake Engineering, Tenth World Conference. Balkema, Rotterdam.

Montuori, G.M., Mele, E., Marrazzo, G., Brandonisio, G., De Luca, A., 2016. Stability issues and pressure–shear interaction in elastomeric bearings: the primary role of the secondary shape factor. Bulletin of Earthquake Engineering 14, 569–597. https://doi.org/10.1007/s10518-015-9819-x

Monzon, E.V., Buckle, I.G., Itani, A.M., 2016. Seismic Performance and Response of Seismically Isolated Curved Steel I-Girder Bridge. J. Struct. Eng. 142, 04016121. https://doi.org/10.1061/(ASCE)ST.1943-541X.0001594

Morales, E.A., Romo, L.M., Haro, A.G., Sinde, I.S., Aroca, J.L., Nikolaou, S., Diaz-Fanaz, G., n.d. 2019 A Real-Life Resiliency Experiment: The Los Caras Bridge of Ecuador. CONHIC 2nd International Conference on Natural Hazards & Infrastructure, 23-26 June, 2019, Chania, Greece

Morita, k., Takayama, M., 2017 “Behavior of Seismically Isolated Buildings during the 2016 Kumamoto Earthquakes”, Proc. of NZSEE Conference, Wellington, New Zealand

Muramatsu, Y., Inoue, K., Katoh, R., Kamitani, N., Sakaguchi, T., Sasaki, Y., Kitamura, H. 2004. Test results of ultimate properties of rubber bearings for buildings. AIJ J Technol Des, (20): 67-70.

Naeim, F. and Kelly, J. M. (1999). Design of Seismic Isolated Structures: From Theory to Practice, JohnWiley & Sons, New York, New York.

Nakazawa T., Kishiki S., Qu Z., Miyoshi A., Wada A. (2011). Fundamental Study on Probabilistic Evaluation of the Ultimate State of Base Isolated Structures, Proceedings, 8th International Conference on Urban Earthquake Engineering, Tokyo Institute of Technology, Tokyo, Japan

Nishi, T., Suzuki, S., Aoki, M., Sawada, T., Fukuda, S., 2019. International investigation of shear displacement capacity of various elastomeric seismic-protection isolators for buildings. J Rubber Res 22, 33–41. https://doi.org/10.1007/s42464-019-00006-x

Nishida, A., Choi, B., Yamano, H., Takada, T., 2018. Development of Seismic Countermeasures Against Cliff Edges for Enhancement of Comprehensive Safety of Nuclear Power Plants: Cliff Edges Relevant to NPP Building System, in: Volume 8: Seismic Engineering. Presented at the ASME 2018 Pressure Vessels and Piping Conference, ASME, Prague, Czech Republic, p. V008T08A028. https://doi.org/10.1115/PVP2018-85066

Pantoli, E., Chen, M.C., Wang, X., Astroza, R., Ebrahimian, H., Hutchinson, T.C., Conte, J.P., Restrepo, J.I., Marin, C., Walsh, K.D., Bachman, R.E., Hoehler, M.S., Englekirk, R., Faghihi, M., 2016. Full-Scale Structural and Nonstructural Building System Performance during Earthquakes: Part II – NCS Damage States. Earthquake Spectra 32, 771–794. https://doi.org/10.1193/012414EQS017M

Pitilakis, K., 2015. Earthquake Risk Assessment: Certitudes, Fallacies, Uncertainties and the Quest for Soundness, in: Ansal, A. (Ed.), Perspectives on European Earthquake Engineering and Seismology. Springer International Publishing, Cham, pp. 59–95. https://doi.org/10.1007/978-3-319-16964-4_3

Porter, K., 2019. A Beginner's Guide to Fragility, Vulnerability, and Risk. University of Colorado Boulder, 119 pp., http://spot.colorado.edu/~porterka/Porter-beginners-guide.pdf

Porter, K.A. (2003). An overview of PEER's performance-based earthquake engineering methodology. Proc. Ninth International Conference on Applications of Statistics and Probability in Civil Engineering (ICASP9) July 6-9, 2003, San Francisco, CA. Civil Engineering Risk and Reliability Association (CERRA), 973-980, http://spot.colorado.edu/~porterka/Porter-2003-PEER-Overview.pdf

Ragni, L., Cardone, D., Conte, N., Dall'Asta, A., Cesare, A.D., Flora, A., Leccese, G., Micozzi, F., Ponzo, C., 2018. Modelling and Seismic Response Analysis of Italian Code-Conforming Base-Isolated Buildings. Journal of Earthquake Engineering 0, 1–33. https://doi.org/10.1080/13632469.2018.1527263

ReLUIS-RINTC Workgroup, 2018. Results of the 2015-2017 RINTC project. ReLUIS-RINTC report, ReLUIS, Naples, Italy. Available at http://www.reluis.it.

Rezaei Rad, A., Banazadeh, M., 2018. Probabilistic Risk-Based Performance Evaluation of Seismically Base-Isolated Steel Structures Subjected to Far-Field Earthquakes. Buildings 8, 128. https://doi.org/10.3390/buildings8090128

Ricci, P., Manfredi, V., Noto, F., Terrenzi, M., Petrone, C., Celano, F., De Risi, M.T., Camata, G., Franchin, P., Magliulo, G., Masi, A., Mollaioli, F., Spacone, E., Verderame, G.M., 2018. Modeling and Seismic Response Analysis of Italian Code-Conforming Reinforced Concrete Buildings. Journal of Earthquake Engineering 22, 105–139. https://doi.org/10.1080/13632469.2018.1527733

Roussis P.E., Constantinou M.C., Erdik M., Durukal E., Dicleli M. (2008). Assessment of performance of Bolu Viaduct in the 1999 Duzce earthquake in Turkey, Technical Report MCEER 02-0001, Multidisciplinary Center for Earthquake Engineering, State University of New York, Buffalo, NY.

Scott Lewis, Engineering News-Records (2017), web article "The 10 Largest Base-Isolated Buildings in the World", https://www.enr.com/articles/42366-the-10-largest-base-isolated-buildings-in-the-world

Scozzese, F. 2017. AN EFFICIENT PROBABILISTIC FRAMEWORK FOR SEISMIC RISK ANALYSIS OF STRUCTURAL SYSTEMS EQUIPPED WITH LINEAR AND NONLINEAR VISCOUS DAMPERS. PhD dissertation

Shao, B., Mahin, S.A., Zayas, V., 2019. Achieving targeted levels of reliability for low-rise seismically isolated structures. Soil Dynamics and Earthquake Engineering 125, 105744. https://doi.org/10.1016/j.soildyn.2019.105744

Shome, N. and Cornell, C. A. 2000. Structural seismic demand analysis: consideration of 'Collapse'. Proc. of 8th ASCE Specialty Conference on Probabilistic Mechanics and Structural Reliability. South Bend, Indiana, USA.

Tubaldi, E., Freddi, F., Barbato, M. (2016). Probabilistic seismic demand model for pounding risk assessment. Earthquake Engineering & Structural Dynamics, 45(11), 1743-1758.

Zayas V, Mahin S and Constantinou MC (2017) Seismic Isolation Standard For Continued Functionality. Technical Report: UCB/SEMM-2017/03

Žižmond, J., Dolšek, M., n.d. Formulation of risk-targeted seismic action for the force-based seismic design of structures. Earthquake Engineering & Structural Dynamics 0. https://doi.org/10.1002/eqe.3206

CHAPTER 3

3 Modelling issues in performance-based assessment of isolated structure

3.1 Introduction

This chapters describes the modelling strategy developed to investigate the seismic performance of isolated buildings. The proposed strategy employs state-of-the-art models for both the isolation system and the superstructure.

The main challenge of a bearing model for a reliability analysis is to reasonably simulate the response under a wide range of seismic input levels, especially beyond the design conditions and up to the collapse of the device. Many aspects of high damping rubber bearing behaviour should be considered under extreme loadings (Kumar et al. 2014 and Kelly, 1997):

- Coupled bidirectional motion in horizontal directions;
- Coupling of vertical and horizontal motion;
- Cavitation and post-cavitation behaviour in tension;
- Strength degradation in cyclic tensile loading due to cavitation;
- Variation in critical buckling load capacity due to lateral displacement;
- Post-buckling behaviour;
- Strength degradation in cyclic shear loading due to Mullin's effect;
- Shear fracture and post failure behaviour;
- Tension fracture.

None of the numerical models available in the literature is able to capture all these phenomena at the same time. For example, only few models (Grant et al., 2004; Tubaldi et al., 2017; Ragni et al., 2018) take into account the degrading cyclic response in shear of *HDRBs*. Anyway, there are some very advanced models recently developed that account for the main features of the HDRB behaviour listed above. Among them, the two models used in this work are the ones already available in OpenSees (McKenna, 2011), which is the software used to numerically evaluate the full three-dimensional behaviour of isolated buildings. The first model is the *HDR Bearing Element* developed by (Kumar et al., 2014). It is specific for high damping rubber bearings because it includes a shear degrading model for the bidirectional horizontal behaviour (Grant et al., 2004), and a newly developed mathematical model for the cavitation and post-cavitation behaviour in tension (Kumar et al., 2015). It is also able to take into account the variation in the critical buckling load capacity due to lateral displacement. However, the coupling of vertical and horizontal motion is considered only in an indirect way by using expressions for mechanical properties in one direction that are dependent on the response parameters in the other direction. The second model is the *Kikuchi Bering Element*, which is the implementation in OpenSees of the model developed by (Ishii and Kikuchi, 2019). Differently to the former, this model takes into account the coupled behaviour in the vertical and horizontal direction directly with a mathematical model, written in large displacement formulation, that is derived from the formulation originally proposed by Koh and Kelly (Koh and Kelly, 1986, 1988) and known in the literature as the *two spring model* (Kelly, 1997).

For the reinforced concrete superstructure, a full three-dimensional model with inelasticity concentrated at the member ends is implemented, modelling also the cyclic deteriorating behaviour of the infills panels. Some information about the model are reported at the end of this chapter.

3.2 Isolation

3.2.1 Experimental investigation

The calibration of the models used in this work is based on an experimental campaign (Brandonisio et al. 2017) carried out on High Damping Rubber Bearings (*HDRBs*) at the SisLab: Materials and Structures Test Laboratory of University of Basilicata (Italy). The aim of experimental tests was understanding the influence of vertical load and the secondary shape factor on seismic performance of *HDRBs*. This data have been also later used to assess the relationship of the code prescription for the maximum vertical load and the real buckling collapse behaviour (Brandonisio et al.,

2019) and also for a preliminary investigation on the effects of vertical loads and bearing geometry on the hysteretic cycles of HDRBs (Ragni et al. 2019). All the three tested circular bearings are made of the same soft rubber compound (code *S*) with nominal values of shear stiffness G=0.4MPa and damping factor ξ=15%, but with different geometrical dimensions, as reported in Table 2. In the table Φ denotes the outer rubber diameter, Φ' the inner steel shim diameter, t_r the single rubber layer thickness, t_e the total rubber layer thickness, S_1 the primary shape factor ($S_1=\Phi'/4t_r$) and S_2 the secondary shape factor ($S_2=\Phi'/t_e$).

Bearing code	Φ [mm]	Φ' [mm]	t_r [mm]	t_e [mm]	S_1	S_2
SI-S-500-176	500	490	5.5	176	22.7	2.8
SI-S-600-217	600	590	7	217	21.4	2.8
SI-S-700-207	700	690	9	207	19.5	3.4

Table 2. Geometrical characteristics of the tested bearings

A specific sequence of tests has been carried out on each isolator: first the code required static compression stiffness test (*Axial test*, test 1-2) and horizontal Shear Cyclic Test (*SCT*, test 3), then a series of Shear Quasi-static test (*SQCT*) alternated with the repetition of the *SCT* (tests 6 and 16). The *SCT* test was performed using a sinusoidal displacement history path composed of 5 cycles at each shear amplitude (0.05, 0.1, 0.2, 0.5, 1.0 and 1.5) and at the frequency of 0.5Hz. The vertical compression applied during *SCT* was 6MPa. Tests 6 and 16 allow to control the variation of G and ξ during the whole sequence. The *SQCTs* instead are quasi-static (low speed) half-cycle (positive shear deformation only) test, organized in group of three with the same maximum shear displacement and increasing vertical compression (6MPa, 10MPa and 14MPa). In this way the effect of increasing vertical load is clearly highlighted. Some special tests have been performed to better assess some extreme condition. SI-S 500-176 have been tested at high shear deformations from 2.81 to 3.92 with a very low vertical load (<1MPa) (Figure 17d). SI-S 700-207 have been tested up to a vertical compression of 20MPa (Figure 9d), inducing an instantaneous buckling at zero lateral displacement of the bearing. More details can be found in (Brandonisio et al. 2017).

Results of all the tests are reported hereafter, for each tested isolator. First all the sequences are summarized (Figure 6, Figure 10, Figure 14) in terms of maximum shear strain reached (bars, left axis) and vertical compression (black dash, right side). The orange bars represent the *SQCT*, the grey ones the *SCT*. Then the three *SCTs* cycles are superimposed to highlight the effects of the repeated tests and at the end all the SQCTs are summarized to show the effect of the vertical load on the shear hysteretic cycles. Coloured crosses define the zero tangent stiffness point, associated to the theoretical buckling.

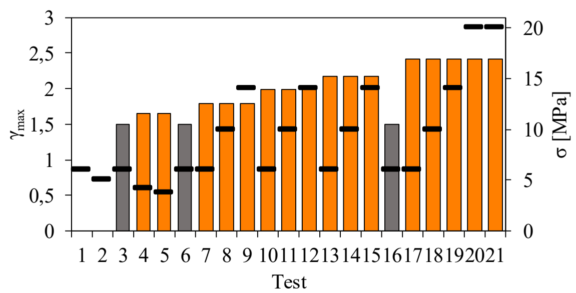

Figure 6. SI-S 700-207 test sequence

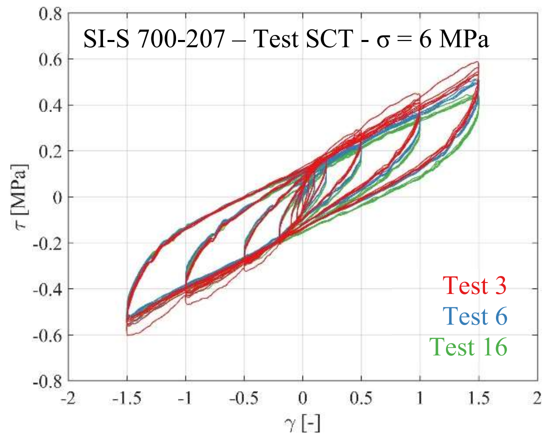

Figure 7. SCTs for SI-S 700-207

In Figure 7, the hysteretic cycles corresponding to the three *SCTs* are superimposed to better highlight the effects of the repeated cycles. During Test 3 the rubber response is affected by a stress-softening often referred to in literature as Mullin’s effect or scragging (Mullin 1969): stiffness reduces at each cycle, from an initial condition of “virgin rubber” to a stable cycle. The largest softening effect occurs in the first cycle, while the stable cycle level depends on the maximum shear strain reached.

Test 6 and 16 cycles are very close to the stable cycle of Test 3 for negative shear deformations, while they are affected by a further stress-softening for positive shear strain. This anisotropic behaviour is associated to the repeated half-cycles of the *SQPTs* performed between the *SCTs*, modifying the stable behaviour only in the positive shear range.

Figure 8 shows equivalent shear stiffness G and damping ξ calculated according to EN15129 for each cycle. In this range the bearing response is mainly controlled by the HDNR material behaviour in simple shear, characterized by dependency on the strain-amplitude (Payne or Fletcher & Gent effect in literature).

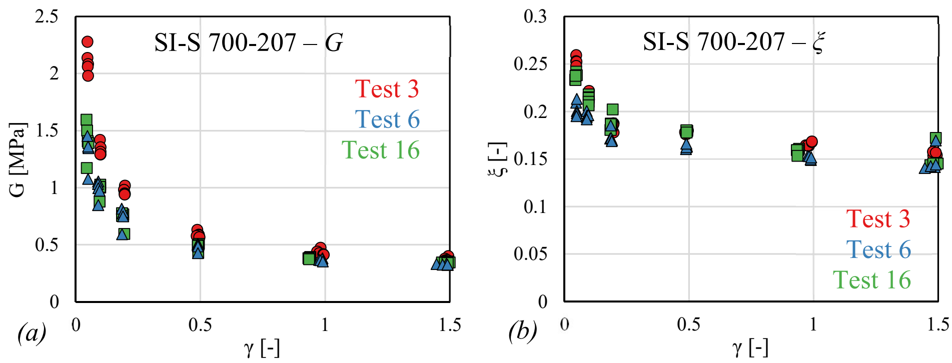

Figure 8. (a) Equivalent shear stiffness G and (b) damping ξ for SI-S 700-207

All the *SQCTs* for SI-S700-207 are summarized in Figure 9. The tests with the same vertical load are grouped in the same graph with different colours. It is worth to note that the stiffness of the first three *SQCTs* (Test 7,8,9, violet) is higher than the subsequent tests, while if the rubber is not affected by the stress-softening behaviour all the cycles should be superimposed. Stress-softening strongly affect the cycles, reducing the stiffness of the rubber and leading to the buckling in test 19 (Figure 9c) for σ=14MPa and a shear strain of 1.49. It is noteworthy that for the same level of displacement and vertical force, no buckling is observed for the other tests (see results of test 9, 12, 15 in Figure 9c). In other words, the Mullin's effect strongly change the buckling limit. However, at the point with zero tangent stiffness, the load supporting capacity is maintained. Therefore, actual instability is reached only at test 20 (Figure 9d) when the shear force becomes zero, as highlighted by the coloured diamond. Repeating the same test instant buckling at zero displacement occurs, confirming the history-dependent behaviour of *HDRB*.

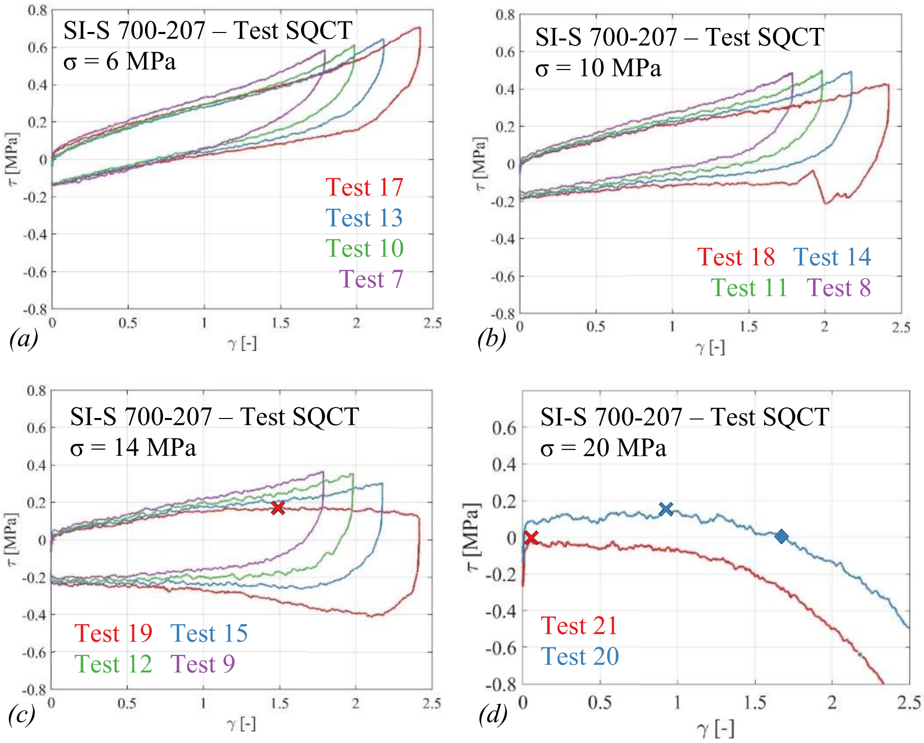

Figure 9. SQCTs for SI-S 700-207

Results for the other two tested bearings are reported hereafter.

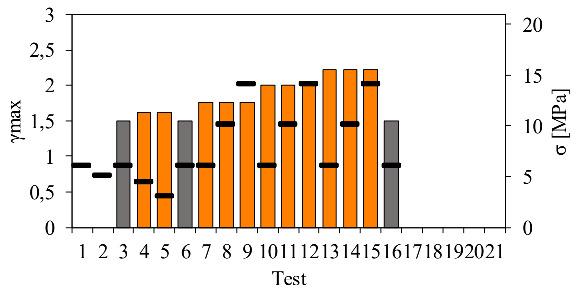

Figure 10. SI-S 600-217 tests sequence

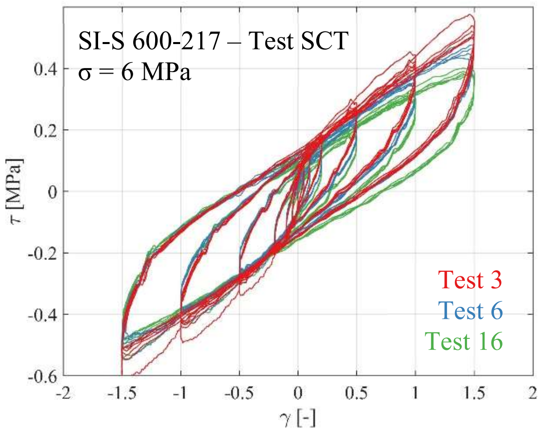

Figure 11. SCTs for SI-S 600-217

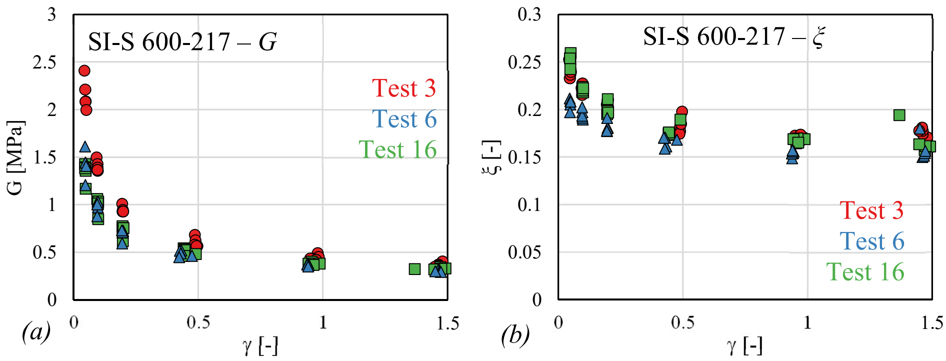

Figure 12. Equivalent shear stiffness G and damping ξ for SI-S 600-217

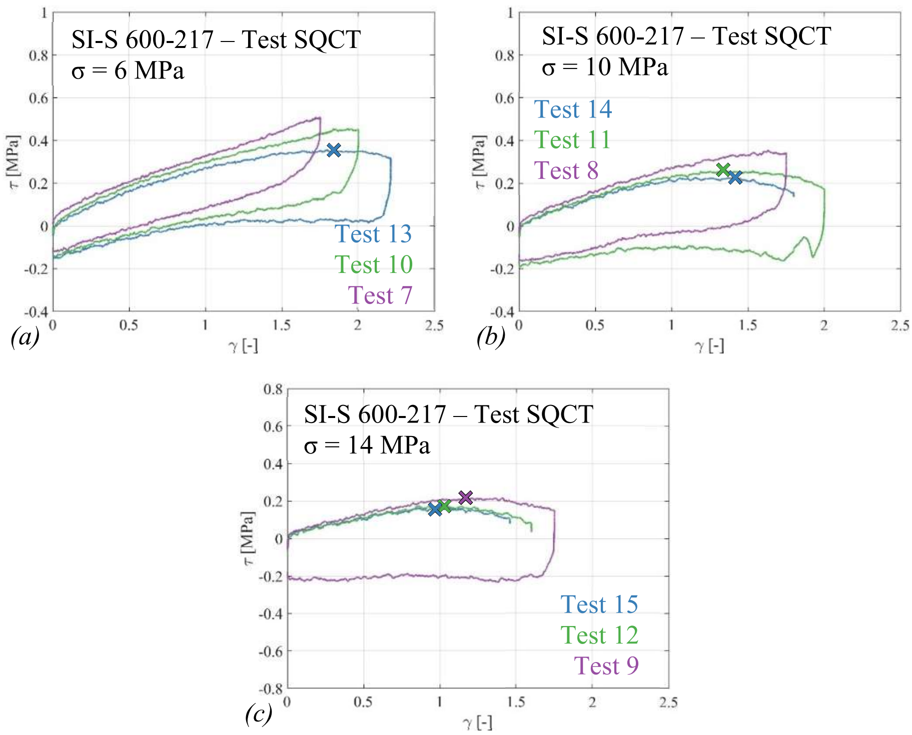

Figure 13. SQCTs for SI-S 600-217

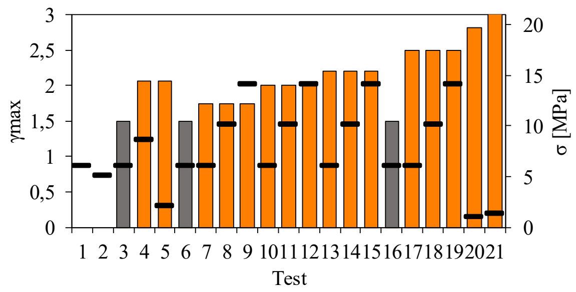

Figure 14. SI-S 500-176 tests sequence

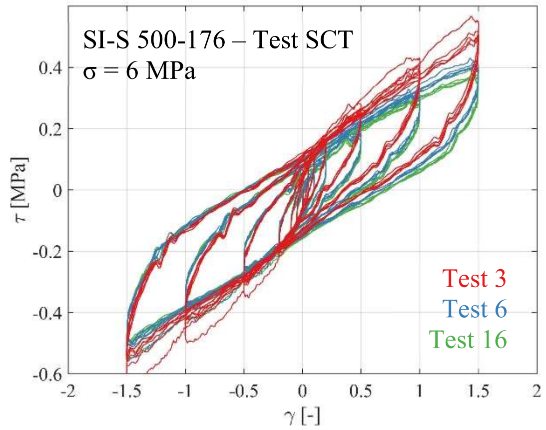

Figure 15. SCTs for SI-S 500-176

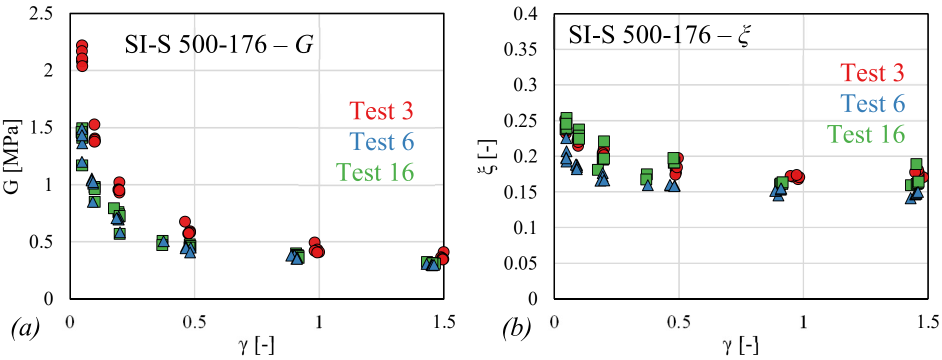

Figure 16. Equivalent shear stiffness G and damping ξ for SI-S 600-217

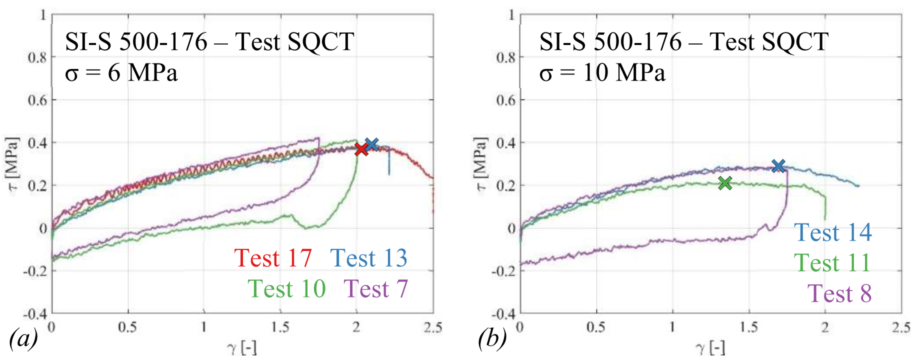

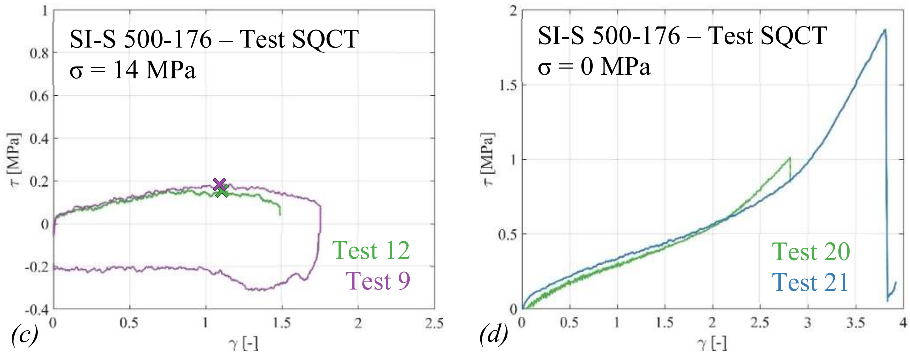

Figure 17. SQCTs for SI-S 500-176.

Figure 17d shows the tests performed at high shear deformation and low vertical force to highlight the stiffening behaviour of the rubber (strain-induced crystallization of the rubber, Yang et al. 2010, Tubaldi et al. 2017).

3.2.2 HDR Bearing Element (Kumar model)

The *HDR Bearing Element*, developed by Kumar (Kumar et al., 2014), is a two-node element with 12 degrees-of freedom. The two nodes are connected by six springs that represent the mechanical behaviour in the six basic directions of the bearing. The shear springs are coupled using an explicit bidirectional model, while the coupling between vertical and horizontal directions is partially considered in an indirect way by using expressions for mechanical properties in the vertical direction that are dependent on the response parameters in the horizontal direction. However, in the current version of the model, for the *HDRBs*, the response in the horizontal directions does not depend on the response in the vertical direction, neither for large displacements (as for the two-spring model of Koh and Kelly, 1986) nor for large pressures (Quaglini et al., 2015). Linear uncoupled springs are considered for the torsional and the two rotational springs. The behaviour in the axial direction is based on a mathematical model developed by (Kumar et al., 2014) that captures the cavitation (occurring at a tensile force value producing a tensile stress of $3G$) and post-cavitation behaviour in tension and the variation of the critical buckling load and the vertical axial stiffness with horizontal displacement in compression. The bidirectional model proposed by Grant (Grant et al., 2004) is adopted to describe the behaviour in the two shear directions. This model is able to capture the degradation of bearing stiffness and damping due to *scragging effects* in shear, which is of particular importance for high dissipative rubbers (Grant et al., 2004; Tubaldi et al., 2017; Ragni et al., 2018). For the rotational behaviour about the two horizontal directions, a linear elastic model is assumed.

The Grant model (Grant et al., 2004) is based on ten parameters which define the behaviour of the entire bearing (a_1, a_2, a_3 for the elastic component, b_1, b_2, b_3 for the inelastic component, c_1, c_2, c_3, c_4 for the damage). Thus, a procedure to convert rubber parameters to bearing parameters has been developed as a function of the rubber area and total rubber thickness

(Cardone et al., 2017; ReLUIS-RINTC, 2018), as showed by the following relations

$$a_1 = \alpha_1 \cdot A / T_r \qquad a_2 = \alpha_2 \cdot A / T_r^{\,3} \qquad a_3 = \alpha_3 \cdot A / T_r^{\,5} \qquad \text{(3-1 a,b,c)}$$

$$b_1 = \beta_1 \cdot A \qquad b_2 = \beta_2 \cdot A / T_r^{\,2} \qquad b_2 = \beta_2 / T_r \qquad \text{(3-2 a,b,c)}$$

$$c_1 = \chi_1 / T_r^{\,3} \qquad c_2 = \chi_2 / T_r^{\,3} \qquad c_3 = \chi_3 \qquad c_4 = \chi_4 / T_r^{\,3} \qquad \text{(3-3 a,b,c)}$$

where A is the rubber area and T_r is the total rubber thickness.

Then, an iterative procedure has been followed to calibrate the model parameters by fitting the experimental results of a series of tests on full scale *HDRBs* with soft rubber. The exact sequence of tests of the isolators, performed at the laboratories of the University of Basilicata and provided by prof. De Luca (Brandonisio et. al., 2017), has been simulated in order to calibrate all mechanical parameters of the model, including damage parameters. More in detail, while all the test sequence has been simulated during the calibration, only the tests with the lower nominal vertical load have been used, because the current *HDR Bearing Element* implementation in OpenSees does not include the horizontal stiffness reduction due to the increased vertical load. The following figures shows the comparison between the calibrated model (blue line) and the experimental data (red line) in terms of shear stress-strain relation. The first (Figure 18) was the cyclic test performed up to a shear strain of 1.5, on a virgin device, whereas the second one (Figure 19) is the repetition of the first test on the same devices after a series of tests at strains larger than 1.5 (up to a shear deformation of 2.21), so is representative of a scragged device. The calibrated model seems to slightly overestimate energy dissipation compared to the experimental data. In Figure 20 stress-strain cycles (red lines) derived from tests at large shear strain amplitude (up to 3.8) are compared to the results of numerical simulations (blue lines), demonstrating that the behaviour at large shear strains is well captured by the model.

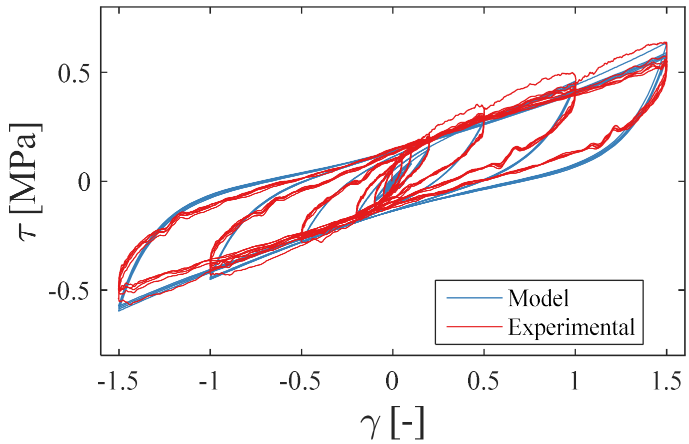

Figure 18. Cyclic shear test on virgin HDRB

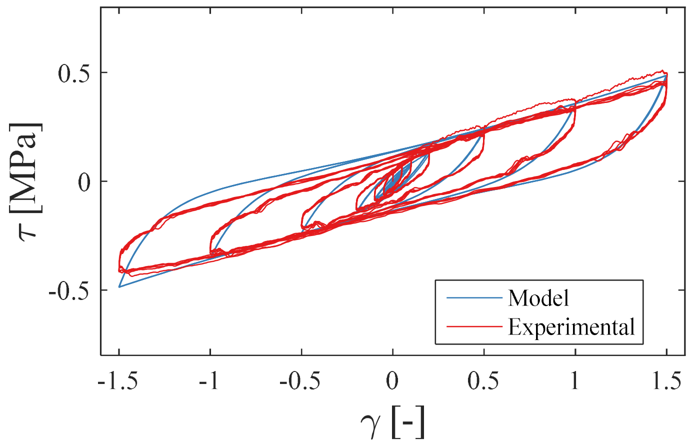

Figure 19. Cyclic shear test on scragged HDRB

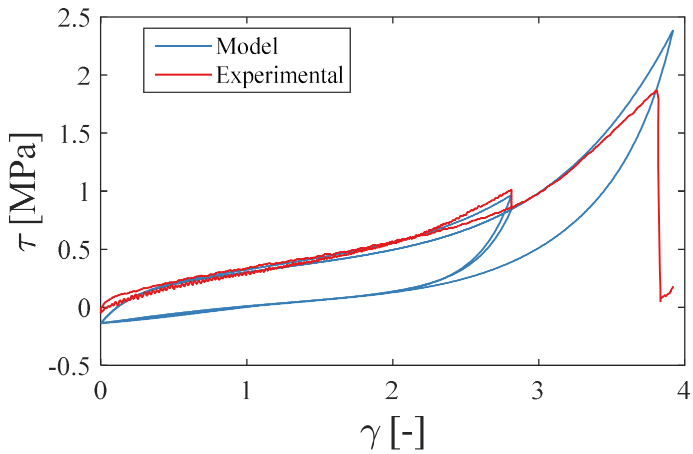

Figure 20. Shear tests up to large strains

Once the model has been calibrated, a final tuning have been done slightly modifying two parameters (α_1 and β_1 in Table 3), in order to obtain at the third loading cycle carried out at the design shear strain $\gamma_s = 2$ the equivalent linear parameters assumed in the design and : $G = 0.4$ MPa and $\xi = 0.15$. The reason is that calibrating the model on a single test, which obviously does not represent the mean property of a batch of manufactured isolators, would lead to a bias in the results since it would not be representative of the real production variability, which is instead assessed later by a statistical model. In Table 3, another set of parameters relevant to a different compound (medium damping, $\xi = 0.10$) is reported. It was used for some specific case studies of the RINTC project. The differences between the two rubber compounds are illustrated in Figure 21, comparing the stress-shear deformation hysteretic cycles.

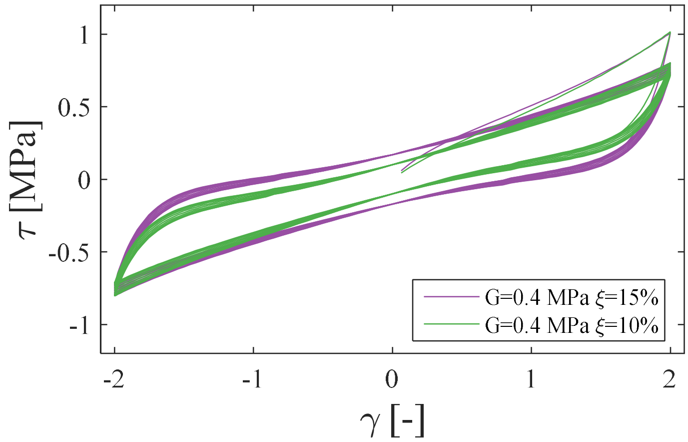

Figure 21. comparison between lower damping and higher damping rubber compounds (numerical hysteresis loops)

Rubber	α_1 [kN/m²]	α_2 [kN/m²]	α_3 [kN/m²]	β_1 [kN/m²]	β_2 [kN/m²]	β_3 [-]	χ_1 [-]	χ_2 [-]	χ_3 [-]	χ_3 [-]
ξ=0.15	276	17.19	3.606	170.4	77.106	5.094	0.0129	0.086	0.831	5e-5
ξ=0.10	315	17.19	3.606	100.2	77.106	5.094	0.0129	0.086	0.831	5e-5

Table 3. Grant's model parameters used for different rubber compounds

3.2.3 Kikuchi Bearing Element (Kikuchi model)

The *Kikuchi Bearing Element* is a full three-dimensional model for rubber bearings. It one of the many models based on the same concept developed the first time by Koh and Kelly (Koh and Kelly, 1986,1988), where the behaviour of the laminated rubber bearing in large displacement is divided in a combination of the Euler column buckling behaviour and pure shear column deformation behaviour. In this case the proposed model by Koh and Kelly is simply a shear spring representing the pure shear behaviour of the bearing connected via two rigid pink to two rotational springs with a stiffness related to the buckling behaviour of the Euler Buckling load neglecting shear deformation.

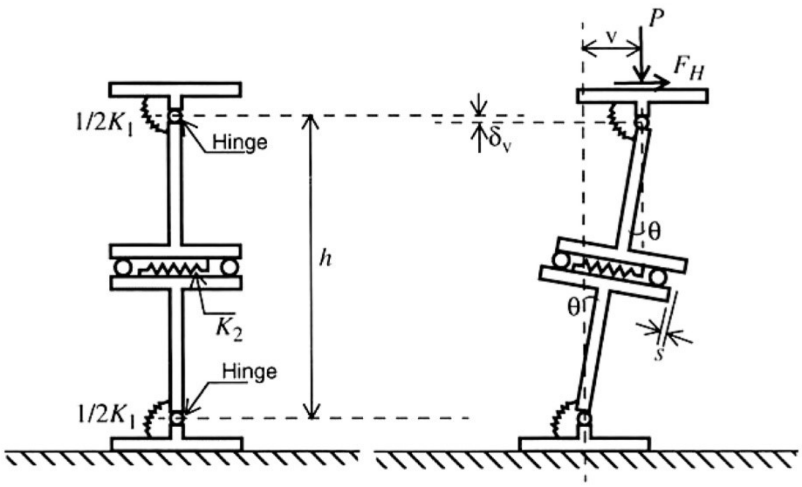

Figure 22. Two Spring model developed by Koh and Kelly (image from Kelly, 1997)

This simple model accurately predicts horizontal and vertical deformation of rubber bearings even for large horizontal displacement, representing the well-known geometric nonlinearity called “P-Δ” effect. The results of seismic response analyses with the two-spring model show that neglecting P-Δ effects can lead to considerable errors for bearings with low buckling safety factors (Koh and Balendra, 1989).

Since the two-spring model consists only of linear springs, it is not suitable for the analysis of high damping rubber bearings that exhibit strong nonlinear behaviour at large shear displacements. Starting from the same philosophy of the *two-spring model*, a model have been developed (Yamamoto et al. 2009) to account for both nonlinear bearing behaviour in large shear deformations and the effect of varying vertical load on bearing properties. This first version was only two-dimensional, as shown in Figure 23.

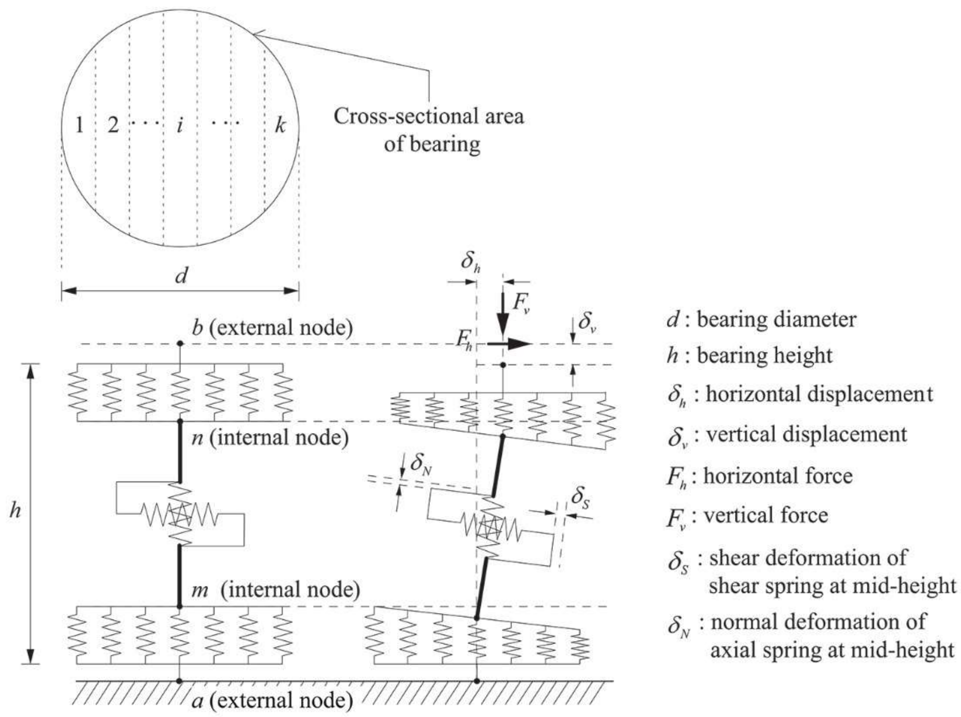

Figure 23. Two-dimensional Kikuchi model (from Yamamoto et al. 2009)

The shear model for rubber is based on a previously work developed by some of the authors (Kikuchi and Aiken, 1997) and it can accurately predict bearing shear behaviour including large deformation and stiffening properties (see Figure 24a). At the top and the bottom of the model there are two series of nonlinear axial springs, each of them representing an individual strip of the bearing cross-sectional area. The axial springs behaviour is reported in Figure 24b. The hysteresis cycle is composed by four loading state:

- Loading and unloading in the elastic region (o–a–b)
- Loading after yielding (b–c), which represents the post-cavitation behaviour
- Unloading after tension yielding (c–d–a)
- Over compression yield stress region (a–e), which represent the real compression failure (for pressure over 100MPa) leading to the yielding of the steel internal plates and not the buckling behaviour.

The rigid links representing the height of the bearing connect the axial springs and the shear spring in the middle. There is also an axial spring in the middle but is considered rigid.

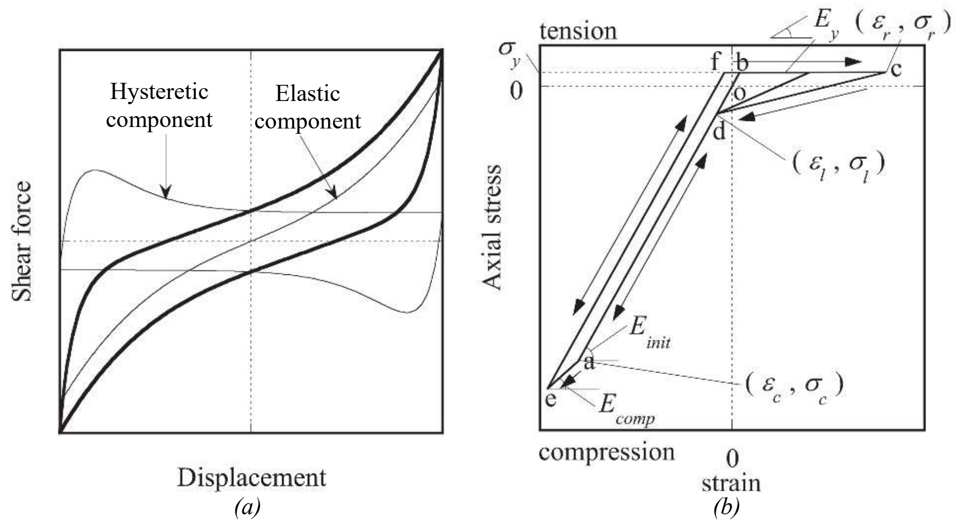

Figure 24. Hysteresis models: (a) shear hysteresis models and (b) axial stress–strain behaviour (from Yamamoto et al. 2009)

It is easy to see the direct coupling of the vertical and horizontal behaviour in the deformed configuration. Vertical and horizontal external forces must be projected in the local configuration of the shear spring in the middle and the projected component of the vertical force becomes additional shear force when the bearing is deformed. Since the vertical force is usually of an higher order of magnitude respect to the horizontal force, even a small rotation of the local orientation could lead to an high increase of the shear forces. In the external response of the bearing this phenomenon shows itself as a stiffness reduction in both the vertical and horizontal direction. For this reason, the force equilibrium condition of this mathematical model takes into account the geometrical relationship of the deformation, the force equilibrium and the P-Δ effects in the definition of the stiffness matrix, according the large displacement formulation.

The two-dimensional model was later extended into a three-dimensional analytical model for elastomeric bearings, featuring triaxial interaction between the two horizontal components and the vertical component (Kikuchi et al. 2010). The extension to the third dimension is based on the use of the *multi shear spring model* (*MSS*) originally proposed by Wada and Hirose (Wada and Hirose, 1987). It allows the use of a simple mono-directional shear model to represent the bi-directional horizontal behaviour by means of a radial arrangement of a set of radial springs. For the tri-dimensional extension each spring in the series of axial springs at the top and bottom boundaries is a uniaxial nonlinear spring and represents an individual fiber of the bearing's cross-sectional area. The set of axial springs is called *multi axial springs* or *multi normal springs* (*MNS*). Other minor revisions of the model (Kikuchi et al. 2012, Ishii and Kikuchi, 2019) led to the final version implemented in the OpenSees software and used in the analyses.

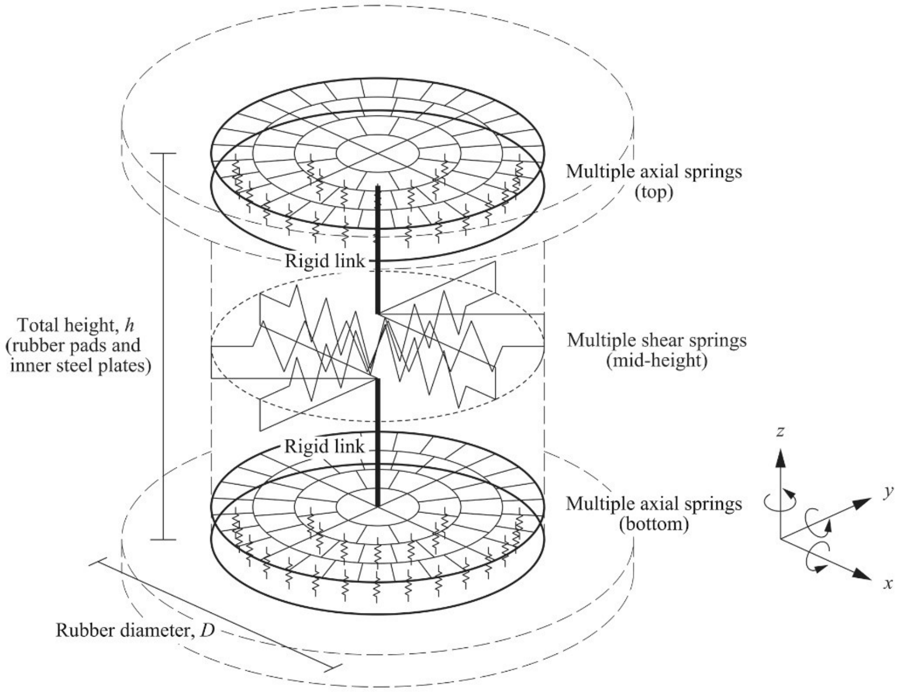

Figure 25. Multi-spring mechanical model for circular elastomeric bearing (from Ishii and Kikuchi 2019)

The stiffness of the axial springs is not constant and its distribution depends on the dimensionless parameter (Ishii and Kikuchi 2019)

$$\bar{\lambda} = \frac{D}{t}\sqrt{\frac{3G}{K_{bulk}}} \tag{3-4}$$

where D is the diameter of the bearing, t is the thickness of the single rubber layer, G is the shear modulus and K_{bulk} is the bulk modulus (usually around 2000MPa). The distribution of the stiffness is almost constant for high values of $\bar{\lambda}$ while is a paraboloid for $\bar{\lambda}$ equal to one, as shown in Figure 26.

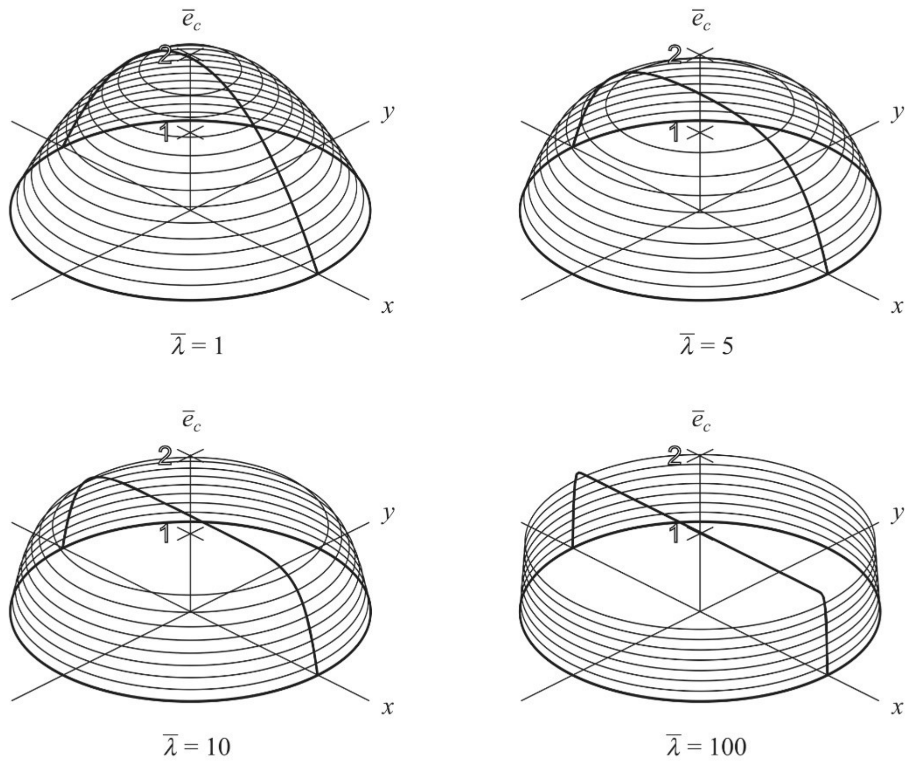

Figure 26. Stiffness distribution of MNS over the area of a circular pad.

The compression modulus of the bearing is computed as follow (Ishii and Kikuchi 2019):

$$E_{init} = K_{bulk} \left\{ 1 - \frac{2}{\bar{\lambda}} \frac{I_1(\bar{\lambda})}{I_0(\bar{\lambda})} \right\} \tag{3-5}$$

where I_1 and I_0 are the modified Bessel function of the first kind of order 1 and 0 respectively.

This model has the advantage that the final horizontal behaviour of the element incorporates the influence of the axial load, which is implicitly captured by the material nonlinearity of the axial springs and the geometrical nonlinearities in the model.

The model is also able to correctly predict the behaviour in the post-buckled condition even for squared bearings and variable vertical load due to the rocking motion of the superstructure during an earthquake, as shown in Figure 27. This is particularly important because the actual hysteresis behaviour of isolation bearings under a structure subjected to severe earthquake shaking is not the same as that obtained from cyclic shear tests of a bearing with constant axial stress, because of the influence of the variation of vertical load due to overturning forces (Kikuchi 2010, Takaoka et al. 2011). For negative shear strain the vertical force increase while for positive shear strain decrease, leading to a strongly asymmetric hysteretic cycle, with a substantial pure shear behaviour for the right side of the cycle and a post-buckled behaviour in the left side. It is also worth to note that for square bearings the buckling "speed" is higher for the case reported in Figure 27a because the two cases differ in the way that the overlapping area is lost. It is also important to highlight the high amount of energy dissipated in the buckling cycle.

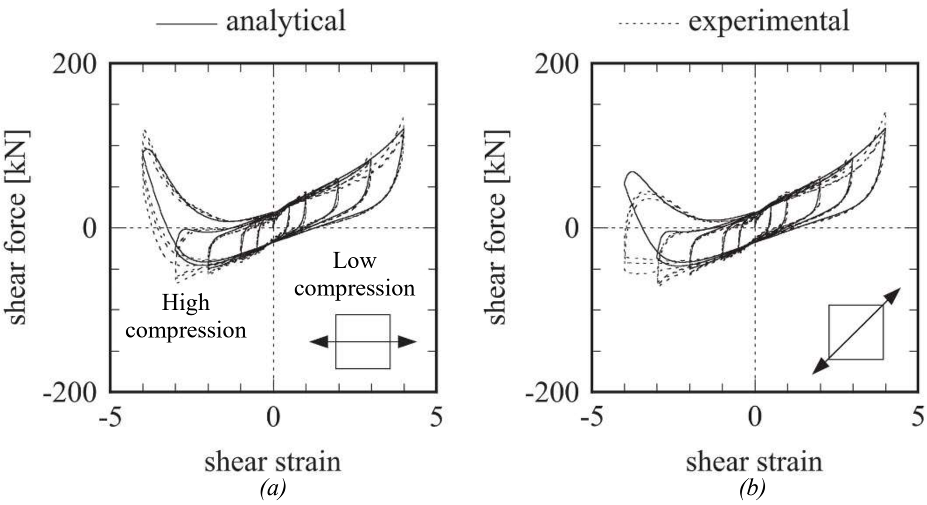

Figure 27. Analysis results for cyclic shear tests with varying vertical load: (a) 0° horizontal loading and (b) 45° horizontal loading.

The *Kikuchi Bering Element,* differently from the *HDR Bearing Element* (Kumar model), is able to capture the reduction of the horizontal stiffness related to the increase of vertical load. This is very important especially for medium-high level of vertical pressure on the bearing as highlighted also by the tests used in this work to calibrate the bearing models (Brandonisio et al. 2017). Consequently, the calibration procedure is different respect to the one used previously.

The *Kikuchi Bering Element* is composed by two different material, one for the *MSS*, called *KikuchiAikenHDR* in the Opensees software representing the pure shear behaviour and one for the *MNS*, called *AxialSP* in the opensees software representing the axial behaviour.

KikuchiAikenHDR: is based on the work of (Kikuchi and Aiken, 1997), but it features only a limited set of pre-calibrated rubber compounds. The model can be slightly adjusted to fit better a specific rubber compound using three correction coefficients: one for equivalent shear modulus (c_g), one for equivalent viscous damping ratio (c_h), one for the ratio of shear force at zero displacement (c_u). Thus, the calibration is quite simple but there is no control for example on the stiffening range for high shear deformation or any damage parameter in the model that can predict the scragging of the rubber and must be calibrated on a specific cycle (usually the third cycle according to EN15129).

AxialSP: is the material used for the *MNSs* according to Figure 24. It is fully defined by the initial elastic vertical stiffness E_{init}, a post elastic stiffness in tension ($1/100E_{init}$) and compression ($1/2E_{init}$), a cavitation stress (1MPa) and a compression yielding stress (-100MPa), as reported in Figure 28. E_{init} is calculated according to Eqn. (5-2).

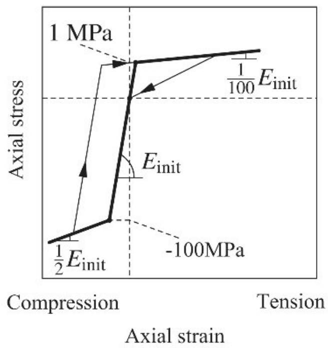

Figure 28. Nonlinear hysteretic model for axial behaviour (from Ishii and Kikuchi 2019)

For low vertical loads and design shear strain the model almost depends only on the pure shear behaviour. Consequently, the cyclic tests at the lower shear deformation have been used to calibrate this material.

Tests on the SI-S 700-207 have been chosen among the three sets because it is the most complete and the only one reaching a pressure of 20 MPa. The other two sets (tests on SI-S 500-176 and SI-S 600-217) have been used to compare the experimental result with the calibrated model.

According the prescription previously presented, the shear material used for the rubber is the X0.4-0MPa (Bridgestone Corporation, 2017), with the three correction coefficients c_g, c_h and c_u equal to 1.15, 0.75 e 0.75 respectively, to better fit the third cycle behaviour, and for the axial behaviour G=0.4MPa and K_{bulk}=2000MPa. Since the tests clearly show the stiffness reduction related to the scragging of the rubber but the model doesn't feature any kind of damage parameter, c_g has been further corrected to better predict the hysteretic response for the Shear Cyclic Tests (*SCTs*). Since all the test sequence take role in the progressive reduction of the stiffness, the same level of stiffness reduction (highlighted as percentage of *k* in the figures) has been maintained constant in all the *SQTs* between two consecutive *SCTs*. Consequently, the axial test and the *Shear Quasistatic Tests* (*SQTs*) don't take any role in the calibration. Figure 29 shows the very good agreement between the axial tests and the vertical model response, confirming that Eqn. (5-2) effective predict the correct vertical stiffness for the loading path (the model has no rate-dependent features for this level of pressure behaves as elastic and cannot predict the unloading path). Figure 30 shows the three *SCTs* of the bearing SI-S 700-207 (Test 3, 6 and 16) on which the calibration of the three correction coefficients is based. It is worth to note that the model cannot predict the asymmetrical damage related to the scragging developed during the repeated cycles in the positive direction, underestimating the stiffness for negative shear deformations. Moreover, for γ>1 the hysteretic cycle start to show the softening behaviour due to the approaching of the buckling of the model.

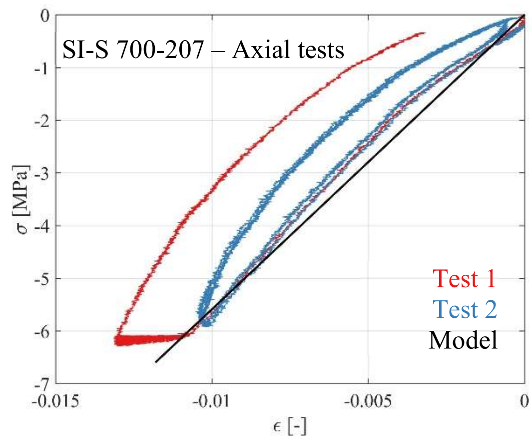

Figure 29. Comparison of axial test experimental results and calibrated model for SI-S 700-207

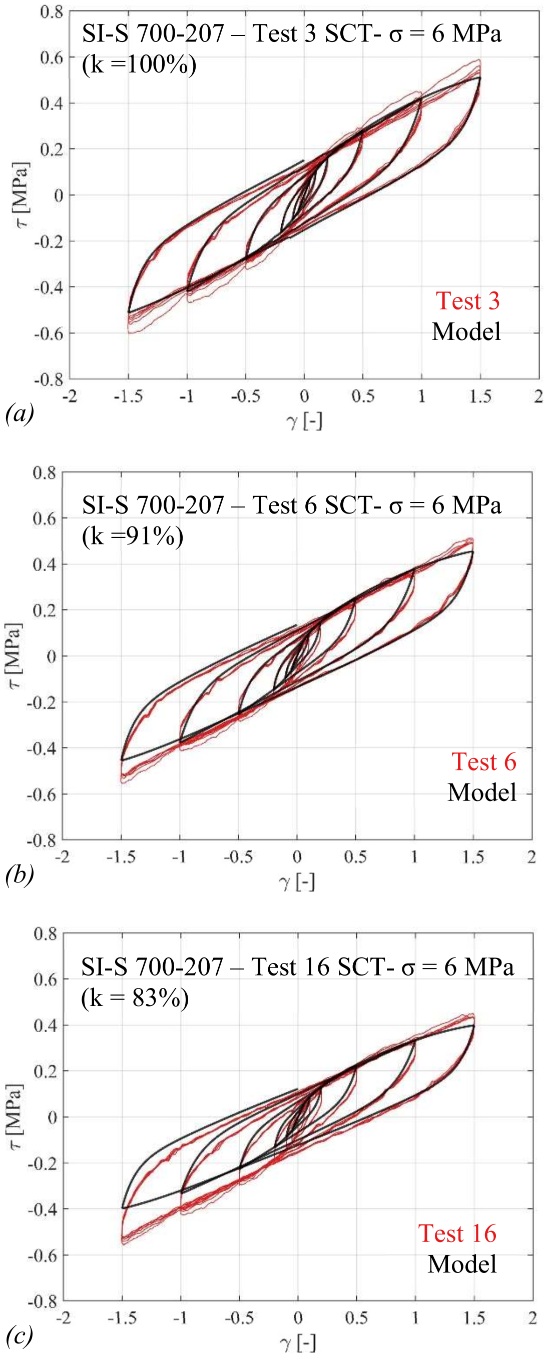

Figure 30. Comparison of SCT experimental results and calibrated model (nonlinear axial springs) for SI-S 700-207

The *Kikuchi Bearing Element* equipped with the *AxialSP* material for the *MNS* seems to strongly overestimate the *P-Δ* effects, leading to an anticipation of the buckling behaviour, as shown for all the *SQTs*, especially for higher vertical pressures.

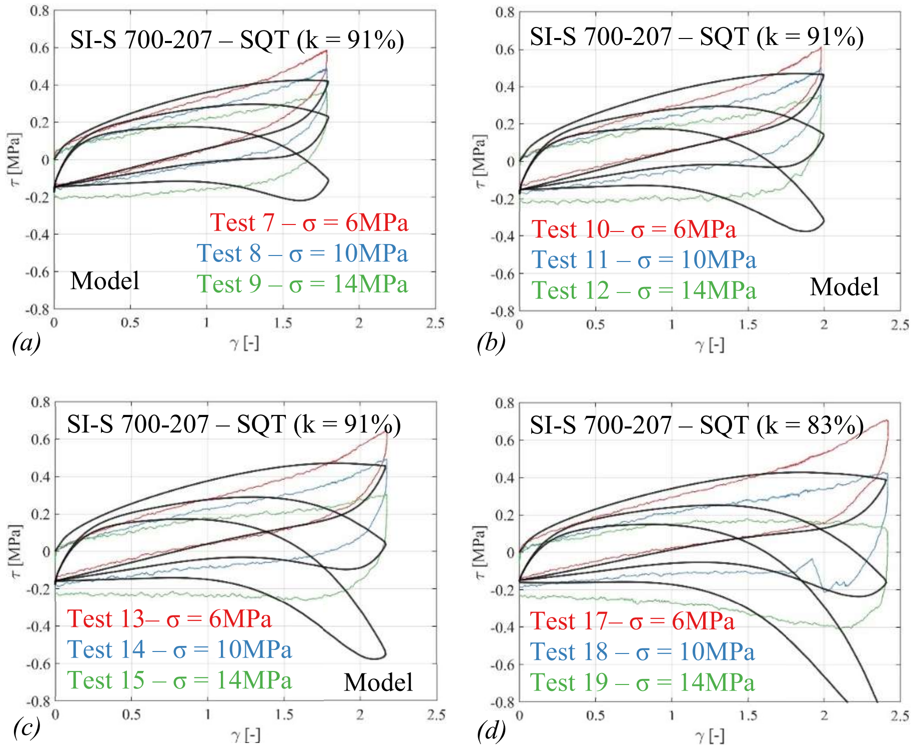

Figure 31. Comparison of SQT experimental results and calibrated model (nonlinear axial springs) for SI-S 700-207

The reason of this shortcoming can be found in the definition of the cavitation phenomenon. First, the value of negative pressure at which the cavitation occurs is quite scattered (a value of $3G$ is a reasonable estimation, but the variability is quite high) (Kumar et al. 2015). Moreover, the behaviour in tension of rubber bearings may also exhibits a tension buckling (Kelly and Kostantinidis, 2011, Kelly and Marsico, 2013, Forcellini and Kelly, 2014) and possibly leads to a tensile strain greatly exceeding the strain cavitation. Kelly clearly explain this behaviour (Kelly and Kostantinidis, 2011):

> *" […] when the isolator is in compression below the buckling load but laterally displaced, the layers in the center experience a rotation which gives the vertical load a component along the layer and induces a shear deformation. In tension, the layers in the center experience a rotation in the opposite direction, which allows a shear deformation caused by the tensile force and permits the top of the isolator to move upwards by a much larger displacement than that which could be sustained in pure tension with no lateral displacement. Thus, the simultaneous occurrence of tension and shear allows the isolator to avoid the damage*

of cavitation. The rubber can sustain only small strains in the state of triaxial stress generated by pure tension on a multilayer isolator with a large shape factor, but can sustain shear strains on the order of 500 or 600%. Thus, the simultaneous occurrence of tension and shear allows the isolator to avoid the damaging effects of cavitation"

This shortcoming of the *Kikuchi Bearing Element* is in contrast with the many comparisons made by the authors (Ishii and Kikuchi, 2019, Kikuchi et al. 2010) where good agreements had been found. The error in modelling these tests could be associated to the hidden hypothesis that is at the base of this model: the behaviour of the single axial spring is the same of the whole bearing. This hypothesis could be true depending on the primary and secondary shape factor: for very high primary shape factors (S_1=30) and normal secondary shape factors (S_2=3) the compression buckling could be triggered by the cavitation of the perimetral fibers subjected to tension while, for lower primary shape factors and higher secondary shape factors, slender bearing could experience buckling before the cavitation of the rubber.

To avoid this issue, under the hypothesis that for the bearings tested in this work the local cavitation is anticipated by the buckling due to the lower primary shape factor, the material used for the *MNS* has been substituted with a simple elastic material with elastic stiffness equal to E_{init}. Moreover, the same stiffness reduction (percentage on *k*) have been applied for both the *MSSs* and the *MNSs*. The results are in better agreement with the experimental campaign, as shown hereafter.

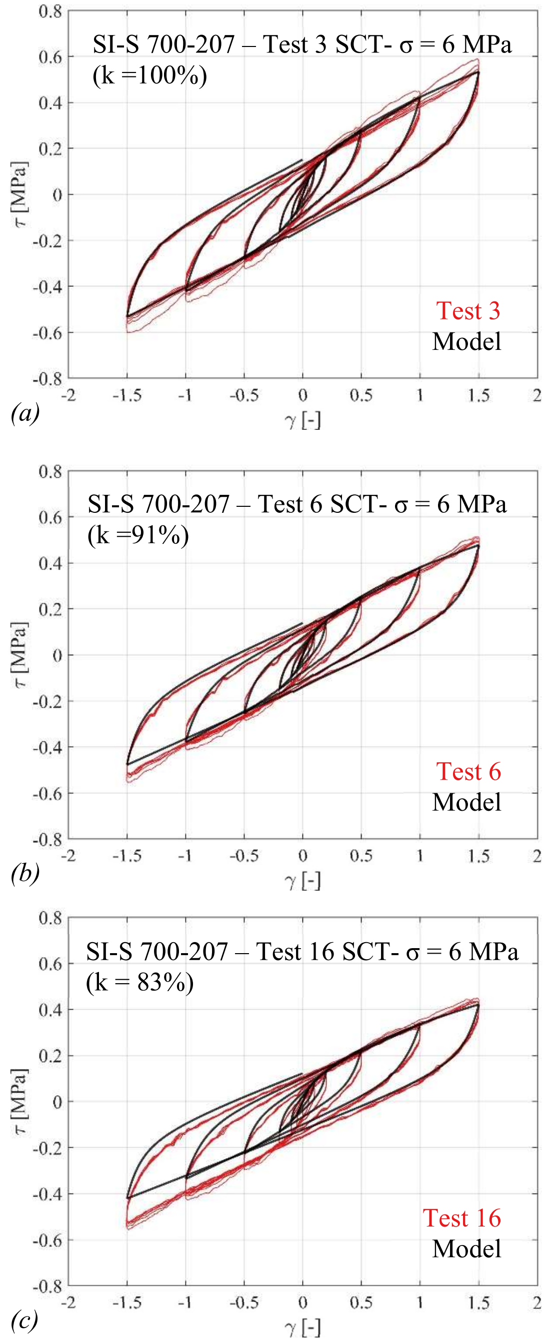

Figure 32. Comparison of SCT experimental results and calibrated model (linear axial springs) for SI-S 700-207

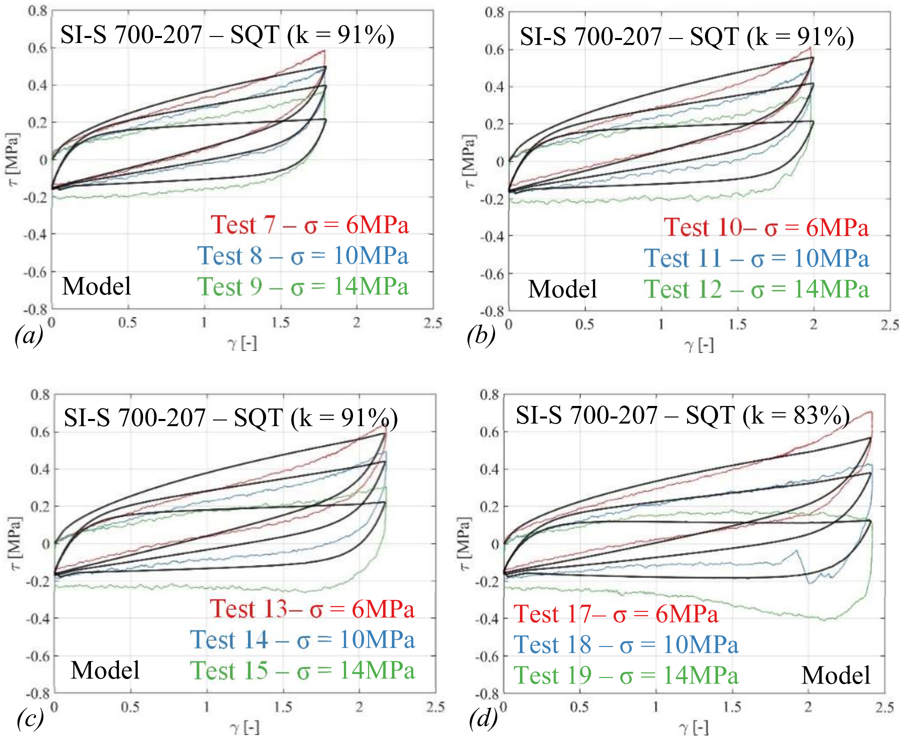

Figure 33. Comparison of SQT experimental results and calibrated model (linear axial springs) for SI-S 700-207

The figures show a very good agreement between the experimental and the numerical results. Obviously the model cannot predict the asymmetrical damage of the rubber due to the repeated cycles only in the positive range of shear deformation (see Test 6 *SCT* and test 16 *SCT*). Nor the model can follow the first loading branch of the *SQTs* because when the rubber reach for the first time the highest shear deformation (SQT 7, 10, 13,17) it behaves as virgin rubber (1^{st} cycle) while the model is calibrated on the third cycle.

All the sequences of tests for the SI-S 500-176 and SI-S 600-217 is presented hereafter, without any change in the model definition. Only the vertical stiffness has been recomputed according to the different geometry of the bearings (according to Eqn. (5-2)). First the results for the SI-S 500-176 are reported.

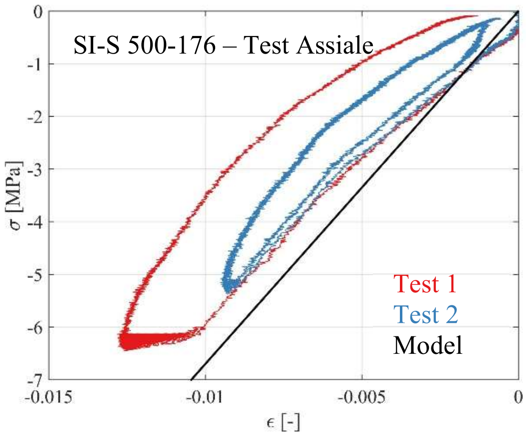

Figure 34. Comparison of axial test experimental results and calibrated model (linear axial springs) for SI-S 500-176

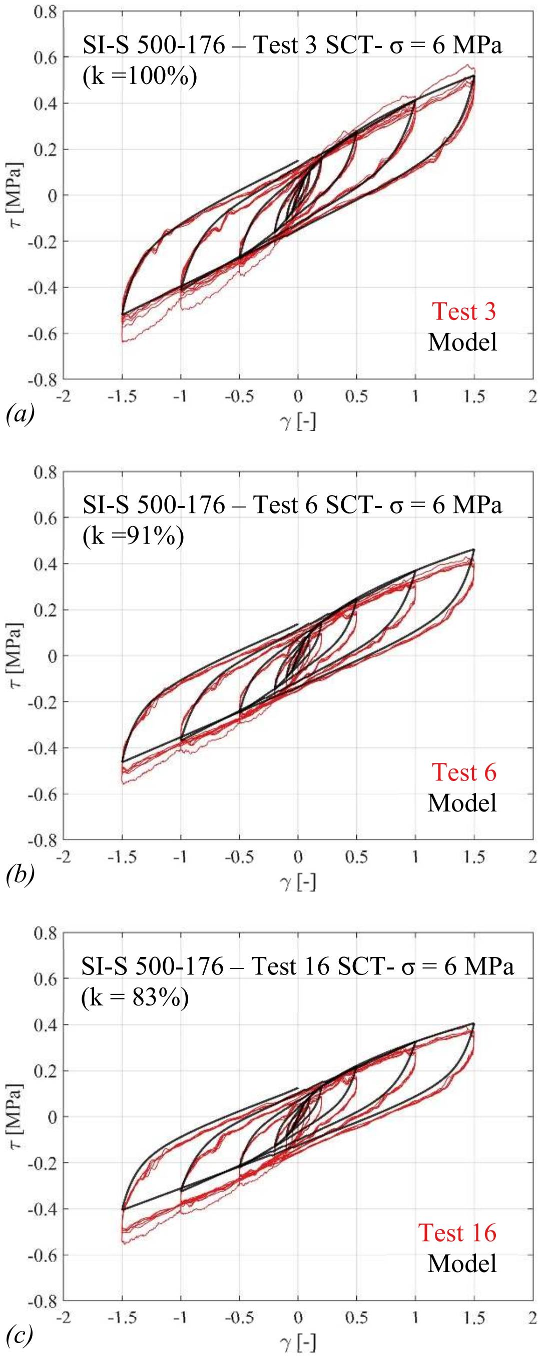

Figure 35. Comparison of SCT experimental results and calibrated model (linear axial springs) for SI-S 500-176

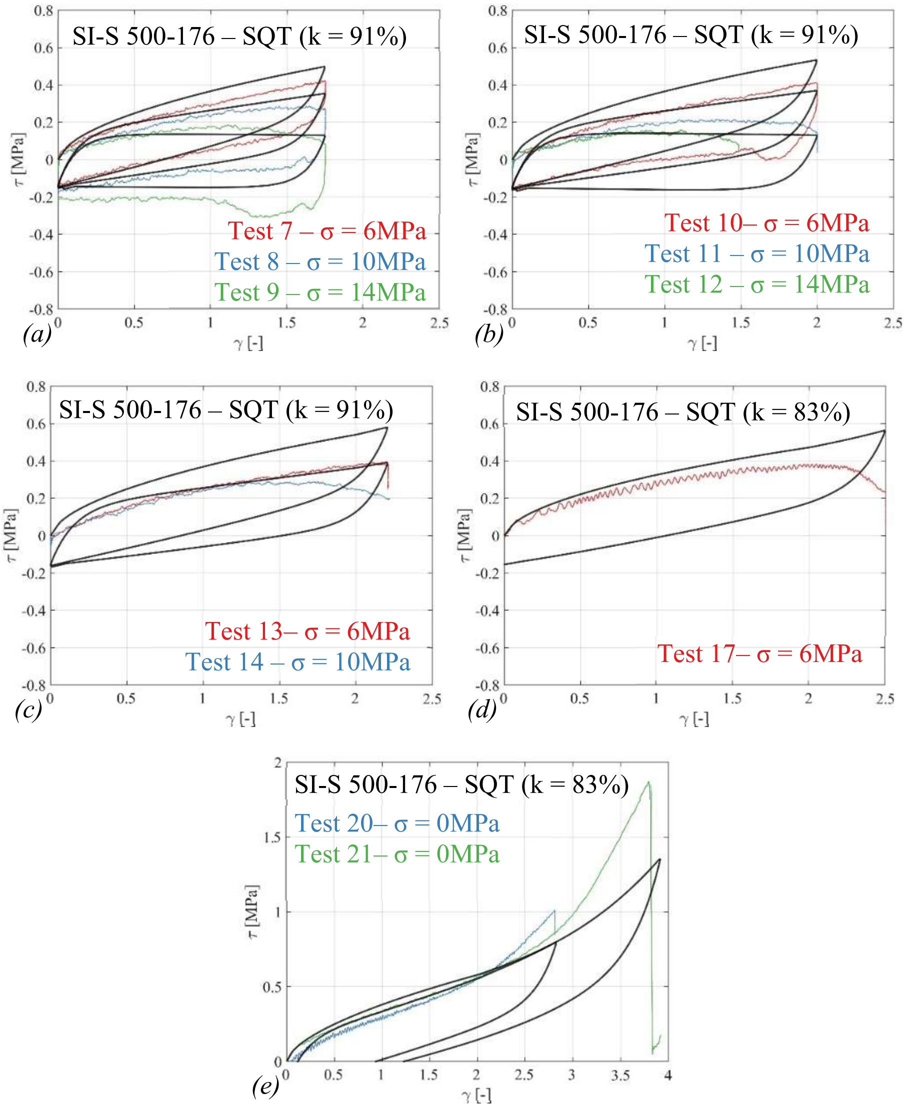

Figure 36. Comparison of SQT experimental results and calibrated model (linear axial springs) for SI-S 500-176

Bearing SI-S 500-176 have been subjected to shear deformations higher than 3.5 (tests 21). As mentioned before, the model doesn't feature any control on the stiffening behaviour for high shear strain and is calibrated on a third cycle behaviour. Consequently, it underestimates the shear stress in the range of 1st cycle shear deformation (γ>2.5 for test 20 and γ>2.8 for test 21). This will be recalled to understand the different results changing the bearing model in the seismic risk analysis.

The results of the SI-S 600-217 are reported hereafter. It is worth to note that this bearing is the slenderest and the buckling behaviour is the most evident (tests have been often suspended to avoid damage to the testing machine).

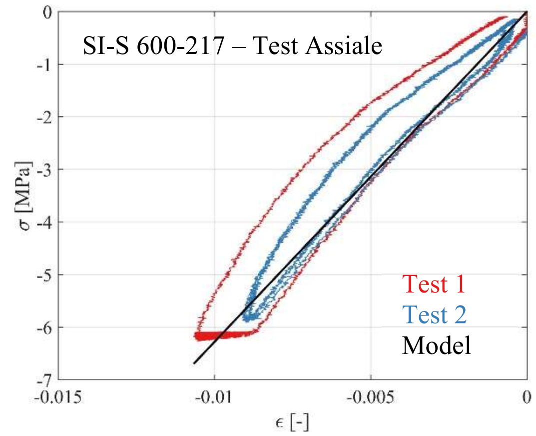

Figure 37. Comparison of axial test experimental results and calibrated model

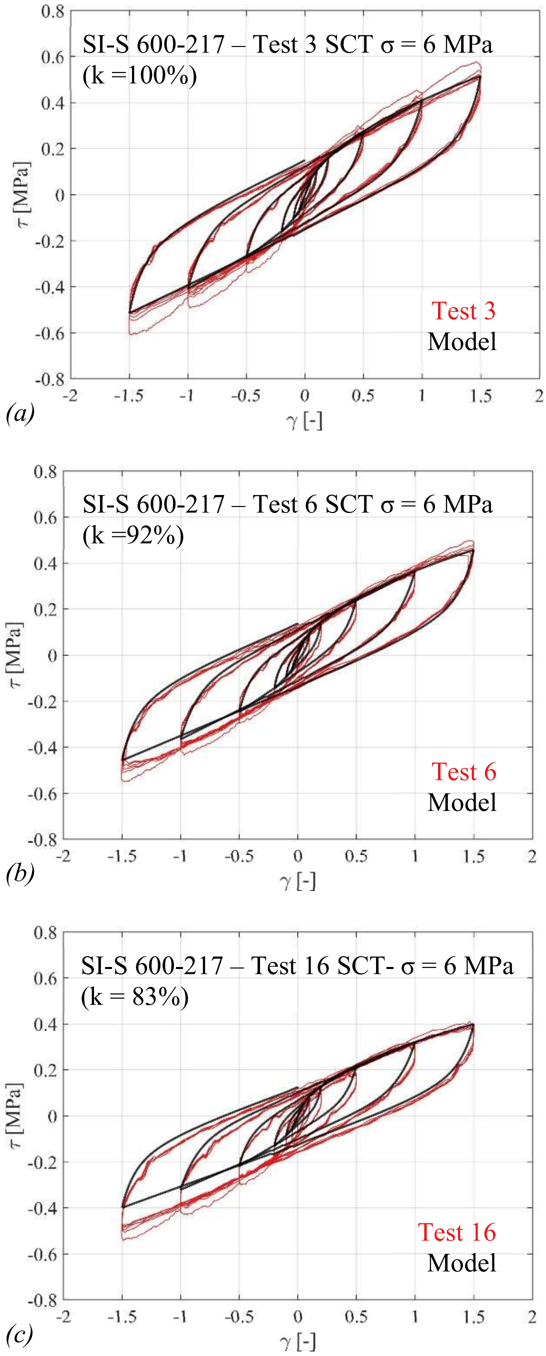

Figure 38. Comparison of SCT experimental results and calibrated model (linear axial springs) for SI-S 600-217

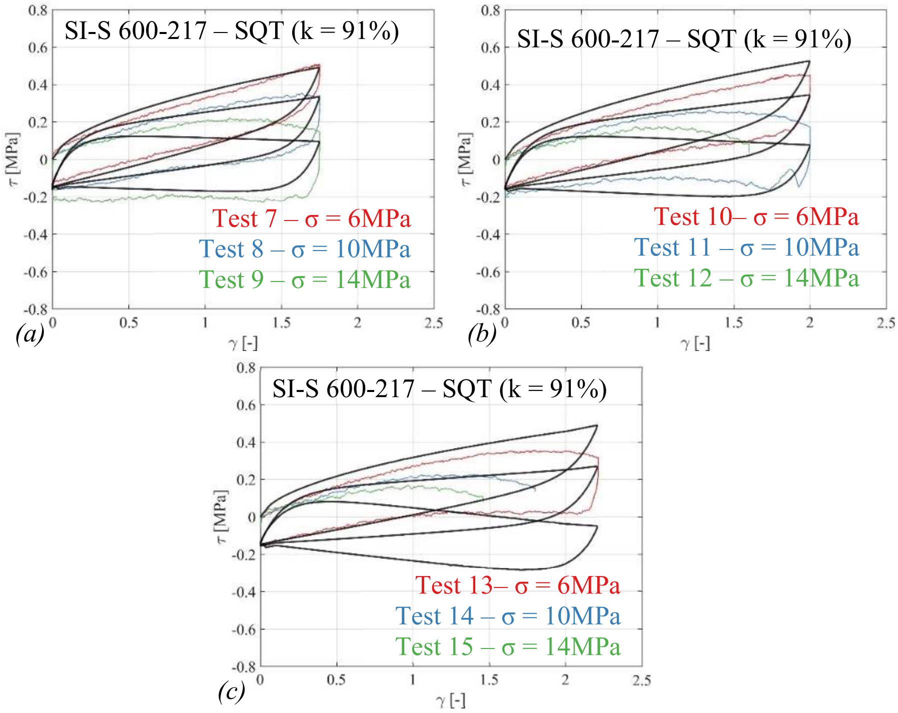

Figure 39. Comparison of SQT experimental results and calibrated model (linear axial springs) for SI-S 600-217

The model in this version is not able to capture the cavitation behaviour because the material used for the *MNS* is elastic. For this reason, the *Kikuchi Bearing Element* has been implemented in the building model in series with a rigid-plastic spring for the axial behaviour. This extra spring is almost rigid for vertical compression and for tension forces lower than 3*GA* (Kumar et al. 2014), i.e. for forces lower than the cavitation, whereas it represent the post-cavitation vertical stiffness of the bearing for forces higher than this limit. In this way, the global building model response is able to capture the influence of cavitation on the rocking motion during the earthquake.

3.3 Superstructure

Pragmatic choices have been introduced for the superstructure model in order to limit the computational effort. The first is the use of a lumped plasticity model that has been chosen for beam and column elements of the superstructure, whereas elastic beams have been used for the base floor grid above the isolation system. The choice of representing the superstructure with a nonlinear model is justified by the results of recent studies on this topic (Cardone et al., 2013, Cardone and Flora 2016), which pointed out the effects of the inelastic behaviour of the superstructure on the seismic response of base isolated buildings. The model also includes the staircase structure (inclined beams and cantilever steps) as well as masonry infill panels. Regarding the RC frames for new isolated buildings, the model selected for the description of the section flexural behaviour is the well-known model by Ibarra (Ibarra and Krawinkler, 2005, Ibarra et al., 2005), implemented in OpenSees as *modIMKmodel*. Reference to (Camata et al, 2017, ReLUIS-RINTC Workgroup, 2018, Ricci et al., 2018) is made for more details on the numerical model of superstructure for new buildings.

In the case of existing buildings, the lumped plasticity model chosen for beams and columns is based on the one used for the new buildings. Some modifications and integrations have been adopted to consider specific failure mechanism that, contrary to new buildings, are not avoided by the adoption of capacity design principles, i.e., shear failures before or after flexural yielding in beam/column elements and in beam column joints. More in detail, all the hinges have been pre-qualified of the hinges as ductile, in which the shear failure is avoided and the moment-rotational backbone model is not modified, or shear critical, in which the backbone is reduced. In this latter case if the shear failure occurs before the yielding the element is defined as “brittle”, whereas if shear failure occurs within the yielding and the maximum moment the element is characterised by a flexure-shear interaction failure mechanism. Regarding the beam column joint, the joint panel model called “scissors model” has been used, a very simple and computationally less demanding joint model, but also sufficiently accurate in predicting the experimental beam-column joint panel behaviour for simulating the seismic response of non-ductile RC frames (De Risi et al., 2016). The adopted constitutive model accounts for two possible failure mode of the beam-column joints: joint shear failure prior to or after the achievement of yielding of the adjacent beams/columns (in strong column-weak beam/weak column-strong beam hypothesis). More information for the superstructure modelling of existing buildings can be found in (Ricci et al. 2019).

The contribution of masonry infill panels is modelled with an equivalent compression-only strut. The skeleton curve of the diagonal strut has been derived according to a modified version of the Decanini model (Sassun et al., 2016). The effects of the openings have been taken into account through suitable reduction factors (Decanini et al., 2014).

Regarding pounding of the isolation system, some case studies have been assessed considering also the possible impact between the base floor deck and a rigid fixed wall around the base floor. The "*Elastoplastic Gap Material*" consisting of an initial gap and an elastoplastic element (with post-yield ratio equal to 0.5) is used to model the retaining wall in OpenSees. For this purpose, two Zero-Length gap elements (one in X direction and the other in Y direction) have been added at each corner of the building. The aforesaid model is not dissipative during the impact unless the impact force exceeds the elastic limit (Fy). In order to determine the parameters of the gap model, it was assumed that the impact occurs between a rigid retaining wall and a deformable base slab. However, since a rigid constraint at the base slab is imposed, the elastic stiffness of the gap model has been calculated as the axial stiffness of the slab portion involved in pounding. Since contact elements are introduced only at the corner nodes of the base slab, half slab width has been considered for each gap element (Nakazawa et al., 2011, Pant and Wijeyewickrema, 2014; Liu et al., 2017). Similarly, the limit elastic force has been taken equal to the axial strength of the half slab width. It is important to highlight that the energy dissipation during the impact for low impact forces as well as the dissipation due to friction for sliding displacements between the slab and the retaining walls are conservatively neglected.

3.4 Hazard

All the information about seismic hazard assessment and record selection can be found in (Iervolino et. al., 2018) and have been carried out in RINTC project framework. Some considerations specifically related to the work about seismically isolated structures and not all the project are reported hereafter.

The RINTC framework, as for any other PBEE framework start with the definition of the hazard model. The project considered 5 sites (i.e., L'Aquila, Naples, Rome, Caltanissetta and Milan) and two soil type (i.e., Type A with $V_{s,30} > 800$ m/s and Type C with $180 < V_{s,30} < 360$ m/s). For each combination a PSHA have been carried out, defining the hazard curves for the following vibration period T_1 = {0.15s, 0.5s, 1.0s, 1.5s, 2.0s}. For L'Aquila and Naples, the only two sites in which seismic isolation systems have been analysed, also the hazard curves for T_1 = 3.0s have been computed to cover the range of isolation period. The hazard curve were computed according to Eqn. (3-6)

$$\lambda_{IM}(x) = \sum_{i=1}^{s} v_i \cdot \int_{M}\int_{R} P[IM > x \mid M = w, R = z] \cdot f_{M,R,i}(w,z) \cdot dz \cdot dw \qquad (3\text{-}6)$$

where v_i, i = {1,2,…,s} is the rate of earthquakes above a minimum magnitude (M) for each of the s seismic source zones affecting the hazard at the site of interest; $f_{M,R,i}(w,z)$ is the joint probability density function of magnitude and source-to-site distance, (R), of the i^{th} zone; and $P[IM>x|M=w,R=z]$ is the exceedance probability conditional to {M, R} as provided by a *ground-motion prediction equation* (*GMPE*, defining probability distribution of ground motion intensity, as a function of many predictor variables such as the earthquake's magnitude, distance, faulting mechanism, the near-surface site conditions, the potential presence of directivity effects, etc, Baker 2013).The source model of Meletti et al. (2008), which is used in Stucchi et al. (2011), was considered. It features the 36 seismic source zones depicted in Figure 40, and no background seismicity.

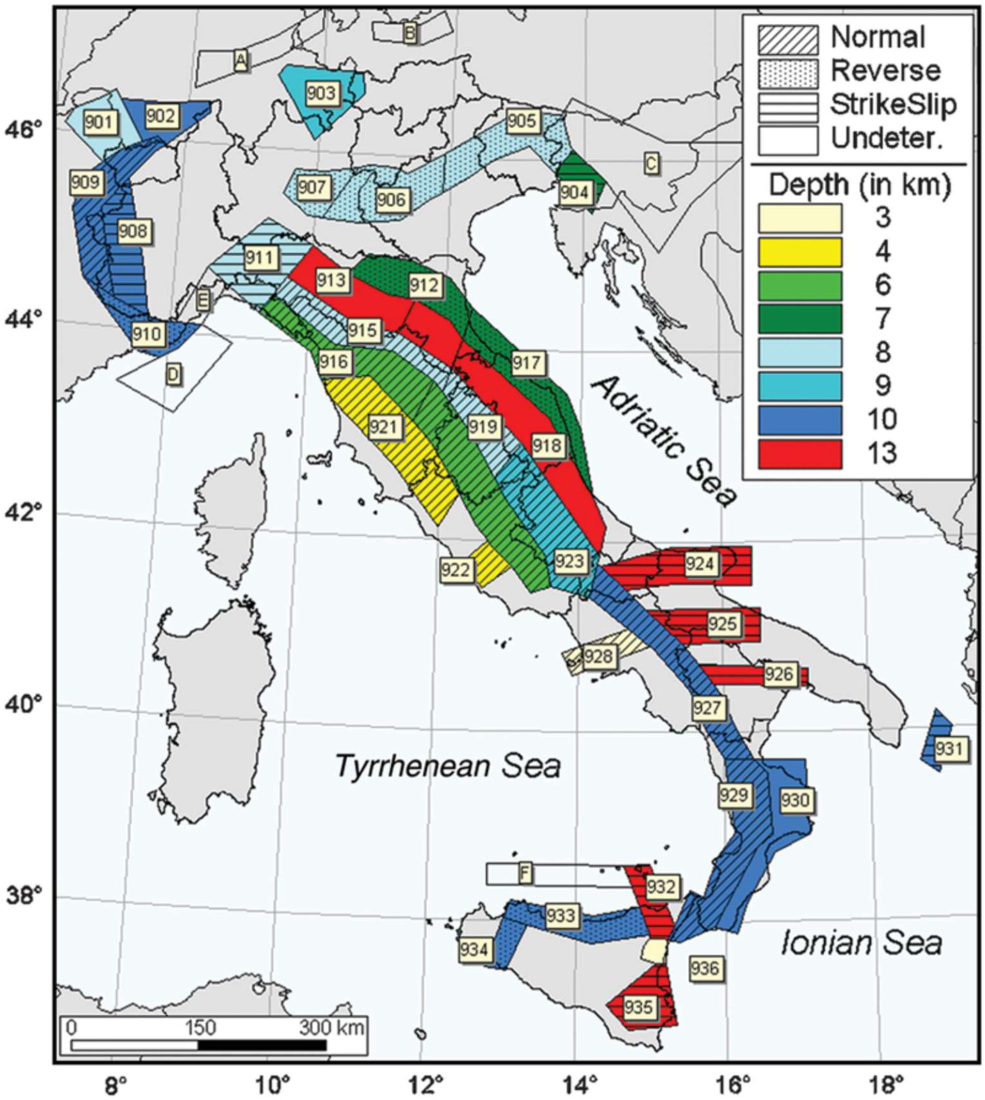

Figure 40. ZS9 source zone model from Stucchi et. al., 2011 (redrawn from Meletti et al., 2008). The numbers in the boxes identify the earthquake source zones; the colours refer to the mean seismogenetic depth (in km); the superimposed shadings refer to the predominant focal mechanism. The source zones with letters were not used in the assessment.

The source characterization in terms of rates and magnitude distribution is that of (Barani et al., 2009), and the *GMPE* selected for computing the hazard for spectral accelerations at periods shorter than 2.0s is the one of (Ambraseys et al., 1996), which use as *IM* the maximum spectral acceleration between the horizontal components. For longer periods, needed for predicting the response of base isolated structure, the *GMPE* of Ambraseys et al. (1996) was not applicable because its maximum period is 2.0s. For this reason, *GMPE* of (Akkar and Bommer, 2010) was employed for T_I=3.0s. Note that the latter use the geometric mean of the two horizontal components. A uniform location distribution in each zone was assumed. All PSHA calculations have been carried out via *OPENQUAKE* (Monelli et al., 2012).

It is worth to note that changing *GMPE* for base isolated structure could have led to a bias in the results, resulting in increasing the probability of failure of this archetype respect to all the other structures analysed in the project. More information can be found in Chpt. 5 . Figure 41 shows the hazard curves of L'Aquila for soil type C based on Ambraseys et al. (1996) except for T=3.0s where Akkar and Bommer (2010) has been used. Vertical axis represent the *probability of exceedance in 50 years* (P_{50y})

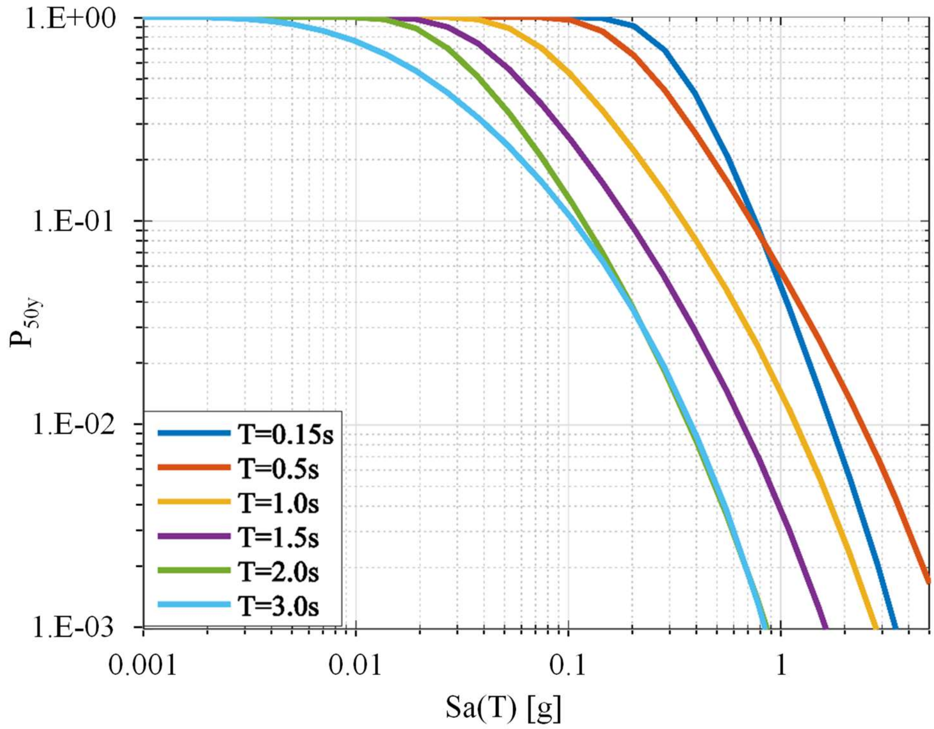

Figure 41. Hazard curves at L'Aquila for Soil Type C; the curve at T=3.0s was computed according to the model of Akkar and Bommer (2010).

It is reminded that if the earthquakes are considered a *HPP*, P_{50y} can be computed as

$$P_t = 1 - e^{\lambda \cdot t} \tag{3-7}$$

where λ is the rate of occurrence (i.e., event per unit time), equal to the inverse of *return period Tr*, and t = 50y.

Although the source model considered for hazard assessment is the same used by the code, the code hazard maps are based on a logic tree while only one branch is considered in this study. More specifically, we implemented Branch 921 of the MPS04 source model of the INGV (Istituto Nazionale di Geofisica e Vulcanologia). Therefore, the design accelerations of the project are expected to be slightly different respect to the ones of the Italian code.

In *multi-stripe dynamic analysis* multiple "stripes" of response are obtained by applying to the structure a set of ground motion records that are scaled to multiple levels of spectral acceleration. In RINTC project the number of stripes have been set to 10 *IML*, corresponding to the following return period T_R = {10y; 50y; 100y; 250y; 500y; 1000y; 2500y; 5000y; 10000y; 100000y}, and so a rate of occurrence λ ranging from 10^{-1} to 10^{-5}. Focusing on periods and sites assessed for seismically isolated buildings, the *IMLs* used in the analyses are reported in Figure 42.

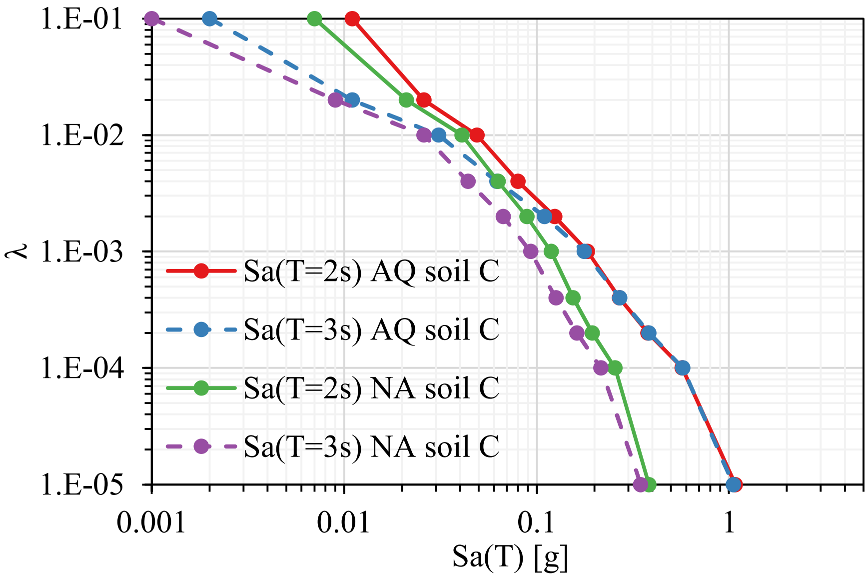

Figure 42. IMLs and corresponding rate of occurrence for spectral ordinates and soil types computed for seismically isolated buildings

To perform nonlinear dynamic structural analyses at each intensity measure level a set of ground motion time histories scaled to the desired intensity have to be defined. It should reflect the site hazard scenario, that is, they should be consistent in terms of magnitude *M* and distance *R* that would likely cause that level of excitation in that particular place. In other words, choosing the ground shaking signals, the information regarding the pairs *M-R* used in Eqn. (3-6) must be taken into account because they affect the duration and frequency content of the ground-motion time history, which in turn affects structural response.

Disaggregation has been carried out according to (Bazzurro and Cornell, 1999). More information can be found in (Iervolino et. al., 2018).

With hazard curves and hazard disaggregation, the selection of the earthquake records have been carried out according the *conditional spectrum* (*CS*) method proposed by (Lin et. al., 2013) and improved using a post-processing procedure to ensure consistency of selected records with magnitude-distance disaggregation, implicitly account for ground-motion record characteristic other than spectral shape (Spillatura, 2018). More in detail this method can be summarized as follow:

- (a) carry out disaggregation conditional to $Sa(T_1) = x$, where x corresponds to the 10 values having exceedance return periods from 10y to 100,000y at each of the three sites;
- (b) build the corresponding *CS* distribution for each x-value;
- (c) simulate an arbitrary number of response spectra, 20 herein, consistent with the *CS* defined at the previous step;
- (d) select 20 records that have spectra compatible with those simulated;
- (e) post-process the selected set substituting the records that are not disaggregation-consistent with other spectrally equivalent ground motions with desired *M* and *R*

The selected records were extracted from the Italian accelerometric archive (http:// itaca.mi.ingv.it/; Luzi et al. [2008]) unless there were no suitable records. In this case the algorithm searched for records in the NGAwest2 (http://peer.berkeley.edu/ngawest2/) database (Ancheta et al., 2014).

The result is 200 pairs of records for each combination of site, *Sa*, and soil conditions, divided in 10 sets (1 per stripe) of 20 horizontal ground-motions (pairs). The selected records have been also processed to reduce their length and so to ease the computational effort for nonlinear analysis of the three-dimensional structural models. This has been done cutting signal maintaining only the $\{t_{0.05\%}$ - $t_{99{:}95\%}\}$ range, where $D_{99.90\%}$ is the 99.90% *significant duration* of the record (Dobry et al., 1978). Synchronization of horizontal components after post-processing was kept.

3.5 Chapter's references

Akkar, S., Bommer, J.J., 2010. Empirical Equations for the Prediction of PGA, PGV, and Spectral Accelerations in Europe, the Mediterranean Region, and the Middle East. Seismological Research Letters 81, 195–206. https://doi.org/10.1785/gssrl.81.2.195

Ambraseys, N.N., Simpson', K.A., Bommer', J.J., 1996. PREDICTION OF HORIZONTAL RESPONSE SPECTRA IN EUROPE. Earthquake Engineering & Structural Dynamics 25, 371–400. doi:10.1002/(SICI)1096-9845(199604)25:4<371::AID-EQE550>3.0.CO;2-A.

Ancheta, T. D., Darragh, R. B., Stewart, J. P., Seyhan, E., Silva, W. J., Chiou, B. S. J., Wooddell, K. E., Graves, R. V., Kottke, A. R., Boore, D. M., Kishida, T. and Donahue, J. L. [2014] "NGA-West2 database," Earthquake Spectra 30, 989–1005. doi:10.1193/070913EQS197M.

Baker, Jack W. (2013) Probabilistic Seismic Hazard Analysis. White Paper Version 2.0.1.

Barani, S., Spallarossa, D., Bazzurro, P., 2009. Disaggregation of Probabilistic Ground-Motion Hazard in Italy. Bulletin of the Seismological Society of America 99, 2638–2661. https://doi.org/10.1785/0120080348

Bazzurro, P. and Cornell, C. A., 1999. Disaggregation of seismic hazard. Bulletin of the Seismological Society of America 89, 501–520.

Brandonisio, G., Guidi, L.G., Luca, A.D., 2019. Stability evaluation for rubber bearings: code requirements and comparison with experimental results, Proc. of 18th ANIDIS Conference, Ascoli Piceno, Italy

Brandonisio, G., Ponzo, F., Mele, E., Luca, A.D., 2017. Experimental tests of elastomeric isolators: influence of vertical load V and of secondary shape factor, Proc. of 17th ANIDIS Conference, Pistoia, Italy

Brandonisio, G., Ponzo, F., Mele, E., Luca, A.D., 2017. Experimental tests of elastomeric isolators: influence of vertical load V and of secondary shape factor, Proc. of 17th ANIDIS Conference, Pistoia, Italy

Bridgestone Corporation (2017) Seismic isolation product line-up.

Camata, G., Celano, F., Risi, M.T.D., Franchin, P., Magliulo, G., Manfredi, V., Masi, A., Mollaioli, F., Noto, F., Ricci, P., Spacone, E., Terrenzi, M., Verderame, G.M., 2017. RINTC PROJECT: NONLINEAR DYNAMIC ANALYSES OF ITALIAN CODE-CONFORMING REINFORCED CONCRETE BUILDINGS FOR RISK OF COLLAPSE ASSESSMENT, in: Proc. of 6th ECCOMAS. Presented at the Thematic Conference on Computational Methods in Structural Dynamics and Earthquake Engineering (COMPDYN 2017), Rhodes Island, Greece. https://doi.org/10.7712/120117.5507.17050

Cardone, D., Conte, N., Dall'Asta, A., Di Cesare, A., Flora, A., Leccese, G., Mossucca, A., Micozzi, F., Ponzo, F.C., Ragni, L., 2017. RINTC PROJECT: NONLINEAR ANALYSES OF ITALIAN CODE-CONFORMING BASE-ISOLATED BUILDINGS FOR RISK OF COLLAPSE ASSESSMENT, Proc. of 6th ECCOMAS Thematic Conference on Computational Methods in Structural Dynamics and Earthquake Engineering (COMPDYN 2017), Rhodes Island, Greece. pp. 1732–1747. https://doi.org/10.7712/120117.5525.19365

Cardone, D., Flora, A., 2016. An alternative approach for the seismic rehabilitation of existing RC buildings using seismic isolation. Earthquake Engineering & Structural Dynamics 45, 91–111. https://doi.org/10.1002/eqe.2618

Cardone, D., Flora, A., Gesualdi, G., 2013. Inelastic response of RC frame buildings with seismic isolation. Earthquake Engineering & Structural Dynamics 42, 871–889. https://doi.org/10.1002/eqe.2250

Decanini, L.D., Liberatore, L., Mollaioli, F., 2014. Strength and stiffness reduction factors for infilled frames with openings. Earthq. Eng. Eng. Vib. 13, 437–454. https://doi.org/10.1007/s11803-014-0254-9

Dobry, R., Idriss, I.M., Ng, E., 1978. Duration characteristics of horizontal components of strong-motion earthquake records. Bulletin of the Seismological Society of America 68, 1487–1520.

EN15129. 2009. Antiseismic Devices, European Committee for Standardization, Brussels, Belgium.

Forcellini, D., Kelly, J.M., 2014. THE INFLUENCE OF LARGE DEFORMATIONS OF ELASTOMERIC BEARINGS. Second European conference on earthquake engineering and seismology, Istanbul.

Grant, D.N., Fenves, G.L., Whittaker, A.S., 2004. BIDIRECTIONAL MODELLING OF HIGH-DAMPING RUBBER BEARINGS. Journal of Earthquake Engineering 8, 161–185. https://doi.org/10.1080/13632460409350524

Ibarra, L.F., Krawinkler, H., 2005. Global Collapse of Frame Structures under Seismic Excitations. Rep. No. TB 152, The John A. Blume Earthquake Engineering Center.

Ibarra, L.F., Medina, R.A., Krawinkler, H., 2005. Hysteretic models that incorporate strength and stiffness deterioration. Earthquake Engng Struct. Dyn. 34, 1489–1511. https://doi.org/10.1002/eqe.495

Iervolino, I., Spillatura, A., Bazzurro, P., 2018. Seismic Reliability of Code-Conforming Italian Buildings. Journal of Earthquake Engineering 22, 5–27. https://doi.org/10.1080/13632469.2018.1540372

Ishii, K., Kikuchi, M., 2019. Improved numerical analysis for ultimate behavior of elastomeric seismic isolation bearings. Earthquake Engng Struct Dyn 48, 65–77. https://doi.org/10.1002/eqe.3123

Kelly, J.M., 1997. Earthquake-resistant design with rubber. Springer London Ltd, .

Kelly, J.M., 1997. Earthquake-resistant design with rubber. Springer London Ltd.

Kelly, J.M., Marsico, M.R., 2013. Tension buckling in rubber bearings affected by cavitation. Engineering Structures 56, 656–663. https://doi.org/10.1016/j.engstruct.2013.05.051

Kikuchi M, Aiken ID, Kasalanati A. 2012. Simulation analysis for the ultimate behavior of full-scale lead-rubber seismic isolation bearings. In: Proceedings of the Fifteenth World Conference on Earthquake Engineering; Lisbon, Portugal:1688.

Kikuchi, M., Aiken, I.D., 1997. An Analytical Hysteresis Model for Elastomeric Seismic Isolation Bearings. Earthquake Engineering & Structural Dynamics 26, 215–231. https://doi.org/10.1002/(SICI)1096-9845(199702)26:2<215::AID-EQE640>3.0.CO;2-9

Kikuchi, M., Nakamura, T., Aiken, I.D., 2010. Three-dimensional analysis for square seismic isolation bearings under large shear deformations and high axial loads. Earthquake Engng. Struct. Dyn. 39, 1513–1531. https://doi.org/10.1002/eqe.1042

Koh CG, Kelly JM. 1988. A simple mechanical model for elastomeric bearings used in base isolation. International. Journal of Mechanical Sciences; 30:933–943.

Koh, C. G., and Kelly, J. M. (1986). ‘‘Effects of axial load on elastomeric bearings.’’ UCB/EERC-86/12, Earthquake Engrg. Res. Ctr., University of California, Berkeley, Calif.

Koh, C.G., Balendra, T., 1989. Seismic response of base isolated buildings including p-Δ effects of isolation bearings. Earthquake Engineering & Structural Dynamics 18, 461–473. https://doi.org/10.1002/eqe.4290180402

Kumar, M., Whittaker, A.S., Constantinou, M.C., 2014. An advanced numerical model of elastomeric seismic isolation bearings: AN ADVANCED NUMERICAL MODEL OF ELASTOMERIC SEISMIC ISOLATION BEARINGS. Earthquake Engineering & Structural Dynamics 43, 1955–1974. https://doi.org/10.1002/eqe.2431

Kumar, M., Whittaker, A.S., Constantinou, M.C., 2015. Experimental investigation of cavitation in elastomeric seismic isolation bearings. Engineering Structures 101, 290–305. https://doi.org/10.1016/j.engstruct.2015.07.014

Lin, T., Haselton, C.B., Baker, J.W., 2013. Conditional spectrum-based ground motion selection. Part I: Hazard consistency for risk-based assessments. Earthquake Engineering & Structural Dynamics 42, 1847–1865. https://doi.org/10.1002/eqe.2301

Liu, C., Yang, W., Yan, Z., Lu, Z., Luo, N., 2017. Base Pounding Model and Response Analysis of Base-Isolated Structures under Earthquake Excitation. Applied Sciences 7, 1238. https://doi.org/10.3390/app7121238

Luzi, L., Hailemikael, S., Bindi, D., Pacor, F., Mele, F., Sabetta, F., 2008. ITACA (ITalian ACcelerometric Archive): A Web Portal for the Dissemination of Italian Strong-motion Data. Seismological Research Letters 79, 716–722. https://doi.org/10.1785/gssrl.79.5.716

McKenna, F., 2011. OpenSees: A Framework for Earthquake Engineering Simulation. Computing in Science Engineering 13, 58–66. https://doi.org/10.1109/MCSE.2011.66

Mechanics of Rubber Bearings for Seismic and Vibration Isolation, 2011. John Wiley & Sons, Ltd, Chichester, UK. https://doi.org/10.1002/9781119971870.fmatter

Meletti, C., Galadini, F., Valensise, G., Stucchi, M., Basili, R., Barba, S., Vannucci, G., Boschi, E., 2008. A seismic source zone model for the seismic hazard assessment of the Italian territory. Tectonophysics 450, 85–108. https://doi.org/10.1016/j.tecto.2008.01.003

Monelli, D., Pagani, M., Weatherill, G., Silva, V., Crowley, H., 2012. The hazard component of OpenQuake: The calculation engine of the Global Earthquake Model. Proc. of 15WCEE – 15th World Conference on Earthquake Engineering, Lisbon, Portugal.

Mullins L. 1969. Softening of rubber by deformation, Rubber Chemistry and Technology, 42(1): 339-362.

Pant, D.R., Wijeyewickrema, A.C., 2014. Performance of base-isolated reinforced concrete buildings under bidirectional seismic excitation considering pounding with retaining walls including friction effects: BASE-ISOLATED BUILDINGS UNDER BIDIRECTIONAL EXCITATION WITH POUNDING. Earthquake Engng Struct. Dyn. 43, 1521–1541. https://doi.org/10.1002/eqe.2409

Quaglini, V., Dubini, P., Vazzana, G., 2015. Experimental Assessment of High Damping Rubber Under Combined Compression and Shear. J. Eng. Mater. Technol 138, 011002. https://doi.org/10.1115/1.4031427

Ragni, L. , Micozzi, F., Brandonisio, G., Dall'Asta, A., De Luca, A., Di Cesare, A., Mossucca, A., Nigro, D., & Ponzo F.C. 2019. Comportamento dei dispositivi HDRB sotto grandi spostamenti ed elevati carichi assiali, Proc. of 18th ANIDIS Conference, Ascoli Piceno, Italy

Ragni, L., Tubaldi, E., Dall'Asta, A., Ahmadi, H., Muhr, A., 2018. Biaxial shear behaviour of HDNR with Mullins effect and deformation-induced anisotropy. Engineering Structures 154, 78–92. https://doi.org/10.1016/j.engstruct.2017.10.060

ReLUIS-RINTC Workgroup, 2018. Results of the 2015-2017 RINTC project. ReLUIS-RINTC report, ReLUIS, Naples, Italy. Available at http://www.reluis.it.

Ricci, P., Manfredi, V., Noto, F., Terrenzi, M., Petrone, C., Celano, F., De Risi, M.T., Camata, G., Franchin, P., Magliulo, G., Masi, A., Mollaioli, F., Spacone, E., Verderame, G.M., 2018. Modeling and Seismic Response Analysis of Italian Code-Conforming Reinforced Concrete Buildings. Journal of Earthquake Engineering 22, 105–139. https://doi.org/10.1080/13632469.2018.1527733

Sassun, K., Sullivan, T.J., Morandi, P., Cardone, D., 2016. CHARACTERISING THE IN-PLANE SEISMIC PERFORMANCE OF INFILL MASONRY. Bulletin of the New Zealand Society for Earthquake Engineering 49(1), 100–117.

SisLab: Materials and Structures Test Laboratory of University of Basilicata (Italy). https://www.unibassislab.it/

Spillatura, A., 2018. From Record Selection to Risk Targeted Spectra for Risk based Assessment and Design. Ph.D. Thesis, Dipartimento di Costruzioni e Infrastrutture, Istituto Universitario degli Studi Superiori (IUSS), Pavia, Italy.

Stucchi, M., Meletti, C., Montaldo, V., Crowley, H., Calvi, G.M., Boschi, E., 2011. Seismic Hazard Assessment (2003–2009) for the Italian Building CodeSeismic Hazard Assessment (2003–2009) for the Italian Building Code. Bulletin of the Seismological Society of America 101, 1885–1911. https://doi.org/10.1785/0120100130

Takaoka, E., Takenaka, Y., Nimura, A., 2011. Shaking table test and analysis method on ultimate behavior of slender base-isolated structure supported by laminated rubber bearings. Earthquake Engng. Struct. Dyn. 40, 551–570. https://doi.org/10.1002/eqe.1048

Tubaldi, E., Ragni, L., Dall'Asta, A., Ahmadi, H., Muhr, A., 2017. Stress softening behaviour of HDNR bearings: modelling and influence on the seismic response of isolated structures: Stress Softening Behaviour of HDNR Bearings. Earthquake Engineering & Structural Dynamics. https://doi.org/10.1002/eqe.2897

Wada A, Hirose K. 1987. Building frames subjected to 2D earthquake motion. Proceedings, Structures Congress '89, ASCE, San Francisco, CA, 388–397.

Yamamoto, S., Kikuchi, M., Ueda, M., Aiken, I.D., 2009. A mechanical model for elastomeric seismic isolation bearings including the influence of axial load. Earthquake Engng Struct. Dyn. 38, 157–180. https://doi.org/10.1002/eqe.847

Yang, T.Y., Konstantinidis, D., Kelly, J.M., 2010. The Influence of Isolator Hysteresis on Equipment Performance in Seismic Isolated Buildings. Earthquake Spectra 26, 275–293. https://doi.org/10.1193/1.3276901

CHAPTER 4

4 Results

4.1 Introduction

This chapter describes the results of the probabilistic seismic risk assessment of seismically isolated structure equipped with *HDRBs*. First, the design procedure and the design results for the new isolated buildings and the retrofitted buildings are reported. Then, the results of *Multi-stripe dynamic analysis* (Jalayer 2003) are reported for each case study. More in detail, the results are first divided in two groups according the two different bearing models used (Kumar model and Kikuchi model). For each of them, the cases of new isolated buildings and existing buildings retrofitted with *HDRBs* and *HDRB+FSB* for the two sites (L'Aquila and Napoli) have been assessed. The comparison of the results for all the case studies analysed reveals the parameters of the seismic hazard and of the structural systems mostly affecting the reliability of isolated structures.

The following codes are used to denote the various characteristic of the case studies. With regards to the bearing model, the code *Ku* is used for the Kumar model and *Ki* for Kikuchi model; new isolated buildings and existing building retrofitted with base-isolation are identified by the letters *n* and *e* respectively. Existing building are further divided in two categories: one for pre-96 seismic code (existing seismic load building, with a base shear design force around 0.07 the weight of the building) and identified with *eS*, and one for building designed for gravity loads only (existing gravity load building) identified with *eG*. The sites of L'Aquila and Naples are identified with the letters *A* and *N* respectively, and the isolation system with the acronyms *HDRB* for all rubber bearings, *H+F* for hybrid system.

For example, *Ku-n-A HDRB* refers to the results of the new isolated building located in L'Aquila and equipped with *HDRBs* whose behaviour is described with the Kumar model. All the codes are summarized in Table 4.

Table 4. Case study identification codes

Model	Building	Site	System
Kumar *Ku*	New isolated building *n*	L'Aquila *A*	Rubber bearings only *HDRB*
Kikuchi *Ki*	Existing seismic load building *eS*	Naples *N*	Rubber bearings and flat sliders (hybrid system) *H+F*
	Existing gravity load building *eG*		

The seismic reliability has been assessed for two different performance levels, called *usability-preventing damage* (*UPD*) and *global collapse* (*GC*). It is noteworthy that the definition of the *GC* performance level is slightly different for the two bearing models used in the analysis, to take into account their different behaviour and features.

4.2 Design of the new isolated buildings case studies

According to the Italian seismic code *NTC* (CS.LL.PP., 2008, 2018), in line with the Eurocode philosophy, the seismic design of the base-isolated structure can be carried out using the *partial factor design* method (Calgaro and Gulvanessian, 2001, Fajfar, 2018). Among the eligible types of analysis (Equivalent linear analysis, Simplified linear analysis, Modal simplified linear analysis, Time-history analysis), the Modal simplified linear analysis has been used for the design of the new isolated buildings and the isolators of the retrofitted buildings.

The case study is a new building for residential use (ReLUIS-RINTC, 2018; Ricci et al., 2018). Figure 43 show a typical plan of the structure, while Figure 44 a vertical section.

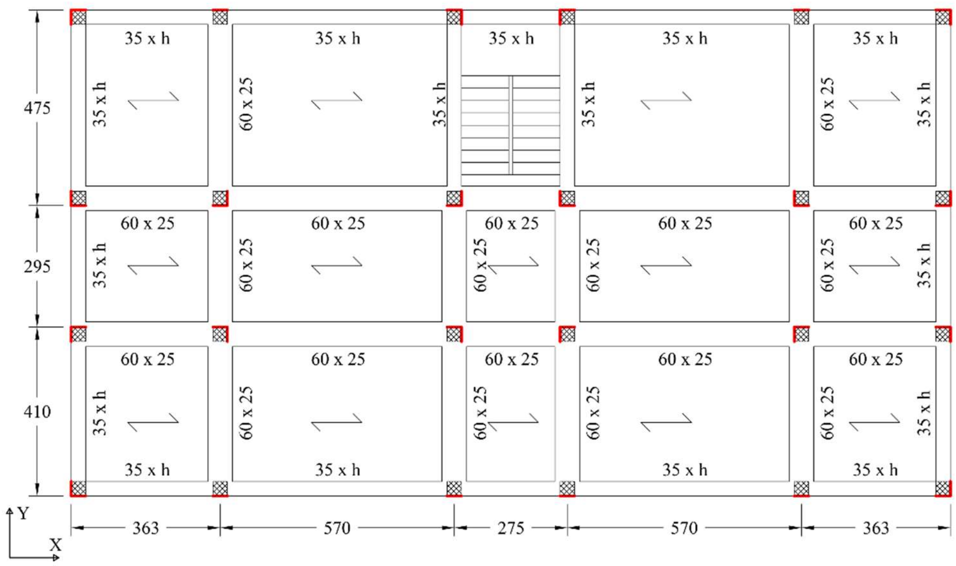

Figure 43. Floor plan

The RC frame superstructure is characterized by a regular plan of approximately 240 square meters with 6 storeys. The storey height is equal to 3.05m except for the ground level, which is 3.4m. The staircase is part of the building structure and has been designed using knee beams. All the storeys have the same slab with 25cm of total thickness (including hollow bricks).

Infill panels have been assumed to be regularly distributed in plan and elevation, with different percentages of openings. In particular, infills have been considered just as dead load in the design process, while they have been included as nonlinear elements in the model for time-history analyses. The elastic response spectra of the selected sites (i.e. L'Aquila and Naples) are reported in Figure 45 and refer to the soil type C.

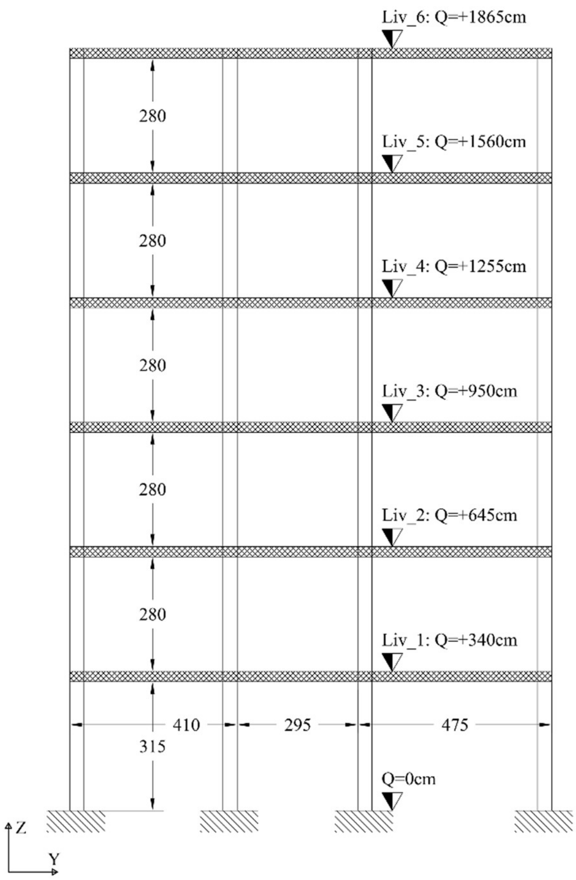

Figure 44. Vertical section

For each site and for each case study, structural elements of the superstructure (dimensions and reinforcements) have been verified, according to the indication given by the Italian design Code *NTC* (CS.LL.PP., 2008, 2018), as illustrated in the following sections. As mentioned before, different isolation systems have been considered in the *RINTC* project. For each isolation system, several case studies have been designed, differing in the geometric and mechanical properties of the isolation bearings. In all the cases, isolation devices have been designed by performing a response spectrum analysis at the *Collapse Limit State* (*CLS*), according to the design requirements and the compliance criteria of Chpt. 7.10.4.2 and C11.9 of the Italian design code (CS.LL.PP., 2008, 2018). However, it should be noted that indications given in the European standard on anti-seismic devices (EN15129, 2009) are similar, as shown in the following sub-sections.

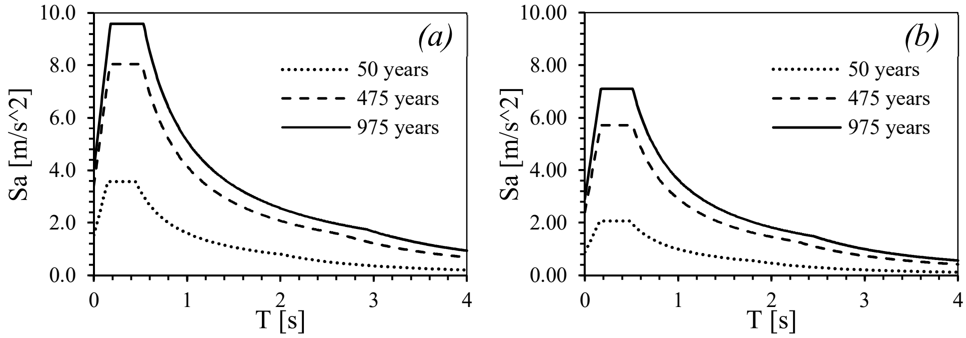

Figure 45. Horizontal elastic response spectra for different return periods for: (a) Naples and (b) L'Aquila.

4.2.1 Seismic isolation system design

Rubber-based isolation systems, including both those based on *HDRBs* only and those based on a combination of *HDRBs+FSBs*, have been designed by performing a response spectrum analysis at the *CLS* based on an equivalent linear model of the rubber (Cardone et al., 2010), without any iteration because rubber equivalent linear properties are constant in the range of shear deformations involved at the *CLS*. The safety verification of HDRB can be summarized as follows:

(a) Shear deformation (γ_s) of rubber layers, due to the seismic displacement (included global torsional effects for eccentricity of the structure):

$$\gamma_s \leq \gamma^* / 1.5 \leq 2 \tag{4-1}$$

where γ^* is maximum shear deformation evaluated in prototype tests, which assess the effectiveness of the rubber-steel adhesion and the strength of the rubber compound;

(b) Total deformation (γ_t):

$$\gamma_t = \gamma_c + \gamma_s + \gamma_\alpha \leq 5 \tag{4-2}$$

where γ_c is the shear deformation of rubber layers due to axial load and γ_α is the shear deformation of rubber layers due to rotation about any horizontal direction;

(c) Maximum tension: it must be lower than a stress of $2G$ (where G is the rubber shear modulus) or 1 MPa, whichever is lower, in order to avoid cavitation phenomena;

(d) Maximum compression force: it should be lower than $V_{max,c}/2$, where $V_{max,c}$ is buckling load evaluated according the following formula:

$$V_{\max,c} = \frac{G\,A_r\,S_1 D}{t_e} \tag{4-3}$$

where t_e is the total thickness of rubber, A_r is the overlapping area of the isolator, S_1 is the primary shape factor and D is the diameter of the bonded rubber area (steel plate diameter).

In this study, a soft rubber with a *shear modulus* (G) of 0.4 MPa and two common values of the *equivalent damping ratio* (ξ) equal to 15% and 10% have been considered. Both the parameters are considered almost constant over the design range of the shear deformation $1< \gamma_s < 2$. In particular, the case study buildings equipped with *HDRBs* have been designed by considering an isolation period of about 2.5s (which is the maximum period obtainable by using all HDRBs) and a damping ratio equal to 15%, in order to minimize the maximum displacements at the base of the structure. Figure 46*a* shows the device layout for the case study located in L'Aquila, where the HDRBs are identified by a three code numbers. Six bigger devices are placed underneath the columns characterized by higher axial load. The same configuration, but with different isolators dimensions, has been adopted for the isolated building located at Naples.

For comparison purpose, hybrid system (*H+F*) devices configuration is shown in Figure 46b (referring to case *n*-A *H+F 1*), where sliders are identified by three numbers, defining the vertical load capacity (V, expressed in kN) and the total displacement capacity in X and Y directions ($d_{tot,x}$ and $d_{tot,y}$ equal to 2 times the displacement capacity, d_{max}, expressed in mm). A number of sliders equal to one third of the total devices has been assumed (8 internal *FSBs* and 16 external *HDRBs*) for all the hybrid case studies. In this case, for the Aquila site, two solutions are designed both with isolation period close to 3s and damping ratio equal to 15%. For the Naples site, the first solution (case *n*-N *H+F* 1) is similar to L'Aquila case studies, whereas the second one (case *n*-N *H+F* 2) has been designed by assuming a lower period and a lower damping coefficient (equal to 10%).

The main geometric characteristics of the devices used for each case-study building and the results of the corresponding safety verification analyses are reported in Tables 1 and 2 for the *HDRB* and *H+F* isolation systems respectively. In these tables T_{is} is the isolation period of the base-isolated building, T_{is}/T_{fb} is the isolation ratio, that is the ratio between the period of the base-isolated building and the period of the same building in its fixed-base configuration. The displacement of *HDRBs* corresponding to the design strain γ_d = 200% is also indicated ($d_{max,HDRB}$), as well as the maximum shear strain (γ_{max}) obtained by the analyses at the *CLS* and accounting for rotational effects. In the same tables, *D/C* represents the *demand/capacity ratios*, expressed in terms of shear strain (*D/C shear*), vertical compression load (*D/C comp.*) and vertical tensile stress (*D/C tens.*).

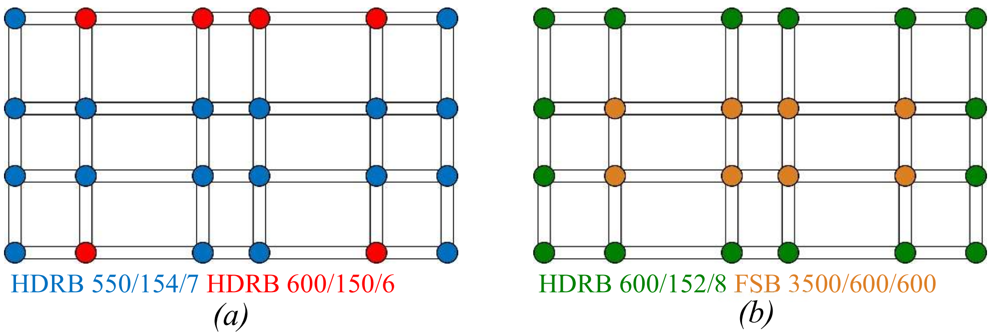

Figure 46. Isolation system layout: (a) Case A for HDRB and (b) Case 1-A for H+F. The three-code number represents Φ (diameter of the isolator, mm), t_e (total rubber layer thickness, mm), t_r (thickness of the single rubber layer, mm)

Case study	*HDRBs* $\Phi/t_e/t_r$ [mm]	ξ [%]	$d_{max,HDRB}$ [mm]	T_{is} [s]	γ_{max} [-]	*D/C Shear* [-]	*D/C compr.* [-]	*D/C tens.* [-]	T_{is}/T_{fb} [-]
n-A *HDRB*	550/154/7 600/150/6	15	300	2.46	1.71	0.86	0.97	0.33	3.46
n-N *HDRB*	500/126/6 550/126/7	15	250	2.52	1.48	0.74	0.84	0.00	2.64

Table 5. Geometrical characteristics and safety verification results for HDRB isolation system.

Case study	*HDRBs* $\Phi/t_e/t_r$ [mm] *FSBs* $V/d_{tot,x}/d_{tot,y}$ [kN/mm/mm]	ξ [%]	d_{max} [mm]	T_{is} [s]	γ_{max} [-]	*D/C Shear* [-]	*D/C compr* [-]	*D/C tens.* [-]	T_{is}/T_{fb} [-]
n-A *H+F 1*	600/152/8 3500/600/600	15	300 300	2.84	1.88	0.95	0.82	0.54	3.05
n-A *H+F 2*	600/176/8 3500/700/700	15	350 350	3.04	1.7	0.85	0.98	0.19	3.27
n-N *H+F* 1	500/102/6 3500/400/400	15	200 200	2.79	1.73	0.88	0.79	0.00	3

Table 6. Geometric characteristics and safety verification results for HDRB-FSB isolation system

It is interesting to observe that the proposed case studies provide a set of possible solutions characterized by different margins with respect to different collapse situations. In particular, for *HDRB* both the case studies of L'Aquila and Naples are characterized by a limiting value (close to unity) of the compression *D/C* ratio. For the hybrid isolation system, the first solution of L'Aquila (case *n*-A *H+F 1* in Table 6) is characterized by a higher value of the shear *D/C*, whereas the second one (case *n*-A *H+F 2* in Table 6) by a higher value of the compression *D/C*. For case studies of Naples, due to the geometry of bearings, the most critical *D/C* ratio is relevant to the shear. A second important remark is that elastomeric bearings have been designed according to indications about primary and secondary shape factors ($S_1 = \Phi'/4t_r$ and $S_2 = \Phi'/t_e$ where Φ' is the steel plate diameter), given by the relevant standard for building (BS ISO 22762-3, 2018). In particular, values of S_2 ranging from 3.5 to 5.8 and of S_1 from 17 to 25 are adopted, as can be evaluated from the geometric characteristics of bearings reported in Table 5 and Table 6. Significantly different indications are given for bridge structures (BS ISO 22762-2, 2018), as also shown and explained in (Tubaldi et al., 2016). Finally, it is highlighted that indications given in the European standard on anti-seismic devices (EN15129, 2009) are similar to those adopted in this paper. In particular, with reference to the design displacement, the Italian design code requires that the displacement demand shall be evaluated at the *CLS*, whereas the European standard on anti-seismic devices requires that a reliability factor (γ_x=1.2) shall be applied to the displacement demand evaluated at design seismic action according to Eurocode 8 (CEN, 2004), i.e. the Ultimate Limit State (*ULS*). The two suggested approaches are different but lead to a similar increased reliability, as also clarified by the updated version of the Italian seismic code (CS.LL.PP., 2008, 2018) in Chpt. 11.9. Some differences between the two design codes regard the maximum shear strain allowed (2.5 instead of 2) in Eqn. (4-1) and indications about the buckling load reported in Eqn. (5-2) and may affect the design of bearings.

4.2.2 Superstructure

According to the Italian design code (CS.LL.PP., 2008, 2018), the *Life Safety Limit State* (*LSLS*) has been considered for the structural design of the superstructure. All the new isolated buildings have been designed based on response spectrum analysis considering *low ductility class* (*CDB* for the Italian code (CS.LL.PP., 2008, 2018) for what concerns the structural details and by assuming a *behaviour factor* q = 1.5. It is worth to highlight that this ductility class allows to design without any global capacity design rule but prescribes that the local capacity design is carried out to avoid brittle failure or other undesirable failure mechanisms, i.e. shear failure of structural elements and failure of beam-column joints are avoided. This is different from the Eurocode 8's requirement (CEN 2004), where no global or local capacity design rules are prescribed for isolated structure.

The superstructure is classified as ordinary building with *usage class coefficient Cu* = 1. It is worth noting that *HDRBs* properties (G and ξ) at the *CLS* and *LSLS* are substantially the same (maximum strains for both limit state are within the interval $1< \gamma s< 2$).

The dimensions adopted for RC column/beam sections are reported in Table 7. Only for the case study with *HDRBs* located in L'Aquila (*n-A HDRB*) beam sections with larger dimension (35cm x 60cm for the lower storeys, 35cm x 50cm for the two middle storeys, 35cm x 40cm at the upper storeys) have been adopted, in order to increase the frame stiffness, thus avoiding high vertical tensile force on the corner bearings. More in detail, there are two types of mechanisms that could induce tensile force on isolation bearing: "*global rocking*" and "*local rocking*". In the former case (Takaoka et al 2011, Matsuda et al. 2015), considering the superstructure as a rigid body, tensile forces are generated in the bearings of the edge for horizontal forces that induce uplifting. In the latter case, instead, base moments of the columns are transferred by the base floor beams (which are usually stiffer) to the adjacent columns. Since this is a repetitive mechanism, the edges bearing, that are not surrounded in all the directions by other columns, are affected by an extra compression-tension force during the earthquake. This last mechanism is more important if the superstructure is flexible and the base beams are rigid, because the superstructure is not able to redistribute the seismic forces. For this reason, the stiffness of n-A *HDRB* is increased using larger columns.

For *HDRB* and *H+F* hybrid isolation system the superstructure reinforcements have been calculated according the relevant demand for each site. Table 8 summarizes some fundamental features of each superstructure model. In particular, $\Sigma A_{col}/A_{floor}$ is the ratio between the total column area at the ground floor and the total floor area; ρ_{b_deep} is the longitudinal deep beams' average steel ratio, ρ_{b_flat} is the longitudinal flat beams' average steel ratio and ρ_c is the base floor columns' average steel ratio. As it can be seen, the column area and the reinforcement ratio are almost the same for all the case studies.

Floor	*Column Dimension* [cm]	*Deep Beam Dimension* [cm]	Flat Beam Dimension [cm]
0	-	-	-
1	35x50	50x50 (staircase)	35x40
2	35x50	50x50 (staircase)	35x40
3	35x40	40x40 (staircase)	35x40
4	35x40	40x40 (staircase)	35x40
5	35x35	35x35 (staircase)	35x40
6	35x35	35x35 (staircase)	35x40

Table 7. RC beam/column sections geometry

Case study	$\sum A_{col}/A_{floor}$ [%]	ρ_{b_deep} [%]	ρ_{b_flat} [%]	ρ_c [%]
n-A HDRB	1.80	1.0	1.1	1.19
n-N HDRB	1.80	1.1	1.0	1.17
n-A H+F	1.81	1.1	1.0	0.9
n-N H+F	1.80	1.1	1.0	1.17

Table 8. Geometric and steel reinforcement ratios characteristics

4.3 Design of retrofit systems with rubber bearings

The case study is based on the one used in the previous chapters: a 6-storeys reinforced concrete structure, located in L'Aquila and Napoli. But while for the new isolated buildings the superstructures have been calculated according the Italian design code (CS.LL.PP., 2008, 2018), the case studies of existing buildings have been defined by means of the design codes in force in the past, according to the hypothetic most common period of construction. The superstructure of the building located in L'Aquila represents a 6-storeys building designed according to pre-96 seismic code (existing seismic load building, *eS*, with a base shear design force around 0.07 the weight of the building); coherently to practice of the period the seismic resisting frames are distributed in the two directions. The superstructure of the building located in Naples represents instead a 6-storeys existing building designed for gravity loads only (existing gravity load building, *eG*), with perimeter frames in the two directions and internal frames only in one direction. Details about the buildings in the fixed base configuration can be found in (Ricci et al. 2019).

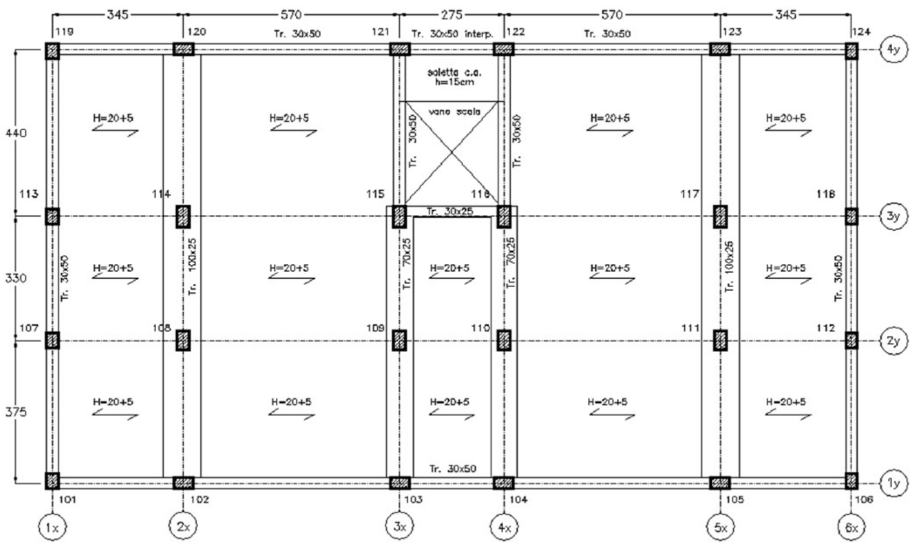

Figure 47. Floor plan of the eG building located in Napoli

Figure 47 shows the typical floor plan of the *eG* building located in Napoli, while the floor plan of the *eS* building is similar to the one of Figure 43. For both the case studies, as for the case study of new building, all floor plans are identical except for column and beam dimensions and reinforcements.

In the base-isolated configuration, a supplementary floor has been added at the bottom of the first storey columns and a grid of RC beams has been implemented at the same level. The devices are installed between the new RC grid and the foundation.
The design procedure of retrofitting with seismic isolation is the same as for new isolated building provided that superstructure strengthening is allowed. But a very interesting feature of retrofitting with seismic isolation is the possibility to work only at the base level of the building, thus keeping the superstructure as is. In this latter case the design procedure is quite different because the property of the superstructure (stiffness and resistance) are fixed.
The isolation system has been designed with the aim of protecting the buildings from any structural damage at the *Life Safety Limit State* (*LSLS*). For this purpose the elastic limit of the base shear (V_e) of the superstructure (in the fixed-base configuration) has been identified for the two existing building (*eS* and *eG*) in the pushover curves at the occurrence of the first yielding of the plastic hinges in the weaker direction (i.e. the minimum base shear at the first yielding), as reported in Figure 48.

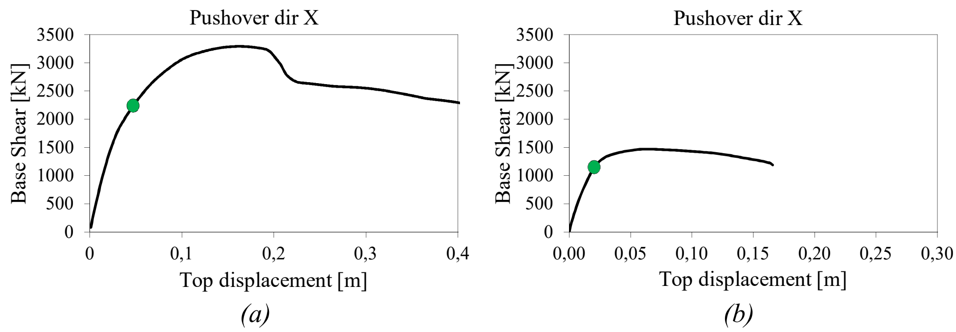

Figure 48. Elastic limit for (a) eS building at L'Aquila and (b) eG building at Napoli in the fixed base configuration

The seismic design of the isolation systems to achieve the retrofitting of the structures has been performed through modal response spectrum analysis, according to the Italian Seismic Code (CS.LL.PP., 2008, 2018), as for new isolated building.
Once the elastic limit of the superstructure has been identified, the isolation system has been designed by entering the design spectrum of the site for the *LSLS* using the spectral acceleration associated to the first plastic hinge ($S_a = V_e/M_{tot}$), where M_{tot} is the total mass of the superstructure. As a result, the

minimum value of the fundamental period of the base isolated system is obtained ($T_{is,min}$). In correspondence of that period the maximum displacement (S_{dmax}) has been evaluated using the displacement spectrum at *Collapse Limit State* (*CLS*). The latter value has opportunely increased using a specific coefficient to account for torsional effects. Finally, commercial devices have been selected from the manufacturers' catalogues.

For the case study buildings with *HDRBs*, by adopting a damping ratio of the isolation system equal to 15% and without considering any safety factor, minimum periods equal to $T_{is,min}$=2.3sec and $T_{is,min}$=2.9 sec have been obtained respectively for the *eS* building at L'Aquila and the *eG* building at Napoli. The associated spectral accelerations are equal to 0.13g and 0.057g for L'Aquila and Napoli (see Figure 49a and Figure 50a). Figure 49b and Figure 50b illustrate the displacement spectra at the *CLS*. The obtained maximum displacements opportunely increased using a coefficient equal to 1.2 to account for torsional effects are S_{dmax}=0.255 m for the *eS* building at L'Aquila and S_{dmax}=0.150 m for the *eG* building at Napoli.

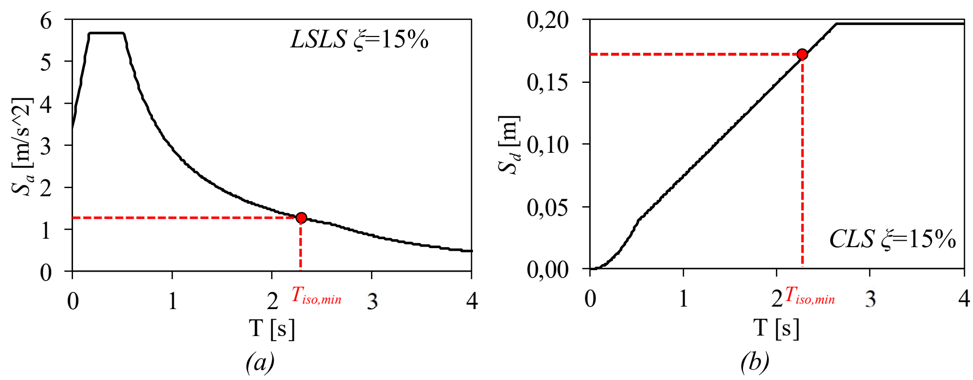

Figure 49. Design procedure for the eS building at L'Aquila

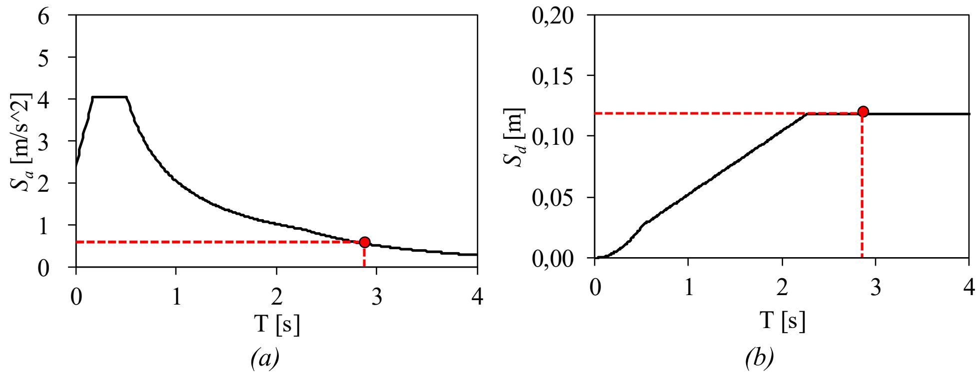

Figure 50. Design procedure for the eG building at Napoli

By adopting a configuration with all *HDRBs* it is not possible to reach the minimum isolation period for the *eG* building at Napoli, because there is a strong interdependency of vertical load capacity of the bearings, period of vibration and displacement capacity for this type of devices. More in detail, the lower is the shear capacity of the superstructure the higher is $T_{is,min}$, leading to very small isolators unable to support the vertical loads. As a consequence, only the *eS* building is considered for *HDRB*s case, for which an isolation period of 2.49 sec is adopted, which is slightly larger than the minimum one.

The isolation system has been designed according the same indications of the Italian code used in the previous section for the new isolated buildings.

Figure 51 shows the device configuration for the *eS-A HDRB* building, with bigger devices placed under the columns with larger axial loads. Table 9 reports the main design results as for Table 6.

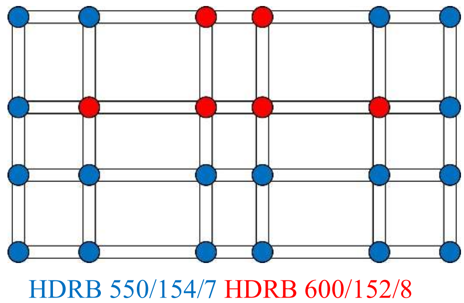

Figure 51. Isolation system configuration of es-A HDRBs. The three-code number represents Φ (diameter of the isolator, mm), t_e (total rubber layer thickness, mm), t_r (thickness of the single rubber layer, mm)

Table 9. Geometric characteristics and design outcomes for HDRB isolation system

Case study	*HDRBs* $\Phi/t_e/t_r$ [mm]	ξ [%]	$d_{max,HDRB}$ [mm]	T_{is} [s]	γ_{max} [-]	*D/C Shear* [-]	*D/C compr.* [-]	*D/C tens.* [-]	T_{is}/T_{fb} [-]
eS	550/154/7 600/152/8	15	300	2.49	1.62	0.81	0.99	0.79	3.46

For comparison purpose also the results for a case of hybrid isolation system (*HDRBs+FSBs*) with the same configuration of the new building (8 *FSBs* at the internal columns, see Figure 46b) are reported in Table 10. More details can be found in (Cardone et al. 2019).

Table 10. Geometric characteristics and design outcomes for H+F isolation system

Case study	*HDRBs* $\Phi/t_e/t_r$ [mm] *FSBs* $V/d_{tot,x}/d_{tot,y}$ [kN/mm/mm]	ξ [%]	d_{max} [mm]	T_{is} [s]	γ_{max} [-]	*D/C Shear* [-]	*D/C compr* [-]	*D/C tens.* [-]	T_{is}/T_{fb} [-]
eS	600/152/8 3500/600/600	15	300 300	2.68	1.63	0.82	0.93	0.14	3.65
eG	450/102/6 3500/400/400	15	200 200	3.30	1.75	0.89	0.98	0.00	4.40

4.4 Seismic response analysis and Failure Criteria

As mentioned before, *multi-stripe dynamic analysis* (Jalayer, 2003) has been used to assess the response of the structures, by performing 20 *TH* analyses for each of the 10 *IML*, leading to 200 three-dimensional time history analyses for each case study and a total of thousand analysis. For each case studies, two performance levels have been considered: the *usability-preventing damage* (*UPD*) and *global collapse* (*GC*). The definition of the performance criteria for the superstructure have been carried out in a simplified way identifying the displacement limits (in X and Y direction) directly on the curves resulting from *pushover analyses* (*POA*).

4.4.1 Global Collapse (*GC*) performance level

As mentioned before, from a reliability modelling perspective in base-isolated buildings, the superstructure and the isolation system can be considered as two components of an in-series system. The *GC* performance level must account for the failure of both components, since the collapse of either sub-system induces the collapse of the whole system.

It is worth to note that the *GC* performance level definition for the isolation system depends also on the type of model used in the analysis. In the case of Kumar model (Chpt. 3.2.2), the buckling of the bearing is controlled a posteriori by the of P/Pcr ratio between the current axial load and the variable critical buckling load. In the Kikuchi model, instead, the buckling behaviour is explicitly modelled via the full coupling of vertical and horizontal responses which simulates the *P-Δ* effects. In this case, the buckling leads to an increase of vertical and horizontal displacement up to the collapse of the bearing. Consequently, only limits in terms of displacements have been defined: a shear deformation limit of 350% and a vertical deformation (tension or compression) of 50%.

For the superstructure, a conventional collapse criterion has been adopted. In particular, for new buildings, the collapse occurs when, in one of the two main directions, the maximum top displacement (with respect to the isolation system), derived from the analyses is greater than (or equal to) the top displacement value taken on the descending branch, corresponding to a decrease of 50% of the maximum registered lateral strength from *Pushover analysis* (*POA*) carried out on the fixed-based superstructure, with a force distribution proportional to the storey masses. Details about this conventional choice can be found in (ReLUIS-RINTC Workgroup, 2018) and (Ricci et al. 2018). Figure 52 shows the limit top displacements derived from *POA* of the fixed-base superstructure of a case study. Similar results have been obtained for the other case studies, as reported in Table 11 (average drifts of the whole building can be obtained by recalling that the total height is 18.65m).

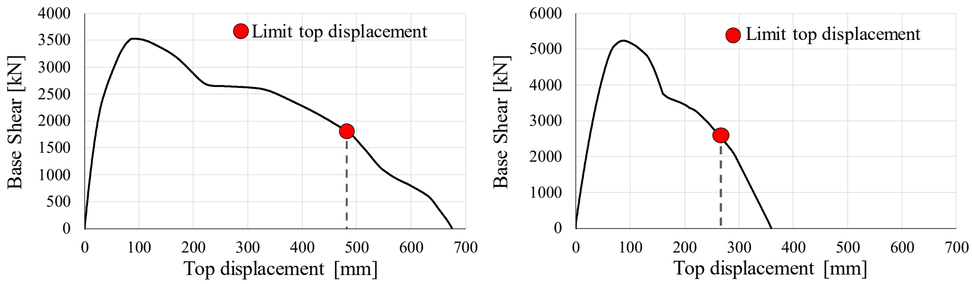

Figure 52. GC limits in X and Y dir. in terms of roof displacements of the superstructure, as derived from POA

	n-A HDRB	n-N HDRB	n-A H+F	n-N H+F
X	501	581	488	565
Y	271	342	267	324

Table 11. GC superstructure limit displacements [mm]

In the case of existing buildings, the superstructure *GC* threshold values are modified because of the possible anticipated shear failure of the hinges. In particular, the collapse of the superstructure is associated to the occurring of the first of the following conditions on the pushover curve: (*i*) a 50% decrease of the lateral strength (the same criteria used for new buildings); (*ii*) the attainment of the zero strength point in a shear-critical elements backbone (specific for existing retrofitted buildings). Therefore, collapse occur when, in one of the two main directions, the maxi-mum roof displacement derived from NTHA, is greater than (or equal to) the roof displacement corresponding to the first of the aforesaid limit conditions. Obviously, the fixed-base configuration was considered to perform the pushover analysis of the examined building. Two values of collapse are determined, one in the X and the other in the Y direction. Push over curves derived from mass proportional loads distribution are reported in Figure 53 and Figure 54.

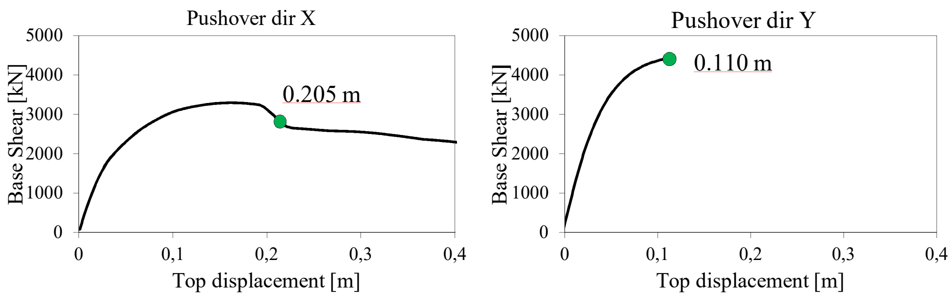

(a) *(b)*

Figure 53. Pushover curves (case eS) and displacement GC thresholds in the X (a) and Y (b) directions.

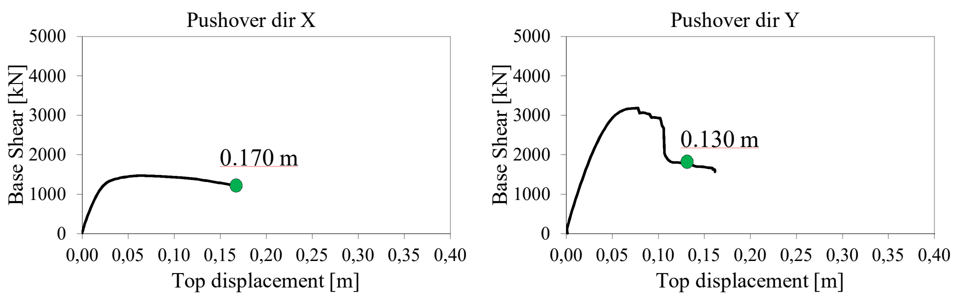

(a) *(b)*

Figure 54. Pushover curves (case eG) and displacement GC thresholds in the X (a) and Y (b) directions.

Table 12. GC superstructure limit displacements for existing buildings [mm]

	eS-A	*eG-N*
X	205	170
Y	110	130

4.4.2 Usability-Preventing Damage (*UPD*) performance level

The *usability-preventing damage* is a performance threshold that combines concepts related to easy and affordable-cost reparability of the building with concepts related to the protection of structural members from any damage under frequent earthquake, to preserve the functionality and avoid injury and also death of occupants due to collapse of non-structural components. In the *RINTC* project this performance threshold is focused on the damage of the infills panels and is defined as a multi-criteria approach. *UDP* is defined in a simplified way, because is considered attained when the first of these three conditions occurs in the *POA* of the superstructure in the fixed-base configuration:

(a) a widespread light damage in 50% of the main non-structural elements (e.g., infills and non-structural partition), corresponding to the attainment of the peak strength (in the relevant skeleton curve) for no more than 50% of masonry infills in each main direction;

(b) a severe damage at least at one of the non-structural elements (infills panels) leading to a significant interruption of use or a risk for human safety, corresponding to the attainment of a strength reduction of 50% (in the relevant skeleton curve) for the most damaged masonry infill;

(c) attainment of 95% of the maximum base-shear of the structure (limit of "elastic" behaviour, no need of structural repair), .

The top displacements for X and Y direction, which are related to the average inter-story drifts, are then used as threshold to assess if the *UPD* is attained or not in each time history analysis. Therefore, the *EDPs* for the *UDP* are only the maximum displacements of the superstructures with respect to the isolated base along the two principal directions.

The selected multi-criteria approach is also described in detail in the Appendix A of (ReLUIS-RINTC Workgroup, 2018) and in (Ricci et al. 2018).

Figure 55 shows the general definition of the *UPD* limit. It can be observed that the lower value of displacement corresponds to case b, related to a severe damage of an infill panel. Figure 56 shows values associated with the attainment of the *UPD* for the case study *n-A HDRB*. Similar values have been obtained for the other new case study buildings, as reported in Table 13.

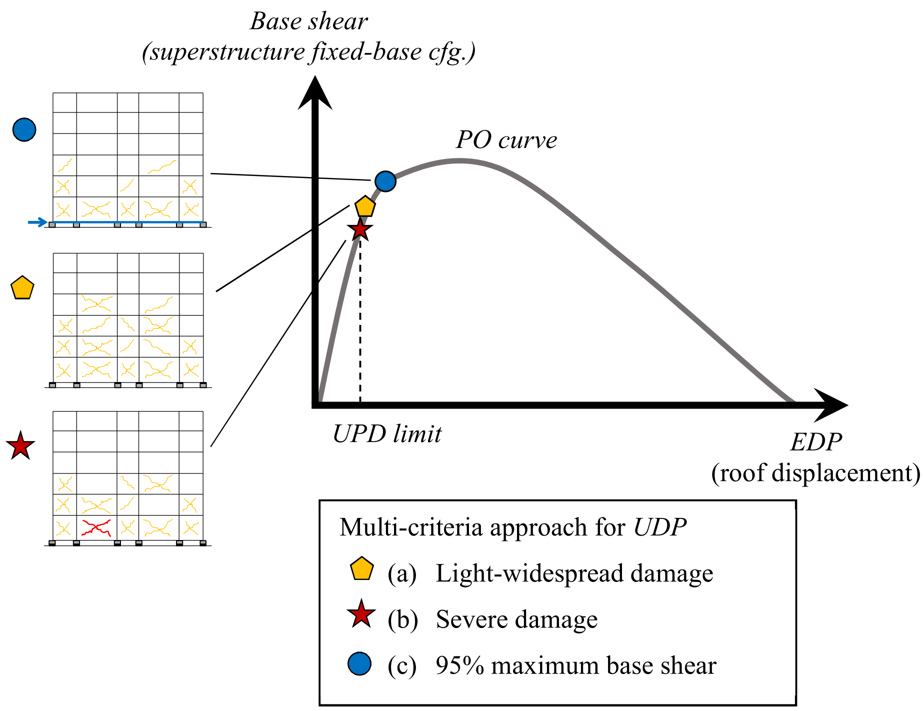

Figure 55. General definition for the usability-preventing damage failure criteria

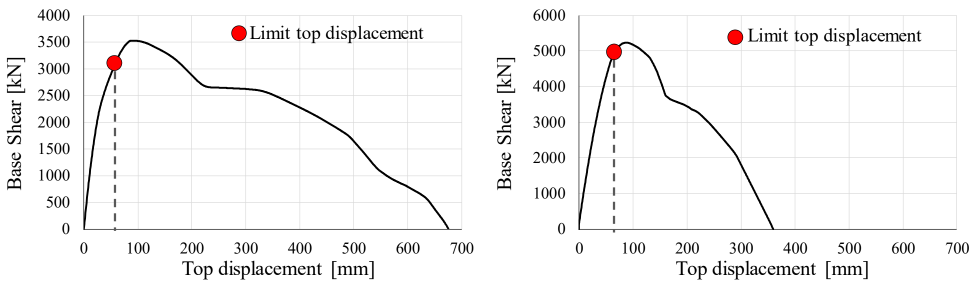

Figure 56. UPD limits in X and Y dir. In terms of roof displacements of the superstructure, as derived from POA

	n-A HDRB	*n-N HDRB*	*n-A H+F*	*n-N H+F*
X	59	60	59	42
Y	57	56	66	61

Table 13. UPD superstructure limit displacements [mm]

Regarding the *UPD*, no significant change in the procedure have been done for existing buildings compared to the new buildings, except for a further check of an anticipated brittle failure of the structural elements. The superstructure displacement limits defined using the *POA* results for the two existing building models are reported in Table 14.

Table 14. UPD superstructure limit displacements for existing buildings [mm]

	eS L'Aquila	*eG* Naples
X	51	37
Y	64	49

4.5 Results for Kumar modelling of rubber bearings

Analyses results about *GC* and *UPD* are summarized in this section, for all the case studies with the rubber bearings modelled using the *HDR element bearing* (Kumar model, "*Ku*"). To better understand the results, it is reminded that *IML2*, *IML5* and IML6 correspond more or less to the return periods of the *Damage Limit State* (*DLS), Life Safety Limit State (LSLS)* and *Collapse Limit State (CLS)* respectively according the Italian seismic code *NTC* (CS.LL.PP., 2008, 2018).

For the *GC* performance level, the total number of records determining a collapse condition for the base isolated building is reported as a function of the *IML*, for each case study building. Moreover, according to the *GC* multi-criteria defined in Chpt. 4.4.1 , the failure mode that occurs first is highlighted for each record by using different colours and is considered the one which leading the system collapse. In particular, for *HDRB* and *H+F* systems, different failure modes (associated to different response parameters) may take place in each time history for the isolation system besides the superstructure collapse. Thus, response parameters required for the identification of all the collapse conditions are monitored and the global collapse is classified based on the first collapse condition occurring.

It is recalled that the *GC* performance level definition slightly changes with the bearing model used. A summary of the multi-criteria limit states for the Kumar model used in this chapter is reported below.

ISOLATION SYSTEM	*FAILURE MODE*	*EDP threshold*	*DESCRIPTION*
HDRBs	Buckling	$P/P_{cr}=1$	50% of elastomeric devices reaches a value of axial compression force equal to the critical buckling load
	Tension	$\varepsilon_t \geq 0.50$	50% of elastomeric devices reaches an axial tensile strain (ε_t) greater than or equal to 50%
	Shear	$\gamma_r \geq 3.5$	50% of elastomeric devices reaches a shear strain (γ_r) greater than or equal to 3.5
FSBs	Over-stroke	$d_u = d_{max,FSB}+\Phi_p/2$	The horizontal displacement of the center of gravity of the isolation floor is equal to the collapse limit value

Finally, for the *UPD*, the top displacement of the superstructure (with respect to the isolation system) is the only *EDP* monitored, thus *demand-capacity ratios* (*D/C*) are calculated for each time history and for each case study building, where displacement capacity values associated to non-structural components damage are the *UPD* limits reported in Chpt. 4.4.2 . The total number of records determining the exceedance of the limit top displacement (*D/C* > 1) is also reported as a function of the *IML*.

4.5.1 *HDRB* Isolation System

Figure 57 presents the results in terms of the *GC* performance for the *Ku-n-A HDRB* (case study of new isolated buildings equipped with an isolation system composed by *HDRBs* only, located in L'Aquila, modelled with Kumar element). In particular, the case study is characterized by an isolation period T_{is} = 2.46s and by a very low margin with respect to the buckling load capacity of bearings (see Table 5) are illustrated in Figure 57. For this case, failures are mainly associated to buckling of bearings. Two failures occur at *IML6*, which is the intensity measure level corresponding the *CLS*, confirming the very low margin from buckling, which is approximately 2. A significant number of failures occur immediately above this *IML7* (1.53 times the *IML6*) mainly due to buckling of bearings, confirming the almost total wear out of the safety margin and the typical "*cliff edge effect*" characterizing isolated structures (Nishida et al. 2018). In few cases the first failure is due to the attainment of the superstructure limit top displacement, derived from the *POA* (reported in Table 11). This result can be explained by observing Figure 58 where time histories of the axial load acting on an external bearing (*P*) and the current buckling load (denoted by *Pcr* and depending on the current bearing shear displacement) are plotted. Results refer to one of the two records leading to buckling of bearings at *IML6*. The attainment of the buckling load is due to the simultaneous increase of the axial force caused by the overturning moment acting in the superstructure and the decrease of the buckling load associated to the bearing shear displacement. These two simultaneous effects are such that for actions slightly greater than the design one, the safety margin assumed in the design is quickly exceeded.

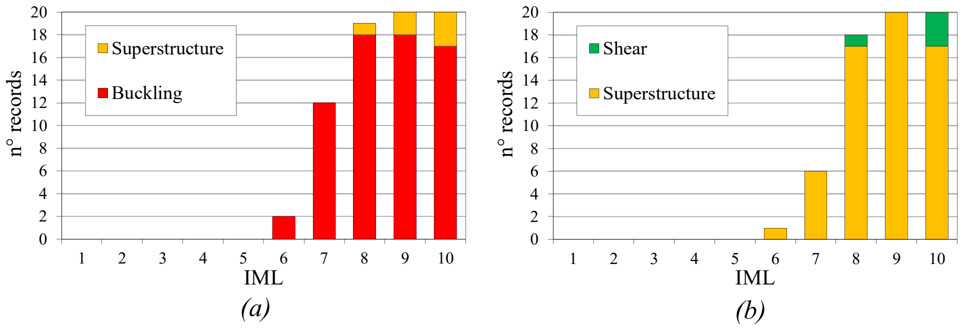

Figure 57. Summary of GC results of Ku-n-A HDRB for (a) normal GC criteria (b) GC criteria without buckling collapse condition

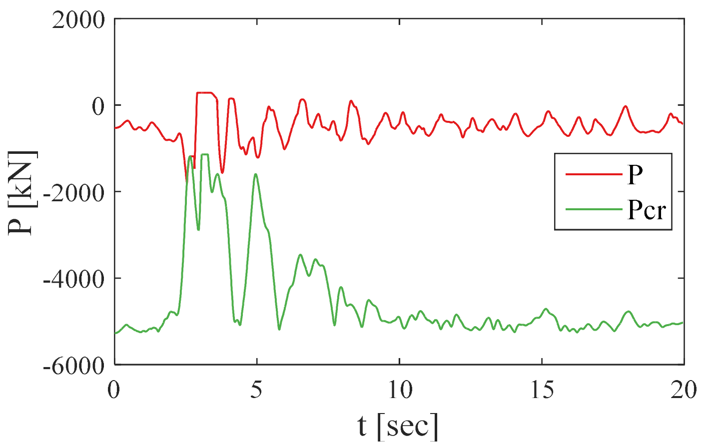

Figure 58. Time history of axial and buckling loads

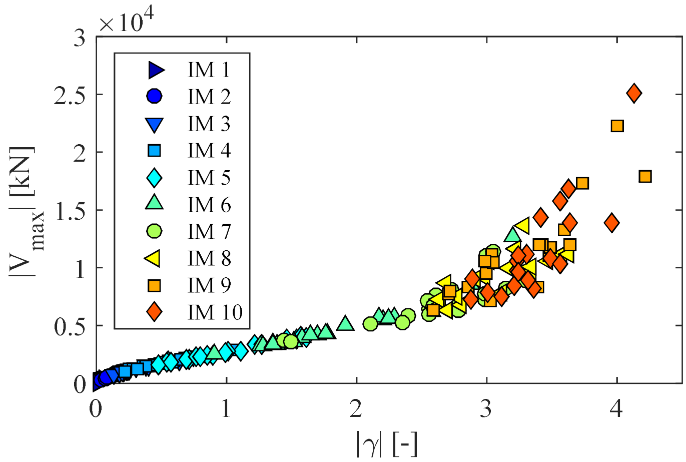

Figure 59. Maximum bearing shear deformation and corresponding shear force

As anticipated, several failure conditions may be attained in the same time history, but only the one occurring first is reported in Figure 57a. In order to better understand these results, Figure 57b refers to the same analyses of Figure 57a, but the buckling of bearings is ignored in the collapse multi-criteria assessment. It can be observed that the number of collapses decreases. For example, at *IM7*, 12 collapse occurrences due to buckling are reported in Figure 57a, whereas in Figure 57b the collapses are 6 and they are associated to the superstructure failure. This means that in six cases after the attainment of the conventional buckling condition of the isolation system also the superstructure collapse condition is attained, whereas in the other six cases this does not occur. At larger *IML* (from *IML8* to *IML10*) the failure rates are similar but in Figure 57b collapses are related to the superstructure, confirming that for higher intensities both the isolation and the superstructure collapse. These collapses are due to the rubber hardening behaviour at large displacements and the significant first cycle effect, as can be observed in Figure 59 where the maximum bearing shear deformation and the corresponding shear force of all bearings are illustrated for each time history. These effects reduce the isolation period and then increase accelerations transferred to the superstructure. Only in few cases, after the buckling of bearings, the second failure mode is associated to the exceeding of the bearings deformation limit of 350% (shear collapse), as can be seen in detail in Figure 57b. The safety margin of the isolation system respect to the shear collapse is bigger than the ones of buckling or superstructure collapse. In fact even if is nominally 2.04 (ratio between 350%, the collapse shear deformation, and 171%, the design shear deformation, see Table 5), the ratio between the design shear force and the shear force at shear collapse is almost the double because of the stiffening behaviour and the first cycle effect. In order to show this, the *D/C* ratios related to the shear failure of the isolation system (*D/C* shear) and to the superstructure collapse (maximum *D/C* ratio in X and Y directions of superstructure displacement) are reported in Figure 60 and Figure 61 respectively, by using a colour scale. For some records the figures shows that both the failures occur, whereas for other records only one type of collapse is involved. *D/C* ratios about tension are not reported because this kind of collapse condition is never attained.

The major approximation introduced in the performed analyses is that the Kumar model adopted for *HDRBs* does not account for the influence of the axial load on the shear stiffness of bearings, i.e. P-Δ effects are not simulated. Thus, the base shear transferred to the superstructure and reported in Figure 59 is overestimated for very large bearings shear deformation. It is recalled that the buckling condition depends on S_2 and the effects are significant only for displacement levels of the same order of magnitude of the diameter of the bearing (Montuori et al. 2016).

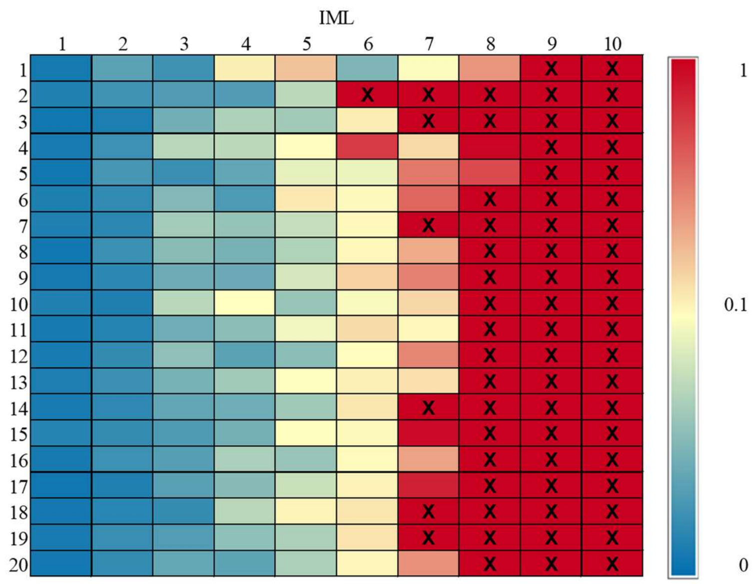

Figure 60. D/C ratio for shear deformation (X→D/C shear>1).

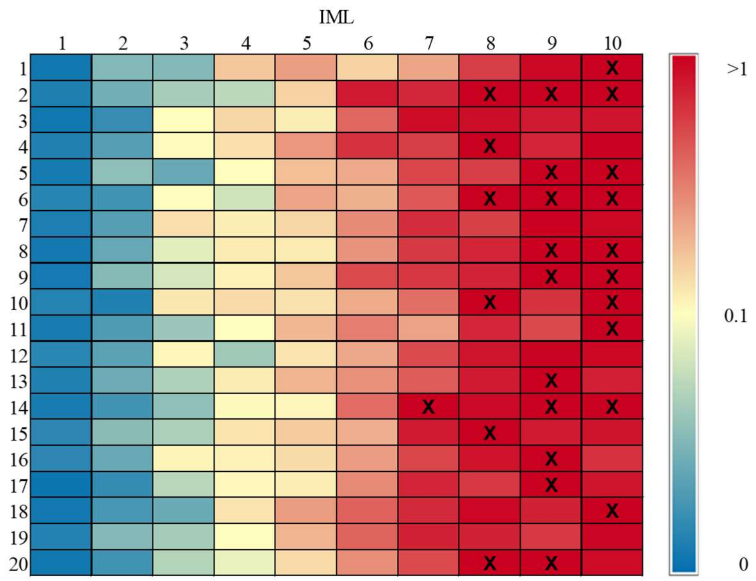

Figure 61 Maximum D/C ratio for the superstructure displacement in X and Y direction. (X→D/C shear>1)

Results of analyses carried out for the same case study building but considering pounding due to the presence of stiff retaining walls are reported in Figure 62a. Italian code (CS.LL.PP., 2008, 2018) required a minimum distance between adjacent structure equal to the value of the design displacement of the isolators at *CLS*. Consequently a gap amplitude equal to the design displacement is assumed for these analyses (300 mm), By assuming a concrete modulus equal to 32620 N/mm^2, a compression strength equal to 37.17 N/mm^2 and a slab effective thickness approximately equal to 0.20 m, the obtained model parameters (implemented in the OpenSees software according to Chpt. 3.3) are those summarized in Table 15.

Table 15. Parameters of gap models in X and Y directions

E_x [kN/mm]	E_y [kN/mm]	$F_{y,x}$ [kN]	$F_{y,y}$ [kN]
1553	6852	42561	89397

The comparison with Figure 57 highlights that the number of collapses is similar, but the type of the first collapse changes. In fact, for the building without stoppers, failure due to the buckling of the isolation system are mainly observed, while for the building with retaining walls superstructure collapses are more frequent, even if some buckling collapses are still attained. The reason is that once gap amplitude is covered by the isolation displacement, the acceleration resulting from the impact is immediately transferred to the superstructure. If the impact is weak, the accelerations transferred to the superstructure are moderate and do not produce the superstructure collapse. Differently, if the impact is strong shear forces induced by such accelerations are large and can cause its collapse. In Figure 62b records where impact (gap closure) occurs (in the X or Y direction) are reported and, among them, those producing the exceeding of the elastic limits (reported in Table 15) are highlighted. Looking for example at *IML6*, it is worth to note that six impact conditions occur but only in one case the impact force is so large to lead to superstructure failure, as shown in Figure 62a. Figure 63 shows displacement trajectories of the four building corners together with the gap amplitude, for the record causing the superstructure collapse at *IML*6. It is evident that the first impact occurs in the Y direction and causes a rotation of the building (corner trajectories do not coincide in Figure 63 after the first impact). The impact force in the Y direction is reported in ,Figure 64a whereas in Figure 64b the cyclic response of one bearing in either case with and without seismic stoppers are illustrated for the same record. Looking at larger *IMLs*, impacts occur for all the records, however in some cases they do not cause any failures, whereas in other cases they lead to either the superstructure collapse or to the bearings collapse for buckling. In fact, even if the impact with the retaining wall limits the shear deformation of bearings, it could cause an increasing of the axial load acting on the external bearings due to the raise of the overturning moment of the superstructure. However, it is worth to recall that by considering a flexible retaining wall, impact forces may be smaller, reducing the effect of pounding on collapse modes.

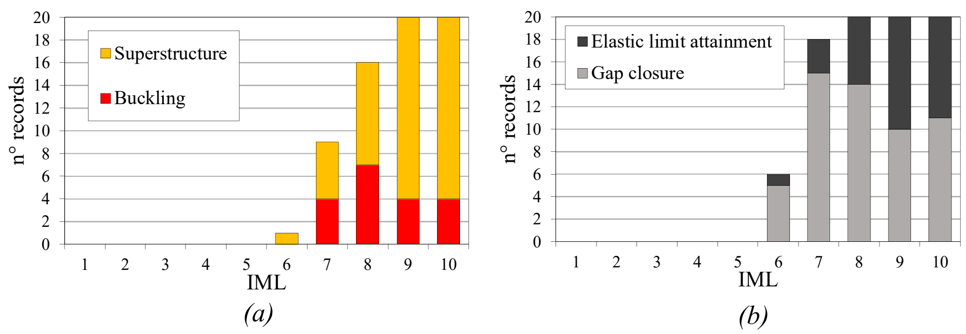

Figure 62. (a) Summary of global collapse results for case Ku-n-A HDRB with seismic stopper and (b) summary of gap closure and elastic limit attainment.

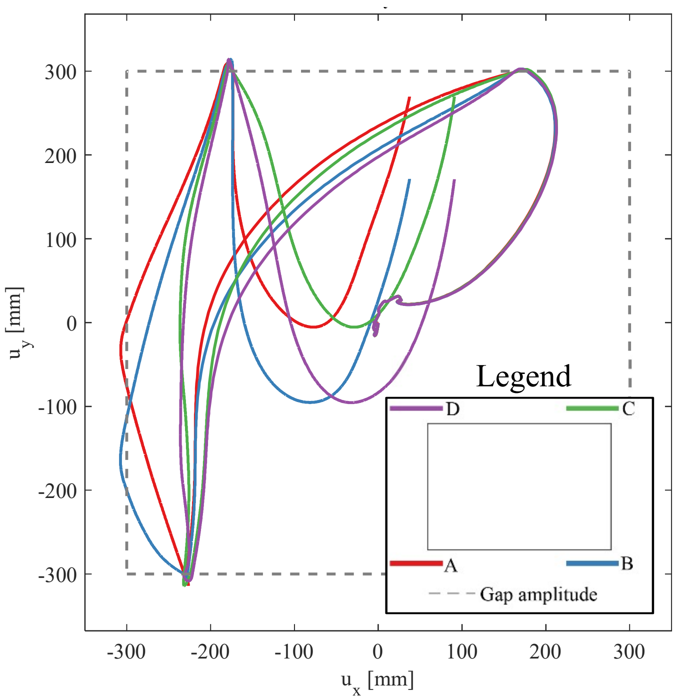

Figure 63. displacement trajectories of the slab corners

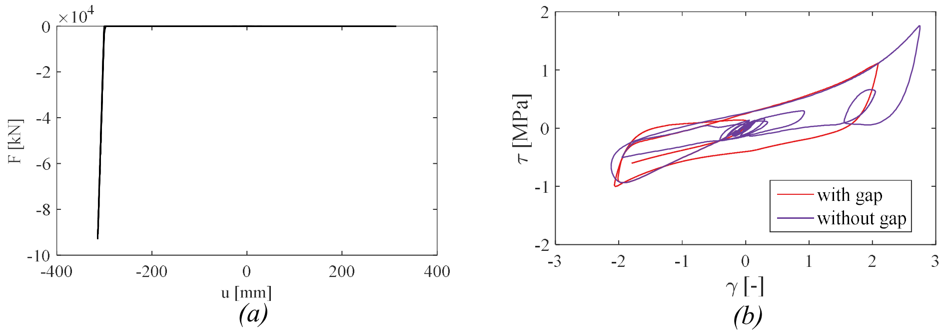

Figure 64. (a) impact force in the Y direction and (b) HDRB cyclic response with and without gap in y direction

Global collapse results of the case *n-N HDRB* (new building, Naples site) are illustrated in Figure 65. As for the one located at L'Aquila, this case study building is characterized by a low margin with respect to the buckling load capacity of bearings (see Table 5). In fact, also in this case the first failure occurrence is mainly associated to buckling of bearings, but failures appear only at *IML9* and *IML10*. The absence of failures at *IML6*, *IML 7* and *IML 8* can be partially explained by observing that the margin with respect to the buckling load is a little larger in the case *n-N HDRB* than in the case *n-A HDRB*, as reported in Table 5. But a more important reason of the deep different failure rates at higher *IMLs* is related to the strongly different seismic hazard characterizing the two sites, as can be observed in Figure 65b, or better the strongly different seismic hazard trends over the design condition. The two hazard curves, expressed in terms of spectral acceleration at $T = 3$s, are compared. Different trends are highlighted normalizing the spectral accelerations respect to the design value corresponding to *IML6* (return period of 1000 years, the design level for isolation systems). After this *IML*, values increase at a faster rate for the site of L'Aquila than for Naples. Therefore, safety margins are "relatively" higher in the case *n-N HDRB* than the case *n-A HDRB*, even if the absolute values are the same. This confirms that the results are strongly dependent to the site seismic hazard, or better, to the seismic hazard rate above the design condition.

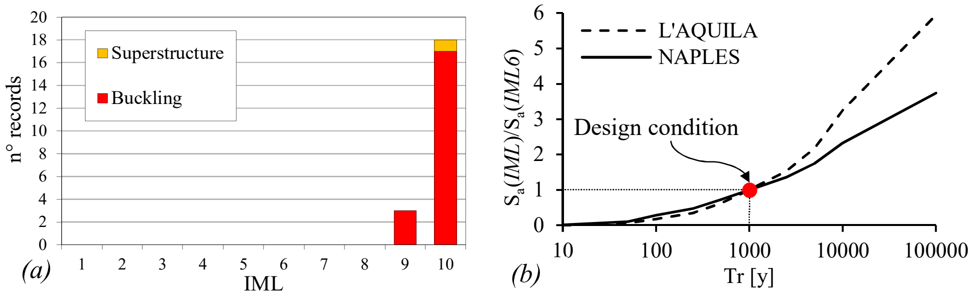

Figure 65. (a) Summary of global collapse results for Ku-n-N HDRB case and (b) normalized hazard curves of L'Aquila and Naples.

Finally, results about the *UPD* are summarized in Figure 66 in terms of *D/C* ratio of the superstructure top displacement. In particular, results refer to case *n-A HDRB* and *n-N HDRB* respectively and to the most critical direction (X direction). For an intensity measure level corresponding to a return period equal to 50 years (i.e. *IML2*), typically assumed as *DLS* according to seismic Italian design code (CS.LL.PP., 2008, 2018), no failures are recorded and *D/C* ratios much lower than 1 are observed. The first failures ($D/C \geq 1$) occur at seismic intensity *IML4* for the case study building located at L'Aquila and at *IML8* only for the case study building located at Naples. Here again differences are due to the different seismic hazard of the two considered sites (Figure 65b). However, in both the cases the obtained results point out that the isolation system works effectively in limiting the building damage of non-structural components for seismic intensities much higher than the design earthquake (*DLS* at *IML2*).

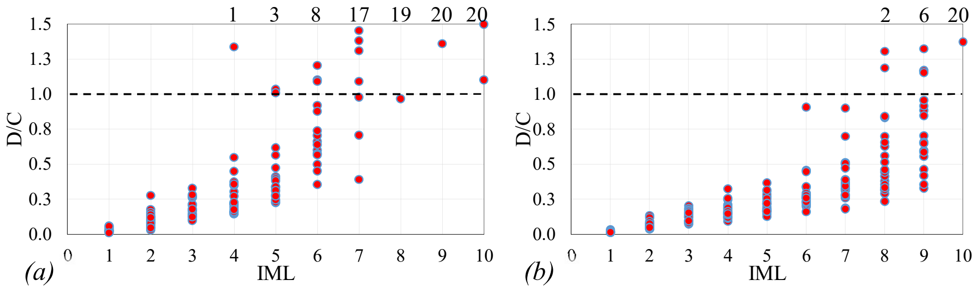

Figure 66. Displacement D/C ratio of the superstructure (UPD) in the X direction for: (a) case Ku-n-A HDRB and (b) case Ku-n-N HDRB.

For existing buildings, only a case study *eS* have been assessed because using only *HDRBs* it is not possible to achieve the minimum isolation period requested for the *eG* case. The attainments of the *GC* performance levels for the case *eS-A HDRB* are summarized in Figure 67.

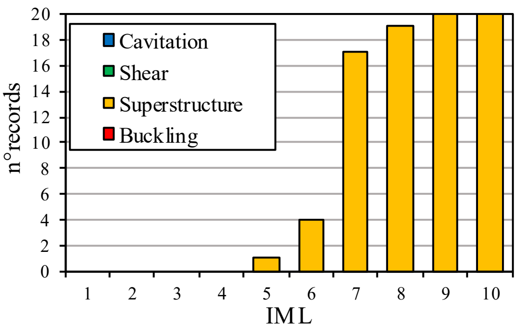

Figure 67. Summary of global collapse results for case Ku-eS-A HDRB.

It is reminded that the new building is equal to the retrofitted one in terms of global geometry (e.g. spans, floors) and it is isolated with a similar bearings configuration, but structural elements and reinforcements are significantly different. Comparing Table 11 with Table 12, lower values are observed for the displacement capacity of the superstructure for the existing case building (*eS-A*) with respect to the new building located at L'Aquila (*n-A*), even if the difference in terms of pushover curves is reduced (Figure 52 and Figure 53).

The obtained results show that for the retrofitted building, one failure occurs for an intensity measure level corresponding to the Life-safety Limit State (*IML*5 with return period equal to 500 years). Some failures occur at *IML*6 and a significant number of failure cases is record-ed from *IML*7. For all the *IML*s, the superstructure collapse is always the first failure mode recorded.

This suggests that the retrofitting design procedure, carried out without any safety factor about the elastic limit of the superstructure base shear, provides a safety margin for the *GC* of superstructure significantly lower compared to a new isolated building. In fact, by comparing the retrofitted building (Figure 67) with the new equivalent isolated building (Figure 57), the number of collapses for the new building is lower and the first collapse mode is buckling instead of superstructure collapse. The reason is that the superstructure design of a new isolated building according to the NTC (CS.LL.PP., 2008, 2018) leads to a superstructure with a better performance, especially in terms of ductility capacity but also in terms of shear strength, mainly because of the minimum requirements for concrete reinforcement and the local ductility ruled (avoiding local brittle failure). Thus, for new building case the low margin with respect to the buckling load capacity of *HDRBs* is the most critical aspect of the design procedure, whereas for the retrofitted existing building case the superstructure is the most vulnerable component if an adequate safety margin of the superstructure capacity is not assumed in the design procedure.

The results of the *UPD* are summarized in the following diagrams in terms of *D/C* ratios associated with each single record pair, in the two directions. As can be seen, for an earthquake intensity level corresponding to a return period equal to 50 years (*IML2*), corresponding to the design level for the verification of the damage limit state according to Italian seismic code, no failure cases are observed. Indeed, the *D/C* ratios are much lower than 1. The first failure cases ($D/C \geq 1$) are recorded for seismic events with return periods greater than 250 years (*IML4*). The obtained results also confirm that existing buildings retrofitted with seismic isolation works effectively in limiting damage to non-structural components for seismic intensities much higher than the design earthquake intensity level. Comparisons between retrofitted and new buildings show that the levels corresponding to damage onset are lower for existing building, mainly due to the higher deformability of the superstructure.

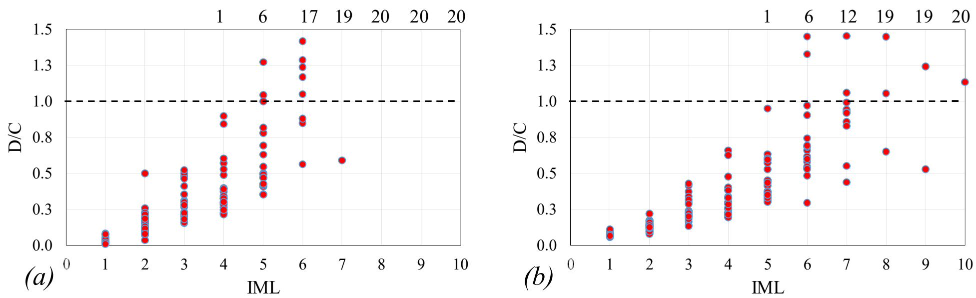

Figure 68. Displacement D/C ratio of the superstructure (UPD) for the case Ku-eS-A HDRB: (a) X direction and (b) Y direction

4.5.2 H+F Isolation System

For comparison purpose some results regarding hybrid systems (*H+F*) are reported hereafter. Figure 69a and b results refer to case *n-A H+F 1* and *n-A H+F 2*. In line with case study *n-A HDRB* previously showed, the obtained results show that, for the *IML* corresponding to the *CLS* (i.e. *IML6*) no failures are recorded for case *n-A H+F 1* whereas only one failure is recorded for case *n-A H+F 2*. In both cases several failures are recorded above *IML6* and they are ascribed mainly to the sliders in case *n-A H+F 1* and to bearing buckling in case *n-A H+F 2*. Here again, differences about the first collapse condition observed can be explained by consider design outcomes reported in Table 6. In fact, case *n-A H+F 1* is characterized by a low margin of *D/C* shear ratio and thus by large displacements close to the sliders displacement capacity, whereas case *n-A H+F 2* is characterized by a low margin of the *D/C* compression ratio, as a consequence of larger S_2 shape factor of the isolators. This leads to a prevalence of slider collapses in the first case and of buckling collapses of elastomeric bearings in the second one. However, it should be highlighted once again that, as explained for the *HDRB* system, only the first failure is reported in Figure 69 and that multiple instances of failure occur during the same time history.

In Figure 69c results of *n-A H+F 1* with retaining walls are reported. As the *HDRB* isolation system, a gap amplitude equal to the isolation displacement capacity (300 mm) is assumed. Another time the number of collapses is very similar for buildings with and without stoppers while the first collapse mode changes. In the case with pounding, collapses can be mainly ascribed to the superstructure, as an effect of the impact that causes a sudden increment of the forces in the superstructure. Like the full *HDRB* isolation system, some collapses due to buckling still occur due to the overturning moment and the consequent axial load increment on external bearings. The slider collapse is completely avoided as the gap dimension is smaller than the displacement capacity of the sliders. It is worth to note that the *FSB* plates are considered squared. This is important because the maximum displacement reachable in the case of retaining walls is the composed distance in X and Y direction (300*1.414 = 424mm). If the plate is circular, a possible slider collapse could be reached for a diagonal trajectory of the displacement. In Figure 69(d) results of a case study building located at Naples are illustrated. In particular, results refer to case *n-N H+F 1* and show that, in line with results obtained for *HDRBs*, the number of failures is significant only above *IML8*. For almost all the records the first collapse is due to overcoming of the sliders displacement limit.

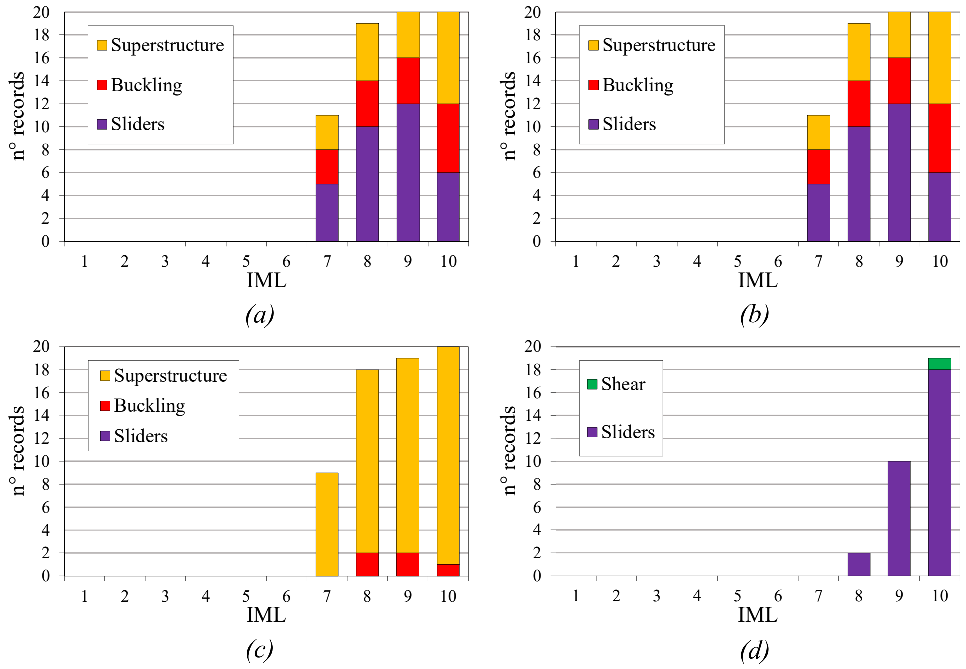

Figure 69. Summary of global collapse results for: (a) case Ku-n-A H+F 1, (b) case Ku-n-A H+F 2, (c) case Ku-n-A H+F 1 with seismic stoppers and (d) case Ku-n-N H+F 1.

Finally, results about *UPD* for the most critical direction (X direction) of case *n-A H+F 2* and case *n-A H+F 1* are summarized in Figure 70 and they are in good agreement with case study buildings equipped with *HDRBs*. They confirm that the isolation systems work effectively in limiting the building damage for seismic intensities much higher than the design earthquake corresponding to the DLS (*IML*2). The performance is even higher than the *HDRB* case, because of the higher isolation period and so the higher isolation capability of the system.

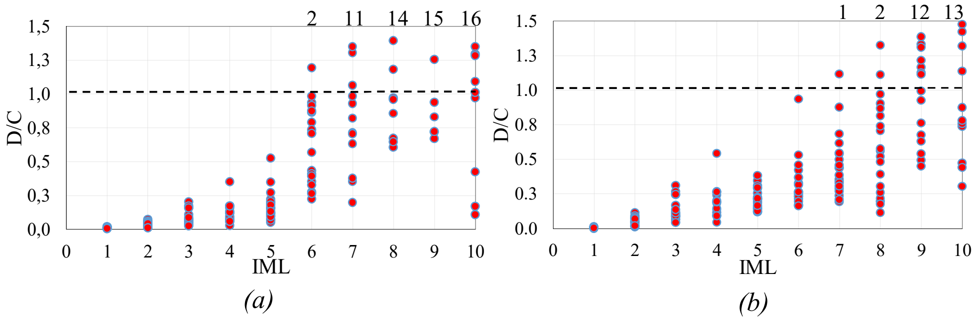

Figure 70. Displacement D/C ratio of the superstructure (UPD) in the X direction for (a) case Ku-n-A H+F 2 and (b) case Ku-n-N H+F 1

Regarding retrofitted structure with hybrid systems (*HDRBs+FSBs*), the results of the same two case studies *eS* and *eG* are reported hereafter (Cardone et al. 2019).

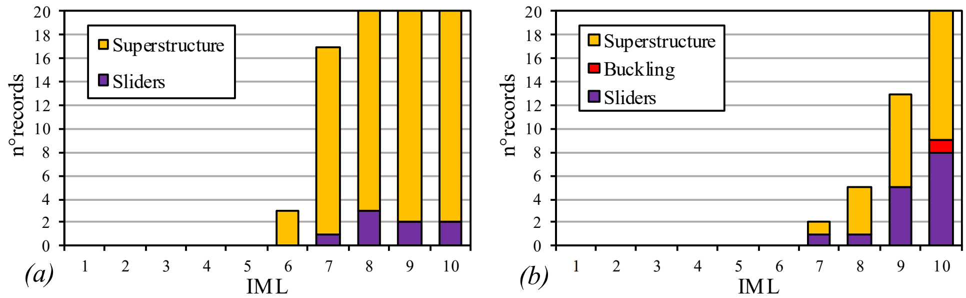

Figure 71. Summary of global collapse results for existing structures isolated with H+F: (a) case Ku-eS-A H+F (b) case Ku-eG-N H+F

For the case *eS-A H+F* (Figure 71a), the first collapse occur for an earthquake intensity level with return period equal to 1000 years (*IML*6), which corresponds to the earthquake intensity level assumed by NTC 2018 (CS.LL.PP., 2018) for the verification of the Collapse Limit State of the isolation system (for residential buildings). A significant number of failures is recorded from *IML*7. As expected, considering that the structure in the fixed based configuration was designed according to an older seismic code, the superstructure collapse is the prevalent failure mode. The comparison of the retrofitted building results to the equivalent new building (Figure 71 and Figure 69) shows that the number of collapses is almost the same but the dominant collapse mode changes from the isolation system to the superstructure.

Figure 71b shows the results relevant to attainment of collapse conditions for the *eG-N H+F* case study building retrofitted by hybrid system and located at Naples. No collapses are recorded up to an earthquake intensity level with a return period equal to 1000 years (*IML*6). Some collapse cases are recorded from *IML*7 increasing only for higher intensity level. The comparison of these results with the equivalent new isolated building (Figure 69d) highlights that the number of collapses increase for the retrofitted building and, in line with the results for the *eS* case, the collapse of the superstructure is more frequent for the retrofitted building respect to the new building. Regarding the *UPD*, similar findings to the ones made for the *HDRB* existing building case can be made.

4.5.3 Effects of model uncertainties

This chapter briefly describes the multivariate statistical model of the structure-related modelling uncertainty used to assess the effect on the seismic response of the variability of material properties as well as the uncertainty associated with the parameters of the adopted building and isolators models. In particular, a subset of cases has been assessed taking into account the model uncertainties to compare the results with the equivalent deterministic "median" models. The general framework for uncertainty evaluation can be found in (Franchin et. al., 2018).

Uncertainties are often classified as either aleatory or epistemic. The former is related to randomness of the physical quantities while the latter has to do with the knowledge on which models are based. Therefore, according to (Franchin et. al., 2018), uncertainty on models can refers:

- model form, that is, uncertainty in the choice of a model among different candidate models, called Type I in the following;
- model parameters, that is, uncertainty in the parameters of the chosen model, called Type II in the following.

While is typical for *PSHA* dealing with both the types of uncertainties, in the structural engineering domain consideration of modelling uncertainty is mostly limited to Type II. In this chapter, variables describing Type II uncertainty can be arranged in a hierarchical model together with aleatory uncertainty (consideration on the Type I uncertainties are made afterwards using the Kikuchi model for the isolation bearings instead of the Kumar mode). In this case the risk analysis yields a single result, incorporating the effect of both aleatoric and epistemic uncertainty. The minimum one-to-one association to the ground motion records describing seismic input uncertainty at each intensity level have been used (as many realizations of the structure-related uncertainties as records). The difference in the case of uncertainties assessment showed hereafter respect to the standard analysis previously exposed is in the use of 20 structural varied models with the parameters generated using the multivariate statistical model.

The reader can refer to Franchin et al. [2018] for a general, cross-typological, discussion of the correlation structures, including the characterization of random variables and of their correlation structures, the efficient sampling procedure, as well as the specific aspects related to RC structures.

The multivariate statistical model of the structure-related uncertainty has been developed with reference to reinforced concrete buildings, describing the variability of material properties as well as model error terms of the adopted response model for both RC member and masonry infills. The readers can refer to papers about the nonlinear modelling of reinforced concrete buildings (Ricci et. al., 2018) and the uncertainties modelling (Franchin et al., 2017, Franchin et al., 2018, ReLUIS-RINTC, 2018-Appendix C) to find all the details. Capacity curves of the 20 models with varied parameters (varied models) obtained by *POA* are shown in Figure 72 for both the X and Y directions together with the relevant curves (red lines) of the reference case without modelling uncertainties. Mean values ($\bar{d}_{lim}$) and standard deviation (σ) of superstructure limit displacements for the *GC* and the *UPD* are summarized in Table 16 and Table 17.

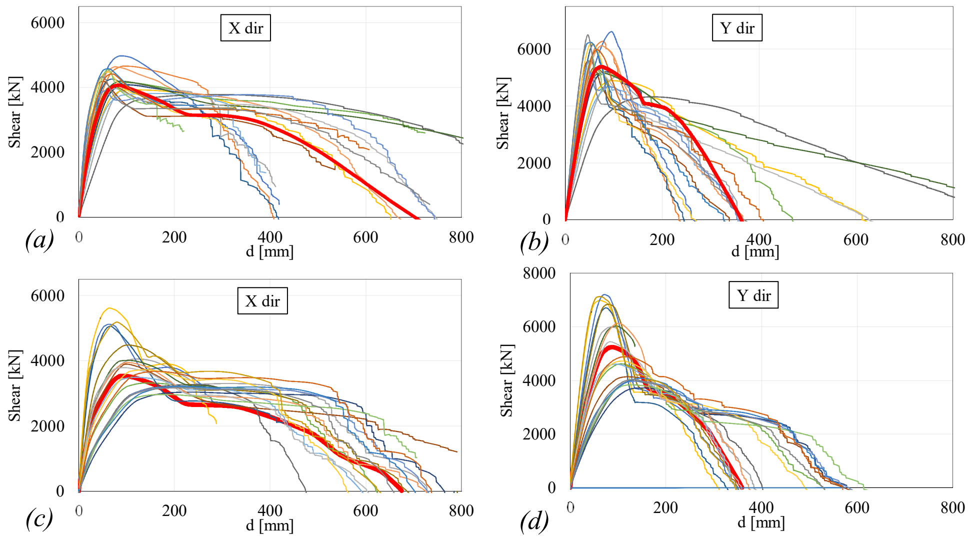

Figure 72. POA curves of varied models for: (a)(b) n-A HDRB, (c)(d) n-A H+F 2

	n-A HDRB		*n-A H+F 2*	
	$\bar{d}_{lim}$	σ	$\bar{d}_{lim}$	σ
X	465	208	488	117
Y	246	119	318	126

Table 16. Mean values and standard deviations of superstructure GC disp. Of varied models (mm).

	n-A HDRB		*n-A H+F 2*	
	$\bar{d}_{lim}$	σ	$\bar{d}_{lim}$	σ
X	53	19	55	11
Y	54	13	73	17

Table 17. Mean values and standard deviations of superstructure UPD disp. Of varied models (mm).

It is worth to note that variability of superstructure displacement limit for both *GC* and *UPD* are very high. This is related to the changing of the *POA* curves in terms of maximum shear forces and ductility. For example, lower maximum shear strength and higher ductility are typical of weaker infill panels compared to the deterministic "median" model, because of a better distribution of the plastic deformations. This obviously leads to an increase of the *GC* displacement capacity directly associated to the higher ductility but also because, hidden in the definition of the *GC* (decrease of 50% of the lateral strength *POA*), a lower maximum base shear increase move to the right the conventional *GC* point only because the starting point is lower. This is somehow a weakness of the *GC* definition because, for example, for two identical frames which are strong enough to develop all the plastic hinge regardless the strength of the infills, the case with stronger infills will show a lower capacity in terms of displacement.

For base-isolated structures, both structure-related and isolation-related uncertainties have been modelled. Thus, in addition to 20 superstructure models, in this case also 20 batches of isolators with varied properties have been generated, according the multivariate sampling process (Franchin et al., 2018). Then, a random one to one association has been done between varied superstructure models and isolation systems with varied properties. Finally, analyses have been performed by associating one of the 20 ground motion records of each *IML* to one of the 20 model with varied properties.

A statistical model has been developed to evaluate isolator-related uncertainties due to the factory production variability, based on a set of available experimental tests carried out on several production batches of *HDRBs* (ReLUIS-Line 6 Workgroup, 2018). Other sources of variability (temperature, aging) have not been considered in this work, even if they could be treated in the same way. In particular, three random variables are considered: the shear modulus G and damping ratio ξ for *HDRBs*. Since seismic isolation devices coming from the same production batch exhibit correlation, the *ANOVA model II* (Kutner et al., 2005), in which the population is divided into classes and each class has random means but the same variance, is adopted to describe isolator-related uncertainties. In the case of isolation bearings, classes are represented by production batches and the computed means and variances of the isolators batches tested have been used to estimate the variability inside each batch (class), that is *within-class variability*, as well as the variability between mean values of each batch, that is *between-class variability*. Reference to (ReLUIS-RINTC 2018), (Franchin et al. 2018) and (Micozzi et. al., 2018) can be made for details.

According to *ANOVA model II* (or *random ANOVA model*, where the acronym *ANOVA* refers to *ANalysis Of Variance*) the j^{th} value from the i class y_{ij} can be expressed as follow

$$y_{ij} = \mu_{..} + \tau_{i.} + \varepsilon_{ij} \tag{4-4}$$

where $\mu_{..}$ is the overall mean (or *grand mean*), $\tau_{i.}$ is the deviation of the class mean $\mu_{i.}$ from the *grand mean* and ε_{ij} is the deviation of the j^{th} value from the class mean $\mu_{i.}$. The random variable $\tau_{i.}$ has a normal distribution with zero mean and variance σ_B^2 (*between-class variance*) while the random variable ε_{ij} has a normal distribution with zero mean and variance σ_W^2 (*within-class variance*). The three parameters $\mu_{..}$, σ_B^2 and σ_W^2 fully define the statistical model. Figure 73 shows a graphic representation of the *ANOVA model II*

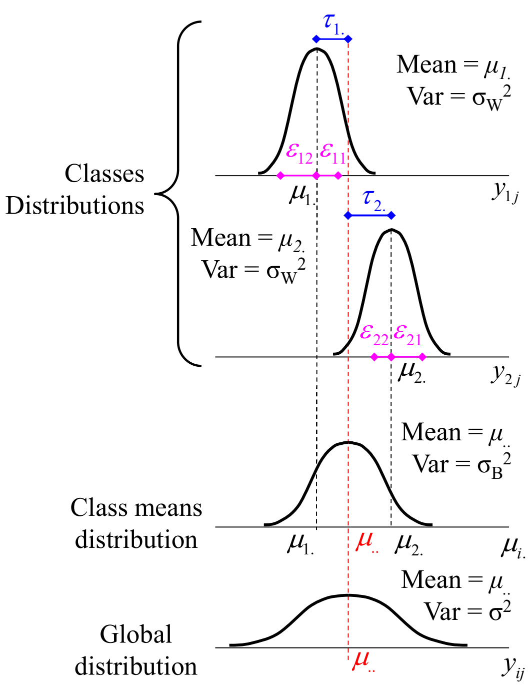

Figure 73. Representation of ANOVA model II

Hereafter the procedure to estimate the parameters of the statistical model from data is shown, starting from the mean and the variance of each batch tested. The grand mean $\mu_{..}$ of the samples is calculated as weighted mean of the batch means:

$$\mu_{..} = \bar{y}_{..} = \sum_{i=1}^{k} \frac{n_i}{n} \bar{y}_{i.} \tag{4-5}$$

where $\bar{y}_{..}$ is the mean of the i^{th} batch, n_i is the number of tested isolators belonging to the batch i, n is the total number of the tested seismic isolators and k is the number of batches. Table 18 summarizes the step to estimate the *within-class* variance (σ_W^2) and *between-class variance* (σ_B^2), where s_i^2 is the variance of the i batch and n' takes into account an unequal number of isolators inside each batch (*unbalanced ANOVA*) and is estimated as follows:

$$n' = \frac{1}{n-1}\left[\sum_{i=1}^{k} n_i - \sum_{i=1}^{k} n_i^2 \Big/ \sum_{i=1}^{k} n_i\right] \tag{4-6}$$

	between-class	*within-class*
Sum of Squares	$SS_B = \sum_{i=1}^{k} n_i \left(\bar{y}_{i.} - \bar{y}_{..}\right)^2$	$SS_W = \sum_{i=1}^{k}\sum_{j=1}^{n_i} n_i \left(y_{ij} - \bar{y}_{i.}\right)^2 = \sum_{i=1}^{k}\left(n_i - 1\right) s_i^2$
Degrees of freedom	$k-1$	$\sum_{i=1}^{k}\left(n_i - 1\right)$
Mean Squares (MS)	$MS_B = \frac{SS_B}{k-1}$	$MS_W = \frac{SS_W}{\sum_{i=1}^{k}\left(n_i - 1\right)}$
Estimator E(MS)	$\sigma_W^2 + n'\sigma_B^2$	σ_W^2

Table 18. ANOVA model II

The overall variance is the sum of the within-class variance and the between-class variance

$$\sigma^2 = \sigma_W^2 + \sigma_B^2 \tag{4-7}$$

Finally, the *intra-class correlation* is computed: it is a simple way to understand relative weight of the between-class variability and the within-class variability. It is defined as the ratio of the between-class variance and the overall variance and can be estimated as follows:

$$IC = \frac{\sigma_B^2}{\sigma^2} = \frac{MS_B - MS_W}{MS_B + (n'-1)MS_W} \tag{4-8}$$

High *IC* indicates a relatively high between-class variability compared to the within-class one.

The *coefficient of variation* (*CV*) is calculated as

$$CV = \frac{\sigma}{\mu} \tag{4-9}$$

The data from 113 *HDRBs* belonging to 30 different batches have been adopted to calibrate the statistical model described above. All the devices of the sample have a design property values $G = 0.4$ MPa and $\xi = 15\%$ for *HDRB*s both measured at the 3rd cycle and at the design shear deformation $\gamma = 1.5$.

First, the correlation between the shear modulus and the damping coefficient is calculated based on mean values of each batch. The low value obtained (-0.24) justifies the assumption of independent random variables, as clearly recognize in Figure 74. Note that the data points represent batch mean values.

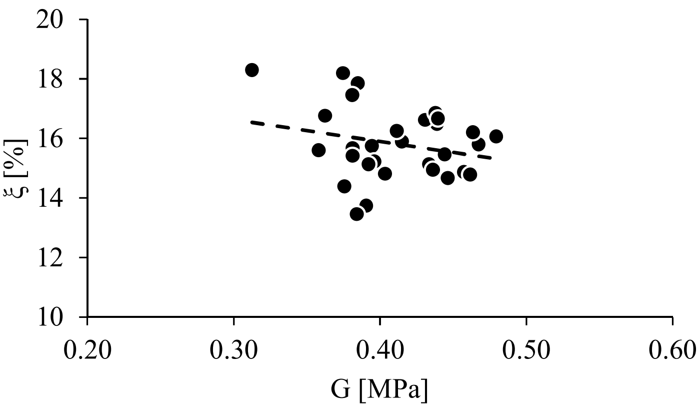

Figure 74. Correlation between G and ξ.

The parameters of the statistical models obtained according Table 18 are summarized in Table 19 for the two varied parameters. In particular, the overall mean, the relevant coefficient of variation (*CV*), the overall standard deviation (σ), the within-class and between-class standard variations (σ_W and σ_B) and the correlation index are reported. The obtained results show that overall mean values $\mu_G = 0.41$ MPa and $\mu_\xi = 15.6\%$ are very close to the nominal ones, moreover the within-class variability is significantly lower than the between-class variability. Consequently, high correlation coefficients are obtained.

	$\bar{y}$ [MPa]	CV [%]	σ [MPa]	σ_B [MPa]	σ_W [MPa]	IC
G	0.417	9.43%	0.0394	0.0362	0.0155	0.845
ξ	0.157	7.36%	0.0115	0.0105	0.0047	0.831

Table 19. ANOVA model II values for G and ξ

Figure 75 shows the experimental distributions of the batches tested and the calculated general distribution for *G* and *ξ*. According to these distributions, a procedure that randomly generates *G* and *ξ* values of bearings belonging to several batches having different sizes (number of isolators for each batch) has been developed.

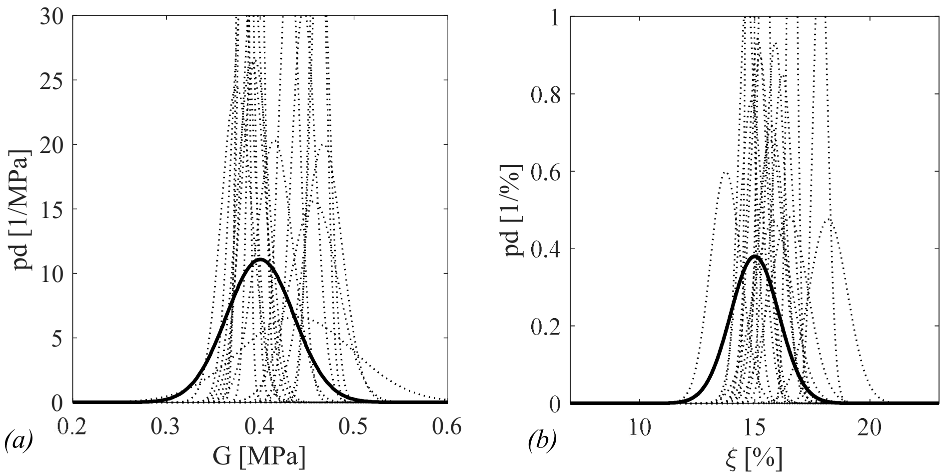

Figure 75. Batches distributions and general distribution of (a) G, (b) ξ.

Based on the statistical models experimentally calibrated, samples with varied properties (*G* and *ξ*) have been generated for the case studies *n-A HDRB* (24 bearings for each batch) and *n-A H+F 2* (16 bearings for each batch). Then, according to the Italian design code (CS.LL.PP., 2008, 2018), a control test has been simulated. It gets randomly the 20% of the isolation devices belonging to the same batch (5 on 24 or 4 on 16) and controls if the parameters of each isolator are within the limits imposed by the code (± 20% with respect to the nominal value of *G* and *ξ*). For the applications illustrated in this paper, it is conservatively assumed that if one of the isolation device parameters is out of the limits imposed by the code, the entire batch is rejected. Finally, once acceptable random values of *G* and *ξ* have been generated, a procedure that automatically calculates the varied parameters of the *HDR Bearing Element* (Kumar model) used in OpenSees (equivalent parameters G and ξ at the third cycle) has been implemented by using a nonlinear regression procedure. For the *FSBs*, considering the low lateral friction resistance of the sliders, the uncertainties associated to their mechanical properties have been neglected.

As an example, Figure 76 shows random values generated for the parameter G of each isolator of each batch. Red dots are related to the virtually tested isolators. Tolerance limits are also reported in the figure. (0.32 ÷ 0.48 MPa marked by dashed lines) and dots out these limits correspond to the non-conforming isolators. For this case study, 21 batches of 24 isolators each have been generated and checked, and only one (batch 21) resulted non-conforming because 2 out of 5 tested isolators do not fulfil the tolerance. It should be noted that some accepted batches might include isolators that do not respect tolerance limits because they were not selected for the control test.

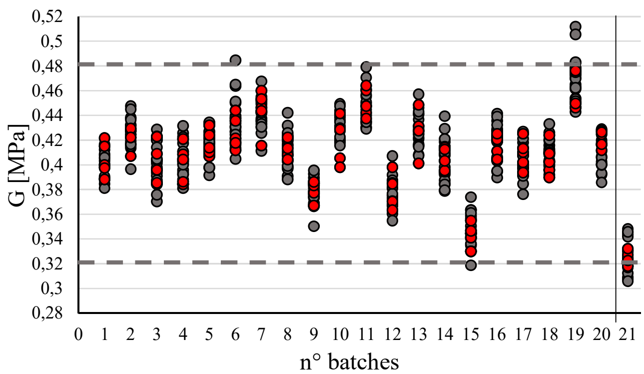

Figure 76. Random values of G of HDRB batches

In Figure 77a and c *GC* results of nonlinear dynamic analyses carried out accounting for model uncertainties are reported. In particular, two case study buildings (*Ku-n-A HDRB* and *Ku-n-A H+F 2*) are analysed. By comparing the observed results with those of the relevant reference cases without uncertainties, it is noticeable that the variability of the isolation system and of the superstructure does not modify significantly the number of collapses. Only the collapse modalities change. Significant differences are not evident even for the usability-preventing performance level (Figure 77b and d). As a general trend, model uncertainties increase the number of collapses and damage *D/C* ratios, however differences are not so evident, meaning that their influence on the response of isolated structures is very low compared to the influence of the seismic input variability (record-to-record variability).

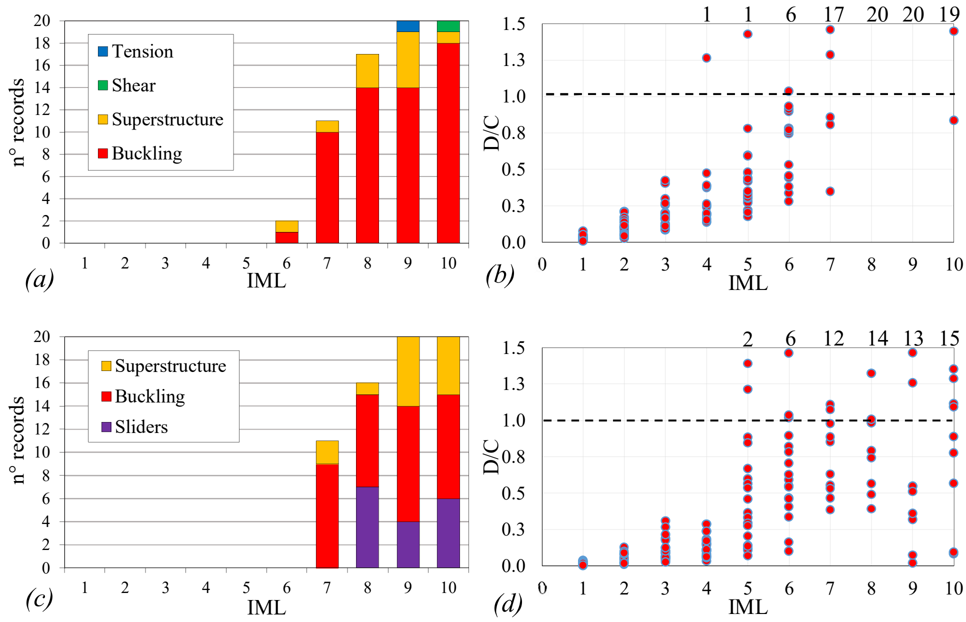

Figure 77. Summary of results with modelled uncertainties: (a)(b) GC and UPD for case Ku-n-A HDRB, (c)(d) GC and UPD for case Ku-n-A H+F 2

This can be better explained by observing Figure 78a, where mean values (continuous line) and dispersions (16th and 84th fractile denoted by dashed lines) of isolation displacement *D/C* ratio are reported, with reference to case *Ku-n-A HDRB*. For all the IMLs, response with uncertainties (red lines) and without uncertainties (black lines) are very similar. Differences arise only for the superstructure displacement *D/C* ratio (reported in Figure 78b with reference to the X direction) at *IMLs* larger than the intensity level of the isolation system design (*IML*6), causing a little increment of the number of collapses.

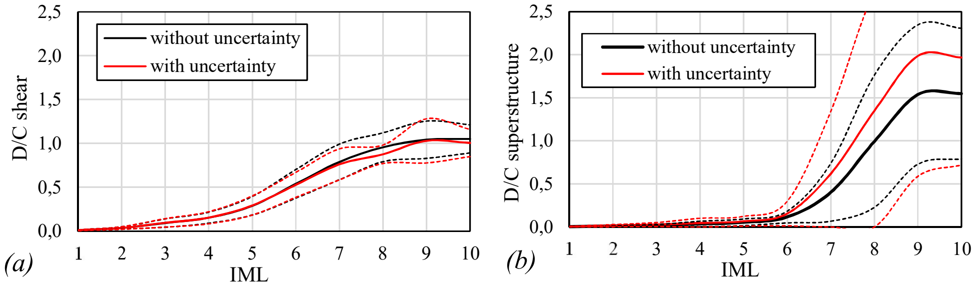

Figure 78. Mean (solid line) and mean±standard deviation (dashed lines) of (a) displacement D/C ratio of bearings and (b) displacement D/C ratio of the superstructure (X direction) for the case Ku-n-A HDRB with and without uncertainties

4.6 Results for Kikuchi modelling of rubber bearings

This chapter reports the results of the same case studies presented before (Chpt. 4.3) analysed using the *Kikuchi Bearing Element* Kikuchi model ("*Ki"*) for the rubber bearings instead of the Kumar model. According to this change also the *GC* definition for the isolation system is slightly changed due to the different behaviour of the model. Since *Kikuchi bearing element* explicitly simulates the post-buckling behaviour, the buckling collapse is replaced with a compression failure mode. The collapse is reached if 50% of elastomeric devices overcome an axial compression strain (ε_c) greater than or equal to 0.5. The vertical deformation limit is prudently fixed to 0.5 even if experimental results (Monzon et al. 2016) showed that buckled bearings can sustain even higher vertical deformation. As the *P-Δ* effects are explicitly simulated by the Kikuchi model, a reduction of vertical and horizontal stiffness is expected, leading to higher displacements and lower base shear forces and consequently to a probable change in the failure mechanism. Another difference between the two models is that the Kikuchi bearing element is not capable of simulating the stress-softening characterizing the first cycles of deformations of bearings. The shear behaviour is instead calibrated on the third cycle of the experimental tests according to the European code (EN15129, 2009) and the stiffening behaviour is not captured as well as by the Kumar model (see Figure 20 and Figure 36e) further reducing the horizontal stiffness for high shear displacement. The shear limit of 3.5 did not affect the collapse result in the previous chapter because it was only barely attained. In this case instead, as shown hereafter, it is the main collapse mechanism registered. As the value of 3.5 is somehow a safety-side choice, a second shear deformation limit of 4.0 is also used to better quantify how this limit affects the final reliability result.

ISOLATION DEVICE	*FAILURE MODE*	*EDP threshold*	*DESCRIPTION*
HDRBs	**Compression**	$\varepsilon_c \geq 0.50$	50% of elastomeric devices reaches an axial compression strain (ε_c) greater than or equal to 0.5
	Tension	$\varepsilon_t \geq 0.50$	50% of elastomeric devices reaches an axial tensile strain (ε_t) greater than or equal to 0.5
	Shear	$\gamma_r \geq 3.5$ (or 4.0)	50% of elastomeric devices reaches a shear strain (γ_r) greater than or equal to 3.5 (or 4.0)
FSBs	Over-stroke	$d_u = d_{max,FSB}+\Phi_p/2$	The horizontal displacement of the centre of gravity of the isolation floor is equal to the collapse limit value

Table 20. GC for the isolation systems (for Kikuchi bearing element)

Figure 79a shows the number of collapses for the case *Ki-n-A HDRB*, for a shear deformation limit of 3.5. Compared to the same case study with the *Kumar bearing model* (Figure 57a), the number of collapses registered is slightly reduced at *IML6* (-1), *IML7* (-5) and *IML8* (-3). As expected, most common failure registered is the shear collapse, due to the explicit simulation of the *P-Δ* effects and the different calibration (third cycle) that increase the horizontal displacement. As the shear break is the main collapse mechanism, the results for shear limit equal to 4.0 are shown in Figure 79b.

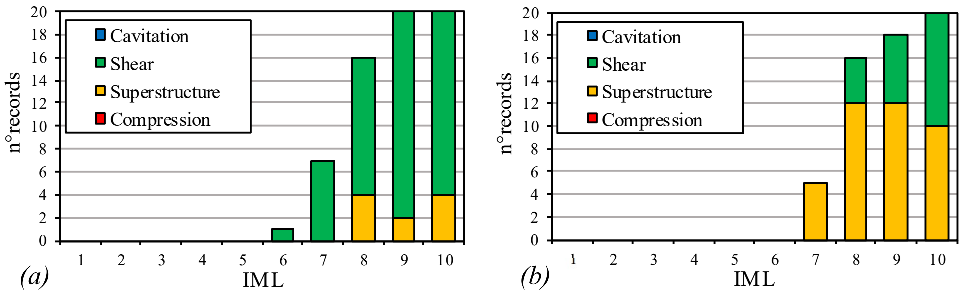

Figure 79. Global collapse results for Ki-n-A HDRB: (a) shear limit 3.5, (b) shear limit 4.0

As for Figure 57b, also in this case it can be observed that the number of collapses decrease. Moreover, many shear failures for a limit of 3.5 are immediately followed by the superstructure collapse, before reaching a shear failure limit of 4.0. Another time considering isolated buildings as in-series system with low safety margin for both bearings and superstructure seems to be in accordance with the results. Changing the model and the *GC* criteria doesn't affect significantly the total number of collapses, confirming the reliability of the analysis. Also in terms of *UPD* the change of the bearing model only slightly affect the results, as confirmed by the comparison between Figure 66a and Figure 80a.

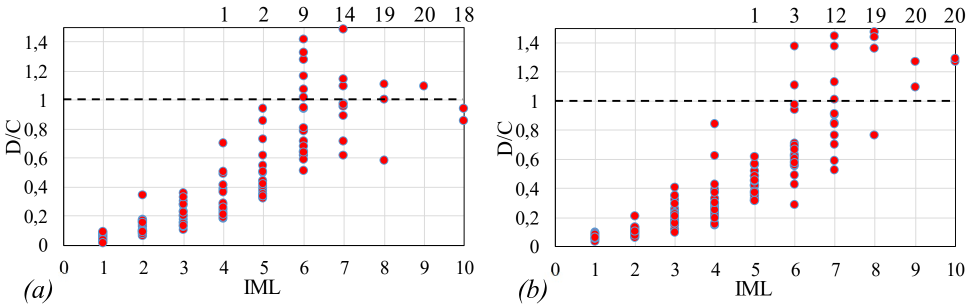

Figure 80. Displacement D/C ratio of the superstructure (UPD) for Ki-n-A HDRB: (a) X direction and (b) Y direction.

The quite good agreement between the two different model can be also checked comparing randomly the horizontal and vertical hysteretic cycles for the same time history used. For a medium intensity time history (*IML*5, record 1) the vertical and horizontal hysteretic cycles comparison between the Kikuchi model and the Kumar model for a corner bearing are reported in Figure 81. It is worth to note the very good agreement for both vertical and horizontal direction. Figure 81b shows that in both the cases the bearing undergoes the cavitation stress probably for the high influence of the rocking motion on the variation of the vertical load (reaching a tension condition but not a tension failure).

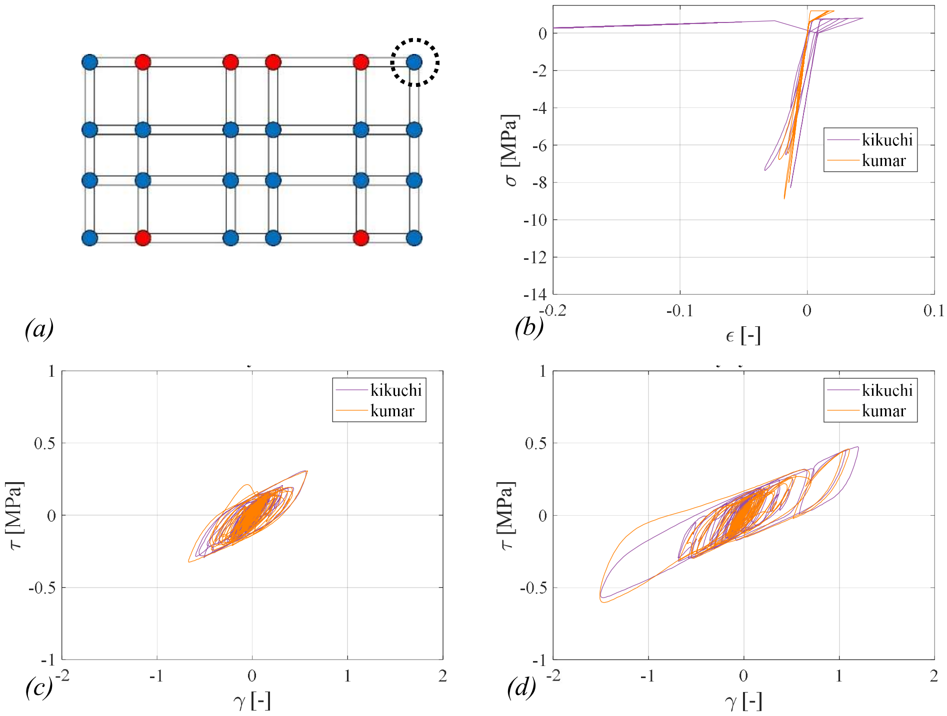

Figure 81. (a) Bearing position and hysteretic cycles comparison for Kikuchi and Kumar model in (b) vertical and (c)(d) horizontal directions for a record at IML5

The same cycles are also showed for an internal bearing in Figure 82. The only main difference is that in this case the rocking effects are strongly reduced and the vertical load fluctuation is reduced.

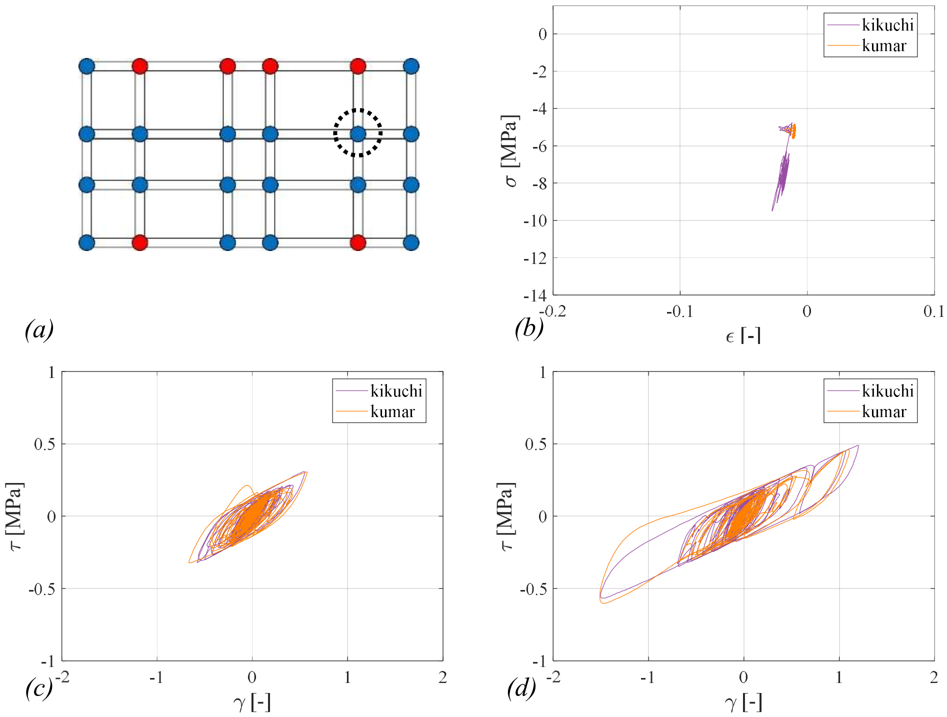

Figure 82. (a) Bearing position and hysteretic cycles comparison for Kikuchi and Kumar model in (b) vertical and (c)(d) horizontal directions for a record at IML5

Looking at a very high intensity earthquake (*IML9*, record 1) the results show a different behaviour for the two different models. More in detail, for the shear behaviour (Figure 83b and c), only the Kumar model is able to simulate the first cycle effect and the stiffening behaviour for high shear deformations. Kumar model also recognises the buckling of the bearing leading to a very high vertical deformation in compression, even if no effects are observed for the horizontal cycles. This is somehow the main shortcoming of the Kumar model for high damping rubber bearings (HDR Bearing element, implemented in the OpenSees software).

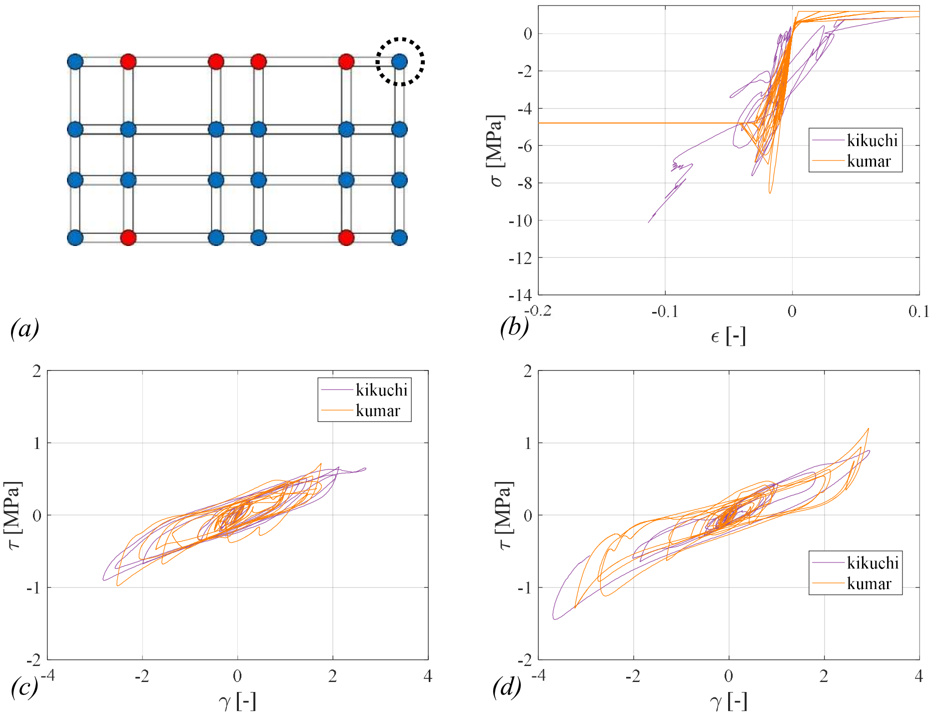

Figure 83. (a) Bearing position and hysteretic cycles comparison for Kikuchi and Kumar model in (b) vertical and (c)(d) horizontal directions for a record at IML9

The same results in terms of *GC* showed before are reported for the case study located in Naples in Figure 84. Another time the failures slightly reduce and change in shear collapses in the case of a shear limit of 3.5 respect to the previous results (Figure 65a). A limit of 4.0 further reduces the collapses, but the superstructure failures increase.

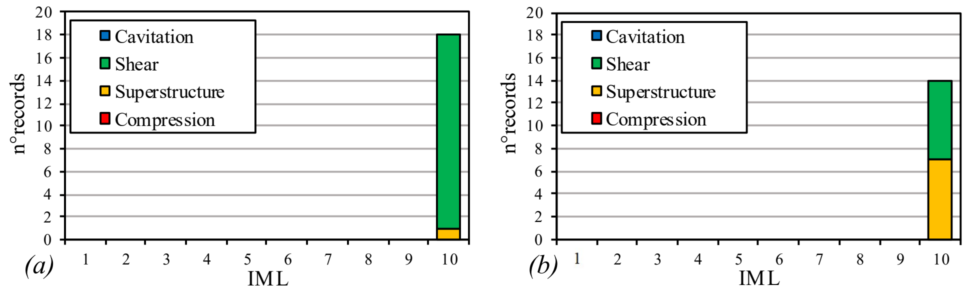

Figure 84. Global collapse results for Ki-n-N HDRB: (a) shear limit 3.5, (b) shear limit 4.0

Almost the same results can be found in terms of *UPD* for the two different modelling choice (Figure 85a and Figure 66b)

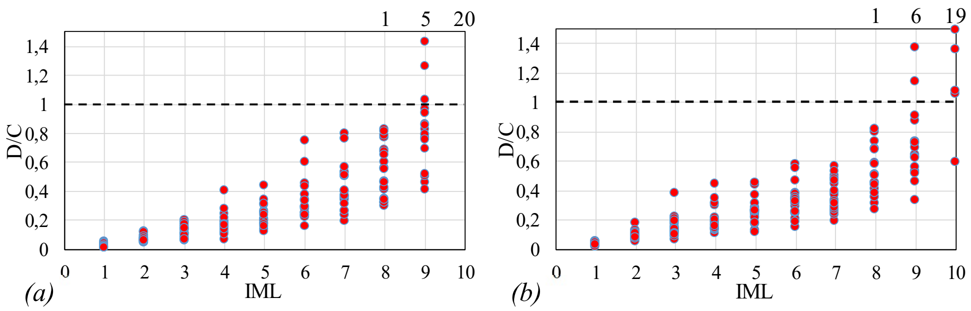

Figure 85. Displacement D/C ratio of the superstructure (UPD) for Ki-n-N HDRB: (a) X direction and (b) Y direction.

Regarding existing buildings retrofitted with *HDRBs*, the results for the *Ki-eS-A HDRB* are reported in Figure 86 and Figure 87. Compared to the previous results (Figure 67 and Figure 68) of the same case study they show only minor differences in terms of both *GC* and *UPD*. In this case changing the shear limit from 3.5 to 4.0 doesn't affect the result.

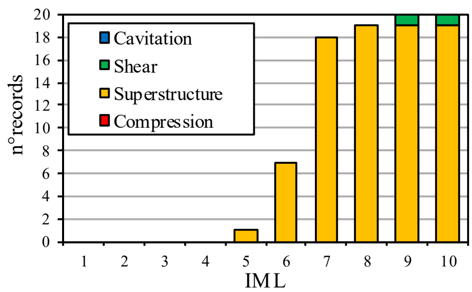

Figure 86. Summary of global collapse results for case Ki-eS-A HDRB.

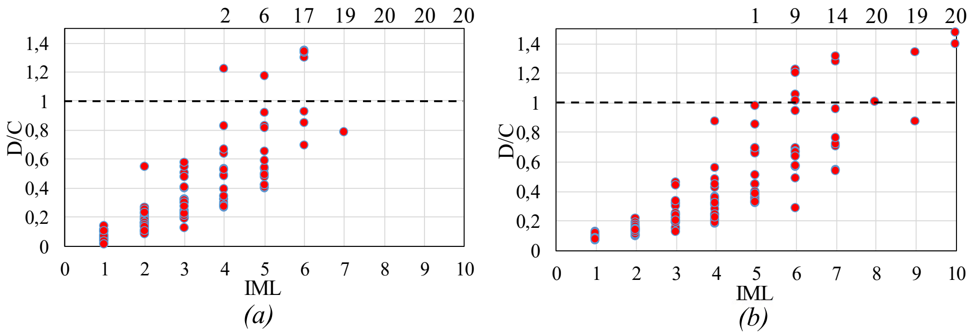

Figure 87. Displacement D/C ratio of the superstructure (UPD) for Ki-n-A HDRB: (a) X direction and (b) Y direction.

Two further consideration can be made, which are strongly related to the in-series reliability model assumed for the isolated systems. The first is that to significantly increase the reliability in terms of collapses both the superstructure and the isolation resistance must be enhanced (as stated also in literature, for example in Kitayama and Constantinou 2018 and Shao et al. 2019). The second, looking at the same problem from a different point of view, is that the collapse should be driven by the element whose capacity can be defined/evaluated in the most accurate way. For example, currently, the shear limit of rubber bearing is not tested during the qualification procedure of the device and actually unknown, even if is one of the most important parameters and it could be introduced in codes in the near future (Nishi, 2019). In this case, a "capacity design" where the collapse is moved to the superstructure using an higher safety margin for the base-isolation system could lead to a more reliable isolated building (if the superstructure collapse is ductile and the shear yielding limit is well defined). On the contrary, assessing better the real collapse limit of the devices, failure of the base isolation system before the superstructure collapse should be preferred.

In conclusion, the *GC* and *UPD* performances are only slightly affected by the bearing model used in the analyses, even if the results in terms of type of collapse behaviour are strongly modified especially for the different definition of the *GC* multi-criteria and, in a minor way, from the different cyclic response and calibration of the Kikuchi model (third cycle calibration, no damage effects, no stiffening control, *P-Δ* effects) and the Kumar model (damage effect considered, stiffening control, no *P-Δ* effects).

4.7 Results resume in terms of annual rate of failure

The results illustrated in the previous sections and concerning the component and system vulnerability can be used to calculate the annual failure rate λ_f (mean frequency with which it occurs or the probability that it will occur in a year the undesirable outcome) for both the *GC* (Figure 88) and *UPD* (Figure 89) performance levels and for each case study previously presented, using the method exposed in Chpt. 2.2.2 . As the results are similar for the case studies located in the same site, only the results obtained for the case studies employing the *HDR bearing element* (Kumar model). This subset is composed by two case studies of new building located in L'Aquila (Ku-n-A HDRB, Ku-n-A H+F 2), two new buildings located in Naples (Ku-n-N HDRB, Ku-n-N H+F 1), the two existing building retrofitted in L'Aquila (Ku-eS-A HDRB, Ku-eS-A H+F) and the case of retrofitted building in Naples (Ku-eG-A H+F). For the case of isolated building with only rubber bearings also the *GC* results for the Kikuchi model are reported (Ki-n-A HDRB, Ki-n-N HDRB) using a transparent marker close to the result of the pertinent Kumar model case. Moreover, for comparison purposes, also the result for the same case studies equipped with concave surface slider bearings (*CSSBs*) are reported (Cardone et al. 2019, Ragni et al. 2018). The figures are divided in two parts, one for L'Aquila results and one for Naples results. The blue markers represent the new isolated building cases whereas the red ones the retrofitted building cases. A dashed horizontal line highlights the target reliability level ($2\cdot10^{-4}$ for *GC*, according to CEN 2017, Dolsek 2017, $1.4\cdot10^{-3}$ for *UPD,* CEN 2002, HANDBOOK2 2004). The annual rate of failure of the equivalent fixed base structure is also reported (Iervolino et al. 2018) to better understand the results.

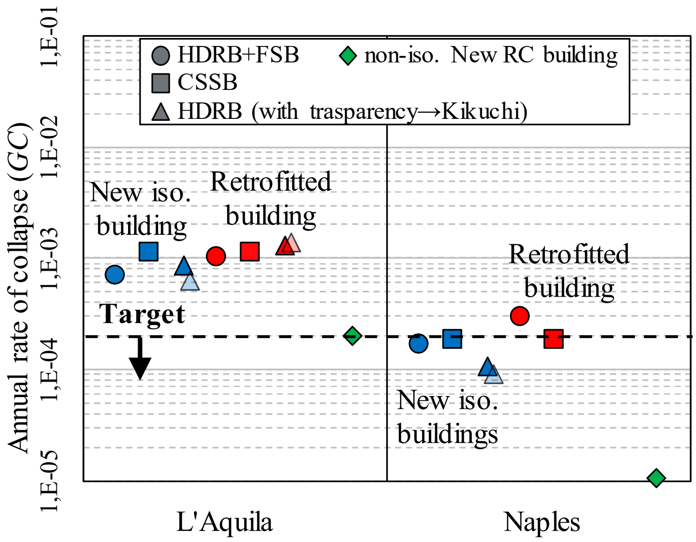

Figure 88. Annual rate of collapse (GC) for the different case studies

The annual rate of failure in terms of *GC* for all the isolated building case studies is almost constant considering the same site. For example, for L'Aquila site the value is $\approx 1 \cdot 10^{-3}$ for both new and retrofitted building with seismic isolation whereas for the Naples case studies it is around $\approx 2 \cdot 10^{-4}$. In the former case the value is of an order of magnitude higher than the code reliability target, showing a very low performance and consequently an inadequate result of the seismic design according the Italian seismic code. In the latter case, instead, the results are around the reliability target. A first conclusion is therefore that even if the code prescription should lead to an equivalent level of security, the hazard of the site strongly influences the reliability level. This is clearly explained by Figure 65b, where hazard curves of L'Aquila and Naples normalized on the design seismic intensity are showed. In the case of L'Aquila, the normalized hazard intensity rapidly increases for return periods higher than the design one and consequently the safety factors used in the design are rapidly "worn out". In the Naples case, instead, the hazard intensity increases with a lower rate and consequently the safety factors are sufficient to achieve the target reliability.

The differences in terms of annual rate of failure for L'Aquila and Naples sites highlight that the design procedure is not in compliance with the implicit performance goals requested by the code, but only in the case of L'Aquila site. Consequently, simply increasing safety factors could lead to over conservativism for medium level hazard sites. A solution could be a risk targeting approach (Gkimprixis et al. 2019) that allows to achieve consistent performance levels for all the case studies

Comparing the annual rate of failures of isolated buildings with the equivalent non-isolated new fixed base structure (RC frame, 6 floor, same geometry, structure designed according to the same Italian building) Figure 88 gives even more rise to concern for the results. The fixed-base structures located at L'Aquila and Naples have an annual rate of failure of an order of magnitude lower than the isolated structures. Also in this case the reliability is strongly affected by the hazard site, but in both cases the reliability of the structures is in compliance with the code target. Even if the lower reliability of isolated structure with respect to equivalent fixed-base structure is confirmed by other authors (Kitayama and Constaninou 2018, Shao et al. 2019), the results needs an insight.

Regarding the *UPD* instead, the superior performance of seismically isolated buildings especially for the site of Naples is shown in Figure 89. It is worth to note that at L'Aquila site the annual rate of damage for retrofitted structure is similar to the one of new buildings. The reason is that the *eS* case study (existing building designed as fixed base according pre-96 seismic code, with a base shear design force around 0.07 the weight of the building) has similar characteristic of a new isolated superstructure. On the contrary, at Naples site the strength of the existing structure (*eG* case, designed for only vertical loads) is lower than the equivalent new isolated structure. Neither the L'Aquila nor the Naples fixed base structures are in compliance with the annual rate of damage target.

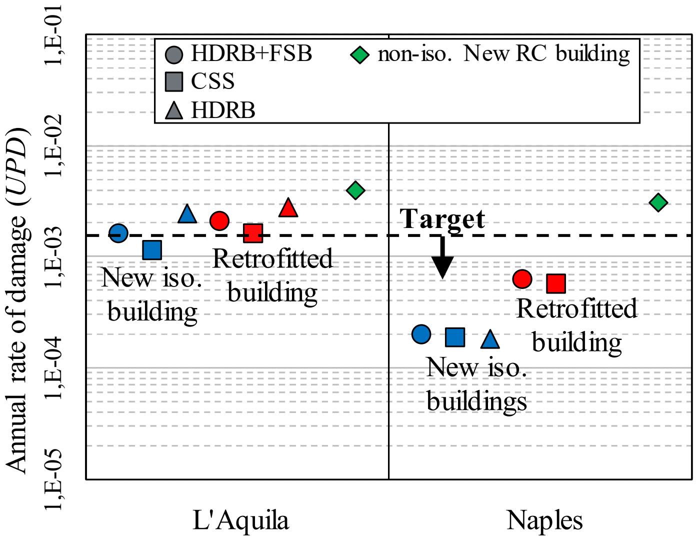

Figure 89. Annual rate of damage (UPD) for the different case studies

4.8 Chapter’s references

AIJ Architectural Institute of Japan Editor (2012), “Preliminary Reconnaissance Report of the 2011 Tohoku-Chiho Taiheiyo-Oki Earthquake” DOI 10.1007/978-4-431-54097-7

BS ISO 22762-2:2018 Elastomeric seismic-protection isolators — Part 2: Applications for bridges — Specifications, 2018.

BS ISO 22762-3:2018 Elastomeric seismic-protection isolators — Part 3: Applications for buildings — Specifications, 2018.

Calgaro, J.-A., Gulvanessian. 2001. “Management of reliability and risk in the Eurocode system”. IABSE International Conference “Safety, Risk and Reliability – Trends in Engineering”, Malta 21-23 mars 2001

Cardone, D., Conte, N., Dall’Asta, A., Di Cesare, A., Flora, A., Lamarucciola, N., Micozzi, F., Ponzo, F., Ragni, L., 2019. RINTC-E PROJECT: THE SEISMIC RISK OF EXISTING ITALIAN RC BUILDINGS RETROFITTED WITH SEISMIC ISOLATION, in COMPDYN 2019 - 7th ECCOMAS Thematic Conference on Computational Methods in Structural Dynamics and Earthquake Engineering, Crete, Greece. https://2019.compdyn.org/proceedings/pdf/19921.pdf

Cardone, D., Palermo, G., Dolce, M., 2010. Direct Displacement-Based Design of Buildings with Different Seismic Isolation Systems. Journal of Earthquake Engineering 14, 163–191. https://doi.org/10.1080/13632460903086036

CEN 2002. European standard EN 1990:2002. Eurocode: basis of structural design. European Committee for Standardization, Brussels

CEN 2004. Eurocode 8: Design of structures for earthquake resistance - Part 1: General rules, seismic actions and rules for buildings. European Committee for Standardization, Brussels, Belgium. EN 1998-1

CEN. 2017. Draft Annex F (Informative): simplified reliability-based verification format, Annex to European standard EN 1998–1. Eurocode 8: design of structures for earthquake resistance. Part 1: general rules, seismic action and rules for buildings. European Committee for Standardization. Brussels (Prepared by Dolsek M, Zizmond J, Kosic M, Lazar Sinkovic)

CS.LL.PP. 2008. Norme tecniche per le costruzioni,” Gazzetta Ufficiale della Repubblica Italiana 29. (In Italian.)

CS.LL.PP. 2018. Aggiornamento delle norme tecniche per le costruzioni,” Gazzetta Ufficiale della Repubblica Italiana 42. (In Italian.)

Dolsek M, Zizmond J, Kosic M, Lazar Sinkovic N (2017) Simplified reliability-based verification format, working material for Annex F to revised EN 1998-1. University of Ljubljana, Ljubljana

EN15129. 2009. Antiseismic Devices, European Committee for Standardization, Brussels, Belgium.

Fajfar, P., 2018. "Analysis in seismic provisions for buildings: past, present and future", The fifth Prof. Nicholas Ambraseys lecture. Bull Earthquake Eng 16, 2567–2608. https://doi.org/10.1007/s10518-017-0290-8

Franchin, P., Mollaioli, F., Noto, F., 2017. RINTC PROJECT: INFLUENCE OF STRUCTURE-RELATED UNCERTAINTIES ON THE RISK OF COLLAPSE OF ITALIAN CODE-CONFORMING REINFORCED CONCRETE BUILDINGS, in: Proceedings of the 6th International Conference on Computational Methods in Structural Dynamics and Earthquake Engineering (COMPDYN 2015). Presented at the 6th International Conference on Computational Methods in Structural Dynamics and Earthquake Engineering Methods in Structural Dynamics and Earthquake Engineering, Institute of Structural Analysis and Antiseismic Research School of Civil Engineering National Technical University of Athens (NTUA) Greece, Rhodes Island, Greece, pp. 1503–1514. https://doi.org/10.7712/120117.5509.17123

Franchin, P., Ragni, L., Rota, M., Zona, A., 2018. Modelling Uncertainties of Italian Code-Conforming Structures for the Purpose of Seismic Response Analysis. Journal of Earthquake Engineering 22, 1964–1989. https://doi.org/10.1080/13632469.2018.1527262

Gkimprixis, A., Tubaldi, E., Douglas, J., 2019. Comparison of methods to develop risk-targeted seismic design maps. Bull Earthquake Eng 17, 3727–3752. https://doi.org/10.1007/s10518-019-00629-w

HANDBOOK 2 - IMPLEMENTATION OF EUROCODES - RELIABILITY BACKGROUNDS. 2004. Guide to the basis of structural reliability and risk engineering related to Eurocodes, supplemented by practical examples LEONARDO DA VINCI PILOT PROJECT CZ/02/B/F/PP-134007. Prague

Iervolino, I., Spillatura, A., Bazzurro, P., 2018. Seismic Reliability of Code-Conforming Italian Buildings. Journal of Earthquake Engineering 22, 5–27. https://doi.org/10.1080/13632469.2018.1540372

Jalayer, F. (2003) "Direct Probabilistic seismic analysis: implementing nonlinear dynamic assessment,"Ph.D. thesis, Department of Civil and Environmental Engineering, Stanford University, Stanford,CA, USA.

Kitayama, S., Constantinou, M.C., 2018. Collapse performance of seismically isolated buildings designed by the procedures of ASCE/SEI 7. Engineering Structures 164, 243–258. https://doi.org/10.1016/j.engstruct.2018.03.008

Kutner, M. H., Nachtsheim, C. J., Neter, J. and Li, W. (2005) Applied Linear Statistical Models. 5th, McGraw-Hill/Irwin, Chicago, IL.

Matsuda, K., Kasai, K., Yamagiwa, H., Sato, D., 2012. Responses of Base-Isolated Buildings in Tokyo during the 2011 Great East Japan Earthquake. 15 WCEE. Lisboa

Micozzi, F., Ragni, L., Dall'Asta, A., 2018. STATISTICAL MODELLING OF HDNR BEARING PROPERTIES VARIABILITY FOR THE SEISMIC RESPONSE OF ISOLATED STRUCTURES. Proc. 6th European Conference on Computational Mechanics (ECCM 6), 7th European Conference on Computational Fluid Dynamics (ECFD 7) 11 – 15 June 2018, Glasgow, UK. http://www.eccm-ecfd2018.org/admin/files/filePaper/p1754.pdf

Montuori, G.M., Mele, E., Marrazzo, G., Brandonisio, G., De Luca, A., 2016. Stability issues and pressure–shear interaction in elastomeric bearings: the primary role of the secondary shape factor. Bulletin of Earthquake Engineering 14, 569–597. https://doi.org/10.1007/s10518-015-9819-x

Monzon, E.V., Buckle, I.G., Itani, A.M., 2016. Seismic Performance and Response of Seismically Isolated Curved Steel I-Girder Bridge. J. Struct. Eng. 142, 04016121. https://doi.org/10.1061/(ASCE)ST.1943-541X.0001594

Nishi, T., Suzuki, S., Aoki, M., Sawada, T., Fukuda, S., 2019. International investigation of shear displacement capacity of various elastomeric seismic-protection isolators for buildings. J Rubber Res 22, 33–41. https://doi.org/10.1007/s42464-019-00006-x

Nishida, A., Choi, B., Yamano, H., Takada, T., 2018. Development of Seismic Countermeasures Against Cliff Edges for Enhancement of Comprehensive Safety of Nuclear Power Plants: Cliff Edges Relevant to NPP Building System, in: Volume 8: Seismic Engineering. Presented at the ASME 2018 Pressure Vessels and Piping Conference, ASME, Prague, Czech Republic, p. V008T08A028. https://doi.org/10.1115/PVP2018-85066

Ragni, L., Cardone, D., Conte, N., Dall'Asta, A., Cesare, A.D., Flora, A., Leccese, G., Micozzi, F., Ponzo, C., 2018. Modelling and Seismic Response Analysis of Italian Code-Conforming Base-Isolated Buildings. Journal of Earthquake Engineering 0, 1–33. https://doi.org/10.1080/13632469.2018.1527263

ReLUIS-Line 6 Workgroup, 2018. Prodotto finale del Task 1.1 isolamento sismico e Task 1.2 dissipazione di energia, ReLUIS report, Roma, Italy (in italian). Available at http://www.reluis.it.

ReLUIS-RINTC Workgroup, 2018. Results of the 2015-2017 RINTC project. ReLUIS-RINTC report, ReLUIS, Naples, Italy. Available at http://www.reluis.it.

Ricci, P., Manfredi, V., Noto, F., Terrenzi, M., De Risi, M.T., Di Domenico, M., Camata, G., Franchin, P., Masi, A., Mollaioli, F., Spacone, E., Verderame, G.M., 2019. RINTC-E: TOWARDS SEISMIC RISK ASSESSMENT OF EXISTING RESIDENTIAL REINFORCED CONCRETE BUILDINGS IN ITALY, in: Proceedings of the 7th International Conference on Computational Methods in Structural Dynamics and Earthquake Engineering (COMPDYN 2015). Presented at the 7th International Conference on Computational Methods in Structural Dynamics and Earthquake Engineering Methods in Structural Dynamics and Earthquake Engineering, Institute of Structural Analysis and Antiseismic Research School of Civil Engineering National Technical University of Athens (NTUA) Greece, Crete, Greece, pp. 554–576. https://doi.org/10.7712/120119.6939.20040

Ricci, P., Manfredi, V., Noto, F., Terrenzi, M., Petrone, C., Celano, F., De Risi, M.T., Camata, G., Franchin, P., Magliulo, G., Masi, A., Mollaioli, F., Spacone, E., Verderame, G.M., 2018. Modeling and Seismic Response Analysis of Italian Code-Conforming Reinforced Concrete Buildings. Journal of Earthquake Engineering 22, 105–139. https://doi.org/10.1080/13632469.2018.1527733

Shao, B., Mahin, S.A., Zayas, V., 2019. Achieving targeted levels of reliability for low-rise seismically isolated structures. Soil Dynamics and Earthquake Engineering 125, 105744. https://doi.org/10.1016/j.soildyn.2019.105744

Takaoka, E., Takenaka, Y., Nimura, A., 2011. Shaking table test and analysis method on ultimate behavior of slender base-isolated structure supported by laminated rubber bearings. Earthquake Engng. Struct. Dyn. 40, 551–570. https://doi.org/10.1002/eqe.1048

Tubaldi, E., Mitoulis, S.A., Ahmadi, H., Muhr, A., 2016. A parametric study on the axial behaviour of elastomeric isolators in multi-span bridges subjected to horizontal seismic excitations. Bull Earthquake Eng 14, 1285–1310. https://doi.org/10.1007/s10518-016-9876-9

CHAPTER 5

5 Effects of Hazard assessment on reliability results

5.1 Introduction

The numerical analyses carried out on a set of seismically isolated buildings showed that the design prescriptions of the current Italian seismic code *NTC* (CS.LL.PP., 2008, 2018) may provide a reliability level that does not satisfy the code target, especially for sites with high hazard. The safety factors used are not adequate and the resulting safety level for both the bearing capacity and the superstructure capacity are sometimes not in compliance with the code targets, especially for the site of L'Aquila. Moreover, equivalent non-isolated reinforced concrete structures, designed according to the same seismic code, have a probability of collapse of an order of magnitude lower than isolated structures.

The common perception regarding seismic isolation safety is that isolated structures are safer than traditional structures. This is true especially in the case of earthquake intensities lower than or equal to the design seismic level as shown before. Indeed, analyses carried out highlighted that for earthquakes intensities a little higher than the design level the probability of collapse is very high and isolated structures show the so called "cliff edge effect" (Nishida et al. 2018).

On the contrary, many isolated buildings have been subjected to seismic actions higher than the design level, but no major collapse has been registered worldwide (see Chpt. 2.1) while, during the same earthquakes, some standard buildings collapsed. It is somehow unlikely that base-isolation systems with a probability of failure of an order of magnitude higher than standard buildings do not collapse during extreme earthquake (like the Tohoku earthquake in 2011).

Previous results are therefore critically analysed in this section by examining more in depth the role of the hazard definition on the overall annual rate of failure.

The comparison carried out in the previous chapter (Figure 88) is correct from a theoretical point of view because the same probabilistic framework has been used for both isolated structures and fixed-base structure, but some aspects must be deepened to better understand why annual rate of failures are so different.

A first point concerns the fundamental period of the structures and its link with the hazard definition and the ground motion selection. The case studies of isolated structures have a fundamental period in the range 2.5s-3.5s, while for fixed-base structure fundamental period is 1.2s in bare frame configuration (0.5s considering also the stiffness contribution of the infills). *Conditional Spectrum* method (*CS*, Lin et al. 2013a, NIST 2011) is used to select ground motions conditioned to fundamental periods of the structures. Consequently, very different conditioning periods were used. This first difference between the assessment carried out on isolated structures and fixed-base structure is not a direct source of difference for annual rates of failure. In fact, Lin et al. (2013a) verified on a case study that risk-based assessments performed on the basis of ground motions selected and scaled to match the *CS* for four different conditioning periods (0.45, 0.85, 2.6, and 5s, the building's third-mode structural period up to approximately twice the first-mode period). Even if the range of conditioning was very large, risk assessments resulted in similar outcomes. They demonstrated that accurate results can be achieved using any conditioning period if ground motions are selected carefully to ensure proper representation of spectral values, i.e. consistency with the site ground motion hazard curves at all relevant periods. In the *CS* method, the ground motion *IM* used to link ground motion hazard and structural response is not a physical part of the seismic reliability problem considered but only a useful link to decouple hazard and structural analysis. This is the main achievement of *CS* respect to the previous *Conditional Mean Spectrum*. The latter uses as target for the record selection only the mean conditional spectra while the former uses both mean and variability in the target spectra, ensuring that the distributions of spectra at all periods are still consistent with all known hazard information for the site being considered. Anyway, Lin et al. (2013a) also explained that the choice of conditioning period is still important because it should be a good predictor of structural response and should reduce the variability in structural response and consequently the number of nonlinear dynamic analyses ("*sufficienty*" and "*efficienty*" properties of the *IM*, according to Luco et al. 2007).

Reasoning on the *CS*, there is another difference in the framework used to assess fixed-base structures and isolated structures: the *GMPE* used and consequently the *IM* associated. In fact, for fixed-base RC structures (and all the other archetypes in the project) the hazard was defined using the *GMPE* of Ambraseys et al. (1996). The choice of this *GMPE* was made to be as close as possible to the seismic hazard used in the Italian code (CS.LL.PP., 2008, 2018) that is based on hazard study of Stucchi et al. (2011). More in detail, the branch named 921 of the logic tree, the one producing the results claimed to be the closest to those provided by full logic tree of Stucchi et al., considers the seismic source model of thirty-six areal zones of Meletti et al. (2008) and the *GMPE* by Ambraseys et al. (1996). Even if the *GMPE* is quite old, the choice to be as close as possible to the hazard of the code is justified because there must be coherency between the design process (that is an *intensity based* assessment, Lin et al. (2013b)) and the risk assessment or, more properly, between the *PSHAs* carried out for the two assessments.

The *GMPE* of Ambraseys use the maximum spectral acceleration among the horizontal components (Sa_{larger}) as *IM* and has a range of period validity of 0-2s. In other words, it is possible to calculate with a *PSHA* the hazard curves only up to 2s and, consequently, to define a *CS* procedure where records selection is controlled in terms of mean and variance only in this range. Sa_{larger} stands for the maximum spectral acceleration of the two components as registered; it is worth to note that this *IM* is orientation-dependent, i.e. it depends on the orientation of the seismometers at the seismic stations where the ground motion signal was recorded while the current state of the art is the use of orientation-independent *IMs* (Boore 2006. Boore 2010, Boore and Kishida 2017). A discussion regarding this topic will be presented afterwards.

The *RINTC* project aims to develop *PSHAs* of different structural typologies by using common criteria for the hazard description. So, different outcomes (failure rates) can be exclusively attributed to differences regarding the design methods (suggested by national code) or the intrinsic dynamic properties of the structural typology. However, an incoherence arose in the assessment of the hazard for isolated systems because the *GMPE* used for traditional buildings does not cover the range of periods of interest in seismic isolation, and a different *GMPE* was introduced in the latter case (Akkar and Bommer 2010). Note that the latter use the geometric mean (Sa_{GM}) of the two horizontal components as *IM*. This *IM* is orientation-dependent too.
It is expected that results coming from different *GMPEs* can be compared in an approximate way only and a more reliable comparison requires an hazard assessment based on the same *GMPE*.
As mentioned before, the use of a different *IM* is not automatically related to a different result in the risk-assessment but the use of a different *GMPE* for producing the hazard curve compared to the ones used for the design spectra is in contrast with the attempt to be as close as possible to the code hazard assessment. In fact, *GMPE* are generally developed using statistical regression on observations from large libraries of observed ground motion intensities. Both the *GMPEs* have been developed using pan-European databases, but not the same database. Moreover, the statistical regression procedure was significantly different. Consequently, a difference in the final hazard is expected. Furthermore, the seismic design intensity could be no longer in compliance with the hazard used in risk assessment. This source of -difference of the annual rates of failure can be defined as "*hazard-generated*".
RINTC project objective is instead the evaluation of the *"design-generated"* effects, e.g. the different safety factors or different structural behaviour factors used in the design. More broadly, *"design-generated"* factors are related, according to Lin et al. (2013b), to a "*missing link between the implicit performance goals and the explicit design checks that needs to be reconciled".*
Regarding the different *IM* of the two *GMPEs*, the possible misusing of Sa_{GM} and Sa_{larger} is known in literature. Baker and Cornell (2006) in the paper titled

“Which Spectral Acceleration Are You Using?” highlighted the common inconsistency between earth scientists, who typically use Sa_{GM} as the *IM* for hazard analysis, and structural engineers, who often use spectral acceleration of a single horizontal component as the *IM* for response analysis, typically Sa_{larger}, and that this inconsistency in definitions is typically not recognized when the two assessments are combined. The use of Sa_{GM} has become widespread in the past years because this *IM* implicitly reduces the variance of the data needed for the definition of the attenuation law (*GMPE*) and allows to estimate the spectral accelerations with greater confidence. In the technical report NIST (2011) it is stated that *“Geometric mean spectral acceleration has been widely used for hazard calculations for more than two decades although until recently few structural earthquake engineers understood the definition and how to apply it”*. This is not the case of the previous applications, relevant to RINTC project, i.e. the framework is theoretically correct because there is no direct connection between the *PSHA* and the seismic intensity used in the design, as it is defined directly by the code.

The chapter, after a brief description of the different *IMs,* aims therefore to provide a comparison among results obtained from different *GMPEs*, both in terms of direct hazard intensities and annual rate of failures. This approach intents to give evidence to the intrinsic influence of *GMPEs* on the risk analysis.

Besides the two *GMPEs* used in the project, also the one of Lanzano et al. (2019) has been used to define a new set of hazard curves and compare the hazard results. This new *GMPE* recently published is a revision of the work of Bindi et al. (2011) for shallow crustal earthquakes in Italy, and it is based on the new data collection of strong-motion records made available in Italy after the occurrence of the most recent seismic sequences (2012 Emilia, Northern Italy; 2016–2017 Central Italy). The new *GMPE* is suitable for isolated structures because it includes vibration periods up to 10s. Moreover, it has magnitude range beyond 6.9 and uses the median of orientation-independent amplitudes (Sa_{RotD50}) as *IM,* that is the state-of-the-art intensity measure.

In order to develop this comparison, the *PSHA* has been completely re-evaluated using the Reassess v.2.0 software (Chioccarelli et al. 2018). Moreover, using results of Lanzano's *GMPE*, the procedure of *CS* (Lin et. al., 2013a) using the code of Baker (2011) and Baker and Lee (2018) has been carried out to select a new set of records to perform the risk assessment on two case studies of isolated structure and compare the annual rate of failure obtained using different *GMPEs*.

The sets of records defined for the three different *GMPEs* have been also studied to understand the real relationship between them using an innovative procedure to calculate directly the hazard curves from the sets of records for any period and any *IM*. In this way a real comparison of the hazard defined by the record selections has been carried out, highlighting the different hazard levels for the three *GMPE* used.

5.2 IM

Three different *IMs* have been previously introduced: Sa_{larger} (maximum spectral acceleration period-by-period of the two components as registered, orientation-dependent), Sa_{GM} (geometric mean of spectral acceleration, calculated period-by-period as the square root of the product of the two spectral accelerations of the two components as registered, orientation-dependent) and Sa_{RotDnn} (nnth percentile of spectral acceleration at each period over all orientations of the two components projected onto all nonredundant directions, orientation-independent) (*Sa* always refers to pseudo-spectral acceleration). The last one, proposed by Boore (2010), has recently become popular due to its simple and orientation-independent definition (Shahi and Baker, 2014), especially in the form of Sa_{RotD50}, and used by Lanzano, but also as $Sa_{RotD100}$, that is the maximum spectral acceleration over all orientations.

For this Thesis, an algorithm has been developed to compute the multidirectional spectral characteristics of the bidirectional signals. It is based on the concept of *projected envelope algorithm* (Dai et al., 2014), but since it has been developed within the MATLAB® environment, it has been improved by using matrices computation to calculate the spectral values of all periods at the same time.

The spectral analysis starts from the bidirectional response of the SDOF; it can be efficiently computed by a linear combination of two orthogonal responses (Huang et al., 2008) using the piecewise exact method (Clough & Penzien, Paultre).

An example of multidirectional spectral analysis carried out on a record of CHICHI 1999 earthquake (from the Next Generation Attenuation database, record sequence number 1194) is reported in Figure 90. The trace (grey line) represents the time history response of an elastic two-dimensional system with period *T* and damping ratio ξ equal along all the directions.

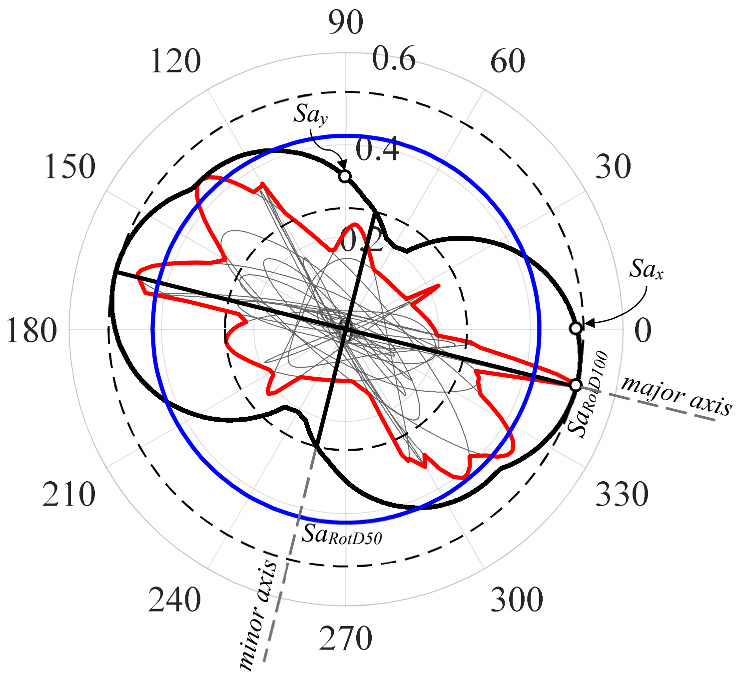

Figure 90. Spectral displacement response trace [m], envelope and projection for T=3s, ξ=5% damping ratio of record from the Next Generation Attenuation (NGA) database, record sequence number 1194 (CHICHI 1999 earthquake).

From this trace it is possible to define the perimeter (red line) and then the projection of this perimeter for all the possible directions (black solid line). The distance from the centre of this "bubbled shape" close curve for a specific direction is the spectral value of the projected ground motion in that direction. Consequently, the black solid line is the projected envelope. It is worth to note that, in this polar representation, the values at 0° and 90° are the spectral values of the two components of the record as registered (Sa_x and

Sa_y). The maximum among them is Sa_{larger} which is not the omnidirectional maximum $Sa_{RotD100}(T)$ (T=3s for Figure 90). The direction of the real maximum is defined by the *major-axis* (Hong and Goda 2007). The orthogonal direction is called minor-axis and it is associated to a spectral value that is different from the real minimum value. The two spectral values of the major and minor axes are highlighted with two dashed circles (as in Grant 2011). The difference between these two values is an approximative measure of the directionality of the ground motion. The blue solid circle is instead $Sa_{RotD50}(T)$, i.e. the median value over all orientations. In fact, half of the projected envelope (black solid line) is inside the circle and the other half outside.

If ground motion approximately provides an equal response along all the orientations at a given period, it is called *unpolarised* (Sashi and Baker, 2014). In this case the difference among max, min and median value (e.g., Sa_{RotD00}, $Sa_{RotD100}$ and Sa_{RotD50}) are negligible. Differently, if the earthquake signal is *polarized*, the ratio between $Sa_{RotD100}$ and Sa_{RotD50} increases and it is limited by the upper bound $\sqrt{2} = 1.414$, as highlighted in Figure 91, where the projected envelope of a very polarized earthquake signal is almost composed by the two circles related to the projection of the maximum (dashed green circles). In this case $Sa_{RotD100}$ is exactly 1.414 times the Sa_{RotD50}. The latter divides the projected circle of the max (dashed green) in two halves. The ratio $Sa_{RotD100}/Sa_{RotD50}$ is therefore a measure of the polarization.

For the case showed in Figure 91, it is clear how much both Sa_{larger} (max(Sa_x,Sa_y)) and Sa_{GM} (($Sa_x \cdot Sa_y)^{0.5}$) are not good estimator of seismic intensity, especially for polarized earthquakes.

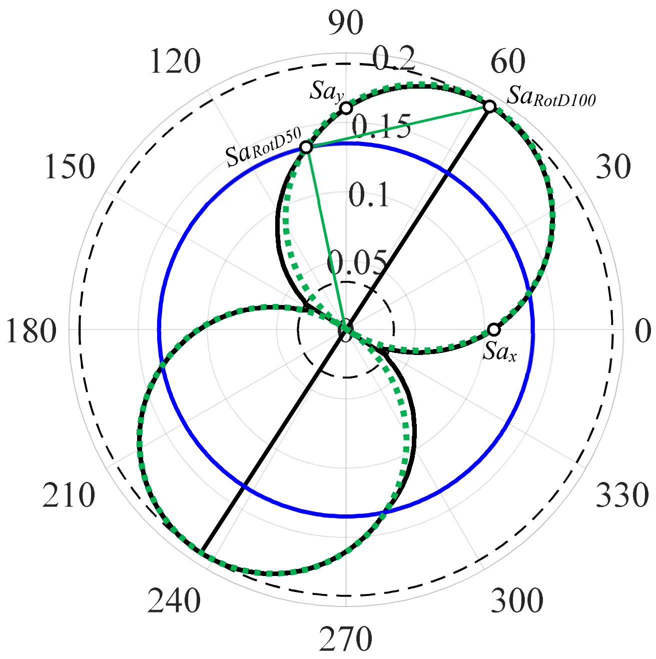

Figure 91. Pseudo Spectral acceleration response trace [m] T=3s, ξ=5% damping ratio for a record from Next Generation Attenuation (NGA) database, record sequence number 1194 (CHICHI 1999 earthquake). Polarized signal with $Sa_{RotD100}/Sa_{RotD50}$*=1.414*

There are many works regarding the relation between $Sa_{RotD100}$ and Sa_{RotD50} at each period and potential magnitude-distance-site condition dependence (such as Shashi and Baker 2014, Boore and Kishida 2017, Baker and Bradley 2017). Generally, $Sa_{RotD100}/Sa_{RotD50}$ increases for increasing period, i.e. polarization is higher for large periods. A reinterpretation of these works on the relation between horizontal component could be of interest considering also Sa_{RotD00} or the minor-axis spectral value for example to better assess the relation of the polarization of the signal.

The problem of comparing different *IMs* and linking one to another has been assessed during time. Boore and Kishida (2017) summarized many papers published in this field and they specifically focused on the three *IMs* previously described and used by the *GMPEs.* They calculated all the ratios between them for all the periods in terms of mean and standard deviation. Considering a period range up to 10s, $Sa_{RotD100}/Sa_{RotD50}$ is in the range of 1.188-1.287, Sa_{RotD50}/Sa_{GM} in the range of 1.009-1.077, Sa_{Larger}/Sa_{RotD50} in the range 1.107-1.178, Sa_{Larger}/Sa_{GM} 1.117-1.266.

The *IMs* used are also characterised by a different level of “sufficiency” and efficiency”, especially related to the particular behaviour of seismically isolated buildings. The choice of a bidirectional measure of ground-motion demand to use should not be made independently of the application for which it is required (Grant 2011).

Beyer and Bommer (2007) studied the effect of the orientation of ground motion on structural response and they suggest that the median response for all possible orientation angles should be used to structural configurations in which lateral-force resisting systems in orthogonal directions are reasonably independent. For example, RC structures are somehow characterized by a behaviour and, most important, a capacity that is almost uncorrelated between the two horizontal directions. For example, considering a RC frame in which collapse is fully "ductile" and plastic hinges are located only in the beam elements and not in the column elements, the collapse domain is essentially a rectangle and consequently the orientation of a polarized record affects results also in terms of reliability. In this cases Sa_{RotD50} seems to be the best indication of bidirectional demands. In fact, even if some engineers believe that $Sa_{RotD100}$ is more meaningful for structural design, it can lead to conservative estimates of structural demand (e.g., Stewart et al. 2011) because of the characteristics of standard structures, in which the real *D/C* ratio depends on the relative orientation of the signal to the capacity domain. Seismic isolation has instead an almost isotropic response (is almost the only real bi-directional systems) but also an isotropic capacity because, for example, maximum shear deformation of rubber bearings can be attained in every direction regardless the orientation of the record. In this case collapse domain is represented by a circle. Isolation system is then characterised by a hidden vulnerability respect to RC structures that could be represented by the lower area of the domain in the horizontal plane (ratio between circle squared shape, correlated to the ratio of the areas $\pi/4$). This is also the case of an hybrid isolated system where flat sliders with squared shape plates have the same displacement collapse capacity of rubber bearings. The latter have the same capacity in all directions while the formers have an increased displacement capacity in diagonal direction due to their shape. Seen in a different light, seismic response of isolated building has a lower variability because it is not dependent on the signal orientation, so results are more reliable. Therefore, for seismically isolated buildings, $Sa_{RotD100}$ is the best indicator of bidirectional demand (Grant 2011).

In this case, as capacity is equal in all directions, the correct D/C ratio is based on the use of $Sa_{RotD100}$ as measure of the demand.

Sa_{Larger} and Sa_{GM} are instead orientation-dependent *IMs* that are not good predictors of the structural response for three-dimensional models. Moreover, Sa_{GM} introduces an extra scatter in the results (Baker and Cornell 2006) essentially because its definition is far from any definition of the structural capacity (geometric mean of the two direction values).

5.3 Seismic Hazard comparison

Having discussed the differences of the *IMs*, a first comparison between the three *GMPEs* can be carried out directly on hazard curves. They have been computed using Reassess v.2.0 software (Chioccarelli et al. 2018), for L'Aquila site and coil type C (Vs30 300m/s) and the seismogenic zones from the embedded database of Meletti et al. (2008) - Magnitude rates from Barani et al. (2009), for the three *GMPEs*. Figure 92 shows a comparison between the hazard curves of Ambraseys et al. (1996) and Akkar and Bommer (2010).

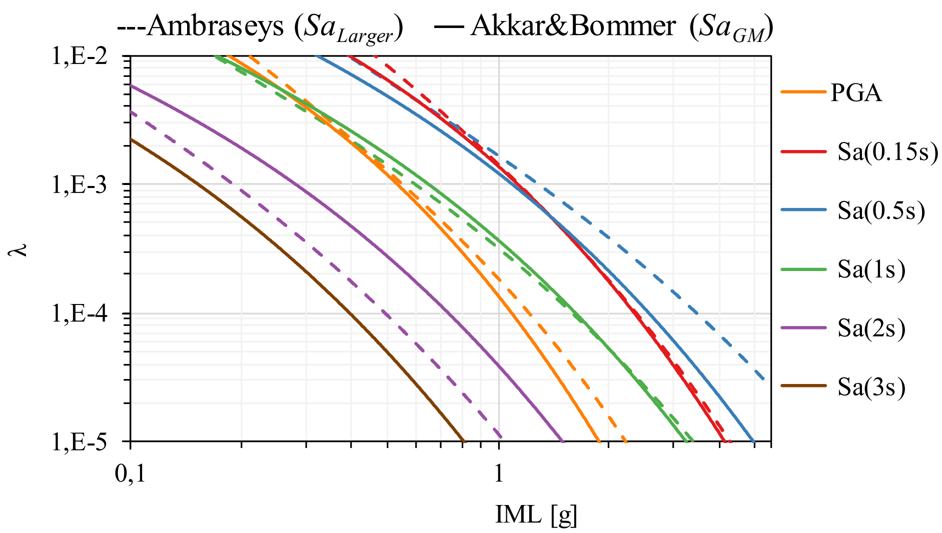

Figure 92. Hazard curves of L'Aquila site for Ambraseys et al. (1996) [Sa_{Larger}] and Akkar and Bommer (2010) [Sa_{GM}].

The first shortcoming highlighted in the figure is that for T=2s (the maximum for Ambraseys) the hazard curve for Ambraseys is significantly lower than the one of Akkar and Bommer, in contrast with the prevision of the ratio Sa_{Larger}/Sa_{GM} >1, while it is almost in line for all the lower periods. This suggests an overestimation of the hazard of Akkar and Bommer with respect to Ambraseys especially for periods higher than 2s, exactly the range of isolated structures.

Figure 93 instead shows the comparison between the hazard curves of Ambraseys et al. (1996) and Lanzano (2019).

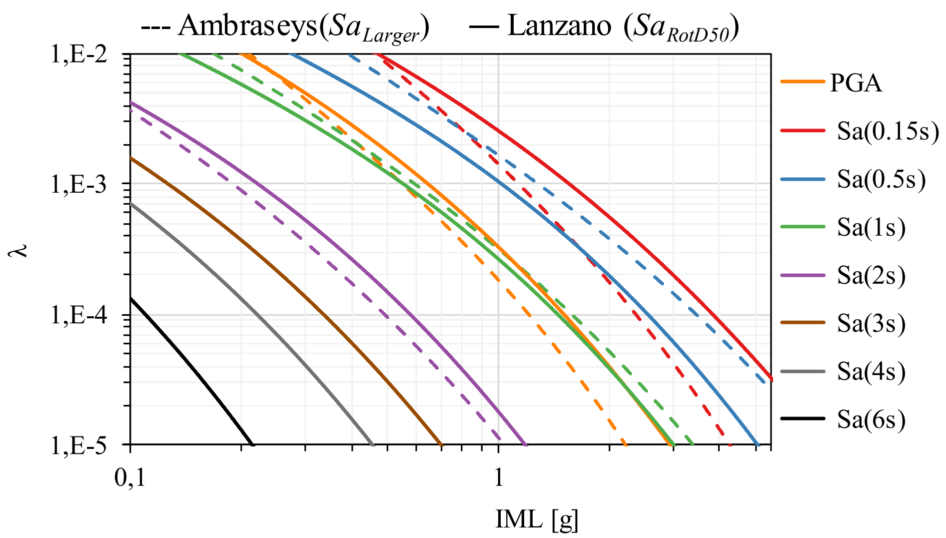

Figure 93. Hazard curves of L'Aquila site for Lanzano et al. (2019) [Sa_{RotD50}] *and Akkar and Bommer (2010)* [Sa_{GM}].

Also in this case the hazard curves do not comply with Sa_{Larger}/Sa_{RotD50} >1, especially for T=0.15s, but for T=2s the difference is lower than the case of Akkar and Bommer. This suggests another time an overestimation of the hazard of Lanzano with respect to Ambraseys for the range of isolated structures, but with lower values. The same comparison can be carried out on the *UHS* computed for the three *GMPEs*. Figure 94 better highlights the different trends of the *UHSs*. Compared to Ambraseys, Lanzano overestimates the hazard for lower periods and higher return periods (*Tr*) whereas Akkar and Bommer strongly overestimates the hazard especially in the range of T>1s.

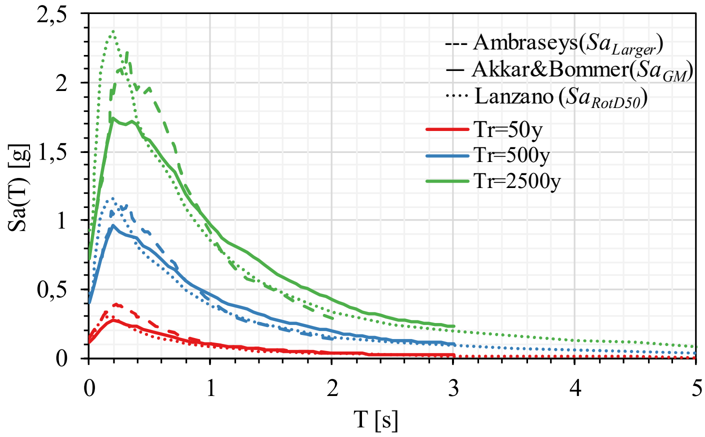

Figure 94. UHS comparison for L'Aquila site

Theoretically, it is possible to convert the hazard curves and also directly the *GMPEs* for different horizontal-component definitions (Beyer and Bommer, 2006) using mean and standard deviation of the ratios between *IMs* (Shashi and Baker 2014, Boore and Kishida 2017, Baker and Bradley 2017) but this would not lead to a better assessment of the hazard comparison because of limitation of range period for Ambraseys (T<2s) that is lower than isolation periods, so a direct comparison at T=3s is not feasible.

5.4 Record selection

A new record selection has been carried out based on the results of the hazard assessment previously described using the new *GMPE* of Lanzano et al. (2019) for both sites of L'Aquila and Naples. Hazard curves for the two sites are reported in Figure 95 and Figure 96.

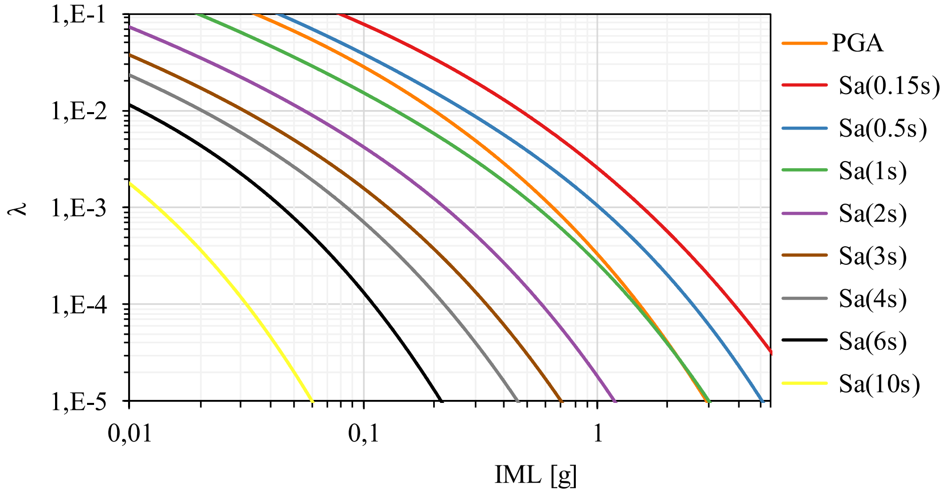

Figure 95. Hazard curves for L'Aquila site using GMPE of Lanzano et al. (2018)

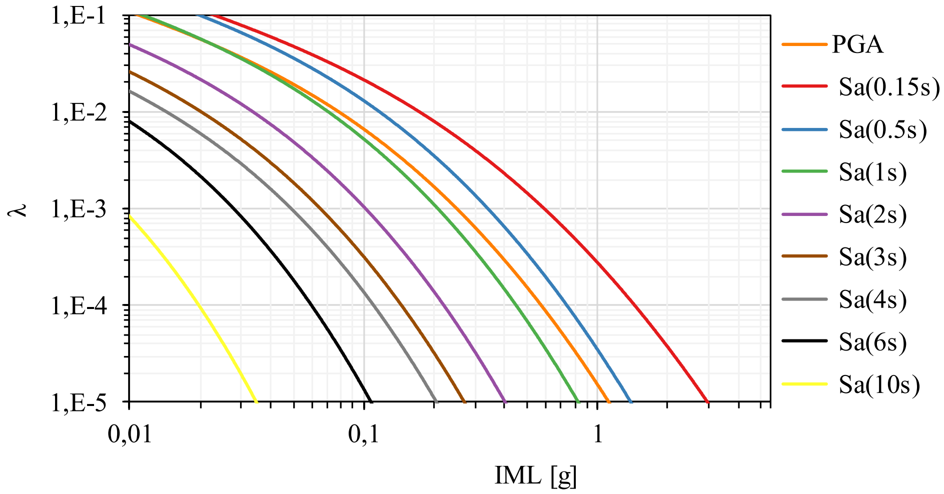

Figure 96. Hazard curves for Naples site using GMPE of Lanzano et al. (2018)

Record selection is another time based on *conditional spectrum* (*CS*) method proposed by Lin et al. (2013a), adapting the last version of the algorithm for selecting ground motions of Baker and Lee (2018). In this case the post-processing procedure (Spillatura 2018) for magnitude-distance disaggregation consistency of selected records is not performed. Therefore, the procedure is almost the same reported in Chpt. 3.4 except for point (*e*). Another difference is that in this case the selected records were extracted from *ESM* database (*European strong motion database*, Luzi, et al., 2016; Luzi, Puglia, Russo, and ORFEUS WG5, 2016).

It is worth to note that the working dataset used by Lanzano et al. (2019) for the *GMPE* is extracted from the flatfile (Lanzano et al., 2018), derived from the same *ESM* database. Consequently, in this case there is coherency between the dataset of the *GMPE* and the record selection.

The results from Reassess v.2.0 software (Chioccarelli et al. 2018), in terms of conditional spectra, have been used as target for the record selection. An automatic procedure to download the record signals has been implemented using web-services from the *ESM* site. In this way, a set of 200 ground motions (two horizontal components and vertical component) has been defined for the two sites. In both sites the conditioning period is T=3s. Scaling of the seed motions was done only in amplitude with a maximum scale factor of 5, except for the higher *IML* for L'Aquila, where there are not enough records in the *ESM* database; in this case a limit of 10 has been used, as in Chpt. 3.4 . It is worth to note that in this procedure it is possible to convert hazard results from Sa_{RotD50} to $Sa_{RotD100}$ according to Shahi and Baker (2014) and to select the records using the latter *IM*. A future work will assess the difference in the use of these two *IMs* on the final reliability results.

The selected record spectra for all the 10 *IMLs* and the hazard disaggregation are reported hereafter, where *IMLs* correspond to the following return periods T_R = {10y; 50y; 100y; 250y; 500y; 1000y; 2500y; 5000y; 10000y; 100000y}. More in detail, reported are the 5%-damped response spectra of the 20 scaled ground motions for each *IML*, their mean values (green crosses) and the mean values ± two standard deviations (mean ± 2σ, green circles). The graphs also show the target *CMS* and the *CMS* ± *2σ*. The quality of the selection can be evaluated as the closeness of record selection statistic values (green markers) with the respective targets (red lines).

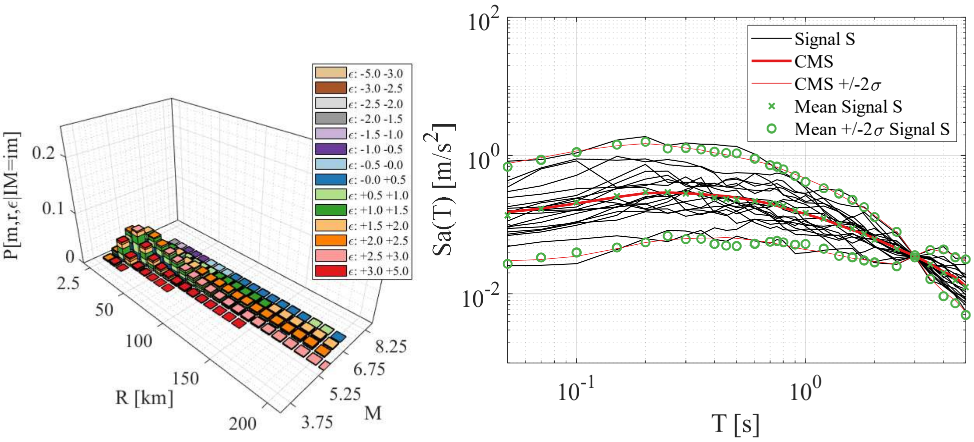

Figure 97. Hazard Disaggregation, spectra of scaled motions and conditional spectra for L'Aquila site IML1

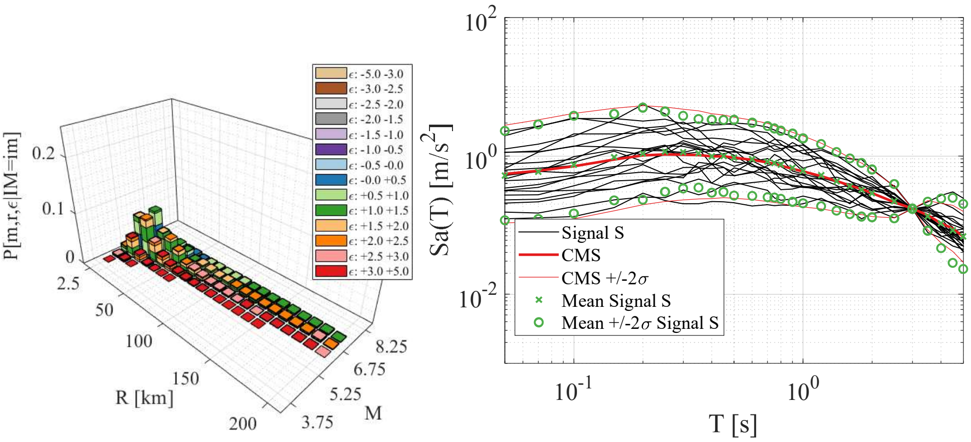

Figure 98. Hazard Disaggregation, spectra of scaled motions and conditional spectra for L'Aquila site IML2

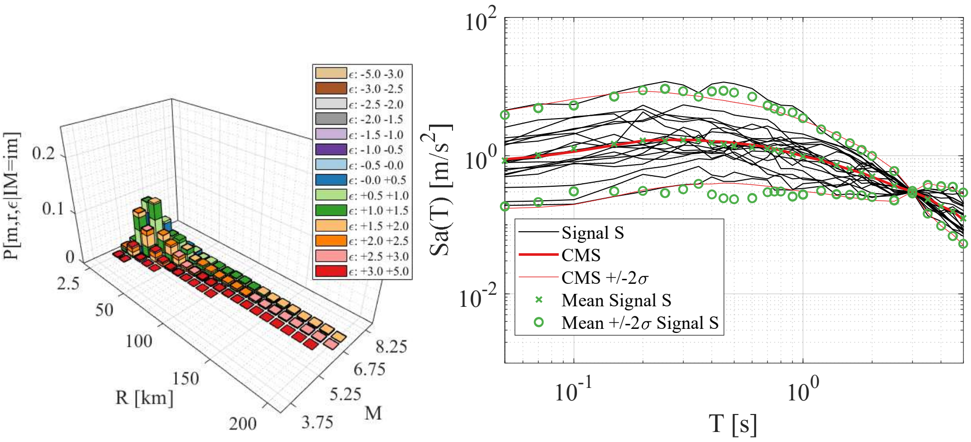

Figure 99. Hazard Disaggregation, spectra of scaled motions and conditional spectra for L'Aquila site IML3

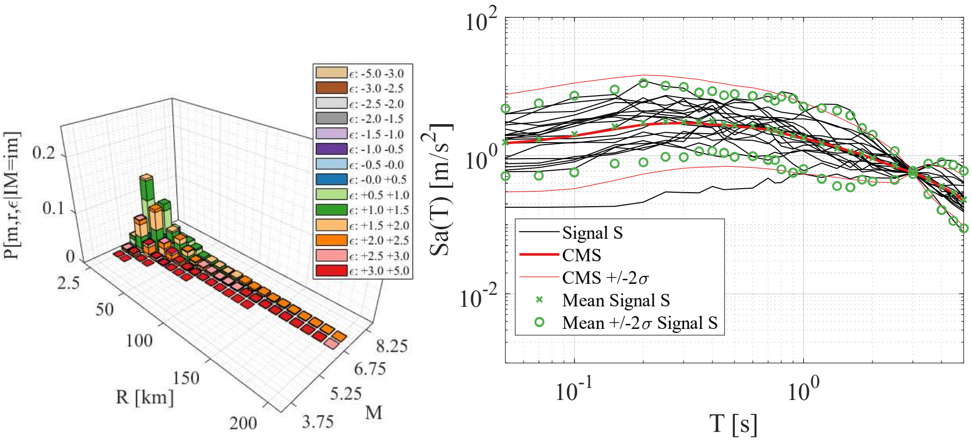

Figure 100. Hazard Disaggregation, spectra of scaled motions and conditional spectra for L'Aquila site IML4

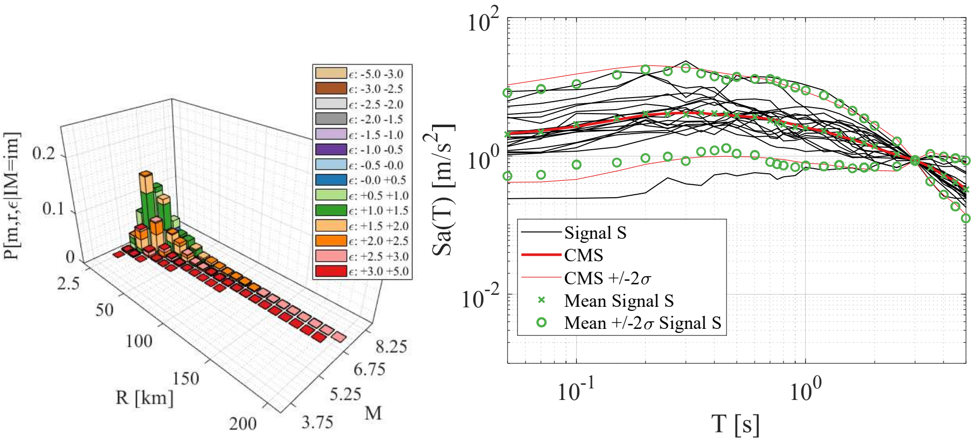

Figure 101. Hazard Disaggregation, spectra of scaled motions and conditional spectra for L'Aquila site IML5

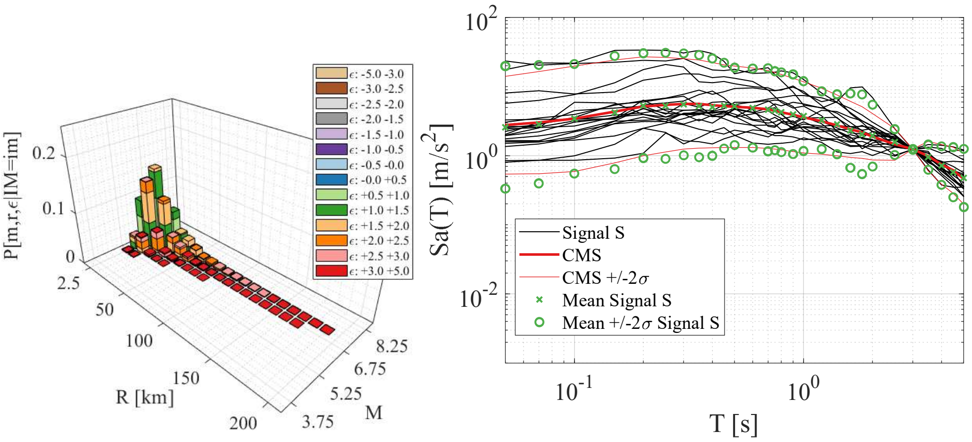

Figure 102. Hazard Disaggregation, spectra of scaled motions and conditional spectra for L'Aquila site IML6

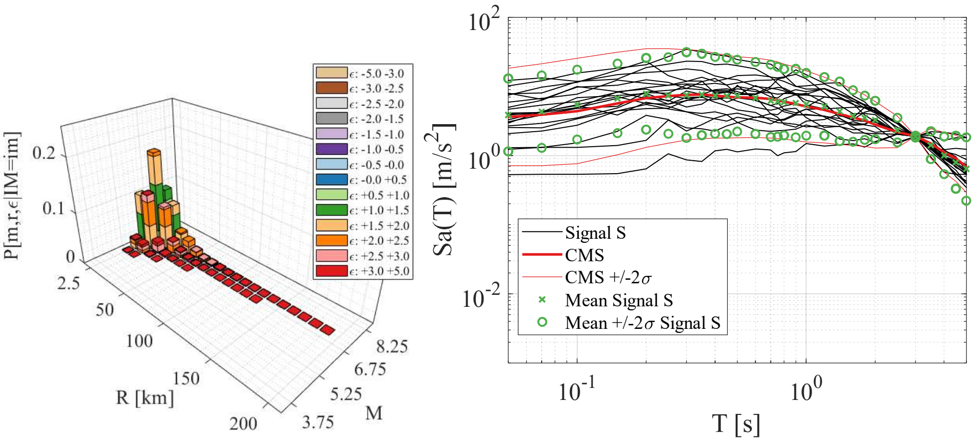

Figure 103. Hazard Disaggregation, spectra of scaled motions and conditional spectra for L'Aquila site IML7

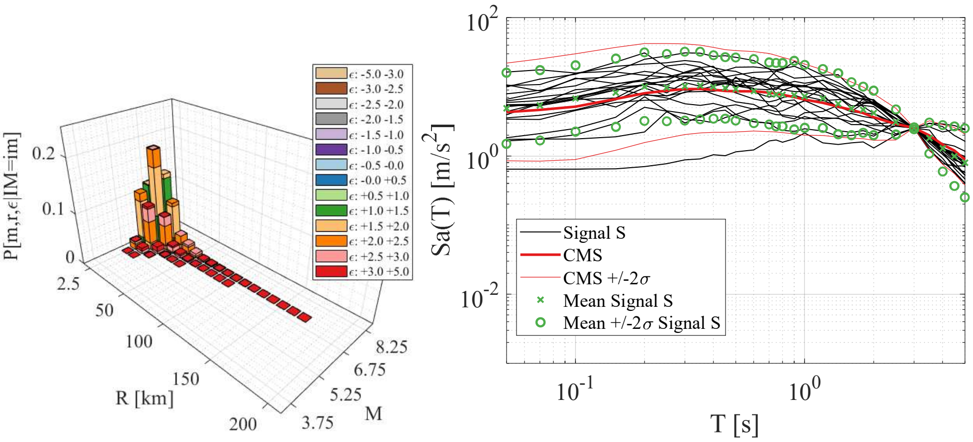

Figure 104. Hazard Disaggregation, spectra of scaled motions and conditional spectra for L'Aquila site IML8

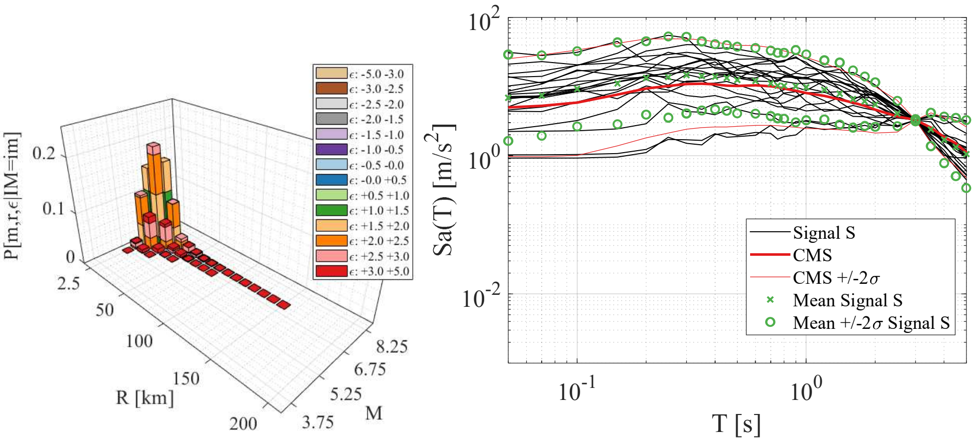

Figure 105. Hazard Disaggregation, spectra of scaled motions and conditional spectra for L'Aquila site IML9

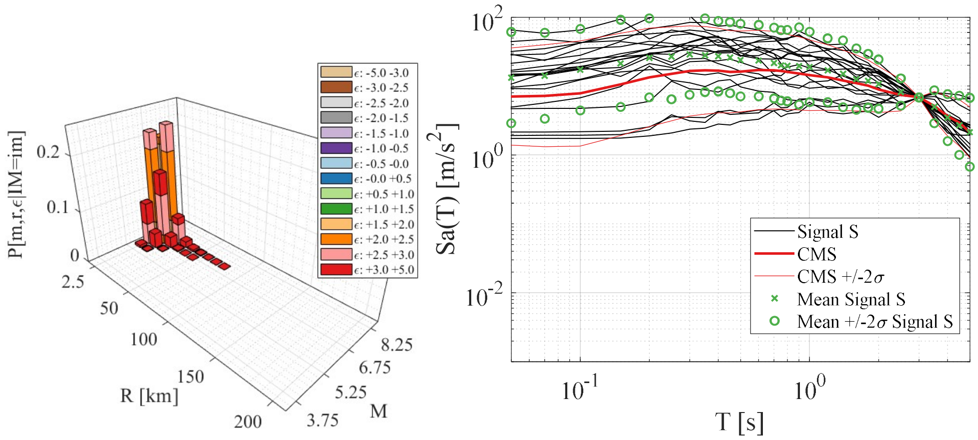

Figure 106. Hazard Disaggregation, spectra of scaled motions and conditional spectra for L'Aquila site IML10

It noteworthy that the quality of the record selection is lower for higher *IMLs* because the records suitable for very large seismic intensity are fewer, but error is significant only in the range of very small periods of vibration (T<0.5s) and on safety side (mean values are higher than target values).

To make a quantitative evaluation of the "hazard consistency" of the selected ground motions response spectra at an arbitrary period *T*, the rate of exceedance of *Sa*(*T*) implied by the ground motions selected conditional on *Sa*(*T**) can be computed by using the following equation (Lin et al. 2013a, NIST 2011, as reported in Kitayama and Constantinou 2019):

$$\lambda(Sa(T) > y) = \sum_{i=1}^{n} P(Sa(T) > y \mid Sa(T^*) = x_i)\lambda_{IM}(Sa(T^*) = x_i) \qquad (5\text{-}1)$$

In this equation, n is the number of considered $Sa(T^*)$ amplitudes (i.e. the number of *IMLs*, 10 in this work) and $P(Sa(T)>y|Sa(T^*)=x_i)$ is the probability that a ground motion selected and scaled to have $Sa(T^*)=x_i$ has a spectral acceleration at period T that is greater than y. This probability was estimated as the fraction of the 20 ground motions with $Sa(T^*)=x_i$ that have $Sa(T) > y$. The calculated rate of exceedance $\lambda(Sa(T) > y)$ is compared with the seismic hazard curve. Note that $Sa(T^*)=x_i$ is the rate of observing $Sa(T^*)$ amplitudes in a small range represented by the discrete amplitude x_i and it is computed from seismic hazard curve using finite differences:

$$\left(Sa\left(T^*\right)=x_i\right)=0.5\left\{\left(Sa\left(T^*\right)>x_{i-1}\right)\left(Sa\left(T^*\right)>x_{i+1}\right)\right\} \qquad (5\text{-}2)$$

In this case T^* is 3s, while other periods assessed are 0.5, 1 and 5s, to consider a wide range of possible periods of interest for isolated structure.

It is recalled that superstructure yielding does not significantly change the fundamental frequency of the overall isolated structural system (Kikuchi et al. 2008) and so it is not affected by the lengthening of the period.

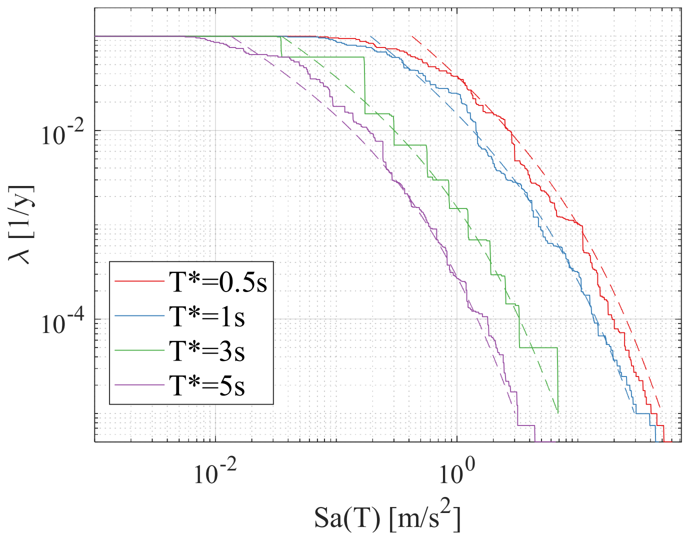

Figure 107. Comparison of calculated mean annual frequency rates based on selected ground motions (solid lines) and hazard assessment for L'Aquila site

The ground motions analysed in Figure 107 are selected using $T^*=3.0$s, therefore they have a stepped plot because of the 10 discrete amplitudes that were considered when selecting motions and the fact that $P(Sa(T)>y|Sa(T^*)=x_i)$, when $T=T^*$, is equal to either 0 when $y < x$ or 1 when $y > x$. Ground motions with other T^* values have smoother curves (Lin et al. 2013a).

If a selected ground motion does not satisfy hazard consistency criteria, the selection process can be repeated, for example, relaxing some parameters of the record selection or using different record databases. The same results are reported for the site of Naples.

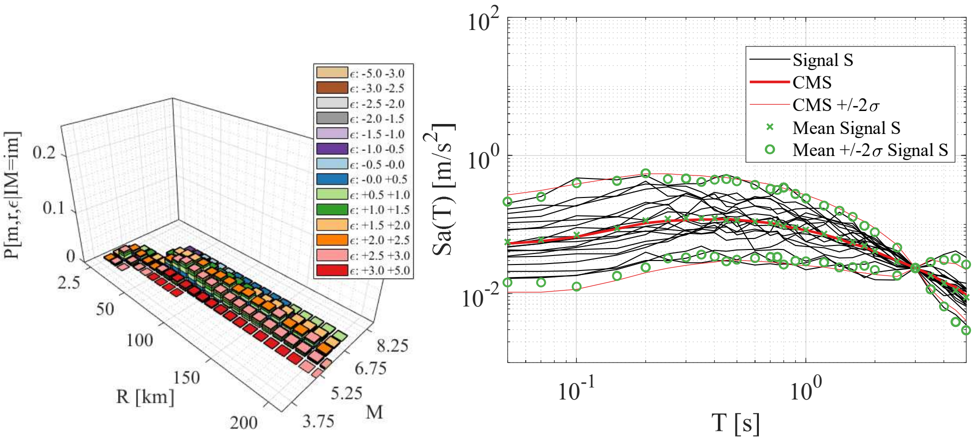

Figure 108. Hazard Disaggregation, spectra of scaled motions and conditional spectra for Naples site IML1

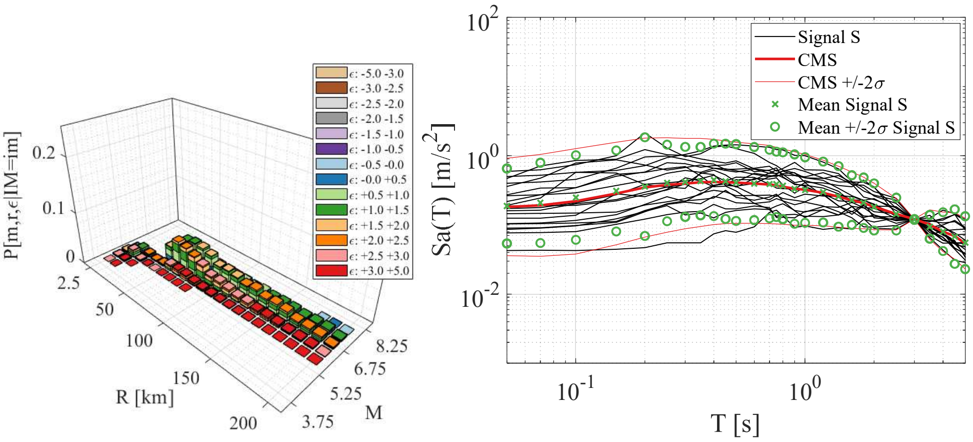

Figure 109. Hazard Disaggregation, spectra of scaled motions and conditional spectra for Naples site IML2

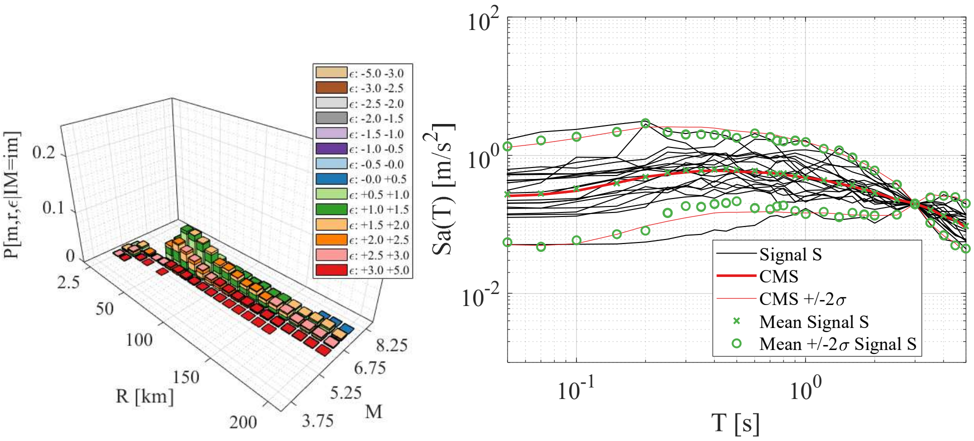

Figure 110. Hazard Disaggregation, spectra of scaled motions and conditional spectra for Naples site IML3

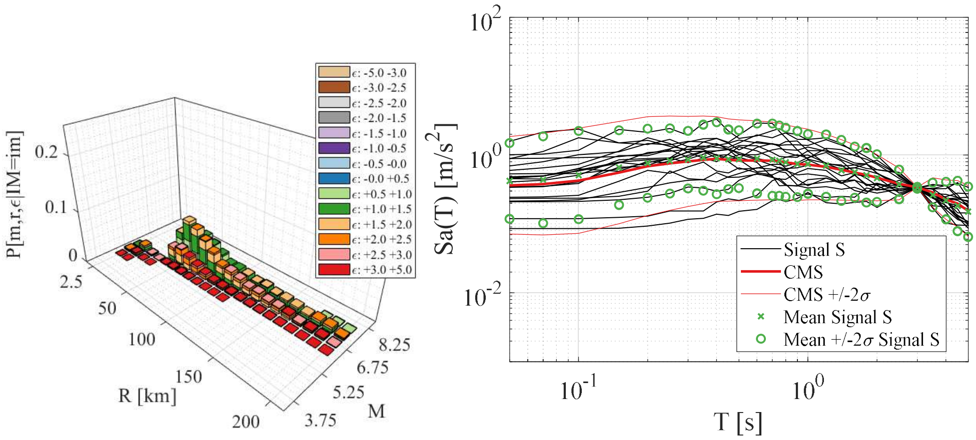

Figure 111. Hazard Disaggregation, spectra of scaled motions and conditional spectra for Naples site IML4

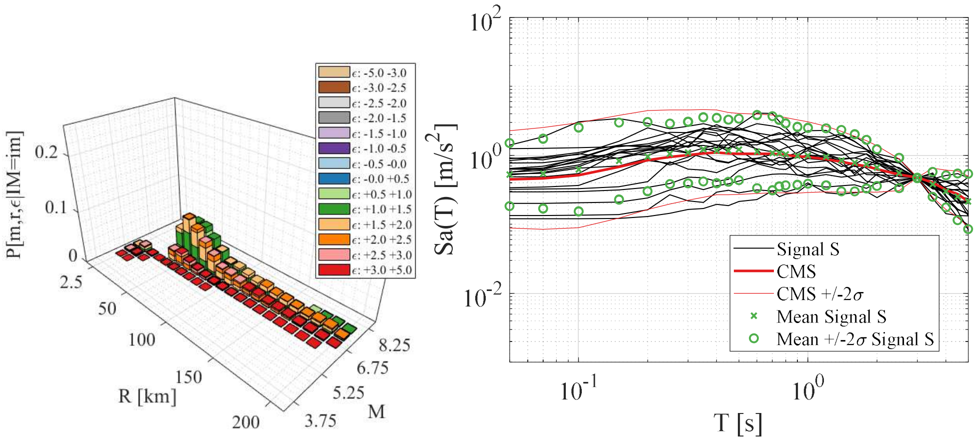

Figure 112. Hazard Disaggregation, spectra of scaled motions and conditional spectra for Naples site IML5

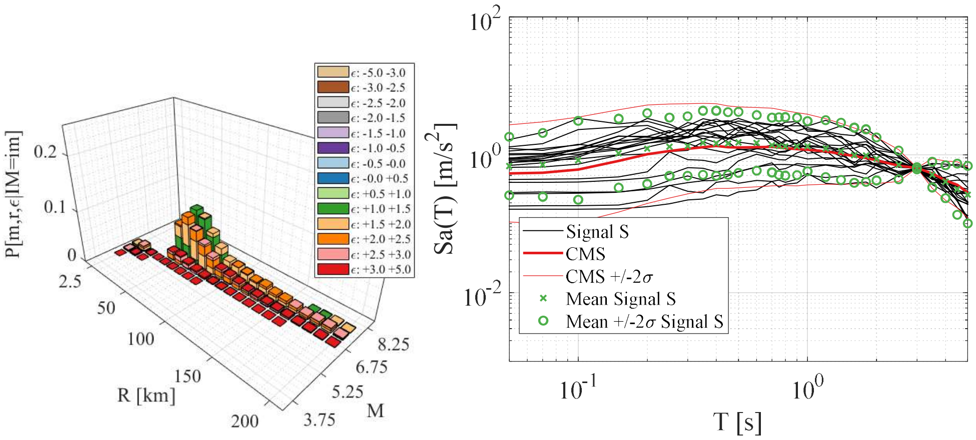

Figure 113. Hazard Disaggregation, spectra of scaled motions and conditional spectra for Naples site IML6

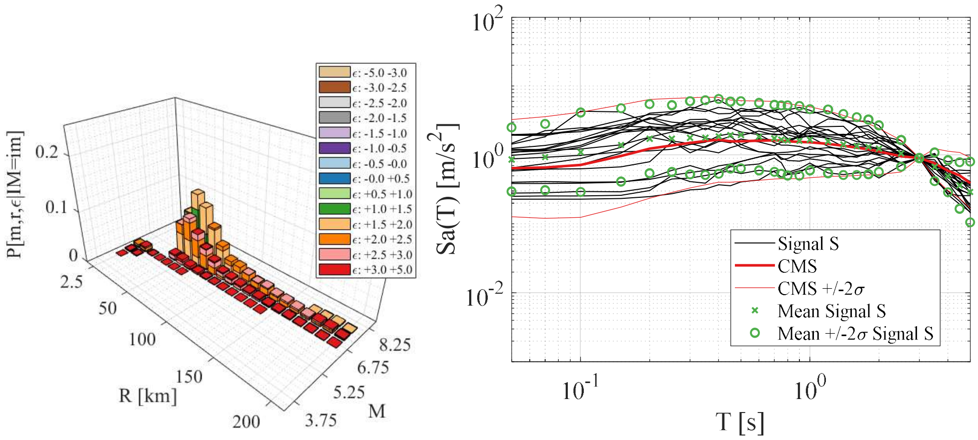

Figure 114. Hazard Disaggregation, spectra of scaled motions and conditional spectra for Naples site IML7

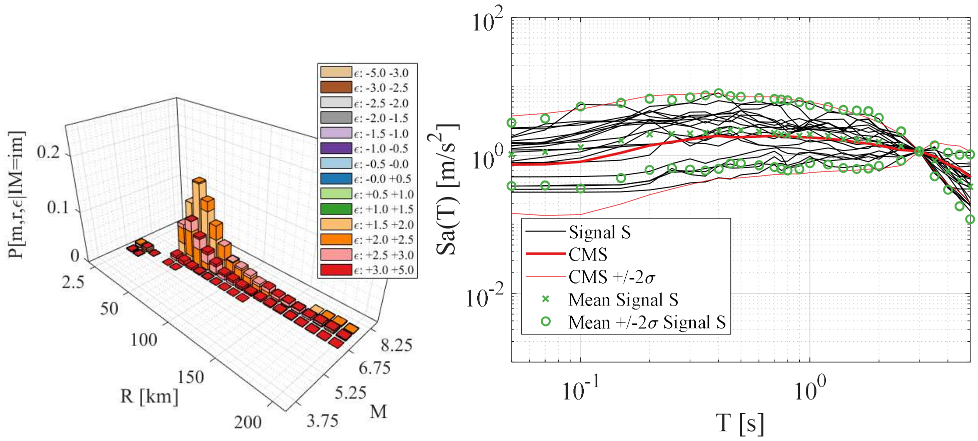

Figure 115. Hazard Disaggregation, spectra of scaled motions and conditional spectra for Naples site IML8

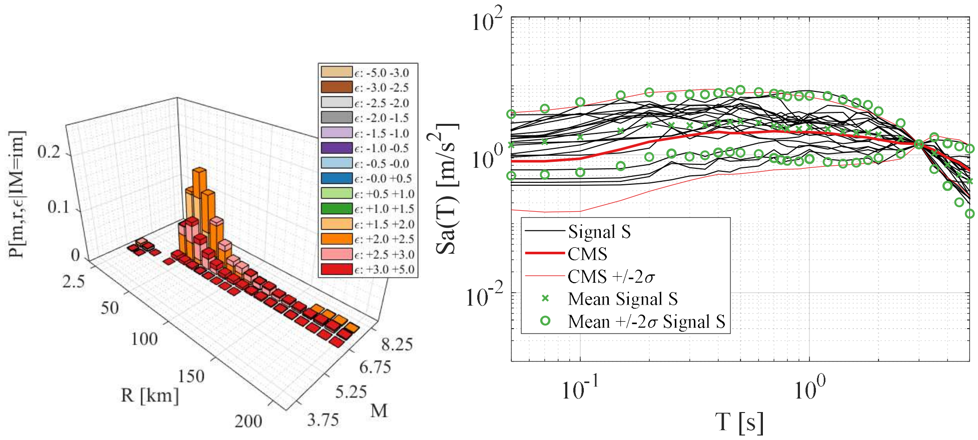

Figure 116. Hazard Disaggregation, spectra of scaled motions and conditional spectra for Naples site IML9

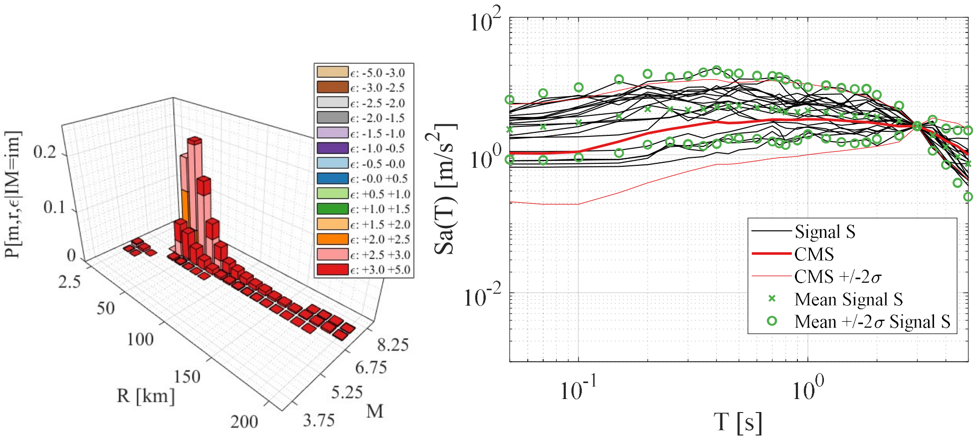

Figure 117. Hazard Disaggregation, spectra of scaled motions and conditional spectra for Naples site IML10

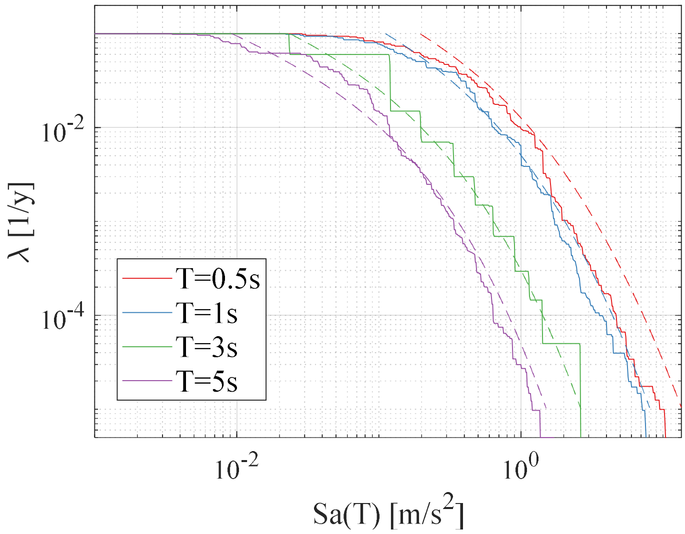

Figure 118. Comparison of calculated mean annual frequency rates based on selected ground motions (solid lines) and hazard assessment for Naples site

5.5 Results for Lanzano et al. GMPE

In this chapter the results for the two case studies presented before (*Ki-n-A HDRB*, and *Ki-n-N HDRB*) are reported. They have been analysed using the new record selection carried out. *GC* failures and *UPD* failures for each *IML* of L'Aquila site are reported in Figure 119 and Figure 120. As expected, number of collapses are strongly reduced with the new record selection based on the hazard calculated with *GMPE* of Lanzano et al. 2019 respect to the same case study analysed with the record based on Akkar and Bommer (2010) *GMPE* (Figure 79a). In this case first collapses occur only at *IML* 8 and reach the maximum number only at *IML*10. Shear breaking (deformation limit equal to 3.5) is also in this case the main collapse mechanism.

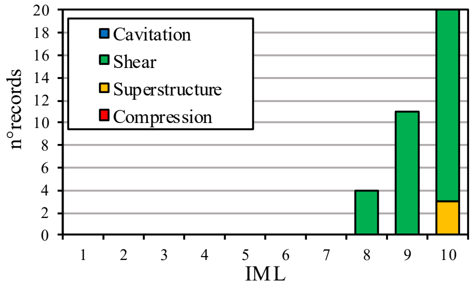

Figure 119. Global collapse results for Ki-n-A HDRB analysed using the new record selection (GMPE Lanzano et al. 2019)

UPD failures, showed in Figure 120 are also reduced compared to the equivalent results for the older hazard assessment (Figure 80).

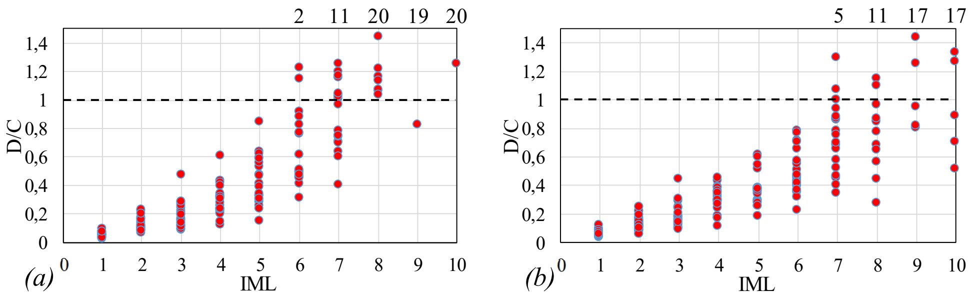

Figure 120. Displacement D/C ratio of the superstructure (UPD) for Ki-n-A HDRB analysed using the new record selection (GMPE Lanzano et al. 2019): (a) X direction and (b) Y direction

Also for Naples case (*Ki-n-N HDRB*) the number of failures in terms of *GC* (Figure 121) and *UPD* (Figure 122) are reduced respect to the equivalent results previously reported (Figure 84 and Figure 85). With the new record selection, failures are registered only for the higher *IML*10 (T_r=100000y) for both the performance indicators.

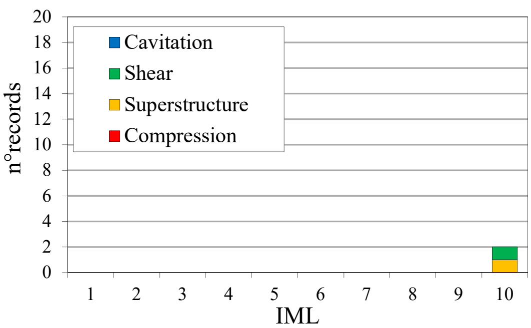

Figure 121. Global collapse results for Ki-n-N HDRB analysed using the new record selection (GMPE Lanzano et al. 2019)

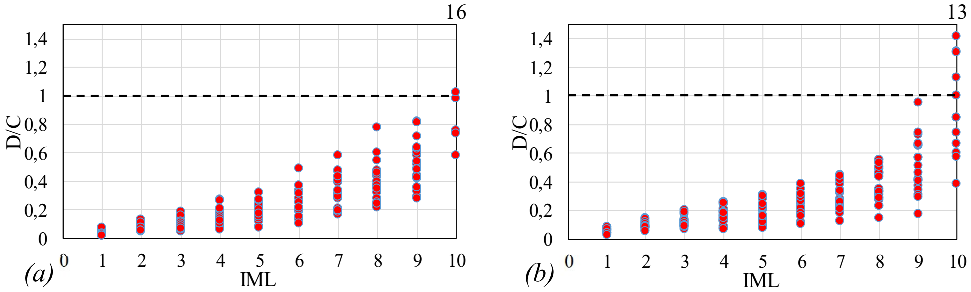

Figure 122. Displacement D/C ratio of the superstructure (UPD) for Ki-n-N HDRB analysed using the new record selection (GMPE Lanzano et al. 2019): (a) X direction and (b) Y direction

These new results can be used to calculate new annual rate of failures λ_f for both the performance levels using the method exposed in Chpt. 2.2.2 and to compare them with the previous ones. In Figure 123 and Figure 124 rates calculated with the hazard based on *GMPE* of Akkar and Bommer (2010) are the same reported in Figure 88 and Figure 89 respectively. The new annual rate of failures for case study recomputed with the new *GMPE* of Lanzano et al. (2019) are strongly reduced in terms of *GC* for both sites respect to the equivalent previous values (highlighted inside dash-dotted area). Moreover, reliability levels are in compliance with the code target for both sites and similar to safety levels of new RC structures.

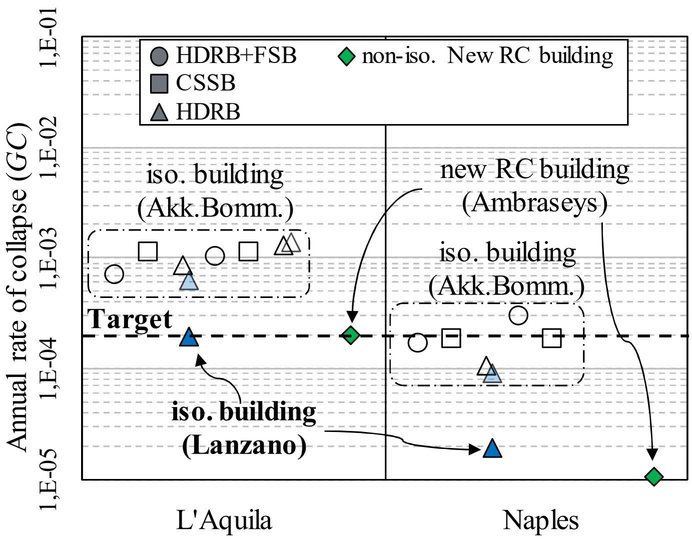

Figure 123. Annual rate of collapse (GC) for the different case studies

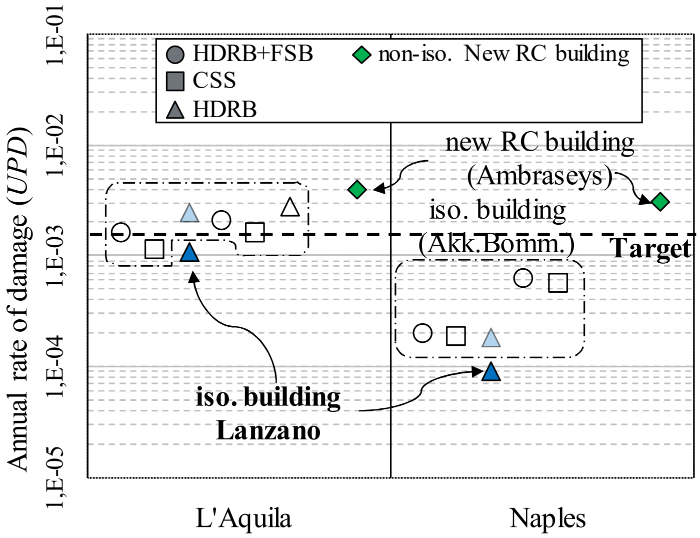

Figure 124. Annual rate of damage (UPD) for the different case studies

In terms of *UPD* the reduction is instead limited, as shown in Figure 124. A possible reason may be found in the different reduction of hazard for different periods: *GC* is mainly related to shear collapse of isolators (see Figure 79a) and therefore associated mainly to the hazard at the isolation period. On the contrary, *UPD* is related to superstructure displacement demand that is affected also by higher modes. As hazard derived from Lanzano seems to be higher than the one of Akkar and Bommer for T<0.5s and lower for T>0.5s (see Figure 94), the change of *GMPE* could affect in different way the range of periods and consequently *GC* and *UPD* performance levels.

5.6 Comparison of hazard curves computed from record sets

As final assessment on the effect of *GMPE* on record selection and reliability results, a quantitative evaluation of the hazard difference between the three sets of selected records is carried out computing the rates of exceedance *Sa*(*T*) by using the same equation (5-1). This is an innovative extension of the purpose of this computation because, instead of assessing set of records conditioned on different *T** (Lin et al. 2013a, NIST 2011), three sets of records with different *T** and different hazards (different *GMPE*) are compared, switching from an *IM* to another.

Figure 125 compares the rates of exceedance of $Sa_{RotD50}(T)$ for T = {0.15, 0.5, 1.0, 2.0, 3.0, 5.0}. Only the curve of Lanzano at *T*=3s is stepped (Figure

125e). It is worth to note that for $T \geq 2$s (Figure 125d e and f) the hazard of Ambraseys is the lowest of the three sets of records, the one of Akkar and Bommer is the higher and Lanzano is in the middle; for T=0.5s and T=1s they are almost the same (Figure 125b and c) whereas, for the lowest period there is a great deviation of Ambraseys (maybe related to the relationship between Sa_{Larger} used by Ambraseys and Sa_{RotD50} used as *IM* for the computation of the rates). The curves confirm that Akkar and Bommer strongly overestimates hazard respect to Lanzano and Ambraseys especially for higher periods. Even lower annual rates of collapse respect to the one calculated are expected for isolated structures using a hazard consistent with the one of Ambraseys.

Regarding equivalent new RC structure results, through this assessment it is expected an increasing of the annual rate of failure for taller buildings using the new *GMPE* of Lanzano. In fact, because of the shifting of periods during the plastic phase, the fundamental period of fixed buildings may increase up to $T \geq 2$s, a range where Lanzano is higher than Ambraseys. For low rise building instead also in the plastic phase the period may be around 1s and consequently in this case no major differences are expected. The same assessment has been carried out also using $Sa_{RotD100}$ (Figure 126), as this one is considered the best *IM* for isolated structures, and it show similar trends.

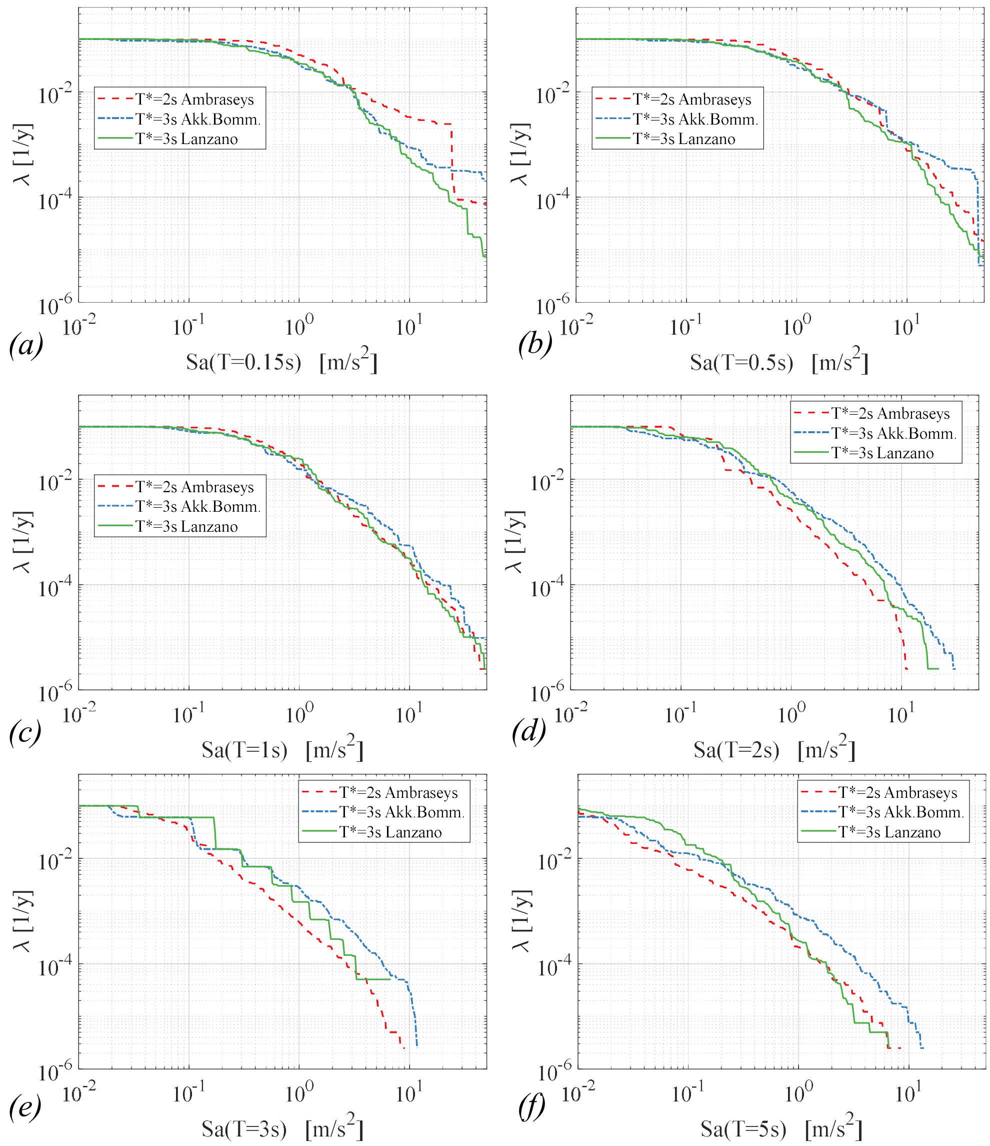

Figure 125. Rate of exceedance (hazard curves) computed for the site of L'Aquila from the sets of records for:(a) Sa(T=0.15)>y, (b) Sa(T=0.5)>y, (c) Sa(T=1.0)>y, (d) Sa(T=2.0)>y, (e) Sa(T=3.0)>y, (f) Sa(T=5.0)>y. (Sa = SaRotD50)

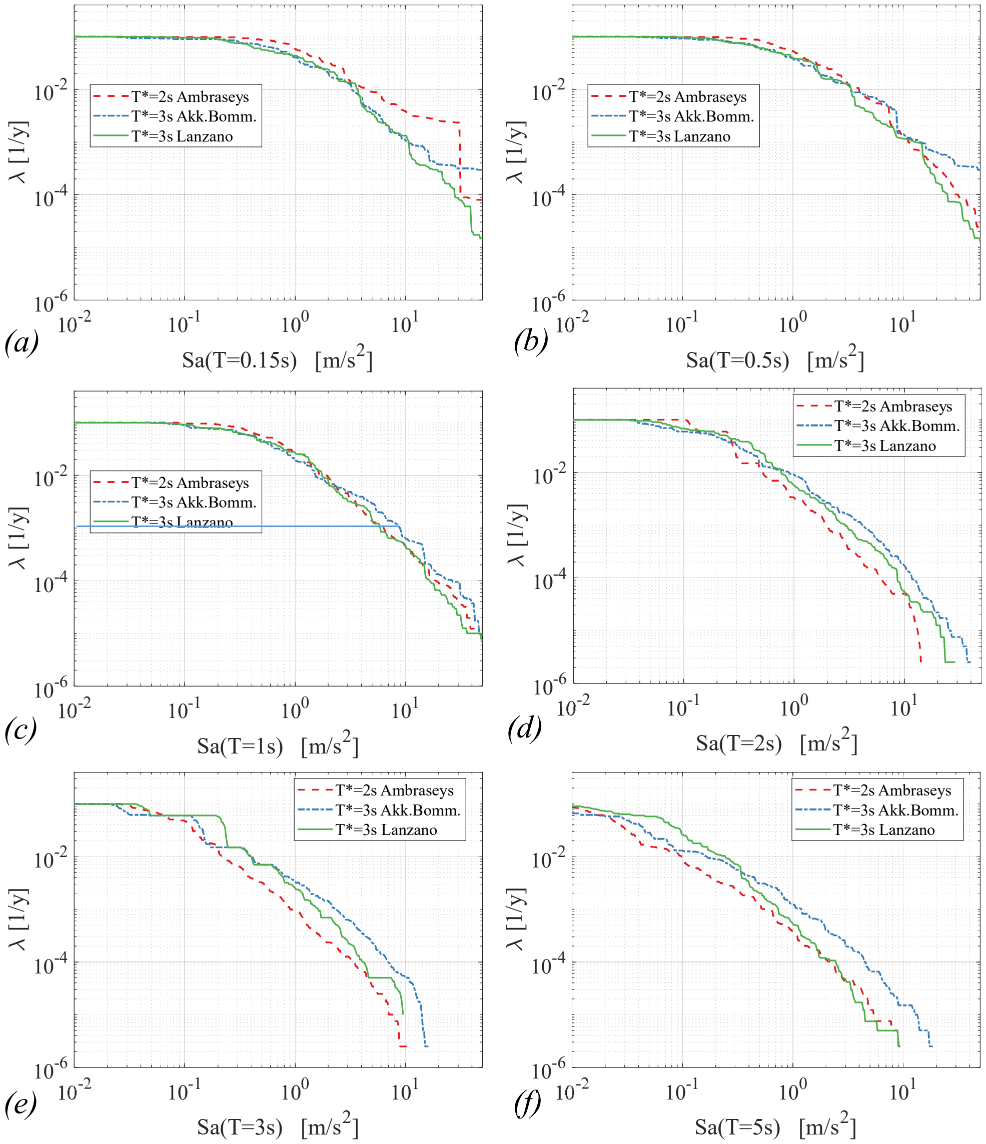

Figure 126. Rate of exceedance (hazard curves) computed for the site of L'Aquila from the sets of records for:(a) Sa(T=0.15)>y, (b) Sa(T=0.5)>y, (c) Sa(T=1.0)>y, (d) Sa(T=2.0)>y, (e) Sa(T=3.0)>y, (f) Sa(T=5.0)>y. (Sa = SaRotD100)

5.7 Chapter's references

AIJ Architectural Institute of Japan Editor (2012), "Preliminary Reconnaissance Report of the 2011 Tohoku-Chiho Taiheiyo-Oki Earthquake" DOI 10.1007/978-4-431-54097-7

Akkar, S., Bommer, J.J., 2010. Empirical Equations for the Prediction of PGA, PGV, and Spectral Accelerations in Europe, the Mediterranean Region, and the Middle East. Seismological Research Letters 81, 195–206. https://doi.org/10.1785/gssrl.81.2.195

Ambraseys, N.N., Simpson', K.A., Bommer', J.J., 1996. PREDICTION OF HORIZONTAL RESPONSE SPECTRA IN EUROPE. Earthquake Engineering & Structural Dynamics 25, 371–400. doi:10.1002/(SICI)1096-9845(199604)25:4<371::AID-EQE550>3.0.CO;2-A.

Baker, J.W., 2011. Conditional Mean Spectrum: Tool for Ground-Motion Selection. J. Struct. Eng. 137, 322–331. https://doi.org/10.1061/(ASCE)ST.1943-541X.0000215

Baker, J.W., Bradley, B.A., 2017. Intensity Measure Correlations Observed in the NGA-West2 Database, and Dependence of Correlations on Rupture and Site Parameters. Earthquake Spectra 33, 145–156. https://doi.org/10.1193/060716EQS095M

Baker, J.W., Cornell, C.A., 2006. Which Spectral Acceleration Are You Using. Earthquake Spectra, Volume 22, No. 2, pages 293–312. Earthquake Engineering Research Institute https://doi.org/10.1193/1.2191540

Baker, J.W., Cornell, C.A., 2006. Which Spectral Acceleration Are You Using. https://doi.org/10.1193/1.2191540

Baker, J.W., Lee, C., 2018. An Improved Algorithm for Selecting Ground Motions to Match a Conditional Spectrum. Journal of Earthquake Engineering 22, 708–723. https://doi.org/10.1080/13632469.2016.1264334

Beyer, K., Bommer, J.J., 2007. Selection and Scaling of Real Accelerograms for Bi-Directional Loading: A Review of Current Practice and Code Provisions. Journal of Earthquake Engineering 11, 13–45. https://doi.org/10.1080/13632460701280013

Bindi, D., F. Pacor, L. Luzi, R. Puglia, M. Massa, G. Ameri, and R. Paolucci. 2011. Ground motion prediction equations derived from the Italian strong-motion database, Bull. Earthq. Eng. 9, 1899–1920.

Boore, D.M., 2006. Orientation-Independent Measures of Ground Motion. Bulletin of the Seismological Society of America 96, 1502–1511. https://doi.org/10.1785/0120050209

Boore, D.M., 2010. Orientation-Independent, Nongeometric-Mean Measures of Seismic Intensity from Two Horizontal Components of MotionShort Note. Bulletin of the Seismological Society of America 100, 1830–1835. https://doi.org/10.1785/0120090400

Boore, D.M., Kishida, T., 2017. Relations between Some Horizontal-Component Ground-Motion Intensity Measures Used in Practice. Bulletin of the Seismological Society of America 107, 334–343. https://doi.org/10.1785/0120160250

BS ISO 22762-2:2018 Elastomeric seismic-protection isolators — Part 2: Applications for bridges — Specifications, 2018.

Chioccarelli, E., Cito, P., Iervolino, I., Giorgio, M., 2018. REASSESS V2.0: software for single- and multi-site probabilistic seismic hazard analysis. Bulletin of Earthquake Engineering 17, 1769–1793. https://doi.org/10.1007/s10518-018-00531-x

Clough & Penzien. Dynamics of structures

CS.LL.PP. 2008. Norme tecniche per le costruzioni," Gazzetta Ufficiale della Repubblica Italiana 29. (In Italian.)

CS.LL.PP. 2018. Aggiornamento delle norme tecniche per le costruzioni," Gazzetta Ufficiale della Repubblica Italiana 42. (In Italian.)

Dai, Z., Li, X., Hou, C., 2014. Orientation-Independent Measures of Ground Motion Made EasyOrientation-Independent Measures of Ground Motion Made Easy. Bulletin of the Seismological Society of America 104, 1268–1275. https://doi.org/10.1785/0120130154

Grant Damian N., 2011. Response Spectral Matching of Two Horizontal Ground-Motion Components. Journal of Structural Engineering 137, 289–297. https://doi.org/10.1061/(ASCE)ST.1943-541X.0000227

Hong, H. P., and Goda, K. (2007). "Orientation-dependent ground-motionmeasure for seismic-hazard assessment." Bull. Seismol. Soc. Am., 97(5),1525–1538.

Huang, Y., Whittaker, A. S., and Luco, N. (2008a). "Maximum spectral demands in the near-fault region." Earthquake Spectra, 24(1), 319–341.

Kikuchi, M., Black, C.J., Aiken, I.D., 2008. On the response of yielding seismically isolated structures. Earthquake Engng Struct. Dyn. 37, 659–679. https://doi.org/10.1002/eqe.777

Kitayama, S., Constantinou, M.C., 2019. Probabilistic seismic performance assessment of seismically isolated buildings designed by the procedures of ASCE/SEI 7 and other enhanced criteria. Engineering Structures 179, 566–582. https://doi.org/10.1016/j.engstruct.2018.11.014

Lanzano, G., Luzi, L., Pacor, F., Felicetta, C., Puglia, R., Sgobba, S., D'Amico, M., 2019. A Revised Ground-Motion Prediction Model for Shallow Crustal Earthquakes in Italy. Bulletin of the Seismological Society of America 109, 525–540. https://doi.org/10.1785/0120180210

Lanzano, G., S. Sgobba, L. Luzi, R. Puglia, F. Pacor, C. Felicetta, M. D'Amico, F. Cotton, and D. Bindi (2018). The pan-European Engineering Strong-motion (ESM) flatfile: Compilation criteria and data statistics, Bull. Earthq. Eng. 1–22, doi: 10.1007/s10518-018- 0480-z.

Lin, T., Haselton, C.B., Baker, J.W., 2013a. Conditional spectrum-based ground motion selection. Part I: Hazard consistency for risk-based assessments. Earthquake Engineering & Structural Dynamics 42, 1847–1865. https://doi.org/10.1002/eqe.2301

Lin, T., Haselton, C.B., Baker, J.W., 2013b. Conditional spectrum-based ground motion selection. Part II: Intensity-based assessments and evaluation of alternative target spectra. Earthquake Engineering & Structural Dynamics 42, 1867–1884. https://doi.org/10.1002/eqe.2303

Luco N, Cornell CA . 2007. Structure-specific scalar intensity measures for near-source and ordinary earthquake ground motions. Earthquake Spectra; 23(2):357–392.

Luzi L, Puglia R, Russo E & ORFEUS WG5 (2016). Engineering Strong Motion Database, version 1.0. Istituto Nazionale di Geofisica e Vulcanologia, Observatories & Research Facilities for European Seismology. doi: 10.13127/ESM"

Luzi, L., R. Puglia, E. Russo, M. D'Amico, C. Felicetta, F. Pacor, G. Lanzano, U. Ceken, J. Clinton, G. Costa, et al. (2016). The engineering strong-motion database: A platform to access pan-European accelerometric data, Seismol. Res. Lett. 87, no. 4, 987–997.

MATLAB®, 2018. (R2019b), Natick, Massachusetts: The MathWorks Inc.

Meletti, C., Galadini, F., Valensise, G., Stucchi, M., Basili, R., Barba, S., Vannucci, G., Boschi, E., 2008. A seismic source zone model for the seismic hazard assessment of the Italian territory. Tectonophysics 450, 85–108. https://doi.org/10.1016/j.tecto.2008.01.003

Nishida, A., Choi, B., Yamano, H., Takada, T., 2018. Development of Seismic Countermeasures Against Cliff Edges for Enhancement of Comprehensive Safety of Nuclear Power Plants: Cliff Edges Relevant to NPP Building System, in: Volume 8: Seismic Engineering. Presented at the ASME 2018 Pressure Vessels and Piping Conference, ASME, Prague, Czech Republic, p. V008T08A028. https://doi.org/10.1115/PVP2018-85066

NIST. 2011. Selecting and scaling earthquake ground motions for performing response-history analyses, NIST GCR 11-917-15. Technical Report, prepared by the NEHRP Consultants Joint Venture for the National Institute of Standards and Technology: Gaithersburg, Maryland.

Paultre, P.. Dynamics of Structures

Shahi, S.K., Baker, J.W., 2014. NGA-West2 Models for Ground Motion Directionality. Earthquake Spectra 30, 1285–1300. https://doi.org/10.1193/040913EQS097M

Spillatura, A., 2018. From Record Selection to Risk Targeted Spectra for Risk based Assessment and Design. Ph.D. Thesis, Dipartimento di Costruzioni e Infrastrutture, Istituto Universitario degli Studi Superiori (IUSS), Pavia, Italy.

Stewart, J. P., Abrahamson, N. A., Atkinson, G. M., Baker, J., Boore, D. M., Bozorgnia, Y., Campbell, K.W., Comartin, C. D., Idriss, I. M., Lew, M., Mehrain, M., Moehle, J. P., Naeim, F., and Sabol, T. A., 2011. Representation of bi-directional ground motions for design spectra in building codes, Earthquake Spectra 27, 927–937.

Stewart, J.P., Abrahamson, N.A., Atkinson, G.M., Baker, J.W., Boore, D.M., Bozorgnia, Y., Campbell, K.W., Comartin, C.D., Idriss, I.M., Lew, M., Mehrain, M., Moehle, J.P., Naeim, F., Sabol, T.A., 2011. Representation of Bidirectional Ground Motions for Design Spectra in Building Codes. Earthquake Spectra 27, 927–937. https://doi.org/10.1193/1.3608001

Stucchi, M., Meletti, C., Montaldo, V., Crowley, H., Calvi, G.M., Boschi, E., 2011. Seismic Hazard Assessment (2003–2009) for the Italian Building CodeSeismic Hazard Assessment (2003–2009) for the Italian Building Code. Bulletin of the Seismological Society of America 101, 1885–1911. https://doi.org/10.1785/0120100130

CHAPTER 6

6 Conclusive remarks

6.1 Major development and results

Seismically isolated structures have superior performances with respect to standard structures for seismic intensities lower than or equal to the design level and they are characterised by a reduced probability of damage, especially for sites with medium seismic hazard levels. Despite this good behaviour under design actions, the reliability of code conforming isolated structures under high level actions may be unsatisfactory. The thesis main focuses on this topic, in order to understand this unacceptable behaviour and provide suggestions for improving design methods. The main reasons of this shortcoming are mainly two and they are strongly interconnected: the former concerns the response under increasing loads characterised by the so called “cliff edge effect”, that is an abrupt transition from an operativity condition to the collapse; the latter concerns the safety factors used in the design that may be too low to ensure an acceptable annual rate of collapse.

More in detail, this thesis analysed the annual rate of failure of seismically isolated buildings considering two performance levels, *global collapse* (GC) and *usability preventing damage* (*UPD*), through a deep insight in many different topics related to the whole risk assessment framework.

The major findings of this study can be summarized as follow

- Isolated buildings can be considered as an in-series system composed by the isolation system and the superstructure. Both of them take major role in the final reliability of the whole system. Moreover, high damping rubber bearings may exhibit different collapse mechanisms based on their mechanical and geometric characteristics (shape factors). Consequently, a multi-criteria approach has been developed to identify the collapse limit.

- Nowadays, existing models are not able to describe all the complex features of the HDRB response. at the same time. Two of the most advanced models have been used in the risk assessment, the *HDR bearing element* (Kumar model) and the *Kikuchi bearing element* (Kikuchi model). Both of them have been critically analysed and compared, highlighting strength and weakness of their features. Moreover, based on an extensive experimental investigation, both of them have been calibrated, showing their capabilities in simulate different hysteretic behaviours typical of high damping rubber bearings up to collapse conditions. For the superstructure modelling and the hazard definition state-of-the-art methods and tools have been implemented. The use of refined models has led to original results about the collapse modalities of code conforming seismic isolated structures. Part of this work has been developed within the *RINTC project*, supported by the National Department of Civil Protection.
- A set of selected case studies of new seismically isolated buildings and existing buildings retrofitted with rubber bearings have been assessed, defining the performance levels for *GC* and *UPD* for all of them through risk analysis. These results are grouped in different chapters based on the specific isolator model used. A specific chapter has been dedicated to the effects of model parameter uncertainties on the reliability results. An original statistical model has been developed to describe the variability of bearing mechanical parameters. The results have shown that this variability does not affect significantly *GC* or *UPD* results. At the end of each chapters, all the annual rates of collapse and the annual rates of damage are resumed, showing that annual rates of failure are strongly affected by the hazard site, or, more precisely, by the hazard trend after the design level. For L'Aquila site, *GC* rates are not in compliance with the code target while, for Naples site, *GC* are in accordance with the code target. On the contrary, there are no significant differences between new isolated buildings and retrofitted buildings. This result highlights that the code conforming design procedures are not fully in compliance with the reliability level requested by the same code, especially for the L'Aquila

case studies. A solution could be found in the risk targeting approach that allows to achieve consistent performance levels for all the case studies.

- Risk analysis of different structural systems developed within the *RINTC project* have been obtained by using different hazard descriptions, so the relevant comparison of performances led to qualitative conclusions only. In the last part of the thesis the intrinsic role of the hazard on the failure probability has been investigated. To this aims, the PSHA has been completely re-evaluated using the Reassess v.2.0 software and Lanzano's *GMPE*. A first comparison of the hazard curves showed a non-coherent ratio between the hazard levels of the three *GMPEs*. Moreover, the procedure of *CS* has been carried out to select a new set of records to perform the risk assessment on two case studies of isolated structure. A significant reduction of *GC* rates is registered for the new set of records based on Lanzano *GMPE.*
- The sets of records defined for the three different *GMPEs* have been also studied to understand the real relationship between them using an innovative procedure to calculate directly the hazard curves from the sets of records for any period and any *IM*. In this way a real comparison of the hazard defined by the record selections has been carried out, highlighting the different hazard levels for the three *GMPE* used.

6.2 Future development

The work carried out in this Thesis is a preliminary study regarding the reliability of seismically isolated buildings equipped with high damping rubber bearings. Many problems have been highlighted but further investigations are required to provide more general and robust conclusions. Only a small range of isolation periods has been considered (2.5-3.5s), whereas recently technological advancements are pushing forward to reach periods higher than 4s. In this new range of periods the dynamic behaviour of isolated systems could influence the reliability and also the hazard trends over the design condition could be completely different. Moreover, the reliability analysis should be also assessed using advanced probabilistic method other than *CS,* e.g. Subset simulation (Au and Beck 2001) as in Scozzese et al. (2019).

A further investigation is also required for what concerns the assessment of seismic performance of seismically isolated buildings by estimating the mean annual frequency of exceeding of specific engineering demand parameters, instead of the use of simpler *GC* and *UPD,* in order to obtain a better description of damage (peak story drift ratio, peak residual story drift ratio, peak floor acceleration).

There is also a need to extend these studies to other structural systems (e.g. perimeter braced and moment resisting steel frames, masonry building) as also highlighted in Kitayama and Constantinou (2018).

Regarding the modelling of rubber bearings, there is a need of including in a single model all those aspects of high damping rubber bearing that take role under extreme loadings.

6.3 Chapter’s references

Au S.K., Beck J.L., 2001. Estimation of small failure probabilities in high dimensions by subset simulation, Probabilistic Engineering Mechanics. 16 (2001) 263–277. doi:10.1016/S0266-8920(01)00019-4.

Scozzese F., Tubaldi E., Dall’Asta A. (2019). Seismic risk sensitivity of structures equipped with anti-seismic devices with uncertain properties. Structural Safety, Vol.77, 30-47

Kitayama, S., Constantinou, M.C., 2019. Probabilistic seismic performance assessment of seismically isolated buildings designed by the procedures of ASCE/SEI 7 and other enhanced criteria. Engineering Structures 179, 566–582. https://doi.org/10.1016/j.engstruct.2018.11.014

Acknowledgement
The author gratefully acknowledgement prof. Enrico Tubaldi and prof. John Douglas for the valuable discussions and the useful suggestions provided to develop part of the thesis during the period spent in Glasgow at Strathclyde University – Civil & Environmental Engineering department.